# Prediction of dynamic loads and induced vibrations in stall

**Thirstrup Petersen, J.; Aagaard Madsen , Helge; Björck, A.; Enevoldsen, P.; Øye, S.; Ganander, H.; Winkelaar, D.**

*Publication date:*
1998

*Document Version*
Publisher's PDF, also known as Version of record

RISØ

Risø-R-1045(EN)

# Prediction of Dynamic Loads and Induced Vibrations in Stall


**Jørgen Thirstrup Petersen, Risø**
**Helge Aagaard Madsen, Risø**
**Anders Björck, FFA**
**Peder Enevoldsen, Bonus Energy A/S**
**Stig Øye, DTU**
**Hans Ganander, Teknikgruppen AB**
**Danny Winkelaar, ECN**


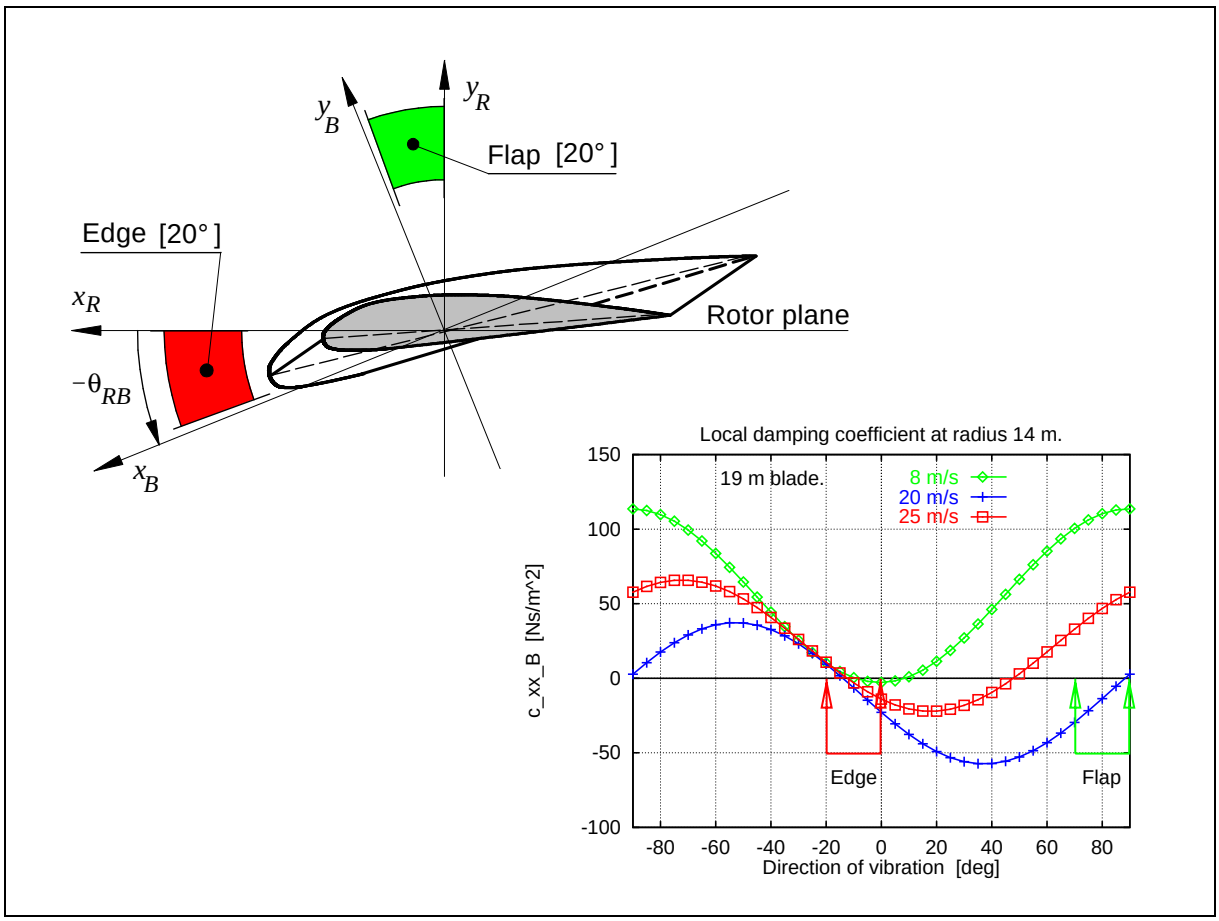



**Risø National Laboratory, Roskilde**
**May 1998**

**Abstract** Results from research in an EC Joule-III project and from national projects are presented. The objectives are improvement of design methods for stall regulated wind turbines with emphasis on stall induced vibrations and dynamic stall. The primary concern is limitation of the edgewise vibrations in the fundamental blade natural mode shape, which have caused trouble on modern wind turbines of approximate size 500 kW nominal power and 40 m rotor diameter. A theoretical study of quasi-steady aerodynamics confirms that the vibrations are driven basically by energy supplied from the aerodynamic forces during stalled operation. This energy exchange is equivalent to negative aerodynamic damping. The theoretical approach identifies the main parameters controlling the phenomenon. These parameters describe the steady and the dynamic airfoil characteristics, the overall aerodynamic layout of the blade, e.g. chord length and twist, the structural properties of the blade, e.g. structural damping and properties controlling the resulting vibration direction. Furthermore, full aeroelastic calculations and comparison with measurements show that the properties of the supporting structure, i.e. the main shaft, the nacelle and the tower, are important, as the global vibration of the rotor on its support may exchange energy with the blade vibration, when the blade natural frequency is close to one of the frequencies of the coupled rotor tilt-yaw mode shapes, usually denoted the global rotor whirl frequencies. It is confirmed that the influence of changing the primary design parameters can be determined by use of qualified aeroelastic calculations. Presented design guidelines therefore build on both the simple quasi-steady models, which can be used for the preliminary choice of the design variables mentioned above, and on full aeroelastic calculations. The aeroelastic calculations refine the design basis and should be used for choosing the final design variables and for final verification of the design. Through this design procedure it is possible to assess the required safety margin against stall induced vibrations.

---

Research funded in part by THE EUROPEAN COMMISSION in the framework of the Non Nuclear Energy Programme JOULE III. EC Contract JOR3-CT95-0047. STALLVIB.

Parts of the work performed by Risø has been funded by The Danish Ministry of Energy through the projects *Kantsvingninger i Stall*, EFP-96 contract ENS-1363/96-0001, and *Program for forskning i aeroelasticitet*, EFP-97 contract ENS-1363/97-0002.

---

ISBN 87–550–2384–3
ISBN 87–550–2437–8 (Internet)
ISSN 0106–2840

Information Service Department · Risø · 1998

# Table of contents

# Preface

The results presented in this report are obtained through research carried out in relation to stall induced vibrations during the years 1996 and 1997. The results are obtained partly in an international EC project and partly in national projects. The research subjects of these projects have supplemented each other, and is has therefore been decided to gather the results in a common report, finding this more coherent presentation beneficial for the presentation of the results.

Risø has been the coordinator of an EC JOULE-III project *Prediction of Dynamic Loads and Induced Vibrations in Stall*, STALLVIB. The main objectives of this project are

- Improvement of the *prediction capabilities* with respect to dynamic loads in stall and stall-induced vibrations and
- establishment of *guidelines* aiming at achieving *safety margins* against stall induced vibrations.

During the same period the Danish participants in the STALLVIB project have taken part in a Danish EFP project *Kantsvingninger i stall*, where the main objectives have been

- Analysis of existing measurements and *identification* of important *parameters*,
- application of *simplified models* to support identification of parameters and to provide *physical insight* and
- application of *aeroelastic calculations* for verification of models.

The participants in the STALLVIB project are:

| Institution | Nationality | Synonym | Participants |
|---|---|---|---|
| Teknikgruppen AB | SE | TA | Hans Ganander |
| Aeronautical Research Institute of Sweden | SE | FFA | Anders Björck |
| Netherlands Energy Research Foundation | NL | ECN | Danny Winkelaar<br>Arno Brand |
| Delft University of Technology | NL | DUT | Albert Bruining |
| Imperial College | UK | IC | Mike Graham |
| The Technical University of Denmark | DK | DTU | Stig Øye |
| Bonus Energy A/S | DK | Bonus | Peder Enevoldsen |
| Risø National Laboratory | DK | Risø | Helge Aagaard Madsen<br>Jørgen Thirstrup Petersen |

The synonyms listed in the table are used when referencing to the participants throughout the report.

Another report is written mainly to document analysis of measurements used for development of dynamic stall models within the STALLVIB project:

> Madsen, H.Aa., Petersen, J.T, Bruining, A., Brand, A. and Graham. M. *Field Rotor Measurements. Data sets prepared for analysis of stall hysteresis.* Risø-R-1046(EN). Risø National Laboratory, Roskilde, May 1998.

# 1 Executive summary

The objectives of the research work are related to improvement of design methods in the area of dynamic stall, 3-D flow effects and stall induced vibrations. Specifically, the work aims at supporting and improving the design phase, where appropriate safety margins must be obtained. The area of work is illustrated in Figure 1.1, which shows an example of stall induced edgewise vibrations measured on a prototype blade. The left time trace shows the quite normal, damped moment dominated by gravity before development of the vibrations, and the right trace shows the moment after the dominating, undamped vibrations at the edgewise natural frequency have started.

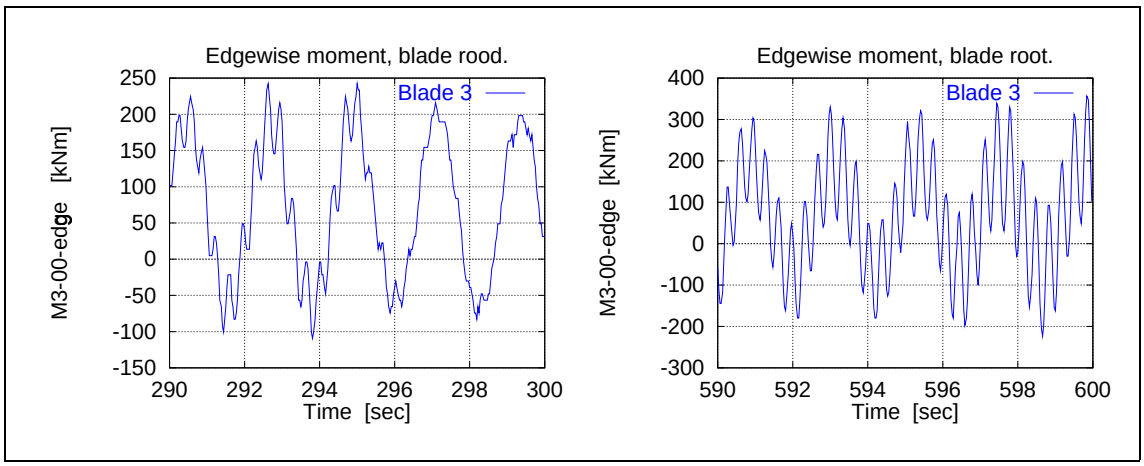


*Figure 1.1. Edgewise blade root bending moment for a 500 kW turbine during operation in stall.*

Below a summary of the covered tasks is presented. The headings are

- analysis by linearized models for the quasi-steady aerodynamics,
- demonstration of the influence of changing the quasi-steady airfoil data,
- analysis of the influence of dynamic pitch of the airfoils,
- development of engineering models for stall hysteresis,
- implementation of the engineering models in aeroelastic codes,
- analysis of coupling between the edgewise blade vibrations (*local blade whirl*) and the supporting structure (*global rotor whirl*),
- analysis of measurements and comparison of measured wind turbine response with response calculated with aeroelastic codes,
- investigation of the influence on edgewise vibration of the blade from a variation of blade and turbine parameters, and
- derivation of design guidelines.

Basically, the objectives of the project are related to improvement of design methods aiming at preventing the occurrence of stall induced vibrations. The project work has confirmed that the source of stall induced vibrations is the energy, which the aerodynamic forces under special operational conditions can supply to the blades, when they vibrate in a natural mode. Such forces have the same direction as the vibration velocity of the blade, and they act as

damping forces. Usually, we denote the phenomenon negative aerodynamic damping, and when it occurs, we face a potentially selfexciting structure, as the vibrations will increase, if the energy is not removed, for example through structural damping.

### Quasi-steady analysis

Due to the importance of this physical condition a thorough analysis has – as a first step – been carried out based on quasi-steady aerodynamics and forced vibration of a single blade in its natural mode. Although not complete, this simplified analysis is capable of explaining the basic physics and to identify the majority of important parameters. The analysis is presented in Section 2, where also simple numerical examples show the basic influence of the main parameters, which are

- the airfoil characteristics, i.e. both absolute values and slopes of the lift- and the drag-curves, $C_L$ and $C_D$,
- the blade mode shapes, i.e. the size and the direction of the blade deflection along the radius of the blade, and
- the planform and the structural properties of the blade.

### Examples of modifications

In Section 3 examples of the influence of different modifications are presented. In Section 3.1 basic changes of typical airfoil data are carried out, mainly to demonstrate the importance of chosen parameters and to provide some insight into the possibilities. The examples concentrate on the local effects, and the requirements to the rotor power output are kept rather loose during this part of the investigation. A more realistic example, aiming at improving the damping conditions without seriously damaging the power output, is presented in Section 3.2, showing how a proper choice of parameters can improve the damping conditions significantly.

A few, but very fundamental examples are presented to show the influence of sectional properties, which can be connected to an angular orientation in the cross sectional plane. The influence of changing this orientation uniformly along the blade is investigated. The first example covers the influence of uniform structural pitch offset along the blade, as presented in Section 3.3. This controls the vibration direction for the mode shapes without influencing the aerodynamics, which has proven to be essential for obtaining optimal damping in the edgewise direction. The second example shows the influence of uniform angle of attack offset along the blade, as presented in Section 3.4. This gives a result, which seen from the damping and the power-production point of view, is identical to the first case, as the structural and the aerodynamical properties are offset with respect to angular orientation. These two examples point out two different ways of obtaining the same important effect. The first is connected to structural properties and the second to airfoil properties. Of course, these properties can not be considered completely independent, as they are connected through the geometry to some extent. The third and the last case is presented in Section 3.5, and shows the influence of tip pitch change. Basically, this leads to a transformation of the damping properties along the wind speed axis, whereas the damping level is almost unaffected. For instance, if a given blade has a minimum negative damping at a certain wind speed, a positive change of tip pitch – the trailing edge moved in downwind direction – will shift this minimum towards higher wind speeds and only change the level slightly. This might suggest a way of using pitching for keeping the minimum damping range outside the immediate operation wind speed range.

Based on the fundamental expressions for aerodynamic damping and logarithmic decrement the influence of changing the blade mass and stiffness is investigated in Section 3.6. The

resulting damping is directly compared with the structural damping, thus providing an overview of the stability margin as function of the resulting natural frequency. From this analysis it can be concluded that the blade structure should be designed for the highest possible edgewise stiffness, even at the expense of added weight, in order to improve the stability margin for the edgewise vibrations.

### Influence of dynamic pitch

The influence of angular rotations of the blade cross sections about the blade axis, corresponding to blade torsion, is investigated in Section 4. It is found that if the rotations are in phase or in counter-phase with the transverse vibrations of the blade, the rotations will have negligible influence on the damping. If, on the other hand, the rotations are leading or lagging the transverse deformation, they might influence the aerodynamic damping. In the leading case by making the damping more positive and in the lagging case by making the damping more negative. No evidence has been found that the rotations should be out of phase.

### Dynamic stall models

The development and implementation of the engineering models for stall hysteresis is described in Section 5. Examples of the influence from different parameter settings in the models are presented. Also, the basic influence from the models on aerodynamic damping in both the fundamental edgewise and flapwise mode shapes is demonstrated here. The 3-D effects have not been addressed specifically, but as they influence the resulting airfoil data, they might be important, if this influence is significant on the outboard part of the blade.

### Coupling between edgewise vibrations and supporting structure

A systematic investigation of the coupling between the edgewise vibrations and the supporting structure – the main shaft, the nacelle and the tower – is presented in Section 6. This coupling has proven to be important as to whether the edgewise vibrations develop or not. The whirl modes of the rotor, which we denote the *global rotor whirl modes*, play an important role in this coupling. In these modes the rotor shaft changes orientation in space, and the rotor center describes an elliptical orbit. Four rotor whirl modes and corresponding frequencies might be of importance. One pair of modes are the $1^{st}$ rotor yaw and tilt modes, and another pair are the $2^{nd}$ rotor yaw and tilt modes. For the wind turbines we consider in the present work, only the $2^{nd}$ modes are involved in the coupling, but generally all modes should be considered. For each pair of modes, for instance the $2^{nd}$ rotor modes, one whirling frequency corresponds to backward whirl of the rotor, and the other corresponds to forward whirl, meaning that the hub moves along the elliptical path either in a direction opposite the rotor rotation (backwards) or in the same direction (forwards). If one of these frequencies, as seen from the frame of reference rotating with the blades, is close to the blade edgewise frequency, the edgewise blade vibration might be easier developed and maintained than otherwise, probably depending on the actual structural and aerodynamic damping of the global whirl modes.

In Section 6.2 the edgewise blade bending modes for a 3-bladed wind turbine are described with the rotor at rest and one blade in a vertical position. In this situation two such modes exist with almost the same frequency. In one of these modes the vertical blade is at rest and the other two vibrate in counter-phase. In the other mode the vertical blade vibrates in counter-phase with the other two. In this mode the amplitude of the vertical blade is two times the amplitude of each of the other two blades. Both edgewise modes are in dynamic equilibrium with respect to moment about the main shaft, but a resulting harmonic force arises in the rotor plane due to the inertia forces. As the resulting force rotates relative to

the hub with the edgewise frequency and describes an elliptical orbit, resembling the path of the hub in the *global rotor whirl modes*, we denote the associated blade deformation the *local blade whirl*. A simple model of the *in-plane* force is presented in Section 6.3. This model, together with a model for the rotor whirl modes presented in Appendix B, illustrates the basics in the coupling between the edgewise blade vibrations and the rotor modes. The full aeroelastic codes include the more complex details of this coupling, and it is concluded from calculations that the aeroelastic programs can support the designer, when decisions are made about masses and stiffnesses, which influence the whirling frequencies and the coupling.

### Comparison of measurements and aeroelastic calculations

In Section 7 full scale measurements performed by Bonus Energy A/S are compared with aeroelastic calculations. Initially, results from a stand still case at 24.2 m/s are presented in order to show the level of fundamental agreement with respect to natural frequencies. Acceptable agreement between measured and simulated frequencies is demonstrated, although the energy content is somewhat underestimated by the simulations at higher frequencies. Comparisons are also carried out for normal operation at two wind speeds, one below stall at 9.5 m/s, and one after stall onset at 23.2 m/s. The comparisons show that the major difference is at the blade fundamental flapwise and edgewise frequencies, where the simulations overestimate the response – most severely at the high wind speed. Addition of a rather limited amount of structural damping for the edgewise mode shape – 1% logarithmic decrement – is sufficient to reduce the calculated response to an energy level at the natural frequencies well below the measured level. This demonstrates how sensitive the response calculation is to the actual damping and that the demand to the accuracy of the damping in the model is of this order of magnitude – better than 1% – when absolute agreement is the aim. At present, the aeroelastic models cannot meet such a demand, primarily due to uncertainty with respect to structural damping and aerodynamic parameters. Still, the models are believed to be capable of determining relative influence from changes of a range of important parameters with good accuracy.

### Full scale parametric studies

Examples of parametric changes on a full scale turbine are shown in Section 8. For instance, it is shown that increasing the stiffness of the rotor shaft results in a reduction of the edgewise vibrations, which – although not shown in the comparisons – has been obtained for a real turbine of similar type. The conclusion from the comparisons is that the aeroelastic codes should be used primarily for determining the relative changes in response originating from changes of structural and aerodynamical properties.

### Design guidelines

The results from the investigations performed during the present work have been used for formulation of a set of design guidelines, particularly aiming at supporting the design of wind turbines with an adequate safety margin against stall induced vibrations. The guidelines are presented in Section 9.

Basically, the results confirm that the edgewise vibrations are caused by negative aerodynamic damping, i.e. energy supplied to the vibrating blade by the aerodynamic forces.

The analytical treatment of the aerodynamic damping based on quasi-steady aerodynamics in Section 2 shows that for a stall regulated turbine operating at constant maximum power in stall, any blade vibrations purely in the rotor plane (in-plane vibrations) will inevitably experience negative aerodynamic damping proportional to the power level. The edgewise

blade vibrations are close to having this direction, but due to blade pitch the edgewise mode has a direction skew to the plane. The conditions for vibrations perpendicular to the rotor plane (out-of-plane vibrations) are quite different and more favourable with respect to damping. The analysis shows that the damping in the out-of-plane direction is always positive, if the slope of the axial force curve versus free wind speed is positive. In particular, the slope of the airfoil lift is important for the axial force slope, i.e. the derivative of $C_L$ with respect to angle of attack, $\alpha$. If airfoils are chosen with this slope positive or close to zero in the whole operating range (a low lift airfoil) the aerodynamic damping for out-of-plane vibrations can be kept positive.

Further, the analysis in Section 2 shows how an arbitrary vibration direction is damped. This leads to the important result that by suitable selection of airfoil characteristics it is possible to design the blade aerodynamically such that positive damping is achieved in two ranges of vibration directions perpendicular to each other. More importantly, these ranges cover the directions, which a blade with proper structural design would have in its fundamental edgewise and flapwise mode shapes, respectively, and overall positive damping for the blade can be achieved. This is the main fundamental concept to avoid the occurrence of both edgewise and flapwise stall induced vibrations.

Combined with the more detailed analysis covering aerodynamical and structural modifications, stall hysteresis and full aeroelastic calculations in Sections 3, 5, 6 and 8, it is shown that the occurrence of stall induced vibrations is controlled primarily by properties related to 4 principal areas, which influence partly the aerodynamic damping, partly the structural damping and partly the properties of the complete structure with respect to either damping or amplification of an existing edgewise vibration:

1. The aerodynamic characteristics of the blade, represented by the steady and the dynamic lift and drag coefficients.
2. The structural characteristics of the blade, which influence the mode shape and the natural frequency. Especially, the orientation of the principal bending axes are of great importance, because the aerodynamic damping depends heavily on the resulting direction of the vibration.
3. The material and structural properties, which influence the structural damping of the blade.
4. The properties of the supporting structure, i.e. the main shaft, the nacelle and the tower. The rotor support participates in coupled mode shapes with the blades and influences the resulting blade movement and damping.

Considering a *new design*, where a great deal of freedom to choose design variables can be expected, the formulated *design guidelines* are in brief:

1. Base the airfoil choice on well documented airfoil data.
2. Choose airfoils, blade planform (chord, aerodynamic twist) and blade structural properties (stiffness, mass, mode shapes – i.e. amplitude and direction of deformation, structural damping, modal mass, modal stiffness and modal natural frequency) considering not only the rotor performance, but also the aerodynamic damping characteristics. Especially, the blade twist should be considered, not only in relation to power performance, but also in relation to mode shape vibration direction.
3. Use the quasi-steady approach presented in Section 2 to calculate the basic aerodynamic damping characteristics for a single blade, considering both the fundamental flapwise and edgewise mode shapes. If not satisfactory – repeat from 2.

4. Extend the quasi-steady analysis and include verified models for dynamic stall on both airfoil lift and drag. Still considering a single blade. If not satisfactory repeat from 2.
5. When the single blade analysis results in appropriate aerodynamic damping, continue the analysis by use of the full aeroelastic model, including verified models for stall hysteresis on both airfoil lift and drag. The structural model must have a sufficiently detailed representation of the blade bending modes and the rotor whirling modes.
6. Carry out full aeroelastic calculations for the wind speeds of interest. These wind speeds can to a wide extent be identified through the single blade analysis.
7. Investigate the damping characteristics by looking at the response at the blade natural flapwise and edgewise frequencies, for instance based on the power spectral densities of the blade root bending moments.
8. Repeat from 2 if the results are unsatisfactory.

In the situation where the designer is dealing with an *existing* wind turbine, the possibilities are much more limited. Still, it will often be possible to achieve considerable improvement of the damping by modifying the existing design, for instance by modifying the airfoil characteristics by use of different aerodynamic devices.

# 2 Basics of aerodynamic damping

When a wind turbine blade vibrates in a natural mode, the aerodynamic force on a section of the blade might have a component, which is proportional to the vibration velocity of the blade section. Such a force is experienced by the blade as a viscous damping force. In the present context we are interested in force terms arising in connection with velocities superimposed on the dominating velocity associated with the rigid body rotation of the blade due to rotor rotation. This principal velocity component together with the free wind velocity gives the main contribution to the force on the blade section, which results in the driving torque and the axial force. Velocities superimposed on the principal velocity contribute with a force, which with good approximation can be considered proportional to the superimposed velocity, and therefore act as a damping force – usually denoted the *aerodynamic damping.*

Under special operational conditions – primarily when the turbine is operating in stall – the aerodynamic damping force can be negative, meaning that the force and thus the flow supplies energy to the turbine structure. This results in a potentially self exciting system. For example, if the blade velocity originates from a vibration in a natural mode shape, a corresponding negative damping force will supply energy to the vibration, which increases, if the energy is not removed, e.q. through structural damping.

Below the basic physics of this damping phenomenon is explained in Section 2.1 by use of linearized, quasi-steady, 2-D aerodynamics for a blade section, describing the damping per unit length of the blade. We apply two equivalent approaches. One makes use of airfoil data directly and the other uses the blade power and axial force as independent variables. The reason that we introduce both types of variables is that when we later are going to discuss possibilities for increasing the aerodynamic damping by choose of suitable airfoil characteristics, we also have to consider the constraints on the power curve, e.g. constant power at high wind. Further, the integrated effect of the damping on a complete blade is described in Section 2.2 as modal damping related to the fundamental mode shapes of the blade.

In Section 2.1.3 the influence of the mode shape vibration direction is paid particular attention, as this proves to be very important for the resulting damping.

The theoretical part is accompanied by numerical examples, illustrating the influence of a wide range of the different parameters.

This quasi-steady theory proves to be adequate for identification of the main parameters in the physics behind the stall induced vibration phenomenon as confirmed by later performed full aeroelastic calculations and measurements. The theory is useful – even in the design phase – when identifying the areas of interest during the analysis of the complex problem for a flexible turbine operating under real conditions, where the dynamic stall and coupled mode shapes play an important role and modifies the quasi-steady results, but not the basic tendencies derived.

## 2.1 Local aerodynamic damping on a blade section

A section of the blade – as shown in Figure 2.1 – is considered, and with the notation in the figure a linearized expression for the aerodynamic damping is derived by use of quasi-steady, 2-D aerodynamics. In order to simplify the problem the influence of induction is neglected. This does not affect the fundamental conclusions, which can be drawn from the results. Initially, in Section 2.1.1 the local damping is expressed as function of the local airfoil data

directly. Alternatively, the damping can be expressed as function of the local power and axial force, which is shown in Section 2.1.2.

### 2.1.1 Damping expressed as function of airfoil data

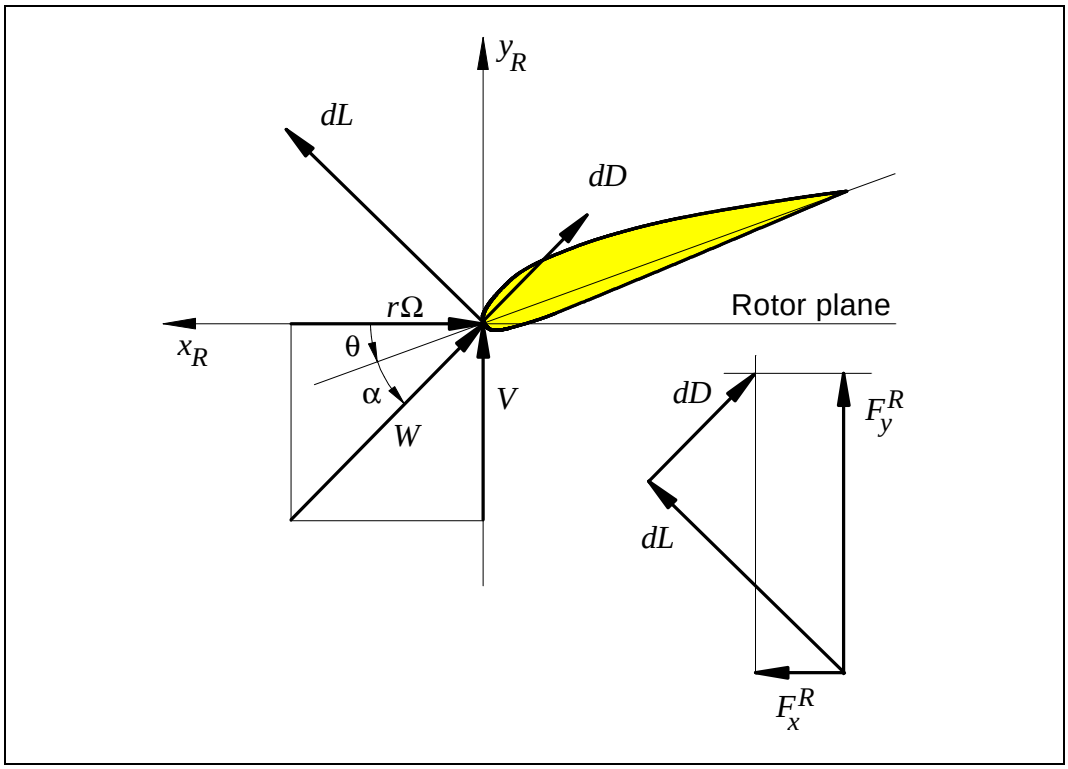


*Figure 2.1. Flow velocities and forces at a blade section.*

In Figure 2.1 and in the expressions below the symbols have the following meaning:

| | |
|---|---|
| $\Omega$ | is the angular velocity of the rotor, |
| $r$ | is the actual blade radius, i.e. the radial position of the considered cross section, |
| $V$ | is the wind speed, which is felt by the blade in the $y$-direction, |
| $W$ | is the resulting wind speed, |
| $\theta$ | is the local pitch-setting, i.e. the angle between chord and rotor plane, |
| $\alpha$ | is the angle of attack, |
| d$L$ | is the lift-force per unit length of the blade, |
| d$D$ | is the drag-force per unit length of the blade, |
| $F_x^R$ | is the resulting force per unit length in the $x_R$-direction – approximately corresponding to the edgewise direction – and |
| $F_y^R$ | is the resulting force per unit length in the $y_R$-direction – approximately corresponding to the flapwise direction. |

Using blade element theory the lift force component per unit length of the blade can more specifically be written

$$\mathrm{d}L = \mathrm{d}L(r,\alpha) = \frac{1}{2}\varrho c(r)W^2(r)C_L(r,\alpha) \ , \tag{2.1}$$

and the drag force component is accordingly written

$$\mathrm{d}D = \mathrm{d}D(r,\alpha) = \frac{1}{2}\varrho c(r)W^2(r)C_D(r,\alpha) \ . \tag{2.2}$$

Here, the meaning of the symbols are:

| | |
|---|---|
| $\varrho$ | air density, |
| $c(r)$ | length of chord at radius $r$, |
| $C_L(r,\alpha)$ | lift coefficient at radius $r$, which in addition is a function of the angle of attack, $\alpha$ and |
| $C_D(r,\alpha)$ | drag coefficient at radius $r$, which also is a function of the angle of attack, $\alpha$. |

The resulting wind speed, $W$, is obtained from

$$W = \sqrt{V^2 + r^2\Omega^2} \ . \tag{2.3}$$

The projection of the lift- and the drag-force onto the axes of the rotor coordinate system, $\{x_R, y_R\}$, gives the resulting force-vector in $R$-coordinates

$$\left\{ \begin{array}{c} F_x^R \\ F_y^R \end{array} \right\} = \left[ \begin{array}{cc} \sin(\gamma) & -\cos(\gamma) \\ \cos(\gamma) & \sin(\gamma) \end{array} \right] \left\{ \begin{array}{c} \mathrm{d}L \\ \mathrm{d}D \end{array} \right\} \ , \tag{2.4}$$

where the transformation angle, $\gamma$, and the trigonometry relations are derived from Figure 2.1:

$$\gamma = \theta + \alpha \ ; \ \cos\gamma = \frac{r\Omega}{W} \ ; \ \sin\gamma = \frac{V}{W} \ . \tag{2.5}$$

In more concentrated form Equation 2.4 is written

$$\left\{F^R\right\} = [T_{LR}] \left\{F^L\right\} \ . \tag{2.6}$$

The components of this force-vector are now linearized by expanding each component in a Taylor-series at a point of operation corresponding to $V = V_0$ and $r\Omega = r\Omega_0$. The linearization is obtained by truncation, so that only the terms of first order are retained in the series.

The expansions result in the $x_R$-component

$$F_x^R\left(\Delta V, \Delta(r\Omega)\right) \simeq F_x^R\left(V_0, r\Omega_0\right) + \frac{\partial F_x^R\left(V_0, r\Omega_0\right)}{\partial V}\Delta V + \frac{\partial F_x^R\left(V_0, r\Omega_0\right)}{\partial (r\Omega)}\Delta(r\Omega) \ , \tag{2.7}$$

and in the $y_R$-component

$$F_y^R\left(\Delta V, \Delta(r\Omega)\right) \simeq F_y^R\left(V_0, r\Omega_0\right) + \frac{\partial F_y^R\left(V_0, r\Omega_0\right)}{\partial V}\Delta V + \frac{\partial F_y^R\left(V_0, r\Omega_0\right)}{\partial (r\Omega)}\Delta(r\Omega) \ . \quad (2.8)$$

These equations express the force as function of the increments in the free wind speed, $\Delta V$, and the speed originating from the rotation, $\Delta(r\Omega)$, respectively, which both are modified by the movement of the blade due to elastic deformation. By arranging the Equations 2.7 and 2.8 in a matrix equation we obtain

$$\left\{ \begin{array}{c} F_x^R \\ F_y^R \end{array} \right\} \simeq \left\{ \begin{array}{c} F_{x0}^R \\ F_{y0}^R \end{array} \right\} + \left\{ \begin{array}{cc} \frac{\partial F_x^R}{\partial (r\Omega)} & \frac{\partial F_x^R}{\partial V} \\ \frac{\partial F_y^R}{\partial (r\Omega)} & \frac{\partial F_y^R}{\partial V} \end{array} \right\} \left\{ \begin{array}{c} \Delta(r\Omega) \\ \Delta V \end{array} \right\} \ . \quad (2.9)$$

According to the conventions defined in Figure 2.1, the increments in velocities as seen from the blade – due to movement of the blade section relative to the instantaneous flow field – correspond to

$$\Delta(r\Omega) = \dot{x}_R = \frac{\mathrm{d}x_R}{\mathrm{d}t} \quad (2.10)$$

for the $x_R$-direction and

$$\Delta V = -\dot{y}_R = \frac{\mathrm{d}y_R}{\mathrm{d}t} \quad (2.11)$$

for the $y_R$-direction, respectively.

This results in the matrix-equation, which expresses the linearized aerodynamic force resulting from the motion of the blade itself

$$\left\{ \begin{array}{c} F_x^R \\ F_y^R \end{array} \right\} \simeq \left\{ \begin{array}{c} F_{x0}^R \\ F_{y0}^R \end{array} \right\} - \left[ \begin{array}{cc} -\frac{\partial F_x^R}{\partial (r\Omega)} & \frac{\partial F_x^R}{\partial V} \\ -\frac{\partial F_y^R}{\partial (r\Omega)} & \frac{\partial F_y^R}{\partial V} \end{array} \right] \left\{ \begin{array}{c} \dot{x}_R \\ \dot{y}_R \end{array} \right\} \ . \quad (2.12)$$

Defining the aerodynamic damping matrix by

$$\left[c_a^R\right] = \left[ \begin{array}{cc} c_{xx}^R & c_{xy}^R \\ c_{yx}^R & c_{yy}^R \end{array} \right] = \left[ \begin{array}{cc} -\frac{\partial F_x^R}{\partial (r\Omega)} & \frac{\partial F_x^R}{\partial V} \\ -\frac{\partial F_y^R}{\partial (r\Omega)} & \frac{\partial F_y^R}{\partial V} \end{array} \right] \ , \quad (2.13)$$

and the section velocity by

$$\left\{\dot{u}^R\right\} = \left\{ \begin{array}{c} \dot{x}_R \\ \dot{y}_R \end{array} \right\} \ , \quad (2.14)$$

Equation 2.12 can be written

$$\left\{F_a^R\right\} \simeq \left\{F_{a0}^R\right\} - \left[c_a^R\right]\left\{\dot{u}^R\right\} \ , \quad (2.15)$$

where still the upper index $R$ indicates that the equation refers to the rotor coordinate system $\{x_R, y_R\}$. Below, we can assume that the mean force is zero, $\{F^R_{a0}\} = \{0\}$, without loss of generality in the conclusions.

The derivation of the terms in the damping matrix, which is straightforward, is omitted here. The single matrix terms – the damping coefficients – are

$$c^R_{xx}(r,V) = \frac{1}{2}c\varrho\frac{r\Omega}{W}\left[\left(\frac{2r^2\Omega^2+V^2}{r\Omega}\right)C_D - V\frac{\partial C_D}{\partial\alpha} - VC_L + \frac{V^2}{r\Omega}\frac{\partial C_L}{\partial\alpha}\right]. \tag{2.16}$$

$$c^R_{xy}(r,V) = \frac{1}{2}c\varrho\frac{r\Omega}{W}\left[-VC_D - r\Omega\frac{\partial C_D}{\partial\alpha} + \left(\frac{2V^2+r^2\Omega^2}{r\Omega}\right)C_L + V\frac{\partial C_L}{\partial\alpha}\right]. \tag{2.17}$$

$$c^R_{yx}(r,V) = \frac{1}{2}c\varrho\frac{r\Omega}{W}\left[-VC_D + \frac{V^2}{r\Omega}\frac{\partial C_D}{\partial\alpha} - \left(\frac{2r^2\Omega^2+V^2}{r\Omega}\right)C_L + V\frac{\partial C_L}{\partial\alpha}\right]. \tag{2.18}$$

$$c^R_{yy}(r,V) = \frac{1}{2}c\varrho\frac{r\Omega}{W}\left[\left(\frac{2V^2+r^2\Omega^2}{r\Omega}\right)C_D + V\frac{\partial C_D}{\partial\alpha} + VC_L + r\Omega\frac{\partial C_L}{\partial\alpha}\right]. \tag{2.19}$$

The $c^R_{xx}$-term corresponds to pure in-plane blade movement, i.e. movement parallel with the $x_R$-axis and mainly edgewise blade movement, and the $c^R_{yy}$-term corresponds to out-of-plane blade movement, i.e. movement parallel with the $y_R$-axis and mainly flapwise blade movement. Usually, the blade movement direction will describe an angle relative to the rotor plane due to the twist of the blade principal bending axis, meaning that both $x_R$- and $y_R$-components are present. In this case both columns in the damping matrix are involved in the damping expression. This direction dependency is addressed in detail in Section 2.1.3.

### Numerical example

In order to illustrate the relative influence of the airfoil characteristics – $C_D$, $\partial C_D/\partial\alpha$, $C_L$ and $\partial C_L/\partial\alpha$ – in the expressions for damping in Equations 2.16-2.19, typical airfoil data are chosen, and the values of the single terms are calculated. The actual airfoil data are shown in Figure 2.2, and the results for the diagonal terms in the damping matrix, $c^R_{xx}$ and $c^R_{yy}$, are shown in Figure 2.3 and in Figure 2.4, respectively.

The main data for this example are listed in Table 2.1.

*Table 2.1. Main data for numerical example*

| | | |
|---|---|---|
| $c$ | = | 1.06 m |
| $\varrho$ | = | 1.23 kg/m$^3$ |
| $r$ | = | 14.00 m |
| $\Omega$ | = | 3.04 rad/s |
| $\theta$ | = | 2.00° |
| Airfoil data in Figure 2.2 | | |

In Figure 2.3 it is observed that the resulting damping coefficient, $c^R_{xx}$, is negative in the shown wind speed range. All terms, except the one connected to the drag, $C_D$, give negative contributions. For $c^R_{yy}$ all terms are positive, except the $\partial C_L/\partial\alpha$-term, as shown in Figure 2.4.

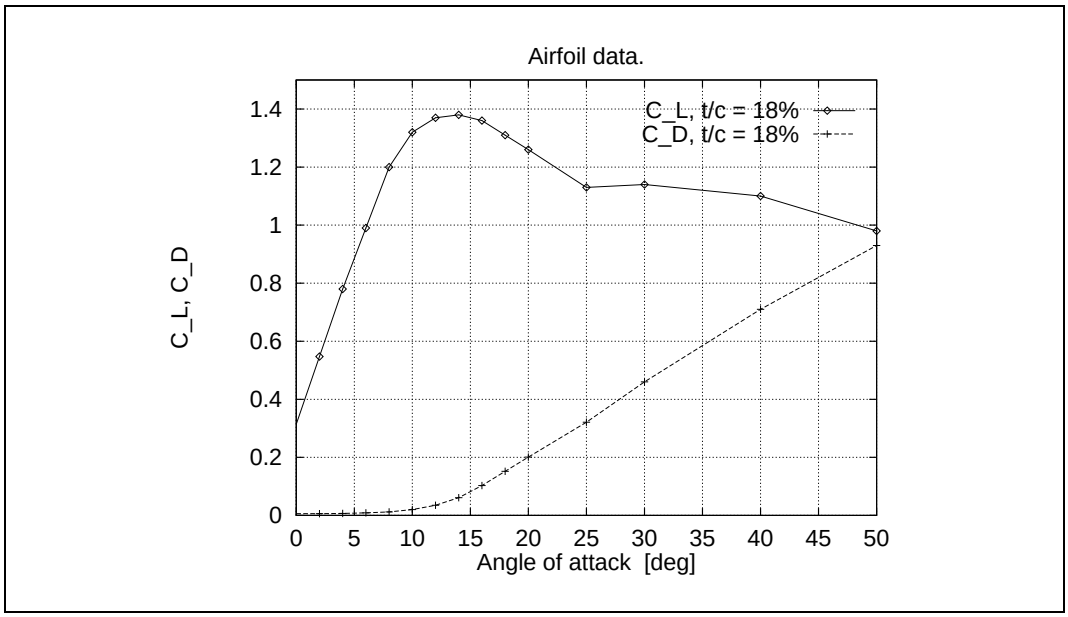


*Figure 2.2. Example of airfoil data for a $t/c = 18\%$ section.*

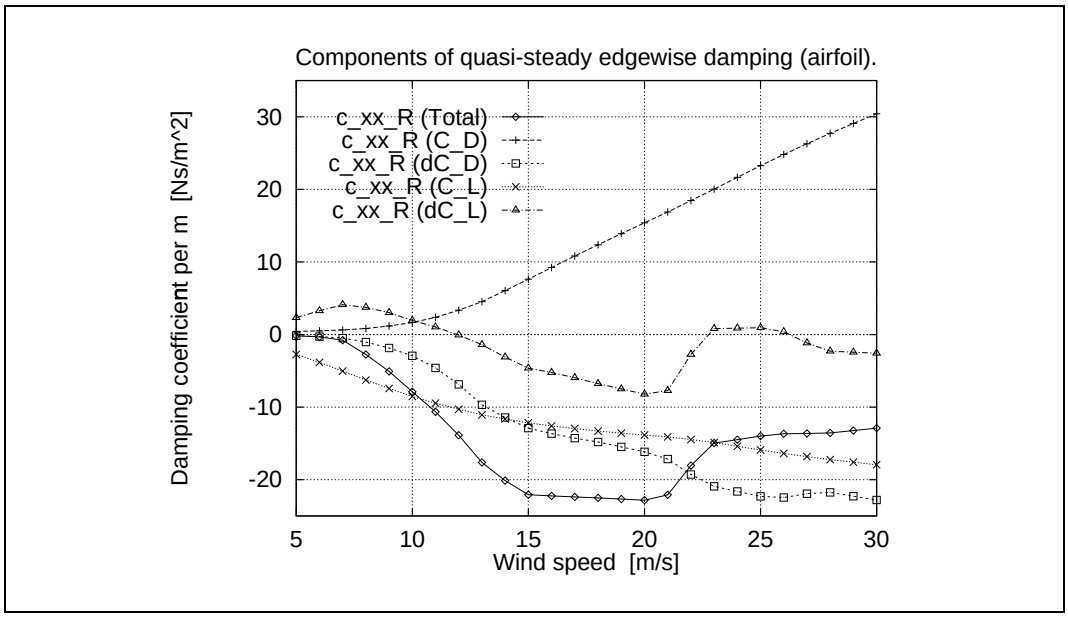


*Figure 2.3. Damping coefficient $c_{xx}^R$ and its components with reference to the $R$-coordinate system.*

### 2.1.2 Damping expressed as function of power and axial force

By combining and rearranging Equations 2.16-2.19 and substituting expressions for power and axial force, the damping can be expressed as function of the new independent variables power and force per unit length, $P_u$ and $F_u$, where

$$P_u = P_u(r,V) = r\,\Omega F_x^R = \frac{1}{2}\,\varrho\, c\, r\Omega W\,(VC_L - r\,\Omega\, C_D)\ , \tag{2.20}$$

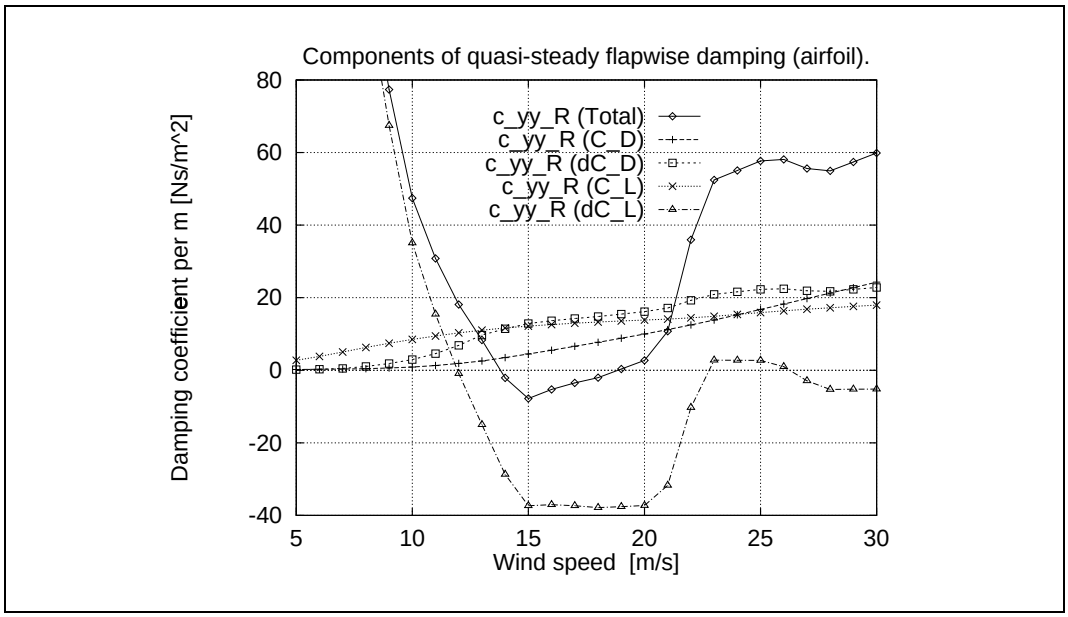


*Figure 2.4. Damping coefficient $c_{yy}^R$ and its components with reference to the R-coordinate system.*

and

$$F_u = F_u(r,V) = F_y^R = \frac{1}{2}\varrho c W (r\Omega C_L + V C_D) \ . \tag{2.21}$$

Using Equation 2.20 and further that

$$c_{xy}^R = \frac{\partial F_x^R}{\partial V} = \frac{1}{r\Omega}\frac{\partial P_u}{\partial V} \tag{2.22}$$

in combination and reduction of Equations 2.16 and 2.17, results in elimination of the airfoil data, expressing the edgewise in-plane damping as function of the power and the derivative of the power with respect to the free wind speed

$$c_{xx}^R = -\frac{2}{r^2\Omega^2}P_u + \frac{V}{r^2\Omega^2}\frac{\partial P_u}{\partial V} \ . \tag{2.23}$$

Equivalently, using Equation 2.21 and further that

$$c_{yy}^R = \frac{\partial F_y^R}{\partial V} = \frac{\partial F_u}{\partial V} \tag{2.24}$$

in combination and reduction of Equations 2.18 and 2.19, results in elimination of the airfoil data, expressing the flapwise, out-of-plane damping as function of the axial force and the derivative of the axial force with respect to the free wind speed

$$c_{yx}^R = -\frac{2}{r\Omega}F_u + \frac{V}{r\Omega}\frac{\partial F_u}{\partial V} \ . \tag{2.25}$$

Collecting and ordering these equations gives the terms of the damping matrix equivalent to Equations 2.16-2.19, but now with the independent variables power and axial force per unit length instead of the airfoil data:

$$c_{xx}^R(r,V) = -\frac{2}{r^2\Omega^2}P_u(r,V) + \frac{V}{r^2\Omega^2}\frac{\partial P_u(r,V)}{\partial V} \ . \tag{2.26}$$

$$c_{xy}^R(r,V) = \frac{1}{r\Omega}\frac{\partial P_u(r,V)}{\partial V} \ . \tag{2.27}$$

$$c_{yx}^R(r,V) = -\frac{2}{r\Omega}F_u(r,V) + \frac{V}{r\Omega}\frac{\partial F_u(r,V)}{\partial V} \ . \tag{2.28}$$

$$c_{yy}^R(r,V) = \frac{\partial F_u(r,V)}{\partial V} \ . \tag{2.29}$$

From these equations a few important characteristics can be observed. $c_{xx}^R$ corresponds to in-plane movement, and the damping in this direction will always be negative if the blade section produces power and the slope of the power curve is negative or zero. The out-of-plane damping on the section, $c_{yy}^R$, is positive if the slope of the axial force curve is positive. Again, a real blade mode has components in both directions, and this makes it possible for an edgewise mode to be positively damped, as it – mainly due to pitch of the principal bending axes – has a component out of the rotor plane.

### Numerical example

The relative influence of the power and axial force characteristics on the damping coefficients in Equations 2.26-2.29 is illustrated by use of the same airfoil section and data as presented in Section 2.1.1, Figure 2.2. The main data are listed in Table 2.1. The local power per unit length, $P_u$, and the derivative with respect to free wind speed, $\partial P_u/\partial V$, are shown in Figure 2.5. The local axial force per unit length, $F_u$, and the derivative with respect to free wind speed, $\partial F_u/\partial V$, are shown in Figure 2.6.

The corresponding damping coefficients and their components are shown in Figures 2.7 and 2.8, $c_{xx}^R$ for *in-plane* and $c_{yy}^R$ for *out-of-plane* directions, respectively.

The resulting coefficients are observed to be identical with the corresponding ones derived on basis of airfoil data, presented in the previous section, thus confirming that the two sets of equations – Equations 2.16-2.19 and Equations 2.26-2.29 – give identical results.

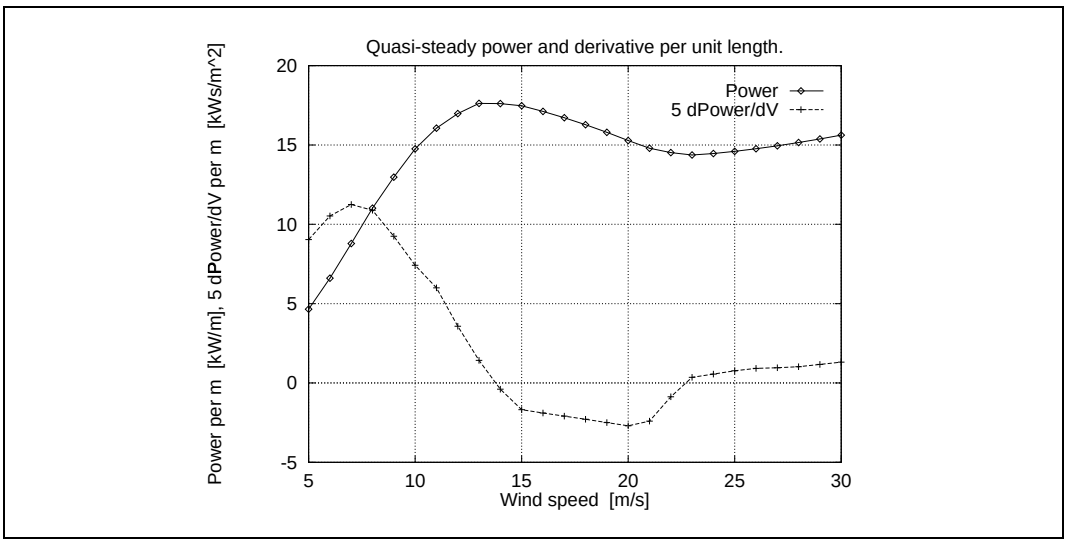


*Figure 2.5. Local power per unit length, $P_u$, and the derivative with respect to free wind speed, $\partial P_u/\partial V$, based on the airfoil data shown in Figure 2.2.*

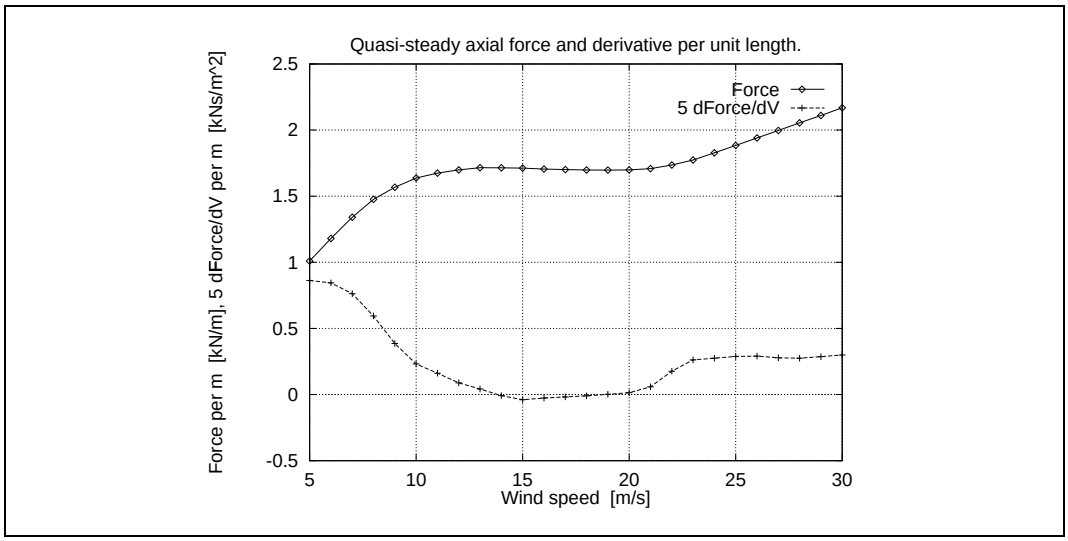


*Figure 2.6. Local axial force per unit length, $F_u$, and the derivative with respect to free wind speed, $\partial F_u/\partial V$, based on the airfoil data shown in Figure 2.2.*

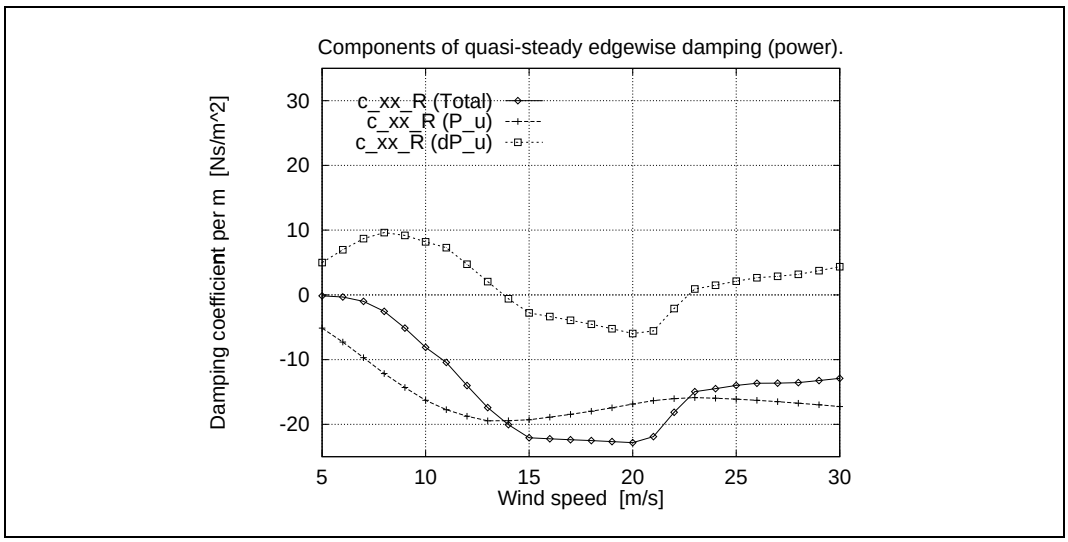


*Figure 2.7. Damping coefficient $c^R_{xx}$ and its components with reference to the R-coordinate system. Based on expression for local power.*

### 2.1.3 Influence of direction of vibration

As the equations above show, the resulting damping also depends on the local direction of the blade section movement. We now want to investigate, how the aerodynamic damping is influenced by the fact that the blade vibrates in arbitrary directions. Usually, we talk about edgewise and flapwise vibrations, and mean by that vibrations in the rotor plane (edgewise) and perpendicular to the rotor plane (flapwise), respectively. However, due to the twist of the blade and the structural properties in general, the principal bending axes will be rotated relative to these two directions, and accordingly the movement of the blade section in the basic mode shapes will follow directions, which are not parallel with the axes of the rotor coordinate system. This is illustrated in Figure 2.9, where the coordinate system $\{x_B, y_B\}$, which has been rotated the angle $\theta_{RB}$ relative to the $\{x_R, y_R\}$-coordinate system, indicates the resulting directions of motion for the edgewise mode shape, the $x_B$-direction, and the flapwise mode shape, the $y_B$-direction, respectively. The direction of $\theta_{RB}$

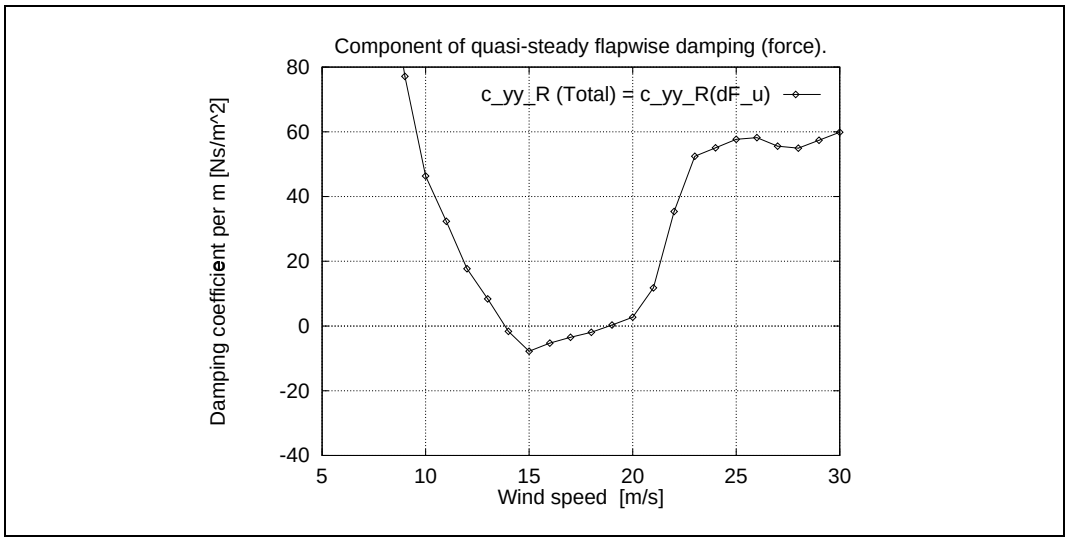


*Figure 2.8. Damping coefficient $c_{yy}^R$ with reference to the R-coordinate system. Based on expression for local force.*

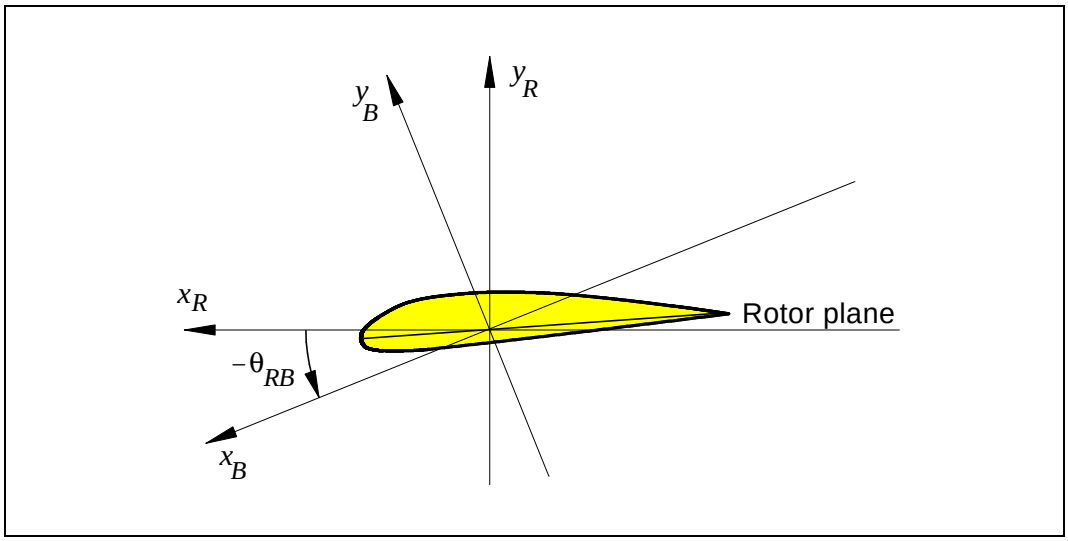


*Figure 2.9. Local B-coordinate system aligned with the local movement directions for a blade section.*

– shown in the figure – is negative according to the chosen convention, as indicated by the sign. The aerodynamic damping in the rotated $B$-coordinates is obtained by transforming Equation 2.15, neglecting the mean force vector $\{F_{a0}^R\}$ and using that

$$\left\{\dot{u}^B\right\} = [T_{RB}]\left\{\dot{u}^R\right\} \ , \tag{2.30}$$

where the transformation matrix is defined by

$$[T_{RB}] = [T_{RB}(r)] = \begin{bmatrix} \cos[\theta_{RB}(r)] & \sin[\theta_{RB}(r)] \\ -\sin[\theta_{RB}(r)] & \cos[\theta_{RB}(r)] \end{bmatrix} \ . \tag{2.31}$$

The final expression for the transformed damping force in $B$-coordinates yields

$$\left\{F_a^B\right\} = -[T_{RB}]\left[c_a^R\right][T_{RB}]^{-1}\left\{\dot{u}^B\right\} \ , \tag{2.32}$$

or

$$\left\{F_a^B\right\} = -\left[c_a^B\right]\left\{\dot{u}^B\right\} = -\begin{bmatrix} c_{xx}^B & c_{xy}^B \\ c_{yx}^B & c_{yy}^B \end{bmatrix}\left\{\dot{u}^B\right\} \ , \tag{2.33}$$

which defines the damping matrix in $B$-coordinates. In this matrix the main diagonal terms give the damping in the local movement directions.

The term giving the damping for vibration in direction of the local $x_B$-axis – the $c_{xx}^B$-term – yields:

$$c_{xx}^B = \cos^2(\theta_{RB})c_{xx}^R + \cos(\theta_{RB})\sin(\theta_{RB})\left(c_{xy}^R + c_{yx}^R\right) + \sin^2(\theta_{RB})c_{yy}^R \ . \tag{2.34}$$

The numerical value of this damping term is shown in Figure 2.10 as function of the vibration direction with the wind speed as parameter. The direction interval shown in the figure – $[-90°; +90°]$ – covers all possible directions, including the ones that usually are referred to as *edgewise* and *flapwise*. The aerodynamic properties are the same as in the previous example in Section 2.1.1, listed in Table 2.1. The data are unchanged for the different directions and wind speeds.

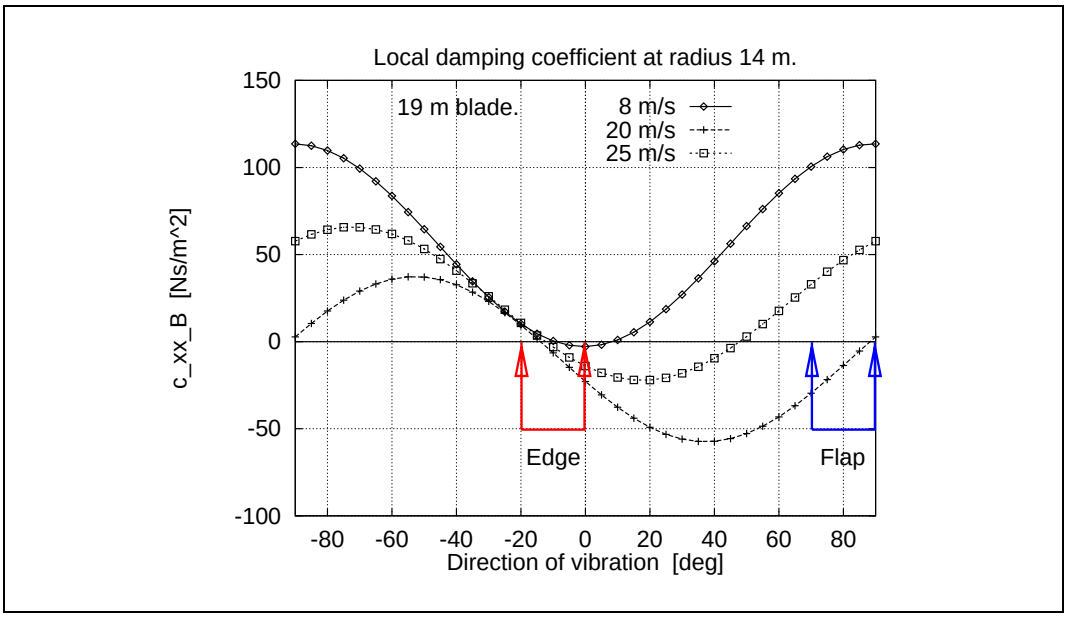


*Figure 2.10. Damping coefficient $c_{xx}^B$ from Equation 2.34 as function of vibration direction – the direction of the $x_B$-axis determined by the local angle $\theta_{RB}$, usually associated with a specific mode shape. The aerodynamic properties are the same as in the previous example (Table 2.1) and unchanged for the different directions and wind speeds.*

The ranges of vibration direction – usually covering the edgewise and flapwise modes for a typical blade – are marked in Figure 2.11 as the two 20° intervals. The vibration directions for a real blade will approximately be perpendicular to each other corresponding to a close to 90° offset in the figure. These ranges are also marked in Figure 2.10. It is observed that with the present airfoil data no principal vibration directions can be found, where the damping is positive in both edgewise and flapwise directions at the higher wind speeds, assuming that the offset between the two directions is 90°. However, the data also form the basis for choosing a pair of directions, where the negative damping is minimized. In Section 3 we show, how airfoil modifications can result in positive damping for both the edgewise and the flapwise directions.

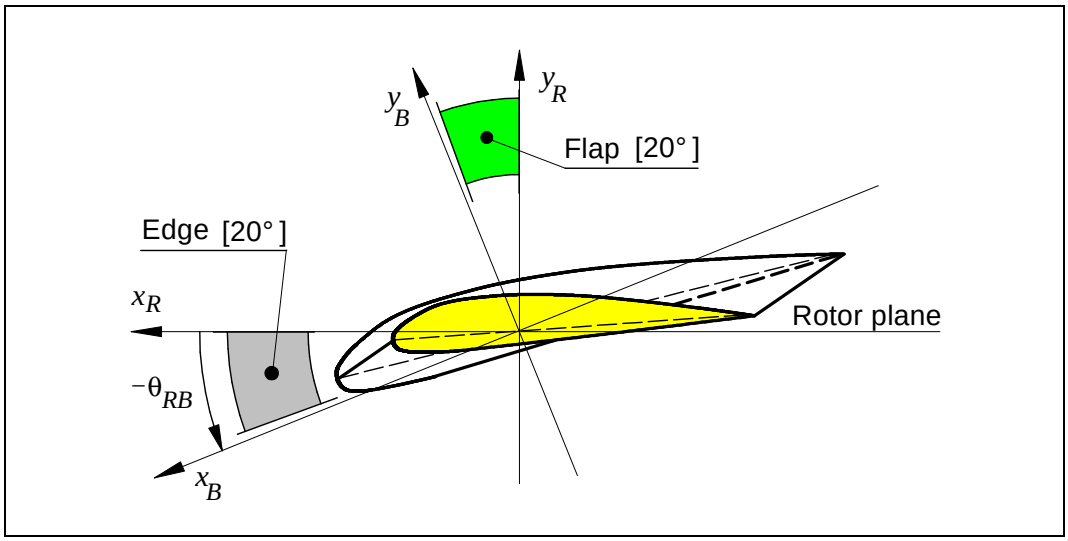


*Figure 2.11. Typical ranges for local direction of vibration. The offset between the edgewise and the flapwise directions is approximately 90° for a real blade, changing along the radius of the blade.*

## 2.2 Modal aerodynamic damping for a blade

The damping for the complete blade is usually described in relation to the mode shape of the blade, because the vibration in a specific mode is the structural response, which is most likely to be involved in the energy exchange related to aerodynamic damping.

In order to facilitate the understanding of the frequently applied references to the terms related to the response resolution in mode shapes and normal coordinates, the basic equations are shown in Appendix A and applied below without further reference.

For many purposes a wind turbine blade can be considered one-dimensional in the sense that the structural properties and the loading vary only with the radial coordinate, $r$. At the same time only the transverse deformation is of interest. This suggests the modal representation of the aerodynamic damping for mode shape number $n$

$$C_n = \int_0^R \left\{\varphi_n^R(r)\right\}^T \left[c_a^R(r)\right] \left\{\varphi_n^R(r)\right\} \mathrm{d}r \ . \tag{2.35}$$

Often, it is convenient to obtain the modal damping by transforming the mode-shape vector locally to the coordinate system aligned with the movement direction, the $B$-coordinates. Then the vector is given in polar coordinates through its size and the direction of vibration identical with $\theta_{RB} = \theta_{RBn}(r)$ defined in Figure 2.9. The index $n$ is added here to emphasize that the angle now belongs to the specific mode shape number $n$.

Following the same steps as in Section 2.1.3 the modal vector is transformed through

$$\left\{\varphi_n^B(r)\right\} = \left[T_{RBn}(r)\right] \left\{\varphi_n^R(r)\right\} \ , \tag{2.36}$$

expressing the modal damping with reference to the $B$-coordinates by

$$C_n = \int_0^R \left\{\varphi_n^B(r)\right\}^T \left[T_{RBn}(r)\right] \left[c_a^R(r)\right] \left[T_{RBn}(r)\right]^{-1} \left\{\varphi_n^B(r)\right\} \mathrm{d}r \ . \tag{2.37}$$

Again, the index $n$ is added on the transformation matrix $[T_{RB}] = [T_{RBn}(r)]$ to stress that the matrix now belongs to the specific mode shape number $n$, and the transformation is based locally on the angle $\theta_{RBn}(r)$.

In Equation 2.37 the modal vector can be described by its amplitude, $\varphi_{n0}$, alone

$$\{\varphi_n^B(r)\} = \left\{ \begin{array}{c} 1 \\ 0 \end{array} \right\} \varphi_{n0}(r) \, , \tag{2.38}$$

as the angle for the polar coordinates are included in the transformation matrix – $[T_{RB}]$ – according to Equation 2.31.

Substituting this vector in Equation 2.37 gives

$$\begin{aligned} C_n &= \int_0^R \left\{ \begin{array}{c} 1 \\ 0 \end{array} \right\}^T \left[ \begin{array}{cc} c_{xx}^{Bn}(r) & c_{xy}^{Bn}(r) \\ c_{yx}^{Bn}(r) & c_{yy}^{Bn}(r) \end{array} \right] \left\{ \begin{array}{c} 1 \\ 0 \end{array} \right\} \varphi_{n0}^2(r) \mathrm{d}r \\ &= \int_0^R c_{xx}^{Bn}(r) \, \varphi_{n0}^2(r) \mathrm{d}r \, . \end{aligned} \tag{2.39}$$

The index $n$ on the damping coefficient terms, e.g. $c_{xx}^{Bn}$, reflects that the coefficient here depends on the mode shape specific local vibration direction, $\theta_{RBn}(r)$, involved through the transformation in Equation 2.37.

The discrete version of Equation 2.39 is

$$C_n = \sum_{i=1}^{M} c_{xx,i}^{Bn} \, \varphi_{n0,i}^2 \, \Delta r_i \, , \tag{2.40}$$

where index $i$ refers to the radial station number $i$, and $\Delta r_i$ is the length of the discrete element at station $i$.

The modal damping per unit length for the continuous description yields

$$c_n(r) = c_{xx}^{Bn}(r) \, \varphi_{n0}^2(r) \, , \tag{2.41}$$

and for the discrete version

$$c_{n,i} = c_{xx,i}^{Bn} \, \varphi_{n0,i}^2 \, . \tag{2.42}$$

### 2.2.1 Numerical examples of modal damping

The calculation of modal damping is demonstrated next in the example denoted Ex1. Based on the mode shapes and the vibration directions in Figure 2.12 and the typical distributed blade properties shown in Figure 2.13, the logarithmic decrements for the edgewise and the flapwise modes have been calculated, using Equations 2.34 and 2.40. The results are shown in Figure 2.14. Further, the logarithmic decrement per unit length for the two modes are shown in Figure 2.15. The concept of logarithmic decrement is defined in Appendix A.1, Equation A.14–A.18.

The natural frequencies are 1.8 Hz and 2.9 Hz for the flapwise and the edgewise mode, respectively. The corresponding modal masses are 70 kg and 100 kg, respectively. The remaining data for this example are listed in Table 2.2 (these data are also used in example Ex2 in Section 2.2.2).

*Table 2.2. Main data common for examples* Ex1 *and* Ex2.

| | | |
|---|---|---|
| $\varrho$ | = | 1.23 kg/m$^3$ |
| $\Omega$ | = | 3.04 rad/s |
| $\theta_{tip}$ | = | 0.00° |
| Tip radius, $R$ | = | 20.5 m |
| Airfoil data used along the whole blade shown in Figure 2.2. | | |

The mode shapes and the vibration directions are typical for a 19 m blade, while the airfoil data, the 18% $t/c$ data from Figure 2.2, applied along the whole blade, only approximates a realistic behaviour. The airfoil data is typically used on a real blade at 3/4 radius, a part of the blade with great influence on the damping results, which makes the approximation reasonable. Later on, when the aeroelastic code is used for the calculations, the true distribution of airfoil data along the blade will be used.

It is observed that the damping is negative for the edgewise mode in the complete wind speed range. The flapwise damping is negative in a limited wind speed range around 18 m/s. Although these results are typical, the character of these damping curves will change fundamentally with the change of airfoil data and mode shapes, as can be seen from the equations above. This is further demonstrated in later examples.

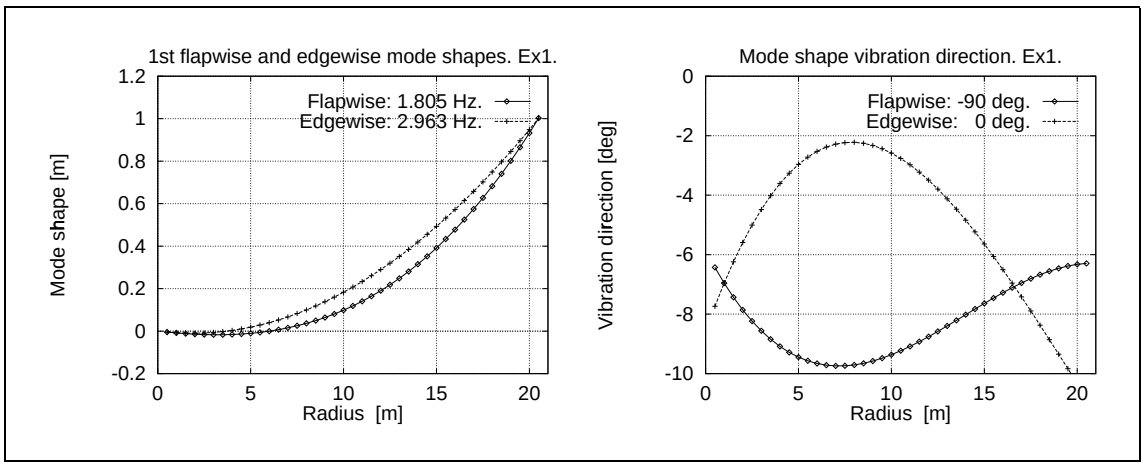


*Figure 2.12. Mode shapes, $\varphi_{n0}$, and vibration directions, $\theta_{RBn}$, for example* Ex1. *The flapwise direction is plotted with an offset of $-90°$. The plots are based on fitted polynomials.*

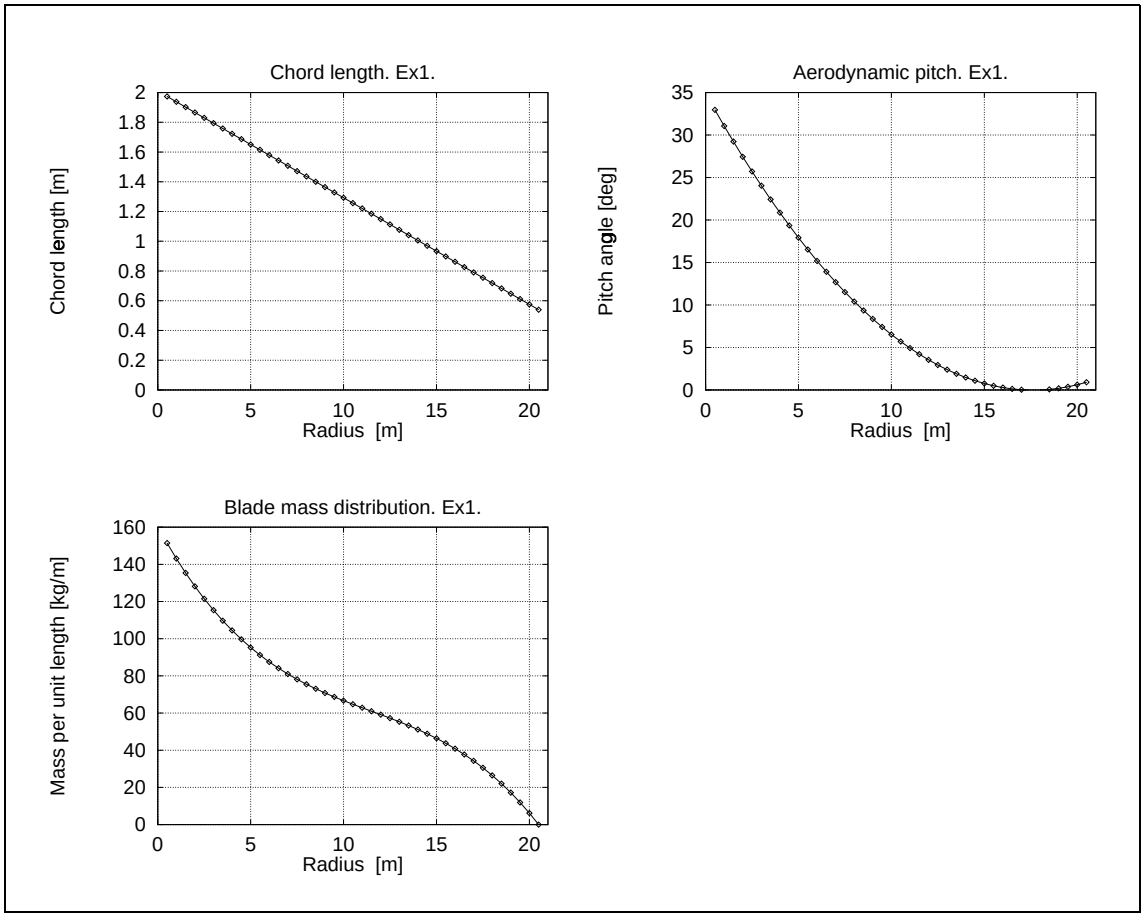


*Figure 2.13. Data common for blade used in examples,* Ex1 *and* Ex2. *The plots are based on fitted polynomials.*

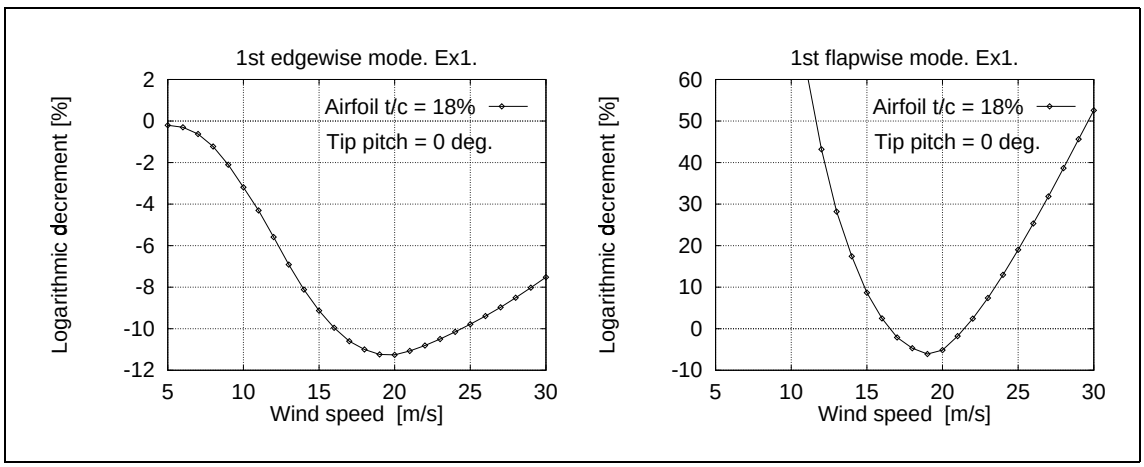


*Figure 2.14. Logarithmic decrement for example* Ex1. *The vibration directions are similar to directions for the mode shapes usually involved in flapwise and edgewise stall induced vibrations.*

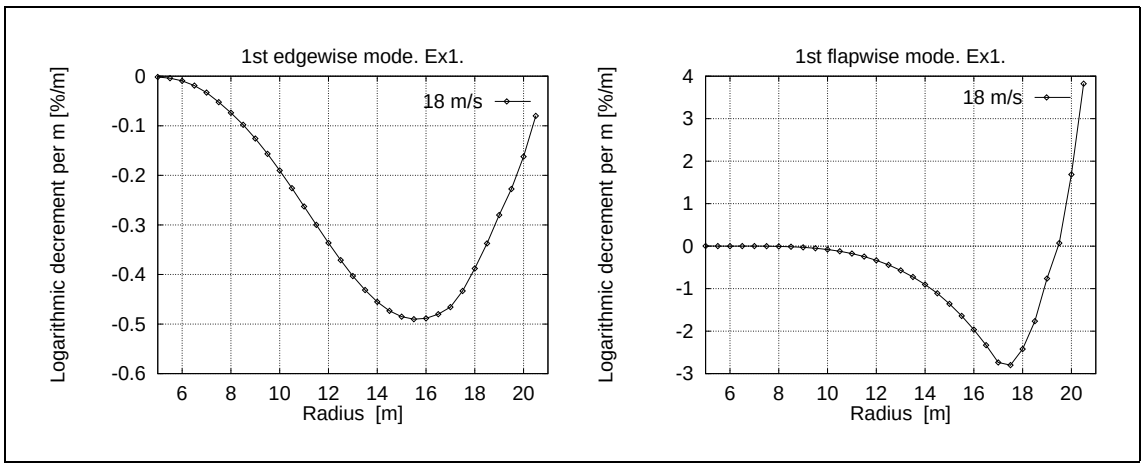


*Figure 2.15. Logarithmic decrement per unit length at 18 m/s for example* Ex1.

### 2.2.2 Modal damping based on power and axial force

It is very informative to demonstrate how the total turbine power and axial force can be connected to the logarithmic decrement of modal aerodynamic damping. We do that below by considering simple blade mode shapes, although these mode shapes are usually not involved in stall induced vibrations.

In Section 2.1.2 the relation between local aerodynamic damping and the independent variables power and axial force was derived. For very simple mode shapes, symbolic expressions for the modal damping can be obtained showing some basic characteristics of the wind turbine rotor. Substituting Equations 2.26-2.29 via Equation 2.34 into the expression for modal aerodynamic damping coefficient, Equation 2.39, yields

$$\begin{aligned} C_n &= \int_0^R \left[ \cos^2\theta_{RBn}(r) \left( -\frac{2}{r^2\Omega^2} P_u(r,V) + \frac{V}{r^2\Omega^2}\frac{\partial P_u(r,V)}{\partial V} \right) \right. \\ &\quad + \cos\theta_{RBn}(r)\sin\theta_{RBn}(r) \left( \frac{1}{r\Omega}\frac{\partial P_u(r,V)}{\partial V} - \frac{2}{r\Omega}F_u(r,V) + \frac{V}{r\Omega}\frac{\partial F_u(r,V)}{\partial V} \right) \\ &\quad \left. + \sin^2\theta_{RBn}(r) \left( \frac{\partial F_u(r,V)}{\partial V} \right) \right] \varphi_{n0}^2(r)\mathrm{d}r \ . \end{aligned} \tag{2.43}$$

Only for very simple expressions of mode shape and vibration direction it is possible to obtain symbolic solutions to this integral and show symbolically a connection between the turbine power curve and axial force and modal damping.

One such simple case occurs for the *flapwise* direction, if the mode shape is a constant function of the blade radius, $\varphi_{10} = u_0$, and the vibration direction is perpendicular to the rotor plane, $\theta_{RB1}(r) = 90°$ along the blade. In this case the modal aerodynamic damping simplifies to

$$C_1 = u_0^2 \int_0^R \frac{\partial F_u(r,V)}{\partial V}\mathrm{d}r \ . \tag{2.44}$$

As the function $F_u(r,V)$ is continuous and differentiable with continuous derivatives, the integration and the differentiation can be interchanged, and the integration performed to give

$$\begin{aligned} C_1 &= u_0^2 \frac{\partial}{\partial V}\int_0^R F_u(r,V)\mathrm{d}r \\ &= u_0^2 \frac{\partial F_b(V)}{\partial V} \ , \end{aligned} \tag{2.45}$$

where

$$F_b(V) = \int_0^R F_u(r,V)\mathrm{d}r \tag{2.46}$$

is the total axial force per blade.

A similar simple case occurs for the *edgewise* direction if the mode shape is a linear function of the blade radius, $\varphi_{20} = r/R$, and the vibration direction is parallel to the rotor plane, $\theta_{RB2}(r) = 0°$ along the blade. In this case the modal aerodynamic damping simplifies to

$$C_2 = \int_0^R \left[ -\frac{2}{r^2\Omega^2} P_u(r,V) + \frac{V}{r^2\Omega^2} \frac{\partial P_u(r,V)}{\partial V} \right] \left(\frac{r}{R}\right)^2 \mathrm{d}r \ . \tag{2.47}$$

Again, the integration and the differentiation can be interchanged, and the integration performed to give

$$C_2 = -\frac{2}{\Omega^2 R^2} \int_0^R P_u(r,V)\mathrm{d}r + \frac{V}{\Omega^2 R^2} \frac{\partial}{\partial V} \int_0^R P_u(r,V)\mathrm{d}r \ . \tag{2.48}$$

The integral of the power per unit length equals the total power per blade

$$P_b(V) = \int_0^R P_u(r,V)\mathrm{d}r \ , \tag{2.49}$$

finally resulting in

$$C_2 = -\frac{2}{\Omega^2 R^2} P_b(V) + \frac{V}{\Omega^2 R^2} \frac{\partial P_b(V)}{\partial V} \ . \tag{2.50}$$

### Numerical example

A numerical example based on these two cases is shown next. The example is denoted Ex2. The mode shapes are shown in Figure 2.16. The assumed natural frequencies are 1.8 Hz and 2.9 Hz for the flapwise and the edgewise mode, respectively. The corresponding modal masses are 1400 kg and 270 kg, respectively. The remaining data are listed in Table 2.2 or alternatively shown in Figure 2.13.

The calculated modal damping for the two situations are shown in Figure 2.17, and the damping per unit length at wind speed 18 m/s is shown in Figure 2.18. It is observed that the damping is negative for the edgewise mode in the complete wind speed range, while the flapwise damping is positive in the complete range.

The present simplified edgewise mode shape corresponds to a rigid body rotation about a root hinge or the main bearing. Rigid body rotations of the whole rotor will thus experience negative aerodynamic damping. However, the energy is usually transferred to the generator and no elastic energy is stored in the blades or the drive train.

The simplified flapwise mode shape corresponds to a rigid body translation of the blade. This situation is on a real turbine represented by a tower bending mode, which involves the blade in a motion approximately like this. This indicates that such a tower mode will experience positive aerodynamic damping.

The per blade power and force curves and the derivatives with respect to free wind speed are shown in Figures 2.19 and 2.20, respectively.

Although the two cases show important characteristics for the rotor, namely that the *in-plane* vibration tends to be negatively damped and that the *out-of-plane* vibration tends to be positively damped, it must be emphasized that the mode shapes involved in the stall induced vibrations usually are quite different from the ones used in the example. The most important difference is that mode shapes important for stall induced vibrations have components both in the plane and out of the plane due to the radial change of the orientation of the principal bending axis, more or less following the twist of the blade.

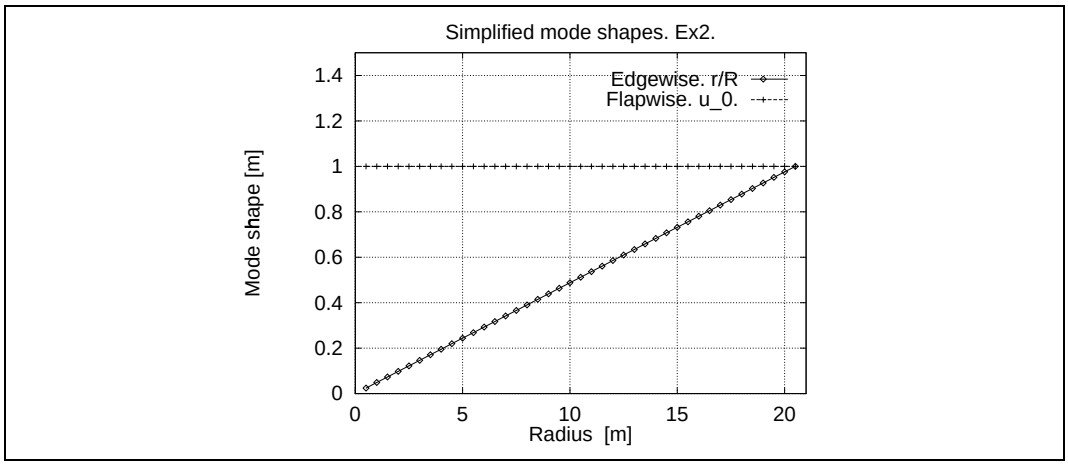


*Figure 2.16. Simplified blade mode shapes for example* Ex2.

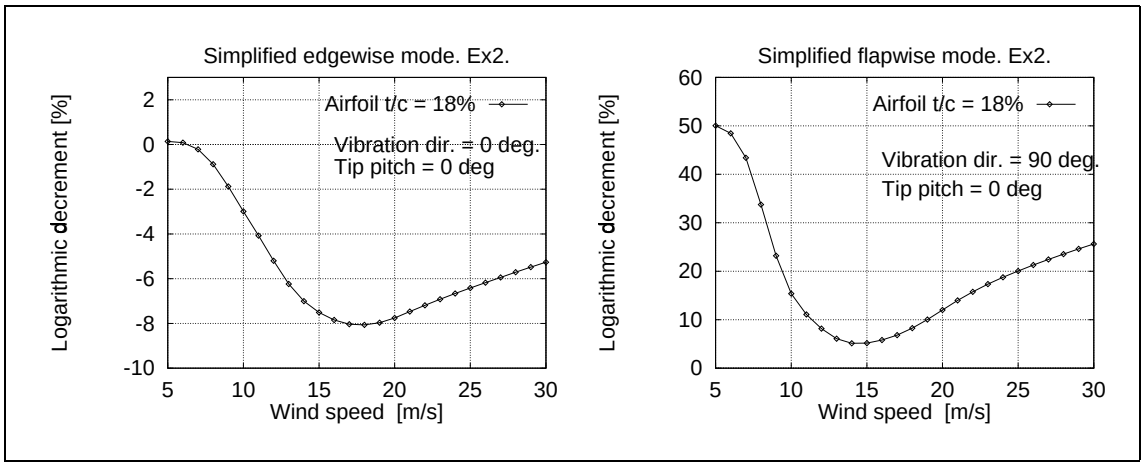


*Figure 2.17. Logarithmic decrement for example* Ex2. *The edgewise mode is linear, proportional with radius and vibrating in the rotor plane. The damping calculation is based on the power curve for the blade. The flapwise mode is constant and vibrating perpendicular to the rotor plane. The damping calculation is based on the axial force curve for the blade.*

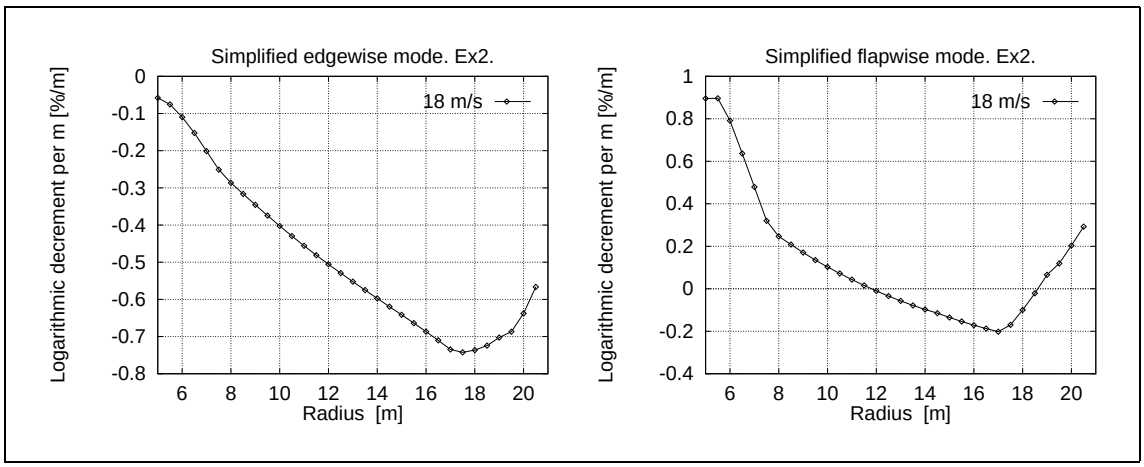


*Figure 2.18. Logarithmic decrement per unit length at 18 m/s for example* Ex2.

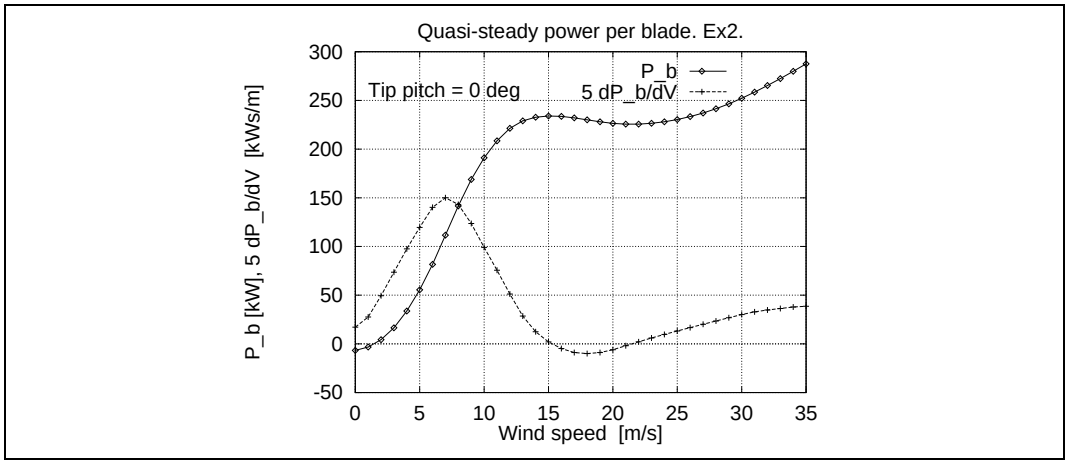


*Figure 2.19. Power curve for one blade, example* Ex2.

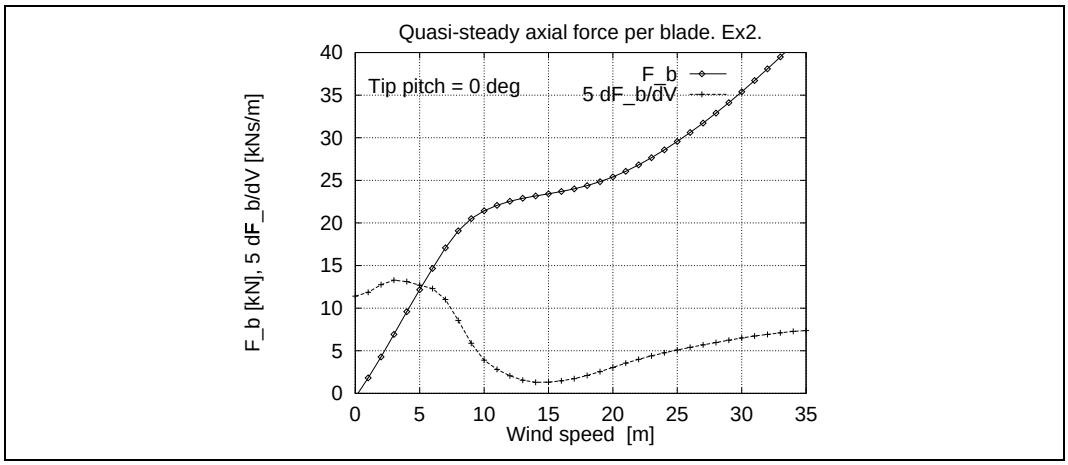


*Figure 2.20. Axial force curve for one blade, example* Ex2.

# 3 Modifications and associated influence on damping

As shown previously in Section 2 the resulting aerodynamic damping depends heavily on the static airfoil data, and so does the power extracted by the blade. In the present section different sets of basic airfoil data are subject to modifications in order to demonstrate some of the possibilities for improving damping properties without damaging the performance of the turbine seriously. The influence of change of aerodynamic and structural pitch is addressed as well. Finally, we discuss how changes of modal mass and modal stiffness affect the aerodynamic damping and the stability margin.

In Section 3.1 we show the influence from chosen modifications to a basic airfoil data set on aerodynamic damping. Both local and global influence is shown. The latter by applying the same airfoil along the blade. The modifications in this section primarily aim at changing the slope of the lift data, $\partial C_L/\partial\alpha$, after stall onset and at demonstrating the associated consequences for the damping without specific requirements on the performance. The influence of changing the vibration direction is demonstrated as well.

More realistic airfoil modifications are carried out in the calculations in Section 3.2. Here the airfoil data are modified along the blade trying to distribute the modifications in a way that considers the power performance, aiming at keeping the power output for the modified blade the same as for the original.

In Sections 3.3, 3.4 and 3.5 we investigate the influence of uniform global changes of direction dependent properties, which can be considered to change with the common angular orientation associated with rotation about the blade axis. More specific, this involves uniform structural pitch offset, uniform offset of airfoil data angle of attack – corresponding to change of camber – and finally change of tip pitch setting.

Changes of modal mass and modal stiffness affect the resulting modal damping and – if not changed proportionally – the natural frequency of the modes. An overview of the influence of such changes on the stability margin is presented in Section 3.6.

In all the examples in the sections below we use the turbine and blade data from Section 2, Table 2.2 and Figures 2.12 and 2.13, if not stated otherwise.

## 3.1 Airfoil modifications – local

The airfoil data shown previously in Figure 2.2 and used in all the examples in Section 2 are the basic data, which we modify. The modifications are performed at a specific radius, which is chosen as $(3/4)R$ with chord length $c = 1.06$ m and twist $\theta = 2.0°$.

A number of preset conditions are met during modification. First a modified lift curve is designed as follows:

- A maximum lift is defined on the original $C_L$-curve corresponding to an angle of attack just above the point where the curve starts to deviate from the attached flow curve segment with slope $2\pi$.
- The maximum lift point is connected with a straight line to the point with coordinates $(\alpha, C_L) = (30°, 1.1)$.
- The remaining parts of the lift curve are unchanged.

Given the lift curve a corresponding drag curve is designed as follows:

- A drag curve is designed, such that the tangential force is kept constant and equal to the tangential force at maximum lift for angles of attack above the maximum lift point. This results in constant power from the blade section above angles of attack corresponding to maximum lift.

Three such airfoil data sets were generated with maximum lift 1.1, 1.2 and 1.3, respectively. The lift curves and the corresponding drag curves are shown in Figure 3.1. The original airfoil data are shown in the figures as well.

The main change in the airfoil drag data is an almost uniformly distributed offset for angles of attack above the angle corresponding to maximum lift. The offset is approximately 0.03.

In order to show how these changes influence the terms in the expressions for aerodynamic damping the resulting power, force and drag airfoil characteristics and their derivatives are shown in the figures below. The power and axial force per unit length – obtained by use of the quasi-steady model – are shown in Figure 3.2 and the derivatives of these in Figure 3.3. The airfoil drag data and the derivatives with respect to angle of attack are shown in Figure 3.4. The most important change with respect to aerodynamic damping is the constant zero slope of the power per unit length versus wind speed. According to Equation 2.26 this is the most optimal situation for the *in-plane* damping $c^R_{xx}$, if the power is not allowed to increase with wind speed. The chosen maximum lift determines the damping in this direction.

The change of damping can also be observed from Figure 3.5, where the damping at 20 m/s is shown as function of vibration direction, with the maximum lift as parameter. The ranges for directions normally covering the edgewise and the flapwise directions are shown as the two 20° intervals close to 0° and 90°. It is observed that it now, for the modified airfoils, is possible to find two directions perpendicular to each other, which both have positive damping within the marked ranges, contrary to the original data. Both the *in-plane* and the *out-of-plane* damping coefficients, $c^R_{xx}$ and $c^R_{yy}$, are shown in Figures 3.6-3.9 for original and modified airfoil data as function of wind speed. These figures also show the influence of change of vibration direction, covering the ranges of interest shown in Figure 3.5. In general decrease of vibration direction angle increases the damping in edgewise direction and decreases the damping in flapwise direction in the relevant ranges.

The modal damping for the whole blade is shown in Figure 3.10. In each case the same airfoil has been used along the blade. The associated power and axial force curves are shown in Figure 3.11. Finally, the influence of changing the vibration direction $-5°$ uniformly along the blade is shown in Figure 3.12.

The main conclusion from these examples is that by reducing the maximum lift and changing the vibration direction it is possible to obtain positive damping both for the edgewise and the flapwise mode shapes. Of course, the influence on power performance has to be considered. In Section 3.2 it is demonstrated how both acceptable damping and performance can be obtained by applying different modifications along the blade. This is possible due to different weighting from the mode shapes along the blade. Finally, it should be emphasized that the change of vibration direction does not have any influence on the power performance.

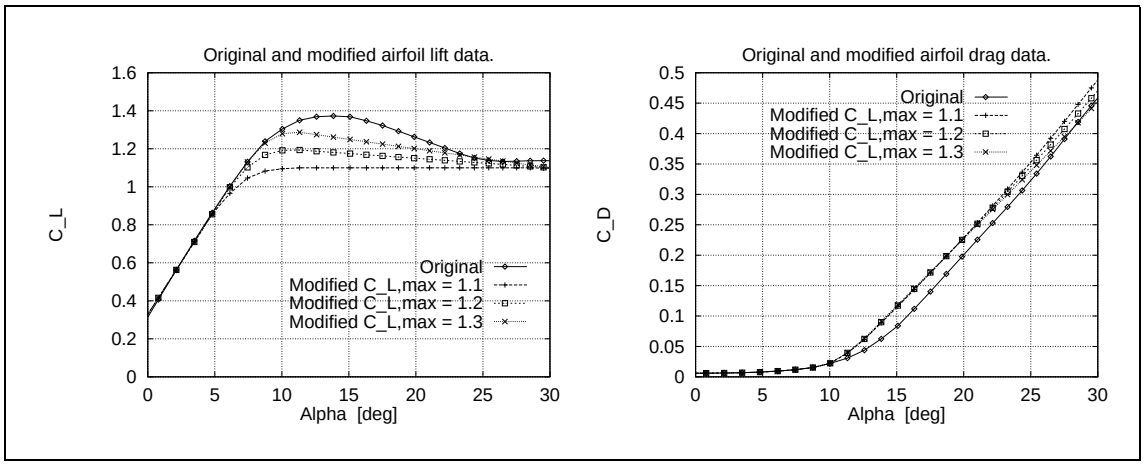


*Figure 3.1. Original and modified airfoil data.*

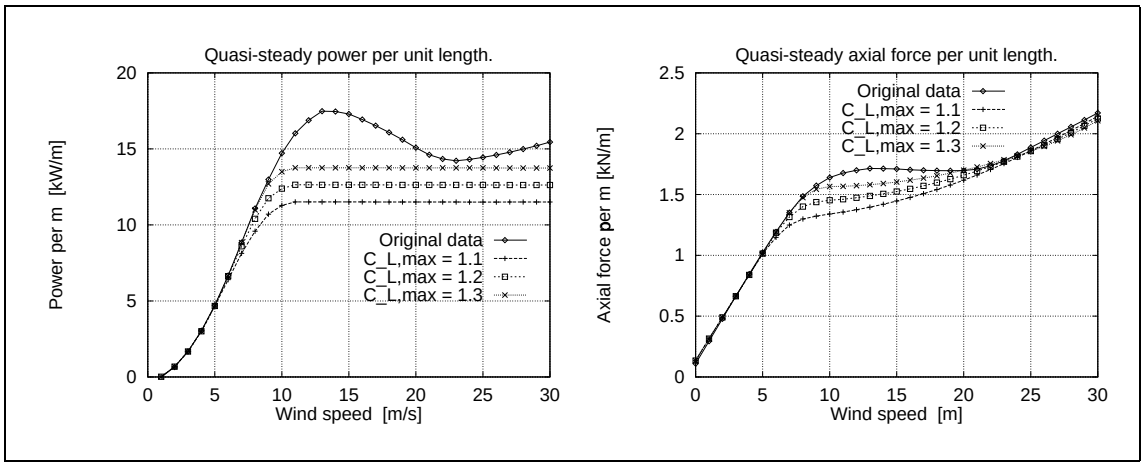


*Figure 3.2. Power and axial force per unit length for original and modified airfoil data.*

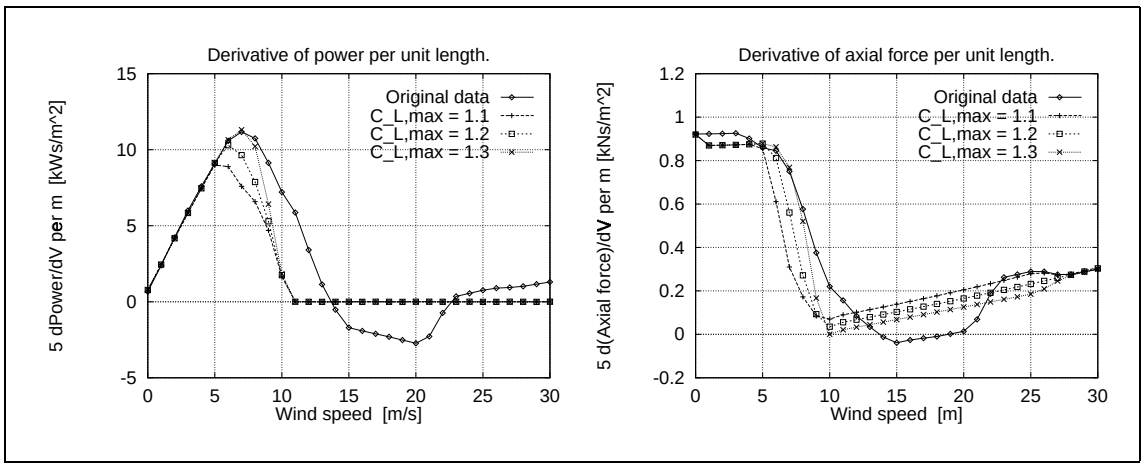


*Figure 3.3. Derivative with respect to free wind speed of power and axial force per unit length for original and modified airfoil data.*

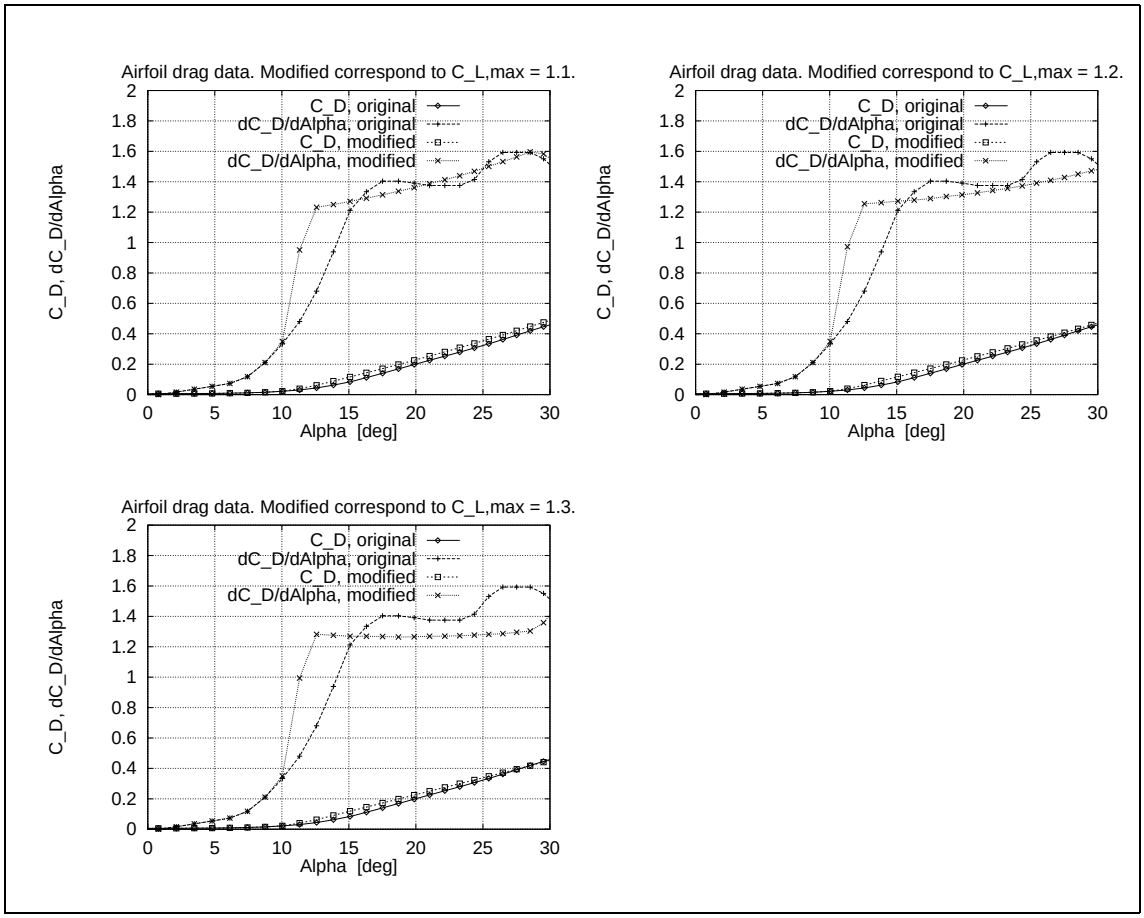


*Figure 3.4. Details of original and modified airfoil drag data.*

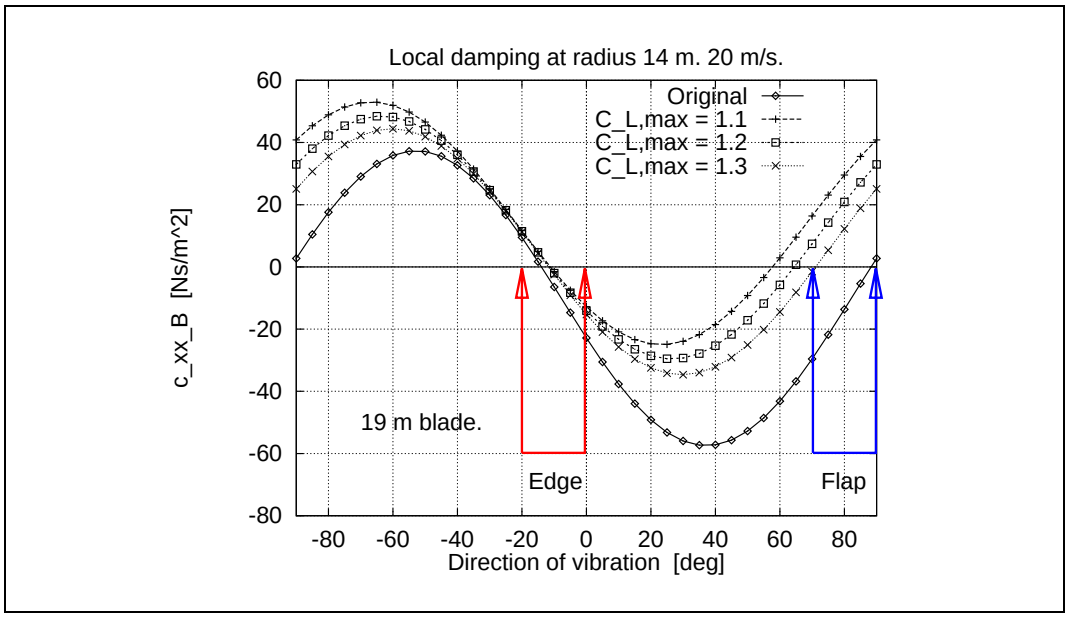


*Figure 3.5. Damping as function of vibration direction – the direction of the $x_B$-axis determined by the local angle $\theta_{RB}$, usually associated with a specific mode shape. Each curve corresponds to one set of airfoil data, either original or modified.*

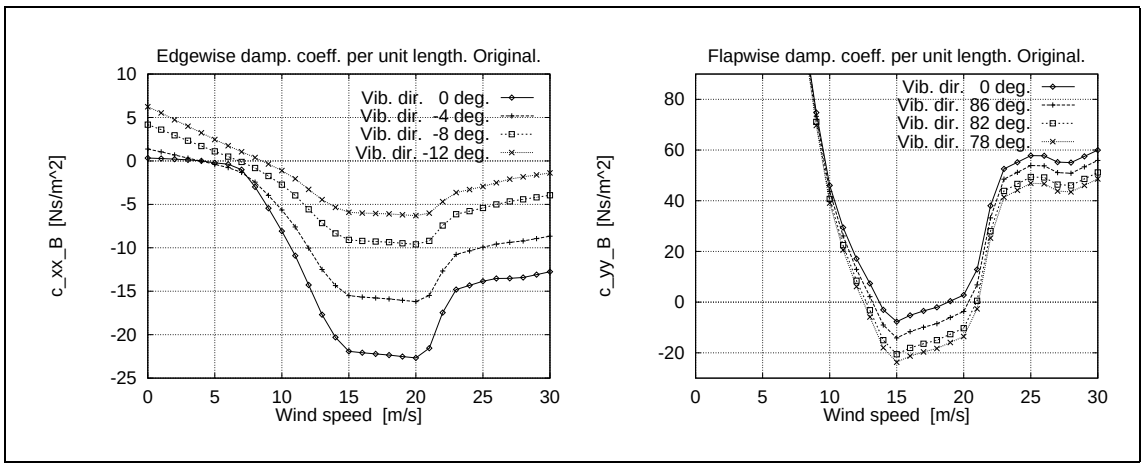


*Figure 3.6. Damping coefficients for original airfoil data.*

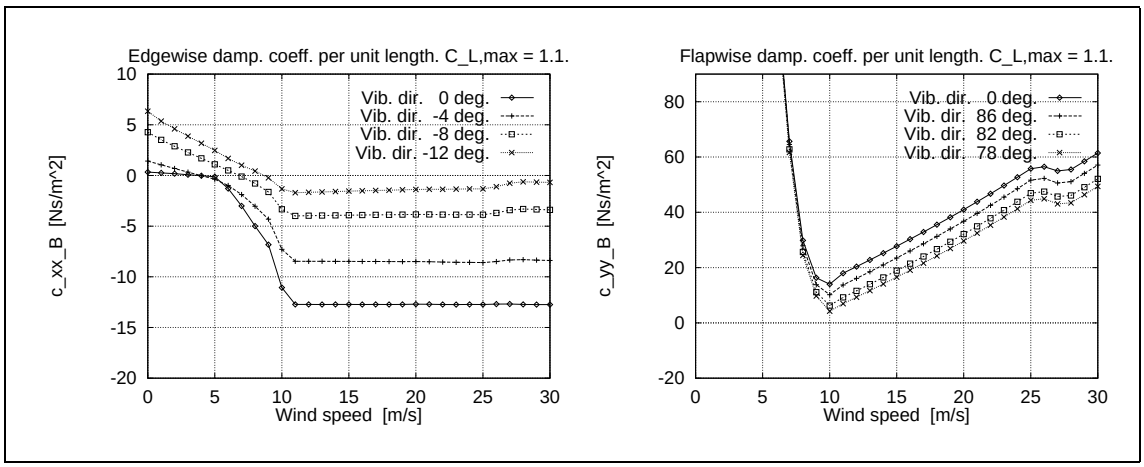


*Figure 3.7. Damping coefficients for modified airfoil data with $C_{L,max} = 1.1$.*

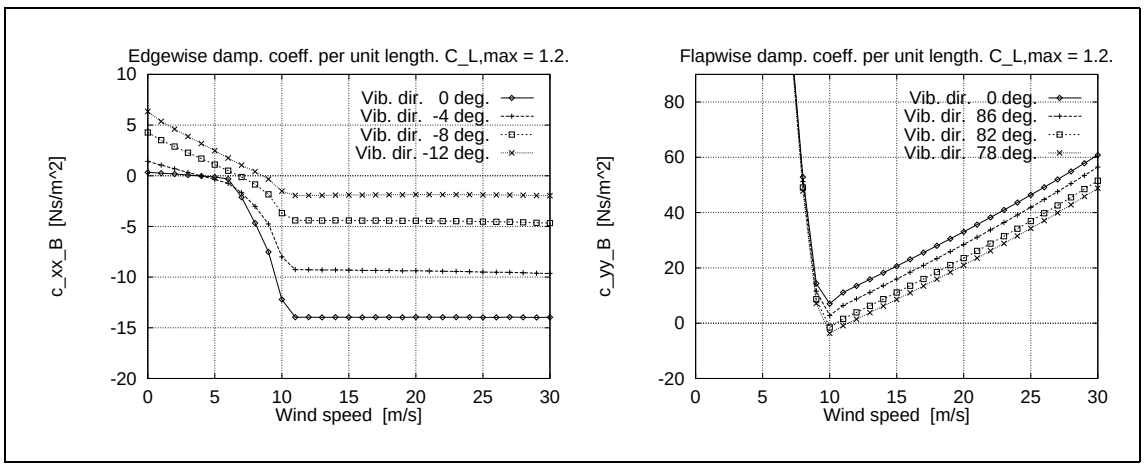


*Figure 3.8. Damping coefficients for modified airfoil data with $C_{L,max} = 1.2$.*

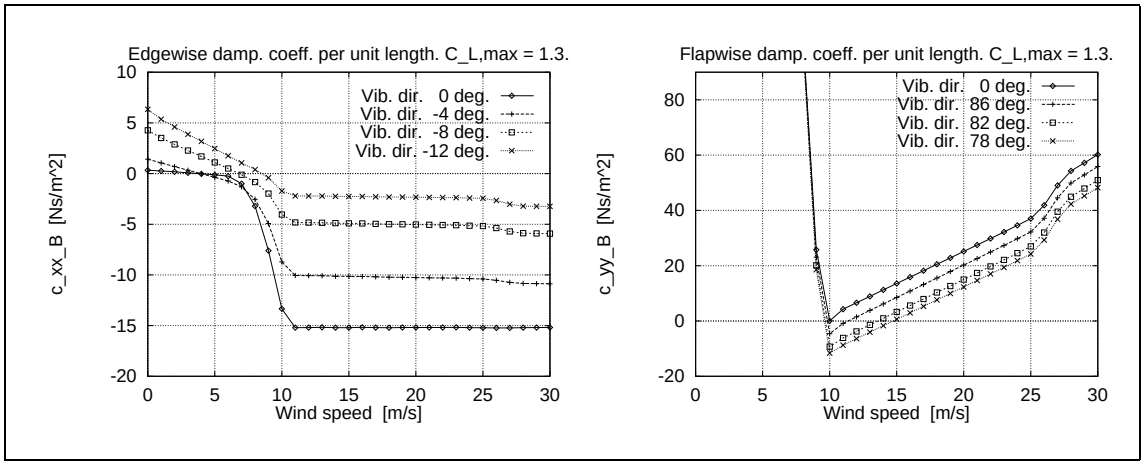


*Figure 3.9. Damping coefficients for modified airfoil data with $C_{L,max} = 1.3$.*

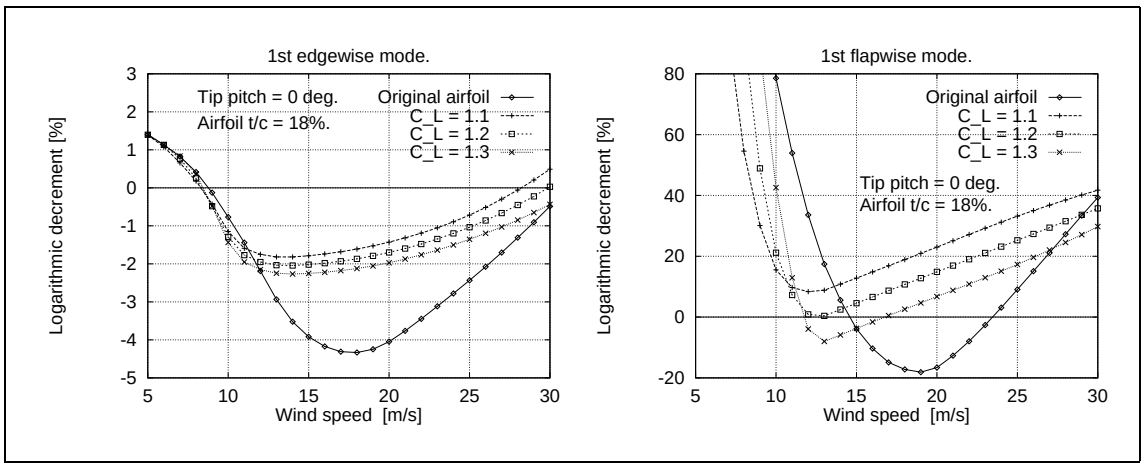


*Figure 3.10. Logarithmic decrement for original and modified airfoil data with the same $t/c = 18\%$ airfoil along the blade.*

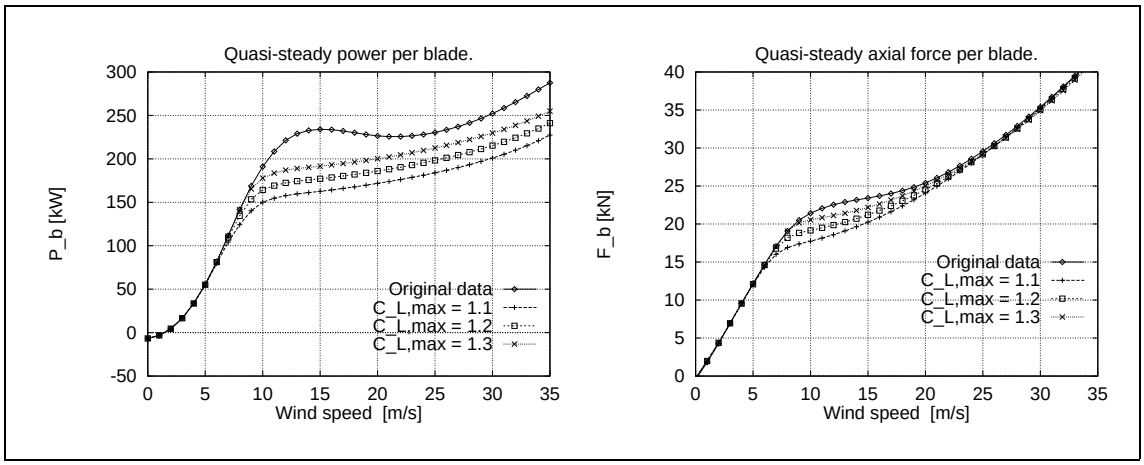


*Figure 3.11. Power and axial force per blade corresponding to original and modified airfoil data with the same $t/c = 18\%$ airfoil along the blade.*

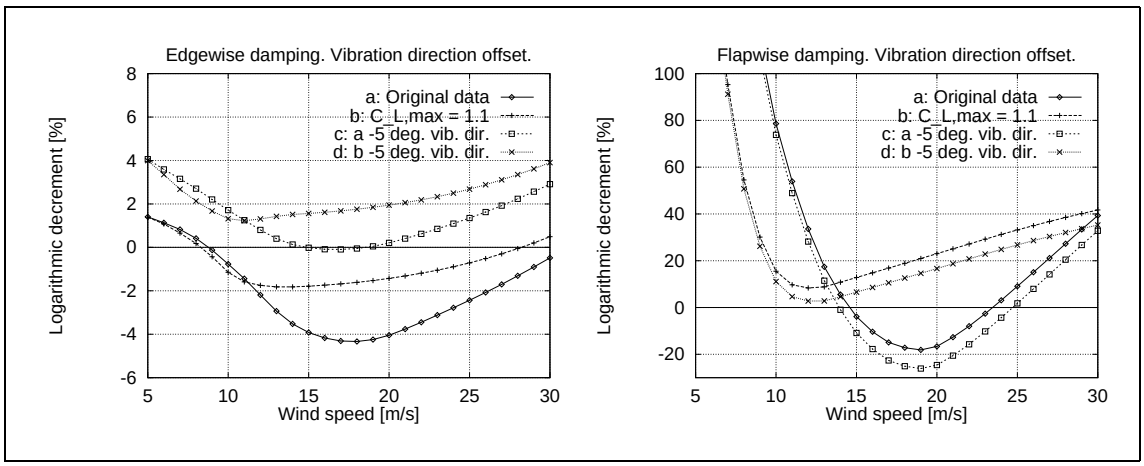


*Figure 3.12. Logarithmic decrement for original and modified airfoil data with the same $t/c = 18\%$ airfoil along the blade. The vibration direction, $\theta_{RB}$ in Figure 2.9, has been offset $\Delta\theta_{RB} = -5°$ for* c- *and* d-*curves, respectively.*

## 3.2 Airfoil modifications – global

In the present section we demonstrate how modifications of airfoil data along the blade can improve the aerodynamic damping conditions and that we at the same time can maintain an acceptable power performance. Still, we apply the quasi-steady model from Section 2 for the calculations, without loss of generality in the conclusions.

A set of airfoil data, which typically could be supplied by the blade manufacturer, is used for the basic turbine, which we modify. These airfoil data are denoted the *original* data, and they are shown in Figure 3.13. The data for the turbine – relevant for the analyses – are listed and referred to in Table 3.1. If not stated explicitly these data are used throughout the analyses. The basic distribution of airfoil data along the blade is determined by the local airfoil thickness, except when specific local modifications are applied. A 3-D plot of the distribution of the original airfoil data is shown in Figure 3.16.

*Table 3.1. Wind turbine main data.*

| | | |
|---|---|---|
| Air density, $\varrho$ | = | 1.23 kg/m$^3$ |
| Rotor angular velocity, $\Omega$ | = | 3.04 rad/s |
| Tip pitch setting, $\theta_{tip}$ | = | $-0.5°$ |
| Tip radius, $R$ | = | 20.5 m |
| Flapwise frequency, $f_1$ | = | 1.805 Hz |
| Edgewise frequency, $f_2$ | = | 2.963 Hz |
| Mode shapes in Figure 3.20. | | |
| Mass and thickness distribution in Figure 3.21. | | |
| Chord and aerodynamic pitch in Figure 3.22. | | |

The initial step in the investigation is a *basic modification* of the original airfoil data guided by the findings in Section 3.1. We use high lift airfoils towards the blade root and low lift data towards the blade tip. The weighting by the mode shapes should then lead to a reasonable distribution of properties relevant for both damping and performance. The airfoil data with this basic modification are shown in Figure 3.14. The maximum lift towards the blade root is $C_L = 1.6$, and the maximum lift towards the blade tip is $C_L = 1.2$. The 3-D distribution of these data is shown in Figure 3.17. The corresponding curves for power, axial force and aerodynamic damping – modal damping and damping per unit length at 20 m/s – are shown in Figures 3.23, 3.24 and 3.25, respectively. The results obtained by use of the original airfoil data are marked in the figure legends with a, and the results corresponding to the basic modified data are marked with b. It is observed that the aerodynamic damping is significantly improved. The negative trough characteristic for the original data – due to the high lift profiles at the tip – is cut off, and the damping is increased for both edgewise and flapwise mode shapes. The power curve for the modified airfoil data is somewhat reduced in a wind speed range in the vicinity of 15 m/s, and the curve is increasing with increasing wind speed. We try to improve both the power curve and the damping by further modifications locally.

The additional modifications make use of local airfoil changes and aim at improving power performance by modifying the airfoil data towards the blade root in direction of higher maximum lift and at improving damping by modifying the airfoil data towards the blade tip to have a higher drag after stall onset. The applied airfoil data are shown in Figure 3.15. The left plot shows data corresponding to what would be obtained by applying stall strips at the leading edge. The main change compared with original data is an increase of drag after stall onset. These data are used towards the blade tip, covering 2 m from radius 16.5 m to radius 18.5 m. The right plot shows data corresponding to what would be obtained by applying vortex generators on the suction side of the profile. The main change compared

with original data is an increase of maximum lift. These data are used towards the blade root, covering 8 m from radius 5.0 m to radius 13.0 m.

A 3-D plot of the distribution of the airfoil data with stall strips in addition to the basic modification is shown in Figure 3.18. The calculation results obtained by using this modification are marked in the figure legends with c. It is observed that the maximum power level has decreased and the damping has improved above stall onset. The 3-D plot in Figure 3.19 shows the distribution of airfoil data, where both stall strips and vortex generators have been applied in addition to the basic modification. The corresponding results are marked in the figure legends with d. For this case the tip pitch has been increased with $+1.0°$, such that $\theta_{tip} = +0.5°$. The power level has increased to approximately the same level as obtained with the original airfoil data at the expense of somewhat decreased damping compared to case c with stall strips alone. Altogether, we have obtained an almost unchanged power curve, but significantly improved damping both for the edgewise and the flapwise mode shapes, comparing with the original layout. Results from a similar calculation example are published in a fact-sheet [22]. The tendencies in these results have been confirmed by full scale tests performed by Bonus Energy A/S [24].

The damping conditions can be even more improved by applying a modest uniform vibration direction offset of $\Delta\theta_{RB} = -2.0°$, corresponding to a change of the vibration direction with the same angle along the blade. The results are shown as the curve marked with e in the legends in Figures 3.24 and 3.25. Of course, this last modification does not influence the power curve.

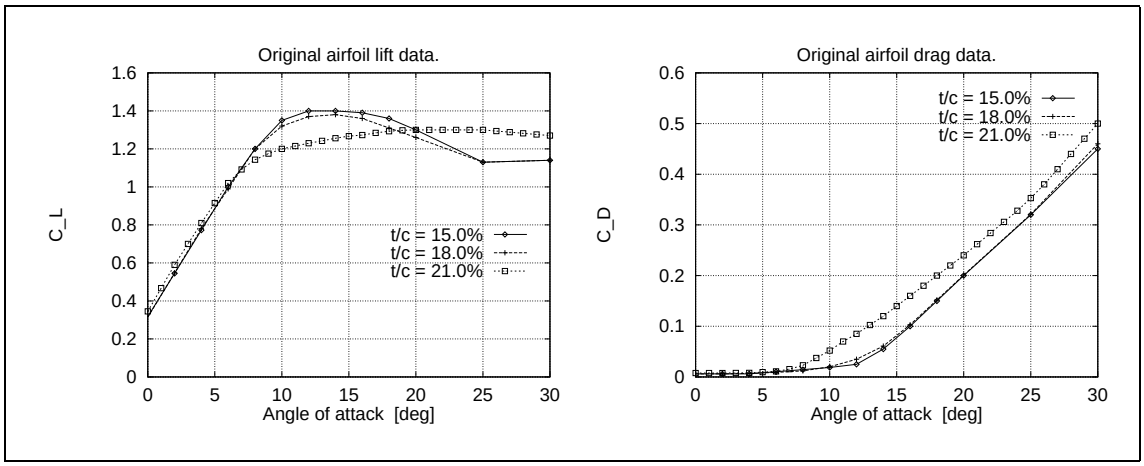


*Figure 3.13. Original airfoil data.*

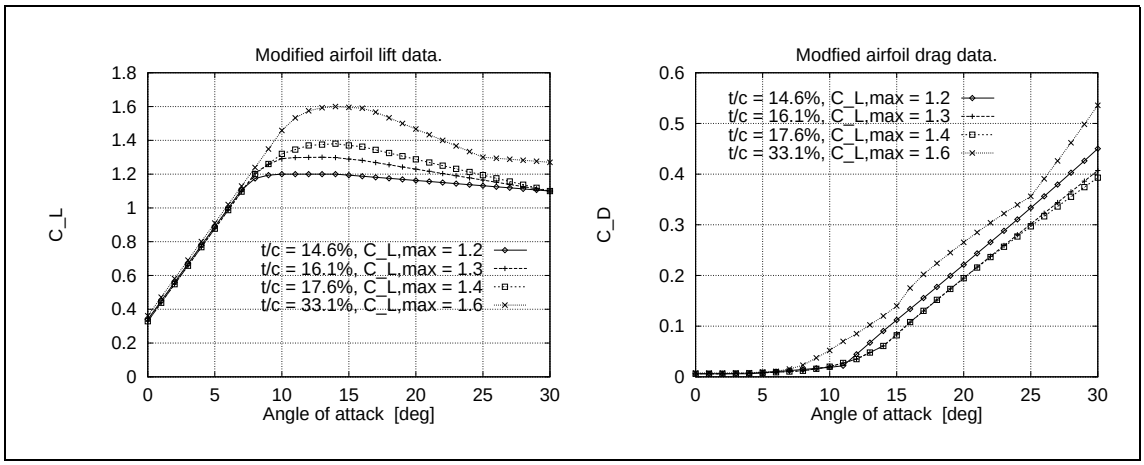


*Figure 3.14. Modified airfoil data, referred to as the basic modification.*

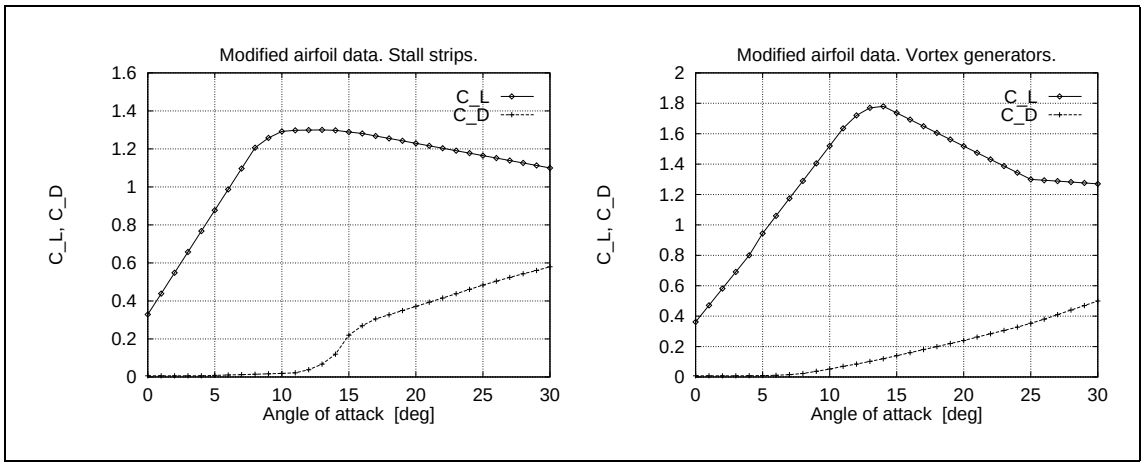


*Figure 3.15. Airfoil data corresponding to what would be obtained by applying stall strips and vortex generators, respectively.*

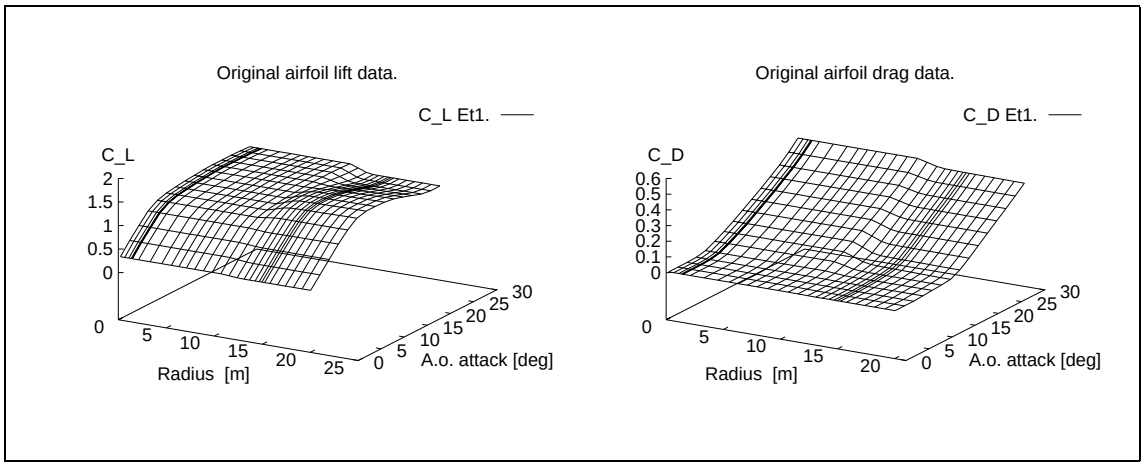


*Figure 3.16. Distribution of original airfoil data along the blade.*

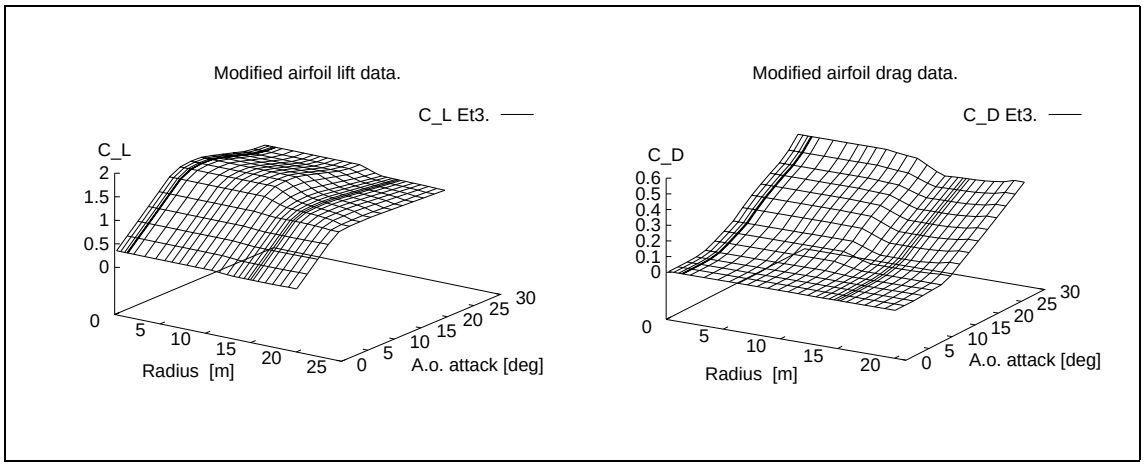


*Figure 3.17. Distribution of modified airfoil data along the blade. Referred to as the basic modification.*

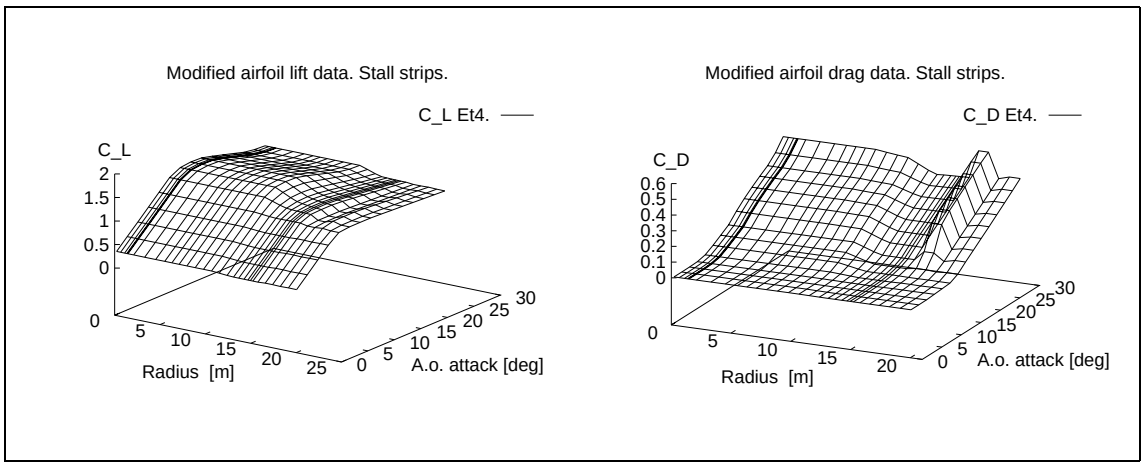


*Figure 3.18. Distribution of modified airfoil data along the blade. Stall strips covering 2 m (r = 16.5–18.5 m).*

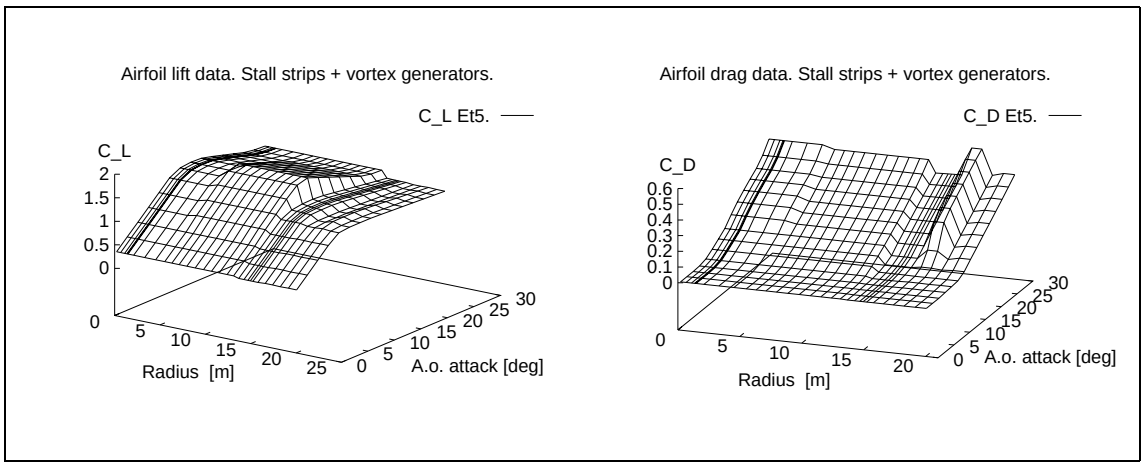


*Figure 3.19. Distribution of modified airfoil data along the blade. Stall strips covering 2 m (r = 16.5–18.5 m). Vortex generators covering 8 m (r = 5.0–13.0 m).*

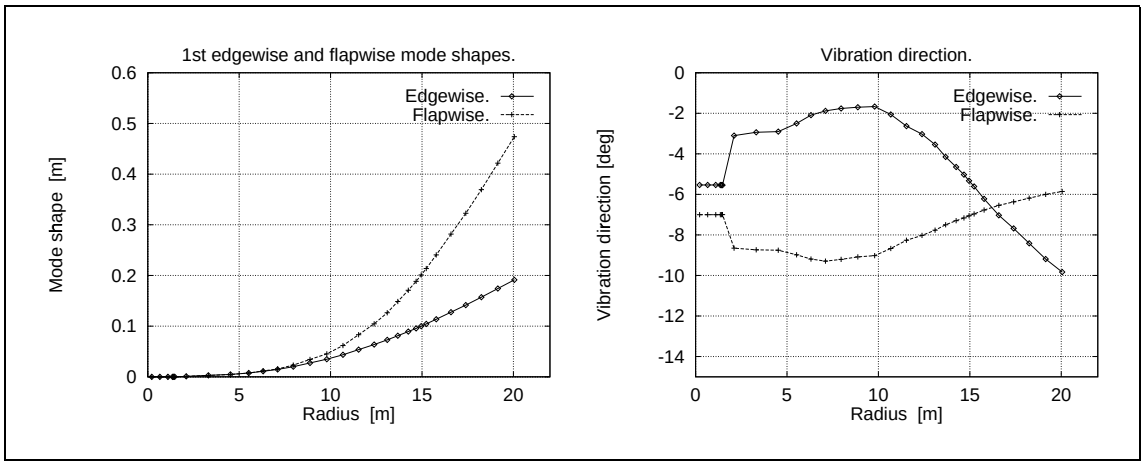


*Figure 3.20. Mode shape amplitudes and vibration direction, $\theta_{RB}$. The flapwise direction is plotted with an offset of $\Delta\theta_{RB} = -90°$.*

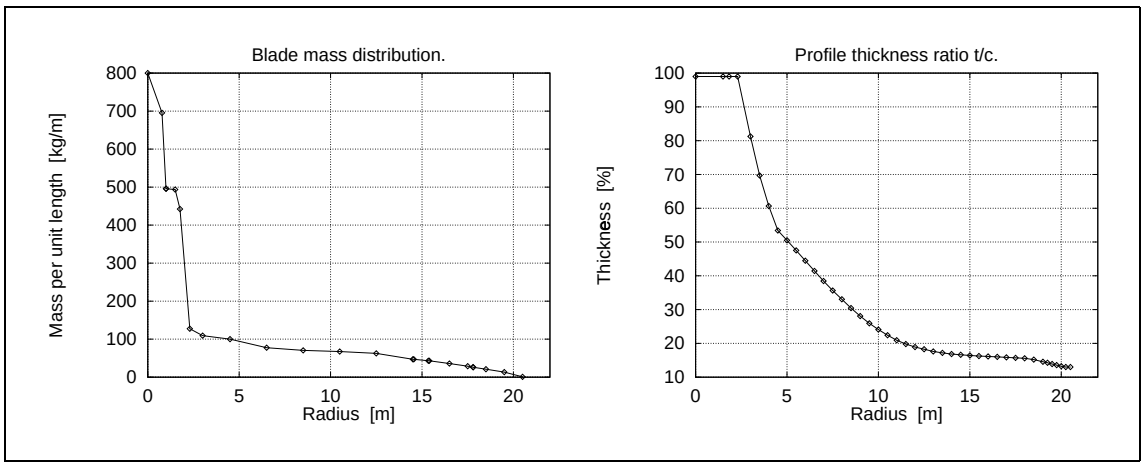


*Figure 3.21. Mass distribution and thickness ratio.*

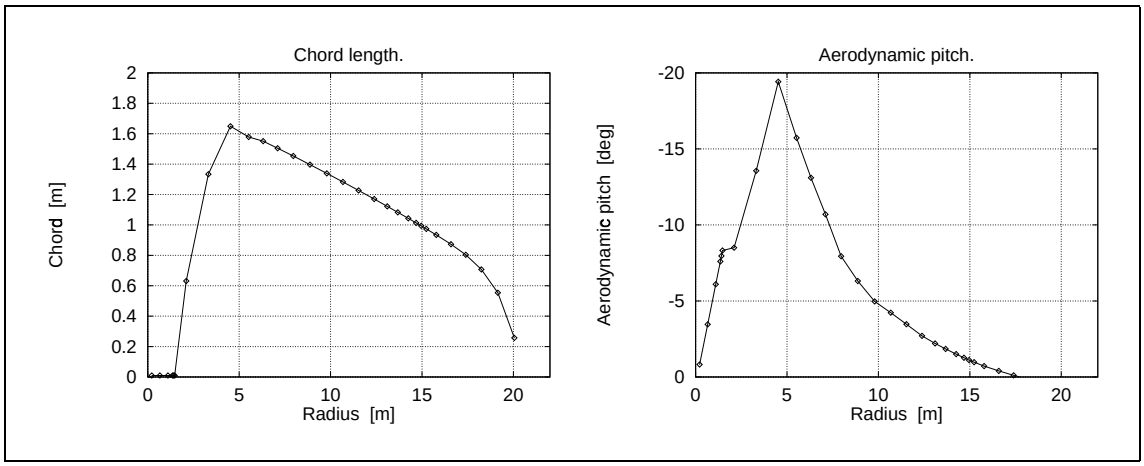


*Figure 3.22. Chord distribution and aerodynamic pitch.*

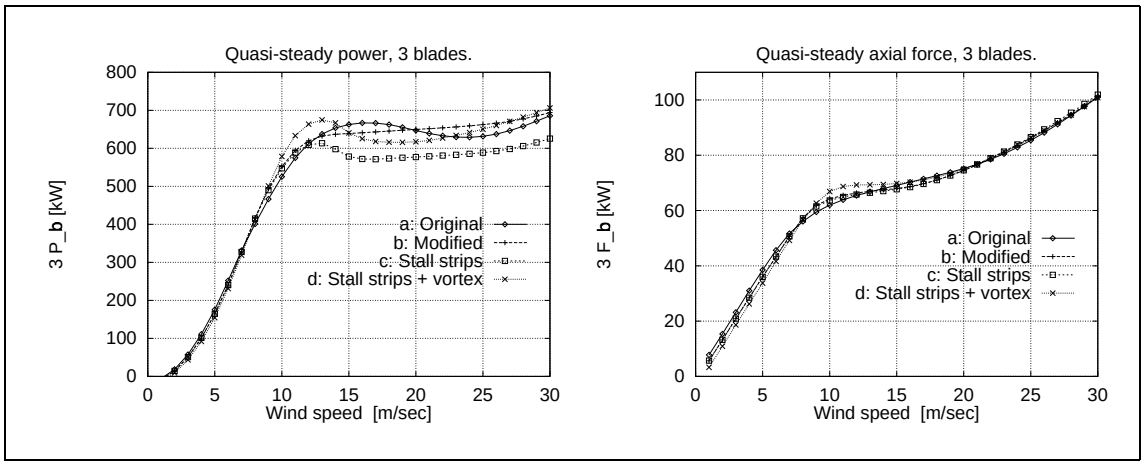


*Figure 3.23. Power and axial force for 3 blades. For the* d*-case, the tip pitch has been increased,* $\Delta\theta_{tip} = +1°$.

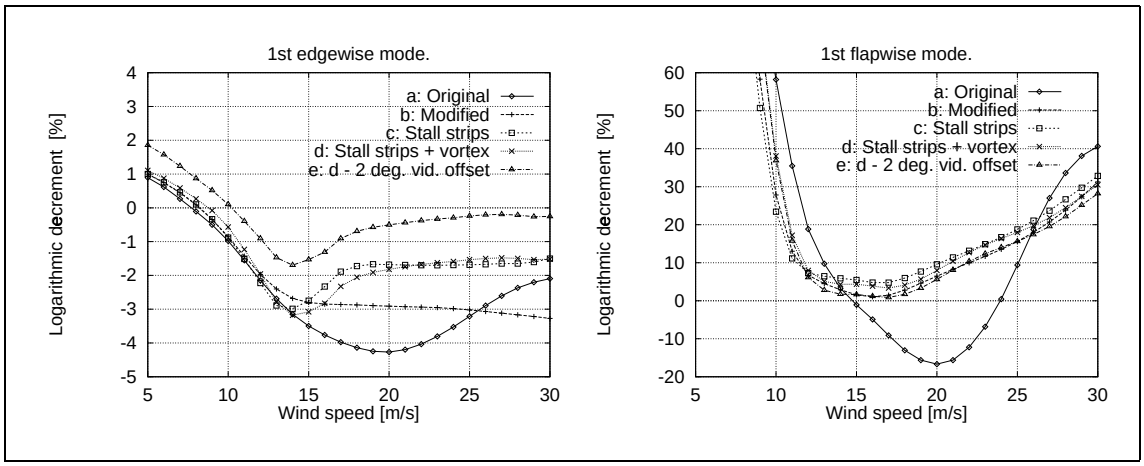


*Figure 3.24. Modal damping for the different choices of airfoil data and distribution along the blades. The* e*-curves correspond to the* d*-curves with a vibration direction offset of* $\Delta\theta_{RB} = -2°$*, changing the vibration direction* $2°$ *more out of the rotor plane – uniformly along the blade – for the edgewise mode.*

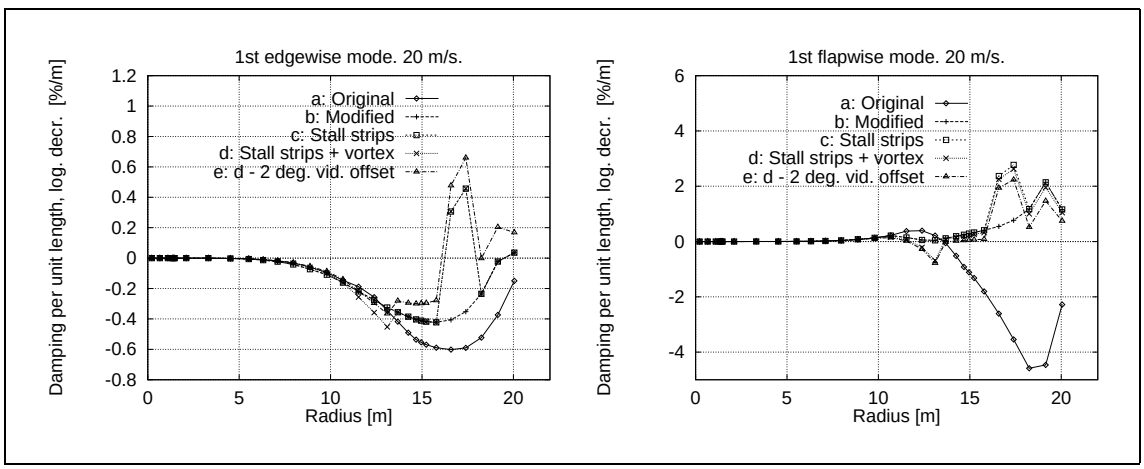


*Figure 3.25. Modal damping per unit length.*

## 3.3 Offset of vibration direction – global

In previous sections we have referred to influence of vibration direction of the mode shapes on aerodynamic damping, often in connection with changes of other parameters. Below the subject is resumed by looking at it isolated and by considering uniform change of vibration direction along the blade and the associated influence on the modal damping. *Vibration direction* and *structural pitch* are often used as synonyms. However, vibration direction is more precise, because it is the direction of the local velocity that really matters. If structural pitch refers to the orientation of the local principal bending axis, then the vibration direction will differ from the structural pitch, as the local vibration direction at a given blade radius will be influenced by the bending behaviour of the blade from its root to the actual radius.

In Figure 3.26 the influence of offsetting the vibration direction uniformly along the blade is shown. The offset angles are $\Delta\theta_{RB} = -3.0°$ and $\Delta\theta_{RB} = +3.0°$, respectively. The turbine data are the same as used in Section 3.2, listed in Table 3.1. We apply the airfoil data denoted *original*. The mode shapes with vibration directions are shown in Figure 3.20. In this figure the offset used in the present context corresponds to moving the direction curves in the right plot parallel with the ordinate.

For the edgewise mode the offset results in change of the level of the damping with approximately $+1.0\%$ logarithmic decrement per $-1.0°$ offset. According to the present sign convention from Figure 2.9 a negative offset increases the damping. The opposite tendency is observed for the flapwise mode. The aerodynamic power and axial force are unaffected by the change as shown in Figure 3.27.

An overview of the influence of vibration direction offset is shown in Figures 3.28 and 3.29 for three different wind speeds. In order to obtain positive damping for the edgewise mode the edgewise direction must be offset approximately $-5.0°$. This is probably not possible with the present data without making the situation worse in the flapwise direction. However, in Section 3.2 it was shown that airfoil modifications along the blade improve the damping conditions generally, and in this case there is more freedom to change vibration direction and obtain positive or close to positive damping for both the edgewise and the flapwise mode shapes. In the example in Section 3.2, Figure 3.24, $-2.0°$ change of vibration direction gave almost zero damping (minimum $-1.5\%$ at 14 m/s) for the edgewise mode, while the flapwise damping was kept positive.

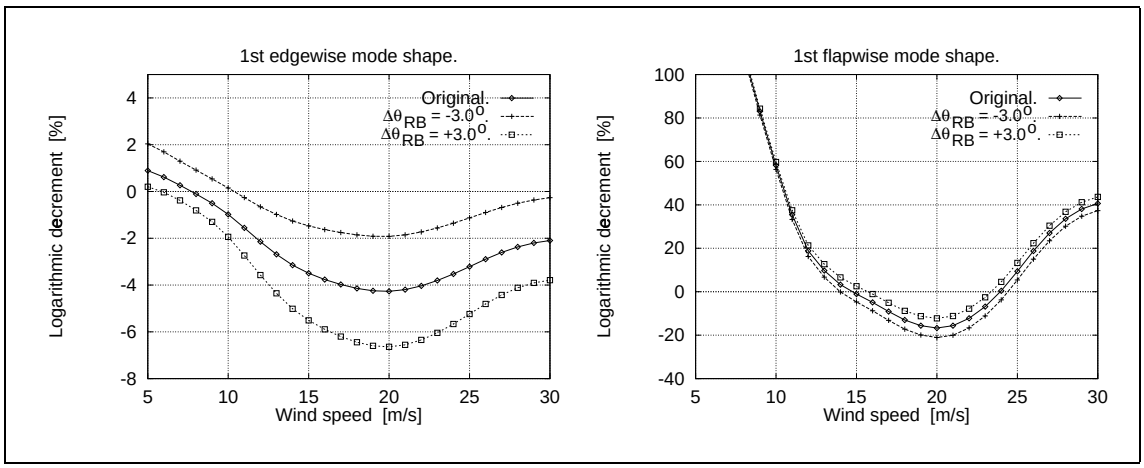


*Figure 3.26. Aerodynamic damping for different offsets of vibration direction.*

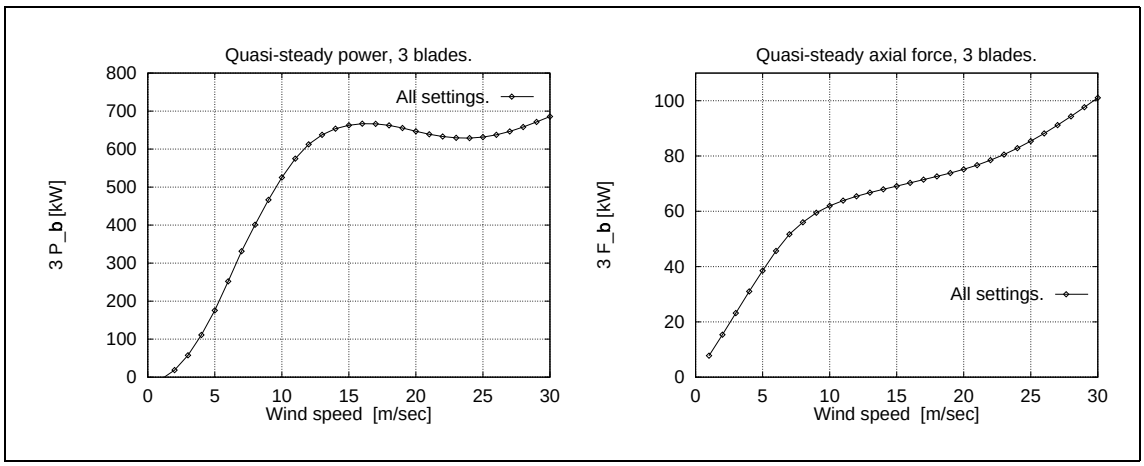


*Figure 3.27. Power and axial force for all settings of vibration direction.*

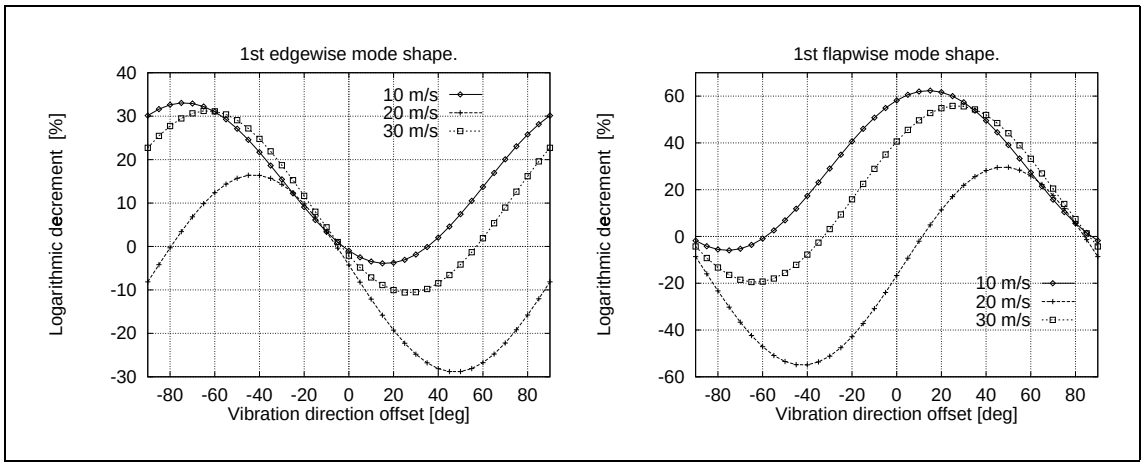


*Figure 3.28. Logarithmic decrement when vibration direction is offset.*

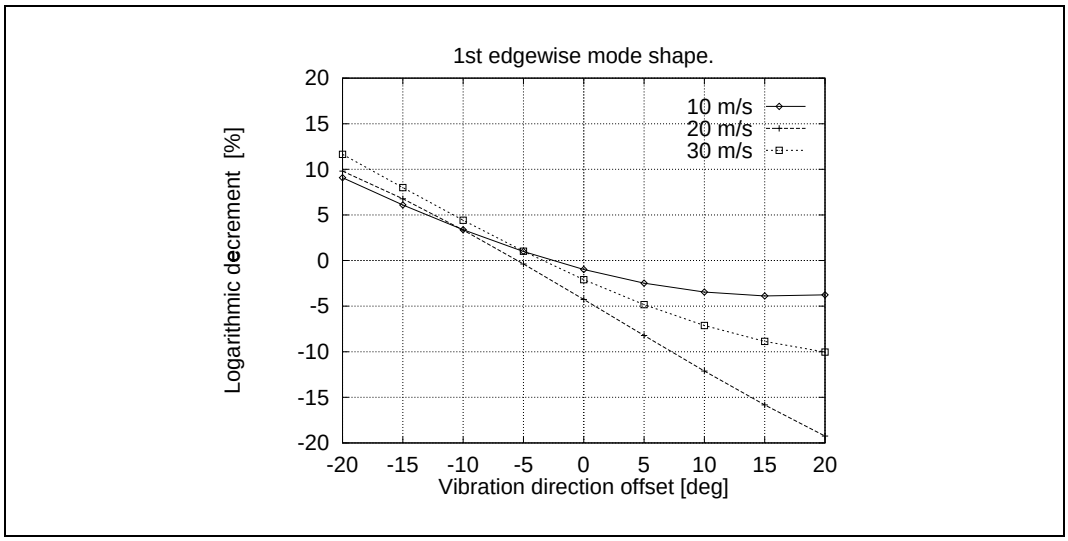


*Figure 3.29. Details of logarithmic decrement for the edgewise mode shape.*

## 3.4 Angle of attack offset

The examples in this section show the influence of offsetting the angle of attack $-3.0°$ and $+3.0°$, respectively. The basic turbine data are the same as used in Section 3.2, listed in Table 3.1. In the plots of airfoil data in Figure 3.30 the original and the offset data are shown for one thickness ratio, $t/c = 18\%$. A negative offset, $\Delta\alpha_0 < 0.0°$, corresponds to moving the airfoil data curves to the left, towards lower angle of attack values, and vice versa. Changes like that could be obtained by changing the camber of the airfoil. The applied values of $\Delta\alpha_0 = \mp 3.0°$ might be exaggerated, compared to what is possible in practice, but our intention is primarily to demonstrate the tendencies. Below negative offset is denoted positive camber, and positive offset is denoted negative camber.

Figure 3.31 shows the influence of camber changes on aerodynamic damping without simultaneous change of tip pitch, $\Delta\theta_{tip} = 0.0°$. Both the damping level and the wind speed corresponding to minimum damping are changed significantly. The left plot in Figure 3.33 and the plot in Figure 3.34 show the accompanying changes in power and axial force. Only through a simultaneous change of tip pitch angle, $\Delta\theta_{tip} = \pm 3.0°$, the power and the axial force will be unaffected.

The situation with simultaneous change of tip pitch is illustrated in the figures as well. Figure 3.32 shows the damping. This case is aerodynamically identical with the vibration direction offset case presented in Section 3.3, Figure 3.26. Increased camber, i.e. the camber changed in positive direction, corresponds to negative vibration direction change, $\Delta\theta_{RB} < 0.0°$.

With positive camber significant improvement of the edgewise damping is observed, while this on the other hand decreases the flapwise damping. The right plot in Figure 3.33 shows that the power is unaffected, and so is the axial force. The force is not shown.

That the vibration direction offset case and the angle of attack offset case with simultaneous change of tip pitch have identical effects can be understood, if we realize that the net effect in both cases is to change the mode shape vibration directions in the cross sectional plane, keeping the aerodynamic properties the same for a given angular direction in the plane.

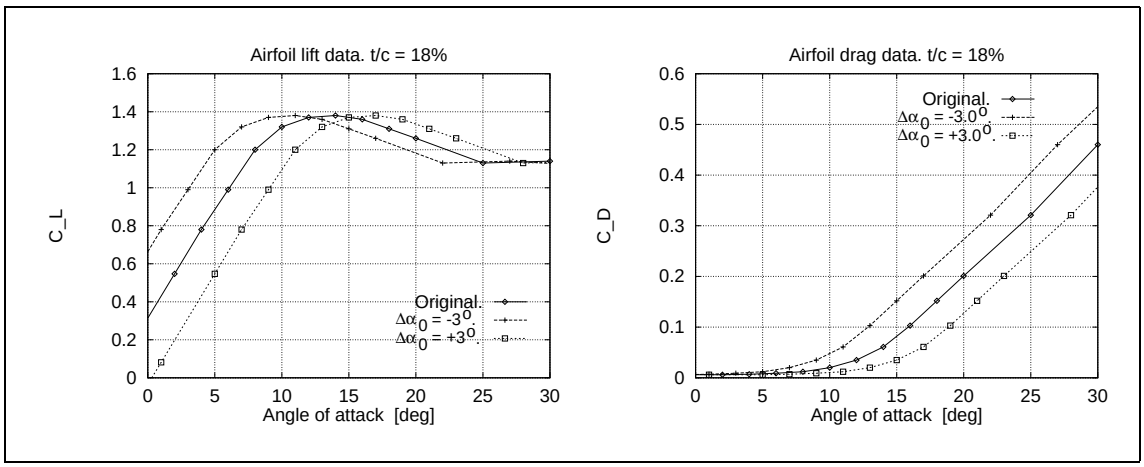


*Figure 3.30. Airfoil data with angle of attack offset. Camber case.*

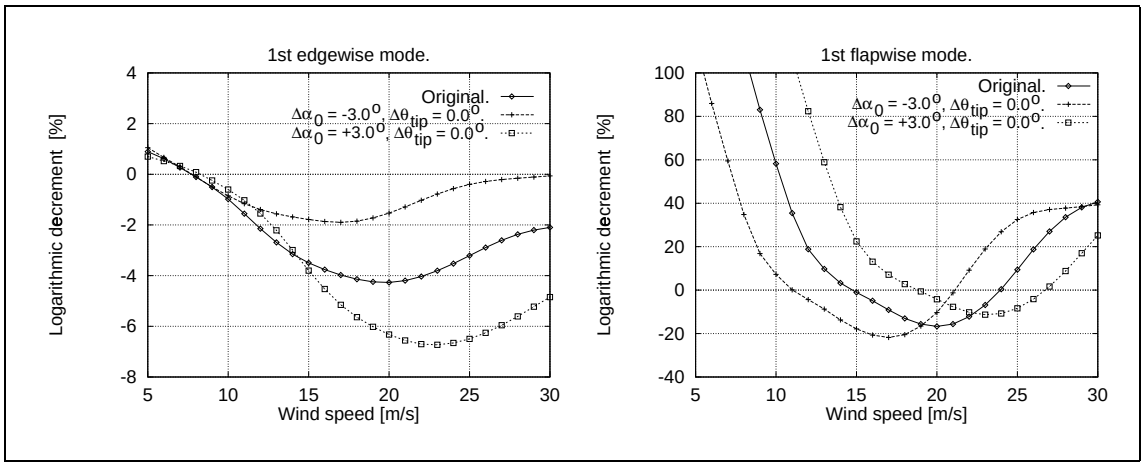


*Figure 3.31. Aerodynamic damping for offset of angle of attack corresponding to camber. No adjustment of tip pitch setting.*

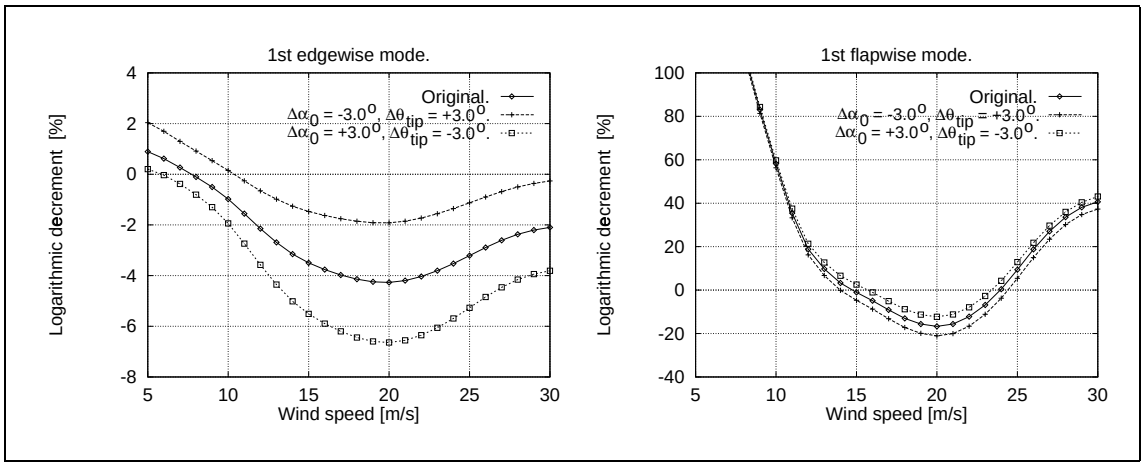


*Figure 3.32. Aerodynamic damping with angle of attack offset and tip pitch setting offset correspondingly in order to compensate for the power change.*

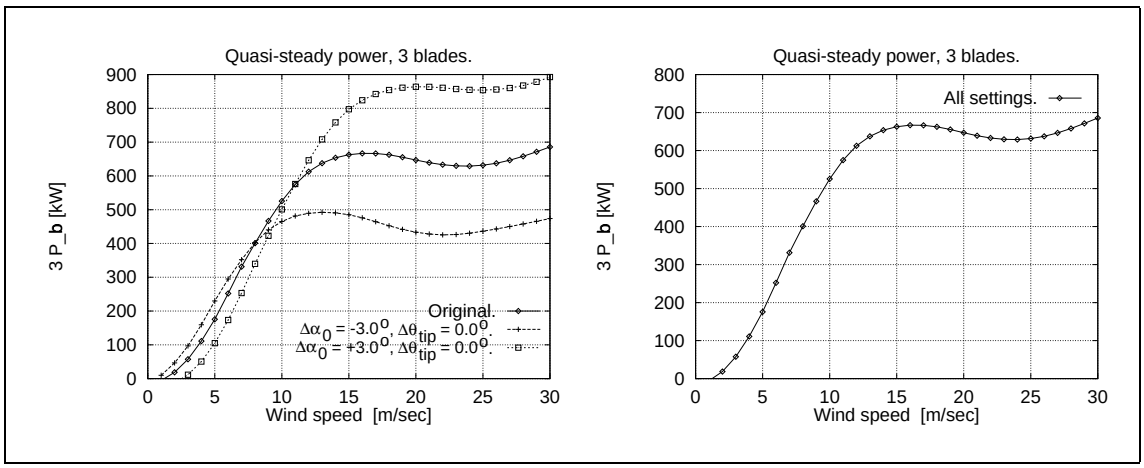


*Figure 3.33. Power for 3 blades, corresponding to the cases in Figures 3.31 and 3.32, respectively.*

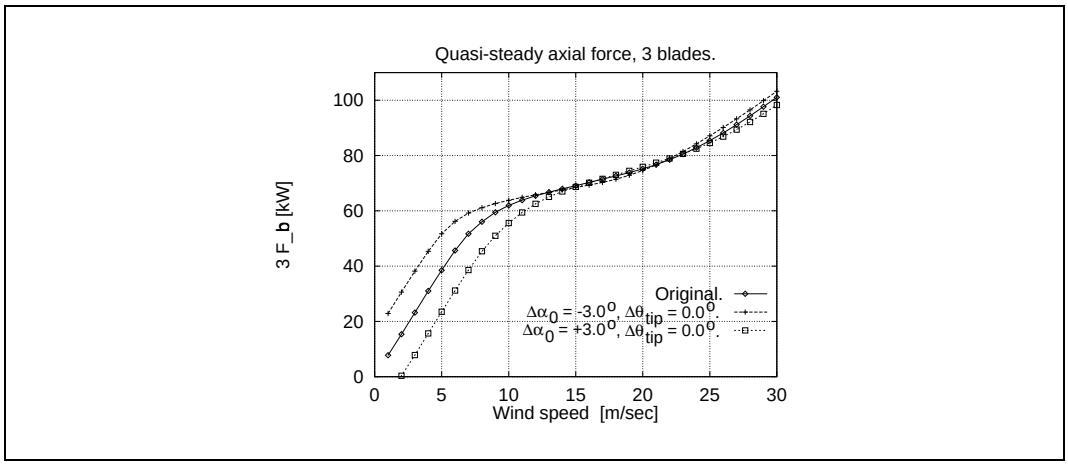


*Figure 3.34. Axial force for 3 blades corresponding to angle of attack offset.*

## 3.5 Tip pitch offset

Below it is demonstrated how the aerodynamic damping changes with offset of tip pitch angle, $\Delta\theta_{tip}$. Again, the basic turbine data – previously used in Section 3.2 and listed in Table 3.1 – are applied. Tip pitch change involves a simultaneous change of both mode shape vibration direction and angular rotation of the aerodynamic properties about the blade axis. In Figure 3.35 the resulting modal damping is shown. It is characteristic that the damping curves practically are shifted along the wind speed axis, and that the level changes only very little. A negative tip pitch offset, $\Delta\theta_{tip} < 0.0°$, shifts the damping curves towards lower wind speed. The sign convention is defined in Figure 2.1 in Section 2.1.1, where $\theta$ is shown positive. A positive change of angle corresponds to moving the trailing edge downwind. The influence on power and axial force is shown in Figure 3.36.

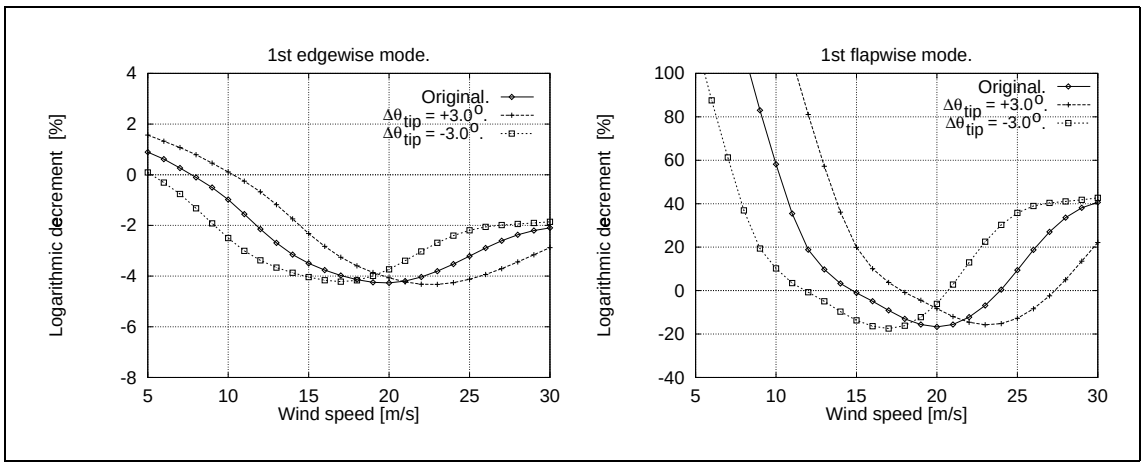


*Figure 3.35. Aerodynamic damping when only tip pitch setting is changed.*

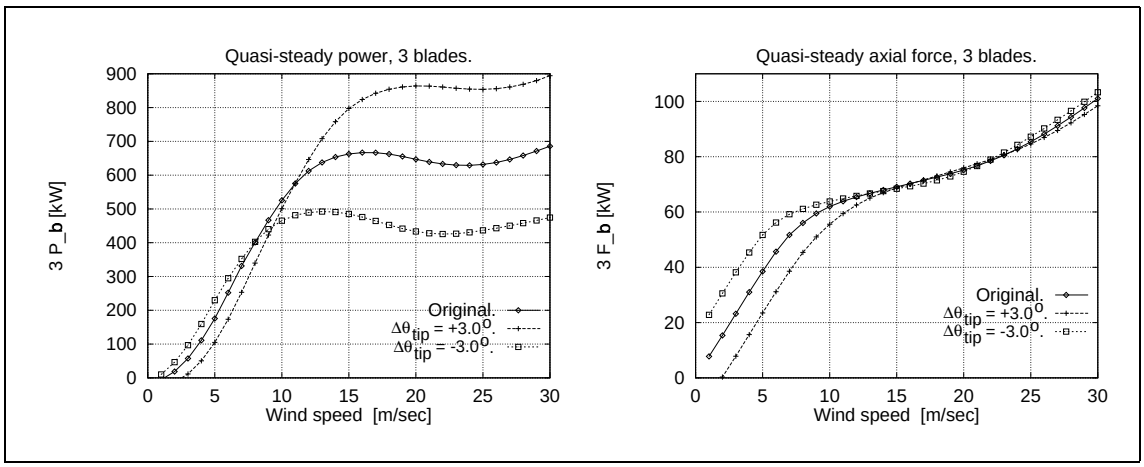


*Figure 3.36. Power and axial force when only tip pitch setting is changed.*

## 3.6 Blade mass and stiffness modifications

The influence from change of the modal mass and stiffness on aerodynamic damping is investigated by using the expression for modal damping in Appendix A.1, Equation A.16

$$\delta_n \simeq \frac{C_n}{2M_n f_n} \quad \text{for } C_n \ll 1 \ . \tag{A.16}$$

Here $C_n$ is the aerodynamic damping coefficient, $M_n$ is the modal mass and $f_n$ is the natural frequency of the actual mode shape.

Alternatively the natural frequency can be expressed by the modal mass and the modal stiffness $K_n$ by using

$$f_n = \frac{1}{2\pi}\sqrt{\frac{K_n}{M_n}} \ , \tag{3.1}$$

giving the new expression for aerodynamic damping

$$\delta_n \simeq \frac{C_n}{2\sqrt{M_n K_n}} \quad \text{for } C_n \ll 1 \ . \tag{3.2}$$

It is obvious from this equation that both mass and stiffness scales the aerodynamic damping such that increasing any of the two will decrease the numerical value of the damping. The aerodynamic damping is shown in Figure 3.37 for three different values of the modal mass as function of modal frequency, corresponding to variation of the modal stiffness. The reference case is a typical 19.0 m blade with modal mass $M_{n0} = 445$ kg, natural frequency $f_{n0} = 2.96$ Hz and assumed aerodynamic damping $\delta_{n0} = -3.0\%$. Note that the sign is changed in the figure. The situation covers a typical situation at 20 m/s.

In Figure 3.37 three curves are shown for different reference values of structural damping, 2.5%, 3.0% and 3.5%. The structural damping is assumed to scale linearly with the natural frequency, which would be the case for viscous damping. In the figure values of aerodynamic damping above the structural damping curves correspond to instability, as the resulting damping is negative here.

The following can be observed and concluded from Figure 3.37 and the equations above:

1. Increasing the mass while keeping the stiffness constant reduces the frequency and consequently the negative aerodynamic damping. At the same time the structural damping will be reduced with nearly the same amount, so the resulting margin against instability will change very little.
2. Increasing the stiffness and the mass with the same factor will keep the frequency constant, but improve the stability. This is clearly seen from Equation 3.2.
3. Increasing the stiffness with a less than proportional increase in mass will increase the frequency and improve the stability margin even more.
4. An 'efficient' lightweight blade with narrow blade chord at the inner and middle part (low edgewise stiffness) will have properties in the upper left part of the diagram, which indicates high tendency towards unstable edgewise vibrations. Yet, it should be remembered that the chord length scales the aerodynamic damping, e.g. $c_{xx} = \frac{1}{2}c\varrho \ \ldots$ as seen from Equation 2.16 in Section 2.1.1.

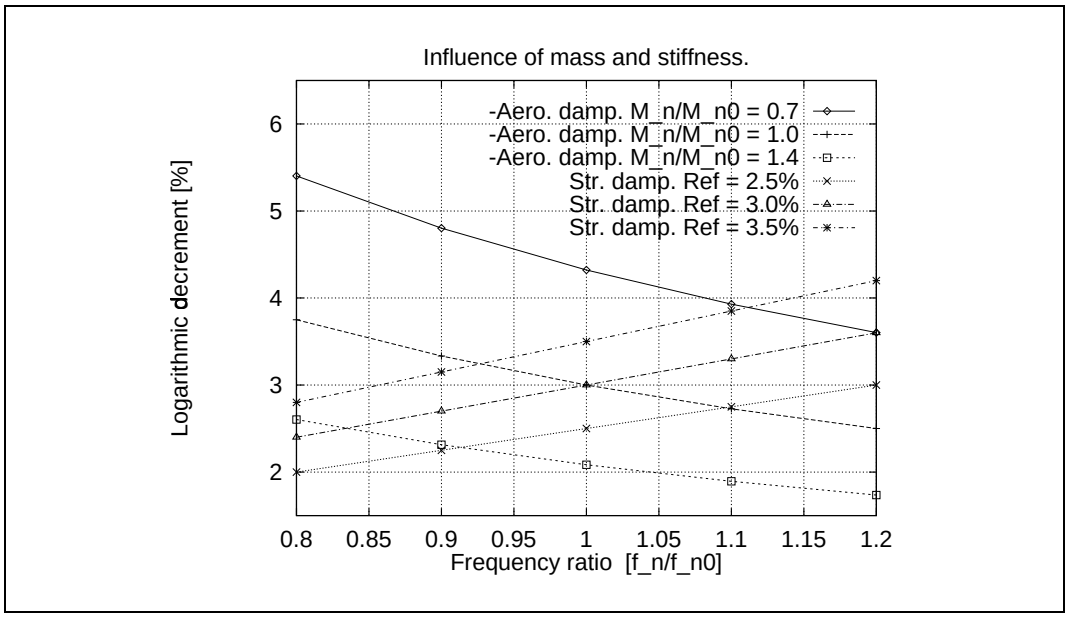


*Figure 3.37. Aerodynamic and structural damping as function of natural frequency ratio. The curves with legends $M_n/M_{n0}$ show the aerodynamic damping and correspond to constant mass, where $M_n$ is the actual mass and $M_{n0}$ is the modal mass of the reference blade. The three linear curves show structural damping, which is assumed to be proportional to the frequency, with the percentage shown in the legend equal to the damping at the reference frequency, frequency ratio $f_n/f_{n0} = 1$.*

# 4 Blade torsional deformation

In order to investigate the influence of torsional rotation of the blade cross section around the blade axis, $z_R$, calculations have been performed involving both the fundamental edgewise and flapwise mode shapes. A typical 19.0 m blade is used, namely the basic, unmodified blade from Section 3.2 with turbine data from Table 3.1. The airfoil data are shown in Figure 3.13, the mode shapes in Figure 3.20 in polar coordinates, the mass distribution and thickness ratio in Figure 3.21 and the chord and twist distribution in Figure 3.22.

The natural frequency for blade torsional vibration is very high for presently manufactured blades, so the pure torsional modes are not considered in the present context. However, torsion of the blade might be important anyway, because the modes of interest have components of torsional deformation. During operation this torsion might be amplified due to increased torsional moment at the inner part of the blade originating from the transverse inertia forces, which will be offset from the blade axis as the blade deflects. For instance, the axial force will deflect the blade flapwise, and the inertia force from the edgewise vibration will generate a moment inwards along the blade.

The sign convention for the angle corresponding to rotation of a blade cross section is shown in Figure 4.1. The shown rotation corresponds to the rotation in the fundamental edgewise mode shape, and the situation just described will amplify this rotation. The torsional rotations accompanying the edgewise and flapwise mode shapes are also shown in Figure 4.2 together with the transversal deformation components. The rotation is heavily exaggerated – approximately a factor $10^{12}$ – meaning that the rotation in the pure mode is practically zero. Still, the above mentioned amplification justifies the investigation, and the rotation might be important for more flexible blades, which are likely to be manufactured in the future.

Calculations of aerodynamic damping are performed by forcing the blade to rotate about the blade axis. The transversal deformation in mode shape $n$ is a harmonic vibration with the natural frequency, $\omega_n$, which in accordance with the formulation of the modal equations in Appendix A can be written

$$\{u^R(r,t)\} = \left\{ \begin{array}{c} u_x^R \\ u_y^R \end{array} \right\} = \{\varphi_n^R(r)\}\, q_{n0} \cos(\omega_n t) \ , \tag{4.1}$$

where the mode shape is normalized, so that the length of the mode shape vector is 1.0 m at the tip, $\sqrt{[(\varphi_{nx}^R)^2 + (\varphi_{ny}^R)^2]} = 1.0$ m, and $q_{n0}$ becomes the resulting amplitude at the tip in the resulting direction of vibration.

The accompanying forced rotations have the same shape as the rotations shown in Figure 4.2 – for mode shape $n$ denoted $\varphi_{nz}^R$ – and they are normalized to 1.0° at the blade tip and multiplied with a normal coordinate, $q_{nz0}$, in order to obtain a specified rotation at the tip. The rotation is further applied with the same frequency as the transversal mode shape and different phases, $\alpha_z$, according to

$$\theta_z(r,t) = \varphi_{nz}^R(r) q_{nz0} \cos(\omega_n t + \alpha_z) \ . \tag{4.2}$$

For $q_{nz0} = 1.0$ (note – the units are carried by the mode shapes) the influence of the rotation of the section on the angle of attack for different phases $\alpha_z$ is shown in Figure 4.3. In the left plot the transversal deformation of the blade is zero, and in the right plot the deflection amplitude in the edgewise mode shape is 0.2 m at the tip, i.e. $q_{n0} = 0.2$. The free wind speed is 20 m/s and the results are at radius 19.2 m.

In Figure 4.4 the aerodynamic damping is shown as logarithmic decrement for both the edgewise and the flapwise mode shapes. It is calculated as work of the aerodynamic forces per cycle (see Appendix A.2). No dynamic stall is applied. In both cases the normal coordinate for the section rotation is $q_{nz0} = 1.0$, meaning that the rotation amplitude at the tip is 1°. The phase is varied in steps of 45°. Denoting the flapwise mode number 1 and the edgewise number 2, the normal coordinates for the transversal deflections are $q_{10} = 0.5$ and $q_{20} = 0.2$, resulting in tip deflection amplitudes of 0.5 m and 0.2 m, respectively. The basic situation with no rotation is shown in both cases. It is observed that the rotations in phase and in counter-phase with the transversal mode, respectively, have almost the same damping as the case with no rotation – in the figures the damping curves for these cases are practically coinciding. If we denote phase angles between 0° and 180° for leading phases and the ones between 180° and 360° for lagging phases, we see that the leading phases increase the aerodynamic damping and the lagging decrease the damping.

Loops showing the relation between the local ( $r = 19.2$ m) edgewise mode shape deformation and the projection of the aerodynamic force on the deformation vector are plotted in Figure 4.5. The arrows show the direction of travelling the loops. For clock-wise rotation the area of the loops corresponds to negative aerodynamic damping, and anti-clockwise rotation corresponds to positive damping.

It should be noted that the work from the aerodynamic moment, which might be important in stall, has been neglected.

At present we have no knowledge about the phase and the size of the rotation angle for actual turbines, so it is difficult to estimate exactly how important this situation is. Still, it is expected that the phase will be close to 0°, meaning that the influence from section rotation is probably negligible. However, as the investigation shows that the phenomenon might result in decreased damping, the case should be given further attention.

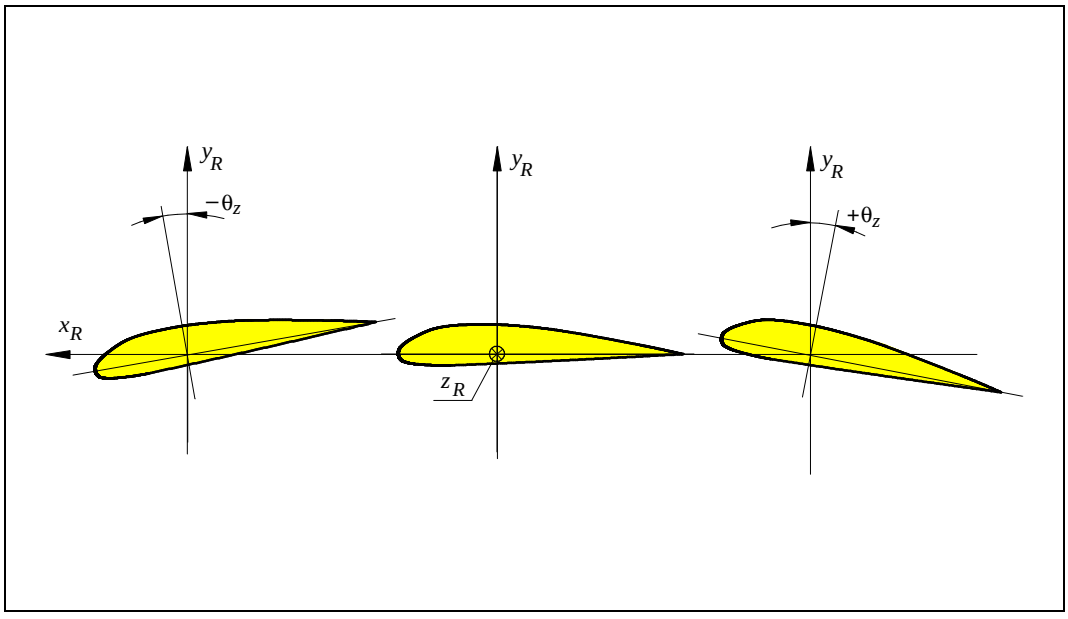


*Figure 4.1. Sign convention for torsional deformation and rotation of blade sections. The blade is seen from the root towards the tip end, and the axis along the blade, $z_R$, is pointing into the paper.*

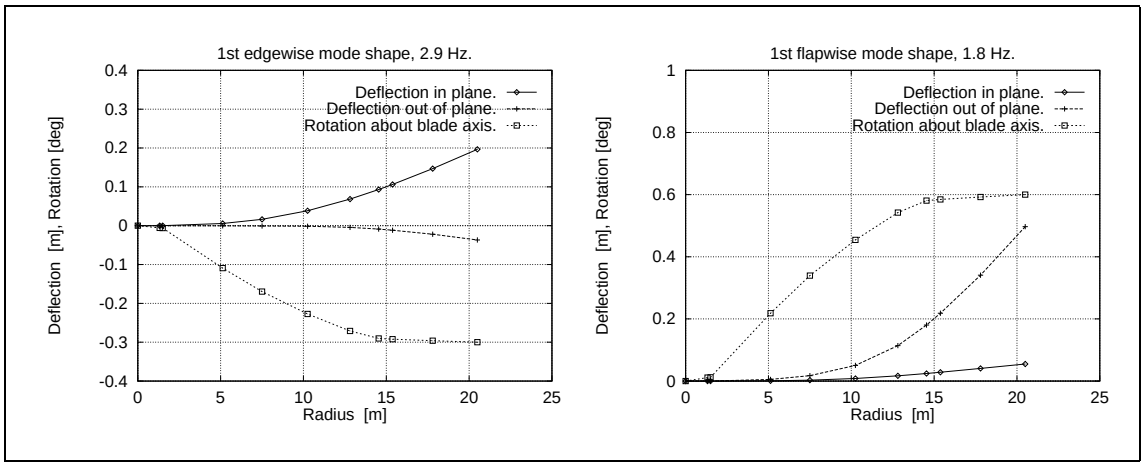


*Figure 4.2. Components of edgewise and flapwise fundamental mode shapes including torsional rotation for a typical 19.0 m blade. The size of the rotations are heavily exaggerated. For known blades the rotations are close to zero.*

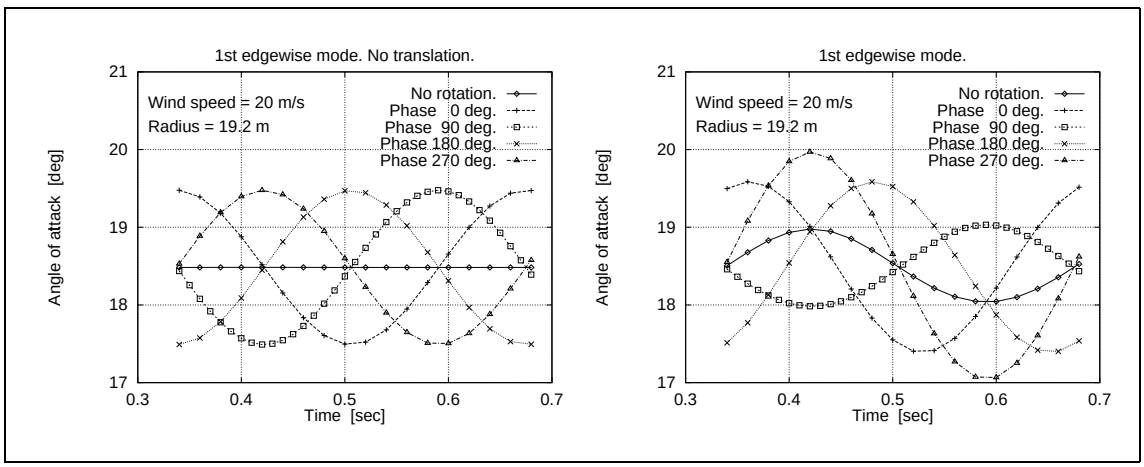


*Figure 4.3. Influence from rotation of cross section on angle of attack for different phases of the rotation of the cross section relative to the transverse deformation of the blade. In the left figure, the transverse deformation is close to zero.*

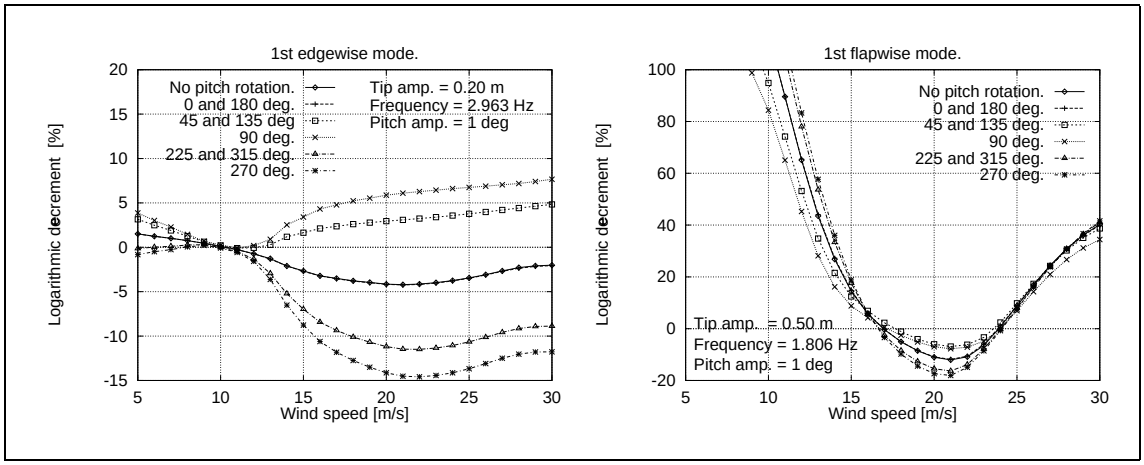


*Figure 4.4. Aerodynamic damping as function of wind speed for different phases of the section rotation relative to the transverse deformation. The curves corresponding to* 0° *and* 180° *phases are practically coinciding with the curve corresponding to no pitch rotation.*

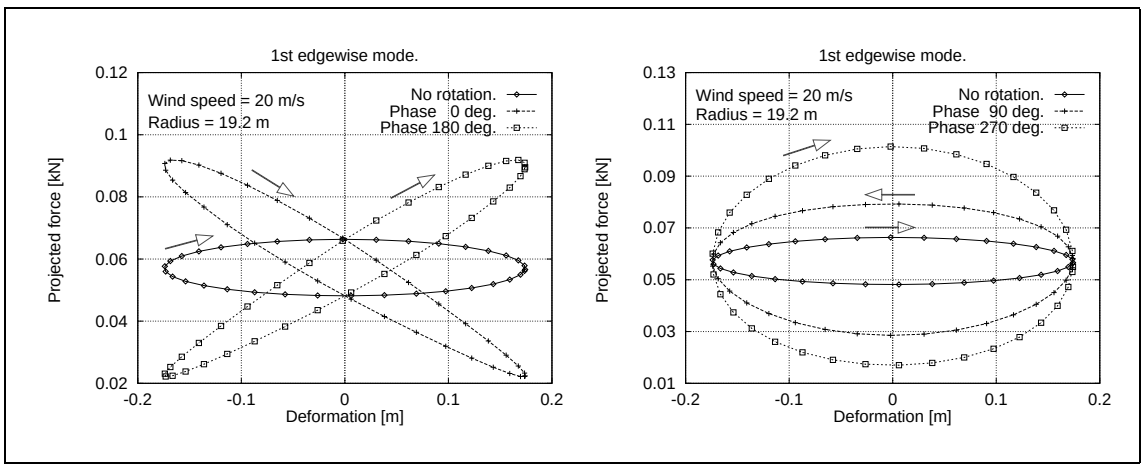


*Figure 4.5. Loops showing the relation between the local ( r = 19.2 m) edgewise mode shape deformation and the projection of the aerodynamic force on the deformation vector. The wind speed is 20 m/s. The arrows show the direction of travelling the loops just below the respective arrows.*

# 5 Modification and implementation of dynamic stall models

So far, the aerodynamic damping has been discussed on the basis of quasi-steady aerodynamics, because this simplifies the equations considerably and allows a clear insight in for example the influence of the airfoil characteristics. However, the importance of dynamic stall and stall hysteresis for the dynamic loading of stall regulated wind turbines operating at high wind is well recognized. This also means that an engineering dynamic stall model must be included in an aeroelastic model in order to provide results, which correlate with measurements and in particular to investigate stall induced vibrations. In a project under the JOULE I programme a first comprehensive study of stall induced vibrations was carried out [7] with particular emphasis on the flapwise vibrations. It was concluded that the dynamic stall models improved significantly the level of agreement with measurements, although the models were considered to be *first generation models.*

The JOULE I project was followed by the JOULE II project *Dynamic Stall and Three-dimensional Effects* [8], where a thorough validation of different dynamic stall models against primarily 2D wind tunnel measurements from Ohio State University was carried out. The main conclusion was that *"the investigated engineering dynamic stall models seem to be sufficiently representative in order to calculate the main dynamic loads for a wind turbine during ordinary operation in stall"*. The influence of the varying inflow velocity was paid some attention, but no unambiguous conclusion could be drawn.

In the present project the further development of the dynamic stall models has continued from the investigations carried out in the JOULE I and II projects, but now with particular focus on the aerodynamic damping for the individual models as well as influence on the damping from the different parameter settings in the stall models. A considerable work has also been carried out to see if the different field rotor measurements could be used for further development of the models and to tune the parameters in the models. The main part of this work is reported in [1]. Further, new dynamic stall wind tunnel measurements have recently become available [19], where the type of airfoil as well as the test parameters – as for instance reduced frequency and amplitude of the pitch oscillations – are chosen in order to fit wind turbine applications. Comparisons will be made with these data later in this section.

The dynamic stall models used by the different participants in the present project are:

- The Øye model [10] [11] used by DTU,
- the Beddoes Leishman model [12] with modifications used by FFA [21],
- the Onera model used by ECN [13] and
- the *fgh* model [15][23] and the Beddoes Leishman model [12] with modifications used by Risø.

A comparison of the models, except the FFA and Risø implementation of the Beddoes-Leishman model, can be found in [8], where also comparisons with wind tunnel data from OSU [9] are presented.

About the individual implementations of the dynamic stall models it should be noted that although the basic model is the same (for example the Beddoes-Leishman model used by FFA and Risø) there are differences, both with respect to the actual sub-models implemented from the basic model and further with respect to the actual numerical implementation. As an example the vortex shedding has not been included in the Risø model. Furthermore,

both FFA and Risø use the following equations to derive $C_L$, which originate from the Øye model [10]:

$$C_L = fC_{L,inv} + (1-f)C_{L,sep} \,, \tag{5.1}$$

where $f$ is the relative position of the lagged point of separation and $C_{L,inv}$ and $C_{L,sep}$ is the lift curve for inviscid flow and for fully separated flow, respectively. Also, the stationary value of $f$, denoted $f_{stat}$, is derived from the equation:

$$C_{L,stat} = f_{stat}C_{L,inv} + (1-f_{stat})C_{L,sep} \,. \tag{5.2}$$

As the FFA and Risø implementations and verifications of the Beddoes-Leishman model have not been described in the previous JOULE projects, these models will be paid some attention in the present report. FFA has further modified the model in order to take into account the variations in inflow velocity, $V_{rel}(t)$, and this will be described in detail.

## 5.1 Influence of variations in relative velocity

Typical variations in angle of attack, $\alpha$, and the relative velocity, $V_{rel}$, as measured in the Risø field rotor experiments [25], are shown in Figure 5.1 and Figure 5.2, respectively. The main frequency content originates from 1P variations due to instantaneous yaw error and wind shear. The question is, how the variations in $V_{rel}$ influence the stall hysteresis.

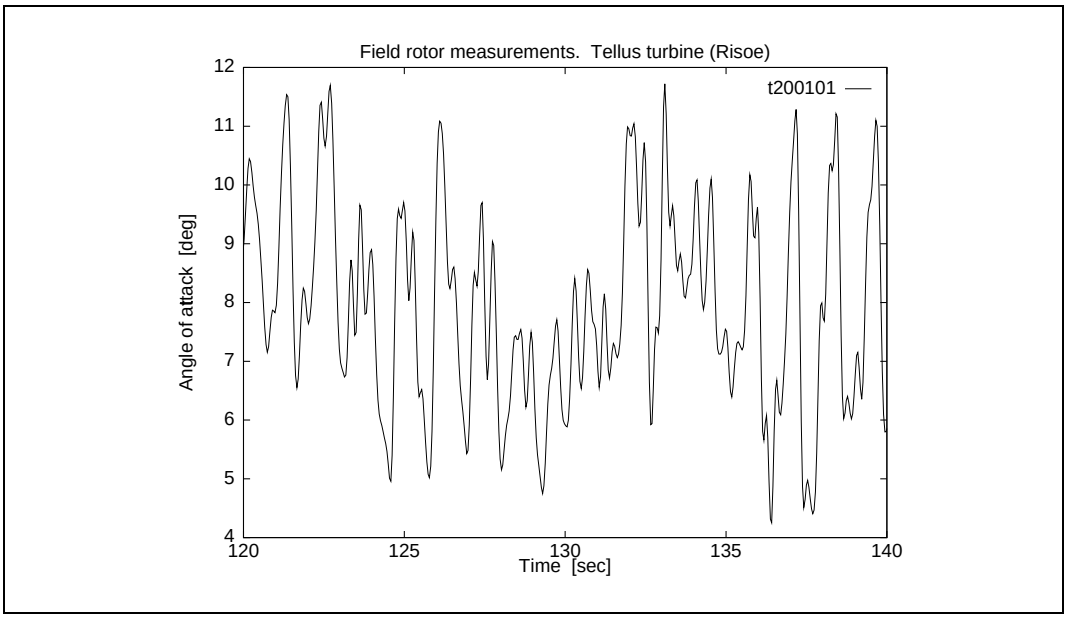


*Figure 5.1. Example of measured time trace of angle of attack, $\alpha$, during normal operation.*

A first attempt to investigate this problem was an analysis of the Risø field rotor data using the *fgh* model [14]. The *fgh* model includes a term for time variations in $V_{rel}$ and has the form:

$$C_L = C_{L,sta}(\alpha) + f(\alpha)\frac{c}{\overline{V_{rel}}}\frac{\mathrm{d}\alpha}{\mathrm{d}t} + g(\alpha)\left(\frac{c}{\overline{V_{rel}}}\right)^2\frac{\mathrm{d}^2\alpha}{\mathrm{d}t^2} + h(\alpha)\frac{c}{\overline{V_{rel}^2}}\frac{\mathrm{d}V_{rel}}{\mathrm{d}t} \,. \tag{5.3}$$

In this expression the operator $[\overline{\ }]$ denotes averaging with respect to time.

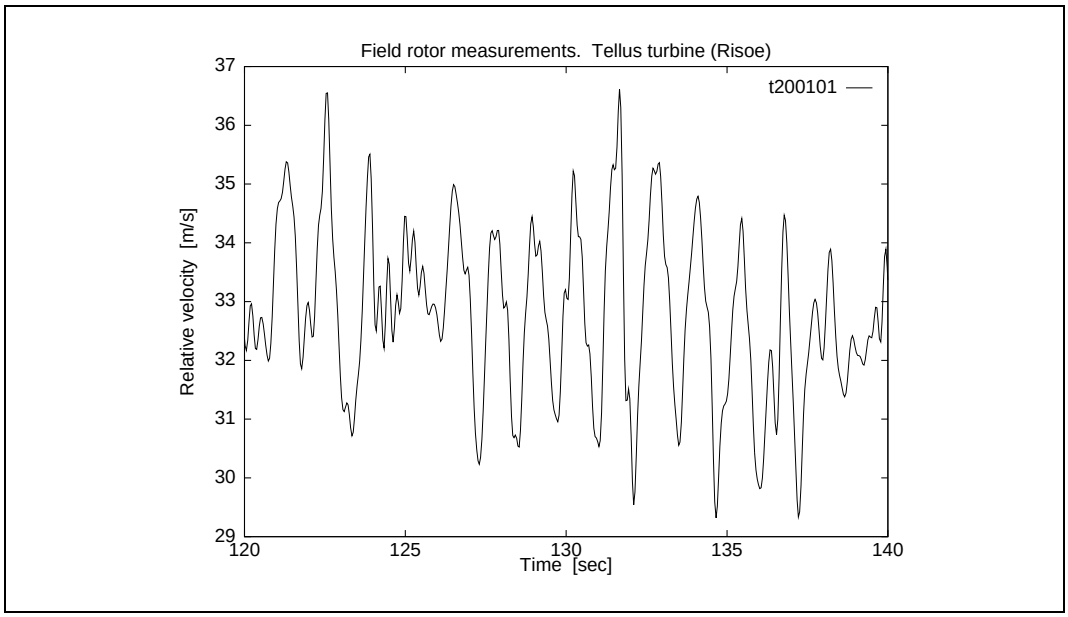


*Figure 5.2. Example of measured time trace of relative velocity, $V_{rel}$, during normal operation.*

Using this expression the coefficients $f$, $g$ and $h$ were derived by numerical optimization in order to minimize the deviation between simulated and measured $C_L$ for selected time series. Next, the coefficients were used to simulate stall hysteresis loops, where both $\alpha$ and $V_{rel}$ were varied harmonically. The conclusion from this investigation was that the phase between $\alpha$ and $V_{rel}$ is very important for the stall hysteresis. If $\alpha$ and $V_{rel}$ are in counter-phase, the influence of $V_{rel}$ is an increase in the size of the loops. The opposite is the case if $\alpha$ and $V_{rel}$ are in phase. Then the size of the loops decreases, and the direction of travelling the loops can even change to counter-clockwise. However, the influence on the aerodynamic damping from the variations in $V_{rel}$ seems to be small, as the damping is related to the $g$-function, which determines the slope of the main axis in the hysteresis loops.

Another investigation of the influence of variations of $V_{rel}$ has been performed within the previous JOULE II Project [8], where 2D CFD computations of dynamic stall with and without variations of $V_{rel}$ were carried out. The conclusion from these numerical simulations was that no major influence on the loops was observed.

Within the present project FFA has investigated different methods to include the effect of time variations of $V_{rel}$ in the Beddoes-Leishman model [17], which will be shown below.

## 5.2 FFA model of influence of variations in relative velocity

The FFA model is based on concepts from the Beddoes-Leishman model. The model includes the influence of the shed wake. The modifications of the original model are essentially:

- Modifications to the inviscid shed wake part.
- Addition of a model to take care of boundary layer effects due to varying relative velocity.
- The model works with $C_L$ and $C_D$ rather than $C_N$ and $C_T$, and the relation between the lift and the separation point, $f$, is different, as the FFA model – in the current version – makes use of Equation 5.2 instead of the original *Kirchoff formulation.*

The two first modifications above were included in order to improve the modelling for cases with time varying relative inflow velocity, $V_{rel}$.

Further, the drag is modelled with three components added to the steady value: 1) the induced drag, 2) vortex drag and 3) separation drag as described in [21].

### 1. Shed wake effects

In the original Beddoes-Leishman model a step change in angle of attack gives the corresponding step change in circulatory lift:

$$\Delta C_{Lc} = C_{L\alpha}\Phi_c \Delta\alpha\,, \tag{5.4}$$

where $C_{L\alpha}$ is the lift curve slope,

$$C_{L\alpha} = \frac{\mathrm{d}C_L}{\mathrm{d}\alpha} \quad \text{and}$$

$$\Phi_c = 1 - A_1 \exp(-b_1\beta s) - A_2 \exp(-b_2\beta s)\,. \tag{5.5}$$

Here $A_1, A_2, b_1$ and $b_2$ are model constants,

$$\beta = (1 - M^2) \quad \text{and}$$

$$s = \frac{2V_{rel}t}{c}$$

is the non-dimensional time obtained by normalization with the time it takes for a particle to travel along the semi-chord, $c/2$. $M$ is the Mach number.

Implementation for time step $n$ yields:

$$\begin{aligned} C_{Lc_n} &= C_{L\alpha}\left(\alpha_n - \alpha_{i_n}\right) \\ &= C_{L\alpha}\left(\alpha_n - (X_n + Y_n)\right) \\ &= C_{L\alpha}\alpha_{E_n}\,. \end{aligned} \tag{5.6}$$

In this equation

$\alpha_n$ is the geometrical angle of attack corrected for pitch rate effects,

$\alpha_{i_n}$ is the induced angle of attack,

$\alpha_{E_n}$ is the effective angle of attack,

$$\left.\begin{aligned} X_n &= X_{n-1}\exp\left(-b_1\beta\Delta s\right) + A_1\Delta\alpha_n\exp\left(-b_1\beta\tfrac{\Delta s}{2}\right) \text{ and} \\ Y_n &= Y_{n-1}\exp\left(-b_2\beta\Delta s\right) + A_2\Delta\alpha_n\exp\left(-b_2\beta\tfrac{\Delta s}{2}\right) . \end{aligned}\right\} \tag{5.7}$$

Pitch rate effects are further included by taking the angle of attack, $\alpha_n$ in Equations 5.6 and 5.7, as the angle of attack at the 3/4 chord position:

$$\alpha_n = \alpha_{\frac{1}{4}} + \dot{\theta}\frac{c}{2V_{rel}} , \tag{5.8}$$

where $\dot{\theta}$ is the pitch rate.

The shed wake effects are a function of the history of variations of the bound vorticity or circulation, $\Gamma$. Equation 5.4 assumes that $\Delta\Gamma$ is proportional to $\Delta\alpha$. This is only true for attached flow and constant velocity. Therefore, the following modifications to the original Beddoes-Leishman model are introduced.

Modification 1 – no restriction to attached flow but constant velocity

As a first step a lift coefficient $C_{L,est,n}$ with no influence from the shed vorticity is computed using Equation 5.6 with $\alpha_{E_n}$ equal to $\alpha_n$. The shed wake effects are now derived as follows:

$$\Delta C_{L,est} = C_{L,est,n} - C_{L,est,n-1} \quad \text{and} \tag{5.9}$$

$$\Delta\alpha_n = \frac{\Delta C_{L,est}}{C_{L\alpha}} . \tag{5.10}$$

$\Delta\alpha_n$ is now used in Equation 5.6 and 5.7 to compute $C_{Lc_n}$.

Modification 2 – varying relative velocity

The basic assumption is that the shed wake is a function of the history of the bound circulation and not of the history of the angle of attack or lift coefficient. The bound circulation is written as:

$$\Gamma = \frac{1}{2}cV_{rel}C_L = \frac{1}{2}cwC_{L\alpha} , \tag{5.11}$$

where $w$ is the velocity normal to the zero lift line. $w$ is related to $\alpha$ and $\alpha_0$ as:

$$w = (\alpha - \alpha_0)\, V_{rel} . \tag{5.12}$$

Equation 5.4 in the original Beddoes-Leishman model is now replaced by:

$$\Delta\Gamma = \frac{1}{2}c\Delta w\Phi_c C_{L\alpha} . \tag{5.13}$$

Equation 5.7 is written as:

$$\left.\begin{aligned} X_n &= X_{n-1}\exp\left(-b_1\beta\Delta s\right) + A_1\Delta w_n \exp\left(-b_1\beta\tfrac{\Delta s}{2}\right) \\ Y_n &= Y_{n-1}\exp\left(-b_2\beta\Delta s\right) + A_2\Delta w_n \exp\left(-b_2\beta\tfrac{\Delta s}{2}\right) \end{aligned}\right\} , \tag{5.14}$$

and the effective angle of attack is computed as:

$$\alpha_{E_n} = \frac{(w_n - X_n - Y_n)}{V_n} + \alpha_0 \ . \tag{5.15}$$

Modification 3 – combination of modifications 1 and 2

This method combines modifications 1 and 2 and applies to time varying inflow, and there are no restrictions to attached flow. First $\Delta w$ is computed as:

$$\Delta w = \frac{C_{L,est}}{C_{L\alpha}}\Delta V_{rel} + \frac{\Delta C_{L,est}}{C_{L\alpha}}V_{rel} \ , \tag{5.16}$$

and the effective angle of attack is computed from Equations 5.14 and 5.15.

## 2. Boundary layer effects due to changes in relative velocity

The unsteady Bernoulli equation at the edge of the boundary layer can be written as, [18]:

$$\frac{\partial C_{pe}}{\partial \xi} = -2q_e\frac{\partial q_e}{\partial \xi} - 2\frac{c}{V_{rel}^2}\left(q_e\frac{\partial V_{rel}}{\partial t} + V\frac{\partial q_e}{\partial t}\right) \ , \tag{5.17}$$

where

$$\xi = \frac{s}{c} \ , \ q_e = \frac{U_e}{V_{rel}} \ \text{ and } \ V_{rel} = U_\infty \ .$$

For an accelerating free-stream with $\frac{\partial V_{rel}}{\partial t} > 0$ the effective pressure gradient at the edge of the boundary layer becomes more favourable, resulting in less separation.

Assuming that $\alpha$ is constant, but the inflow is varying, $V_{rel} = V_{rel}(t)$, Equation 5.17 is written as:

$$\frac{\partial C_{pe}}{\partial \xi} = -2q_e\frac{\partial q_e}{\partial \xi} - 2\frac{c}{V_{rel}^2}\frac{\partial V_{rel}}{\partial t}q_e \ . \tag{5.18}$$

The second term in Equation 5.18 can be viewed as the modification of $\frac{\partial C_{pe}}{\partial \xi}$ due to the varying velocity, and the modification is finally written as:

$$\Delta\frac{\partial C_{pe}}{\partial \xi} = -2\frac{c}{V_{rel}^2}\frac{\partial V_{rel}}{\partial t}q_e = -4\gamma q_e \ , \tag{5.19}$$

where $\gamma$ is the non-dimensional velocity change rate.

The velocity effect on the pressure gradient is next translated into a change in angle of attack

$$\Delta\alpha_v = -\frac{\Delta\frac{\partial C_{pe}}{\partial \xi}}{\frac{\partial^2 C_{pe}}{\partial \xi \partial \alpha}} \ . \tag{5.20}$$

Inserting from Equation 5.19 we get:

$$\Delta\alpha_v = -\gamma \frac{4q_e}{\frac{\partial^2 C_{pe}}{\partial\xi\partial\alpha}} \; . \tag{5.21}$$

The change in angle of attack is used to define a corrected angle of attack, $\alpha_f$, which is used in the derivation of the separation point location

$$\alpha_f = \alpha + \Delta\alpha_v \; . \tag{5.22}$$

Here the angle of attack, $\alpha$, is the effective angle of attack, $\alpha_E$, possibly corrected for the inviscid pressure response using the time constant $\tau_p$ as described in [12].

Based on investigations of different computed and measured pressure distributions it is assumed that $\frac{4q_e}{\frac{\partial^2 C_{pe}}{\partial\xi\partial\alpha}}$ is a constant denoted $f_u$.

The value of $f_u$ used in the present investigations is 0.5 corresponding to

$$\frac{4q_e}{\frac{\partial^2 C_{pe}}{\partial\xi\partial\alpha}} = 0.5\frac{180}{\pi} \approx 30 \; ,$$

where 30 was a typical value found in computed and measured pressure distributions close to the leading edge [21].

## Numerical examples

To investigate the damping properties of the different submodels of the shed wake effects and the velocity effects, FFA has used a forced oscillation of a blade section in a direction defined by the angle $\delta$ shown in Figure 5.3

The aerodynamic force in the direction of translation is:

$$F_p = N\cos(\delta) + X\sin(\delta) \; . \tag{5.23}$$

For constant amplitude oscillations the work per cycle is:

$$W = \oint F_p \mathrm{d}r = c \oint F_p \mathrm{d}s \; , \tag{5.24}$$

where $r$ is the translation in meter and $s$ is non-dimensional translation.

For normalization, the aerodynamic work per cycle, $W_{qs}$, for oscillations in the airfoil normal direction using quasi-steady aerodynamics and small angles, is used. $W_{qs}$ can be derived as:

$$W_{qs} = 4\pi^2 \frac{1}{2}\varrho V_{rel}^2 k \left(cs_{amp}\right)^2 \quad , \tag{5.25}$$

where

$k = \dfrac{\omega c}{2V_{rel}}$ is the reduced frequency and

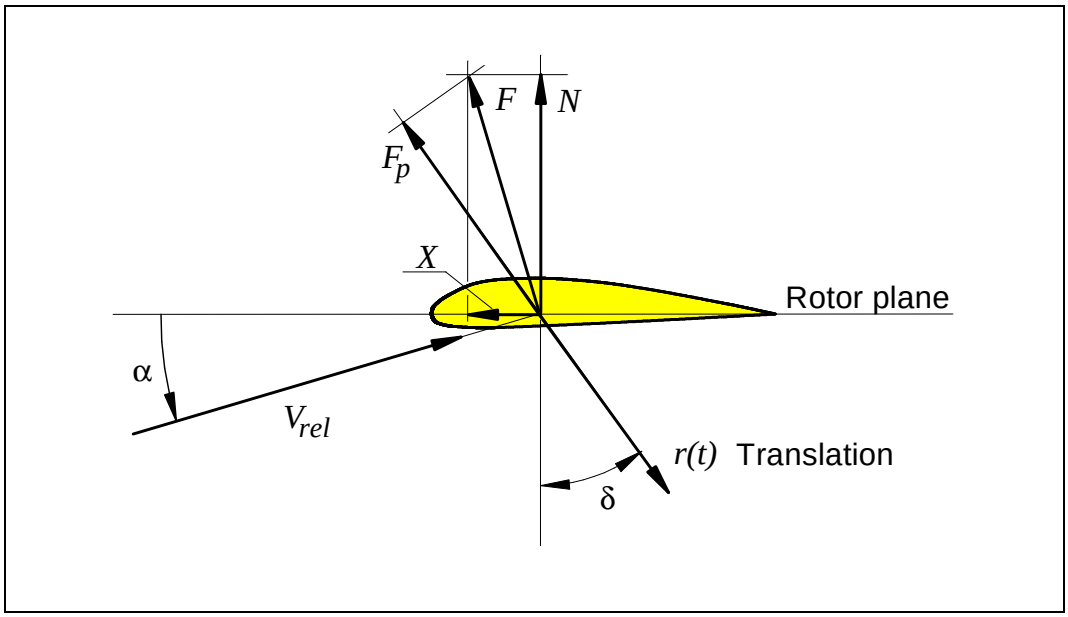


*Figure 5.3. Forced oscillations of a blade section is used to study the damping properties of different versions of the FFA dynamic stall model, including models for shed wake effects and velocity effects.*

$s = s_{amp} \cos(\omega t)$ is the non-dimensional translation.

The aerodynamic damping coefficient $W_{coeff}$ is finally defined as:

$$W_{coeff} = \frac{W}{W_{qs}} \quad . \tag{5.26}$$

The notations for the different models are:

- lpotmeth = 1 $\Longrightarrow$ standard Beddoes model
- lpotmeth = 2 $\Longrightarrow$ modification 1
- lpotmeth = 3 $\Longrightarrow$ modification 2
- lpotmeth = 4 $\Longrightarrow$ modification 3

The influence on the damping from the different models of the shed wake is shown in Figure 5.4 for oscillations in the edgewise direction. The airfoil data are for the 18% airfoil on the LM 19.0 m blade (see Section 6.1, Figure 6.1). Both the assumption that the change in circulation is proportional to the change in lift (lpotmeth 2) and inclusion of the shed wake effects (lpotmeth 3) increases the hysteresis on $C_L$ and decreases the hysteresis on $C_D$. Combining the two gives the same tendency.

Figures 5.5 to 5.8 show the computed damping coefficient as function of wind speed. The reduced frequency is 0.1 for the flapwise oscillations and 0.2 for the edgewise oscillations.

As concerns the damping characteristics, the general tendency is that almost no influence from modelling the shed wake effects is observed on the flapwise oscillations as illustrated in Figure 5.5, whereas a considerable increase of the damping for the edgewise oscillations is found as shown in Figure 5.6. Finally, the inclusion of the velocity effects on the boundary layer seems to decrease the damping slightly for the edgewise oscillations, but still with higher damping than the standard Beddoes model. This is illustrated in Figures 5.7 and 5.8.

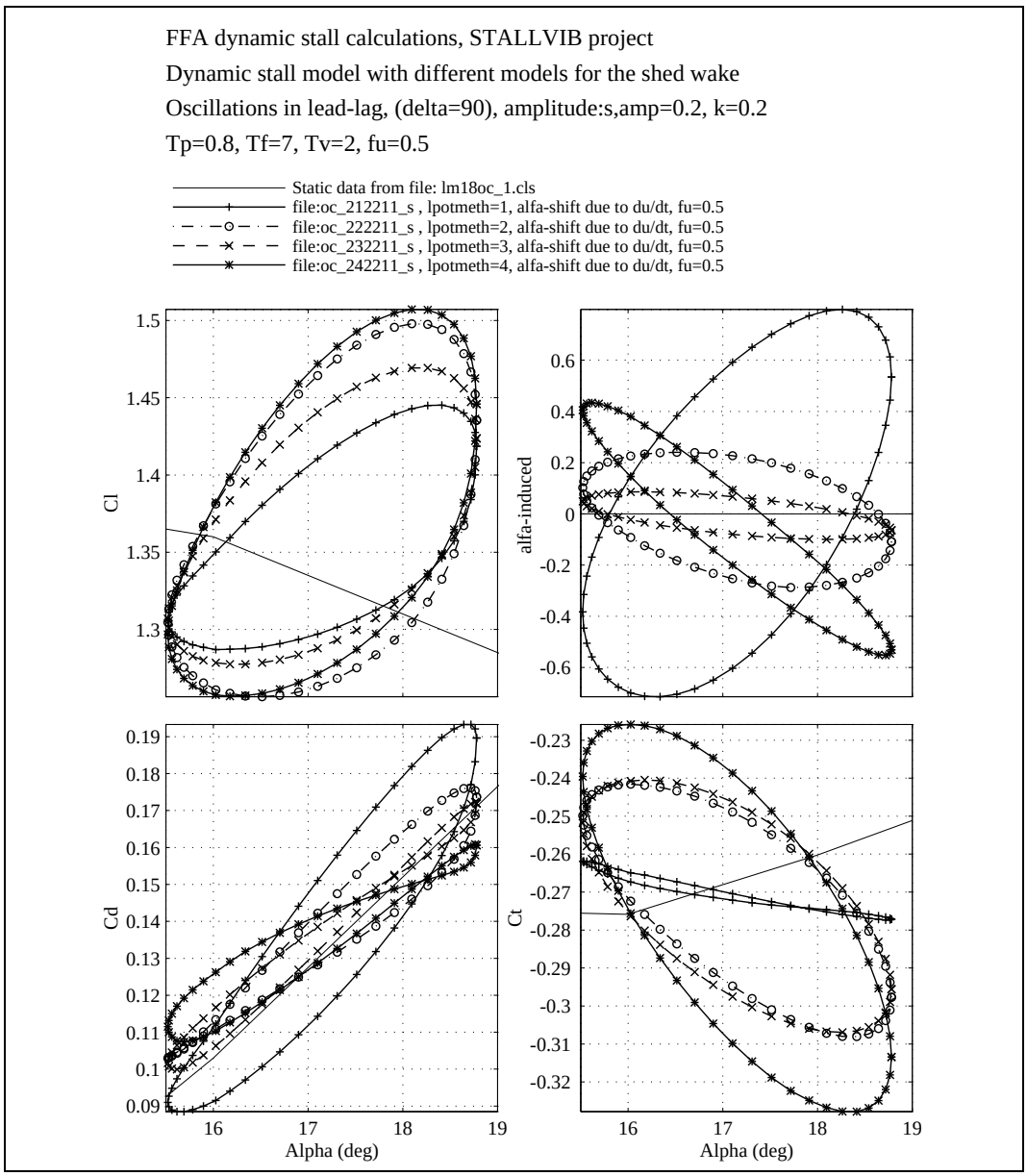


*Figure 5.4. FFA dynamic stall model results with different implementations of the shed wake effect. Oscillations are in the edgewise (lead-lag) direction, the amplitude is 0.2 m and $k = 0.2$.*

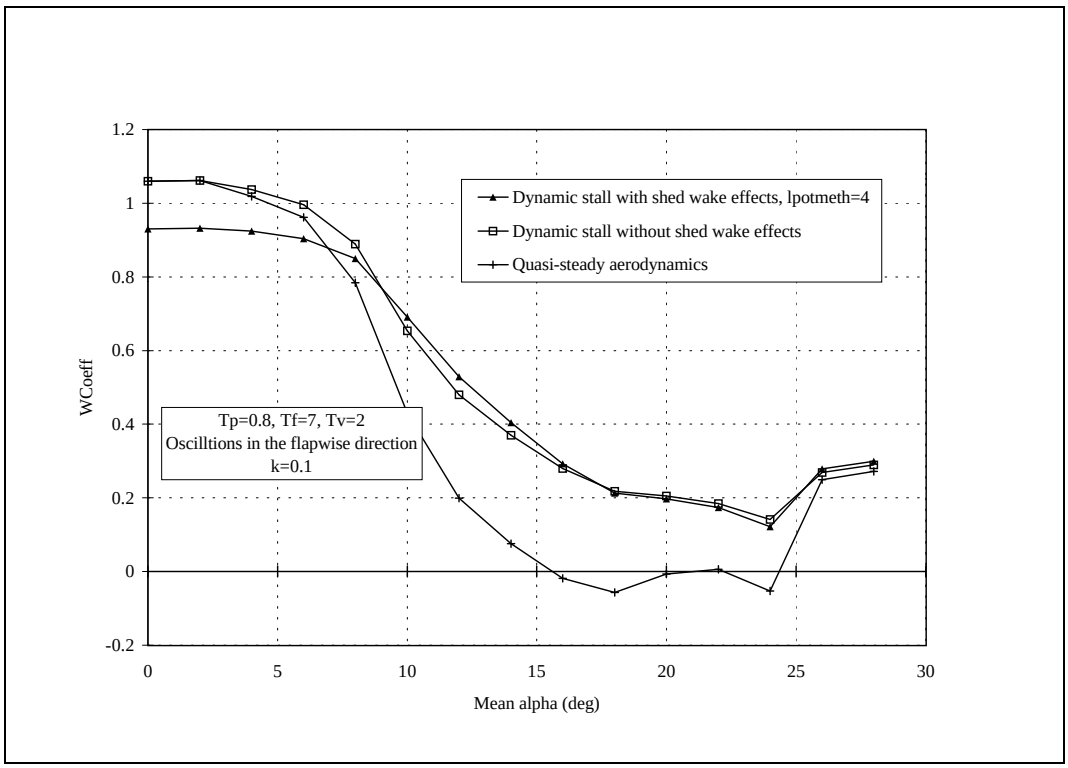


*Figure 5.5. Influence of the shed wake effects on the aerodynamic damping coefficient. Oscillations in flapwise direction.*

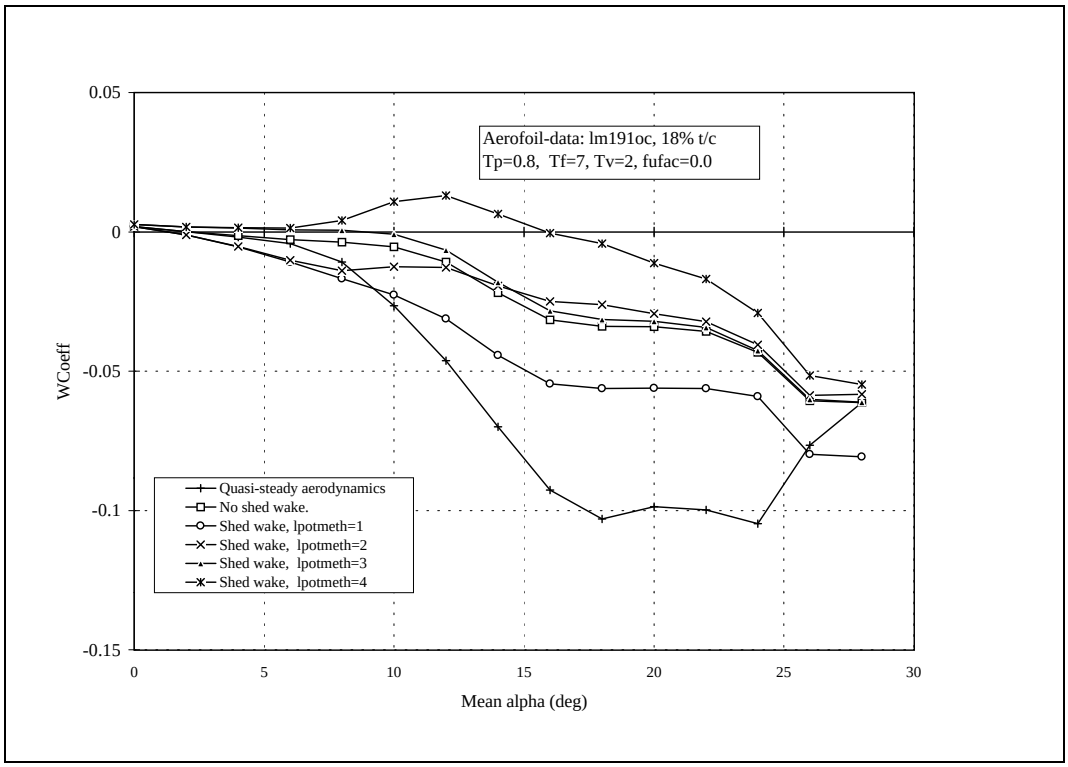


*Figure 5.6. Influence of the shed wake effects on the aerodynamic damping coefficient using different models. Oscillations in edgewise direction.*

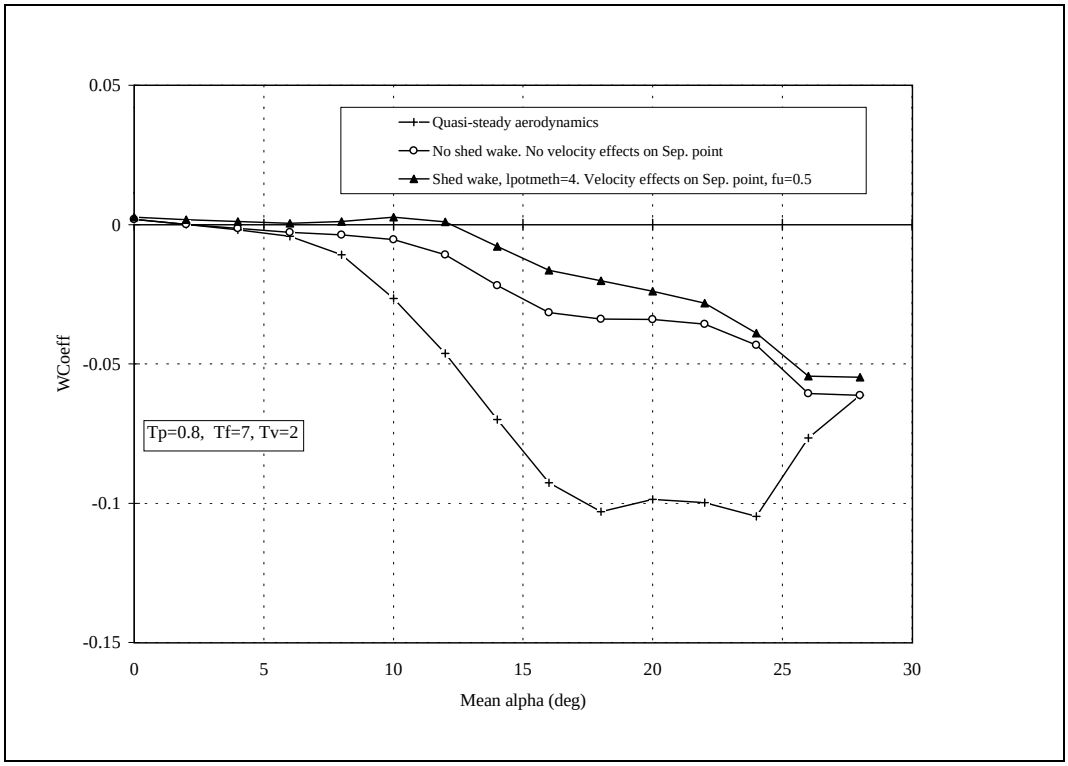


*Figure 5.7. Influence of the shed wake effects and velocity effects on the aerodynamic damping coefficient using different models. Oscillations in edgewise direction.*

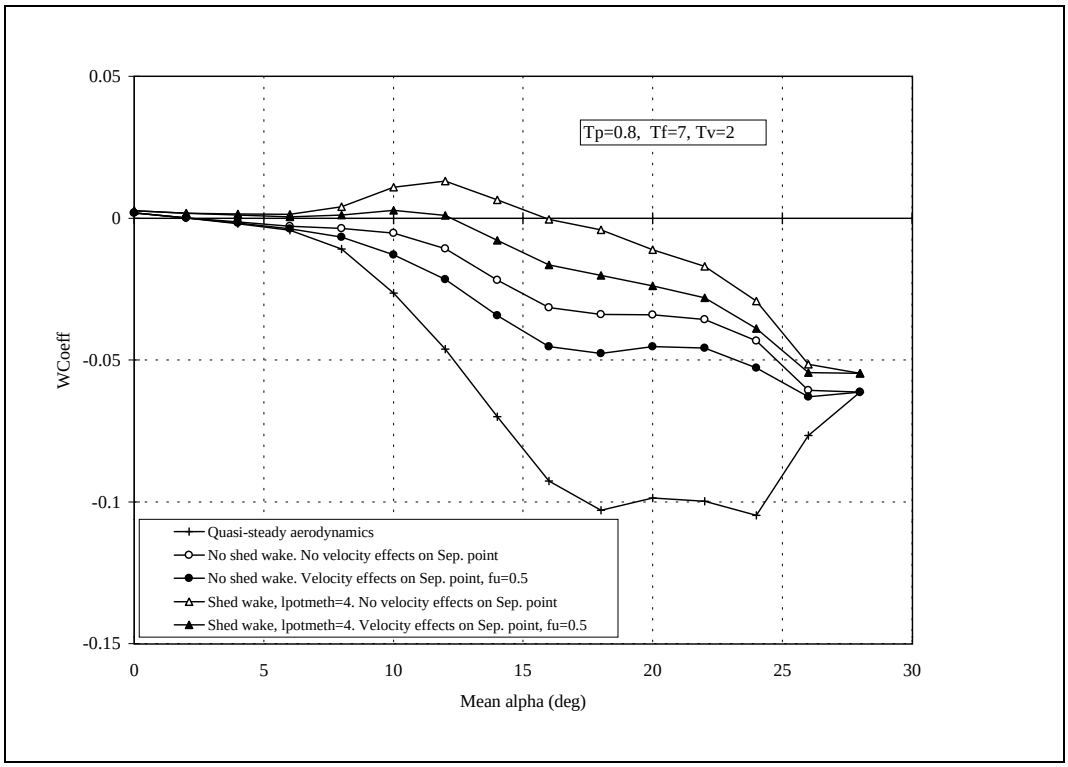


*Figure 5.8. Influence of the shed wake effects and velocity effects on the aerodynamic damping coefficient using different models. Oscillations in edgewise direction.*

## 5.3 Risø implementation of the Beddoes-Leishman model

In the previous studies of dynamic stall carried out within the JOULE II project *Dynamic Stall and 3D Effects* Risø has developed and used the *fgh* dynamic stall model [15]. The model has been an efficient analysis tool for the field rotor measurements [1] and has provided insight into the importance of the type of airfoil motion (pitching or plunging) for the aerodynamic damping. The *fgh* model has been implemented in the aeroelastic code HawC [6], but problems with numerical instability occurs during simulations, due to the fact that the model makes use of both the first and second derivative of the angle of attack. These problems may be solved in the future by using proper numerical filtering techniques as well as an optimal numerical scheme for calculation of the first and second derivative. Due to these problems it was decided to implement the Beddoes-Leishman model in the present project.

The numerical implementation has followed the description in [12] with some minor modifications. As already mentioned, the model for vortex shedding has not been implemented, and for the lift coefficient as function of the separation $f$ the Equation 5.1 due to Øye [10] is used. Basically, the derivation of the unsteady drag coefficient follows the Beddoes-Leishman approach. The unsteady chordwise force is expressed as:

$$C_{C_n} = \eta_c C_{L\alpha} \sin\left(\alpha_{E_n}(t)\right) \alpha_{E_n}(t) \sqrt{f'_n} \quad . \tag{5.27}$$

Subscript $n$ denotes time step number $n$, $\eta_c$ is an efficiency factor, $\alpha_E$ the effective angle of attack and $f'$ is the lagged separation position derived for step number $n$ as:

$$f'_n = f_n - D_{f_n} \ , \tag{5.28}$$

where

$$D_{f_n} = D_{f_{n-1}} \exp\left(\frac{\Delta s}{\tau_f}\right) + (f_n - f_{n-1}) \exp\left(\frac{\Delta s}{2\tau_f}\right) \quad , \tag{5.29}$$

$\tau_f$ is the time constant for the trailing edge separation, and $\Delta s = 2V\Delta t/c$ is the non-dimensional distance in semi-chords travelled by the airfoil during the time step $\Delta t$.

The unsteady pressure drag coefficient $C_{Dpf'}$ is derived from the relation:

$$C_{Dpf'}(t) = C_N(t) \sin(\alpha_n) - C_C(t) \cos(\alpha_n) \quad , \tag{5.30}$$

with

$$C_N(t) = C_{NI}(t) + C_{NC}(t) \quad . \tag{5.31}$$

$C_{NI}$ and $C_{NC}$ are the normal force coefficients for the impulsive and circulatory lift, respectively. In order to get the total drag, the boundary shear layer drag should be added. However, in the present case another approach has been used. The contribution from the unsteady flow to the pressure drag $\Delta C_{Dp}$ is derived as follows:

$$\Delta C_{Dp} = C_{Dpf'} - C_{Dpf} \ , \tag{5.32}$$

where $C_{Dpf}$, the quasi steady pressure drag, is derived in the same way as $C_{Dpf'}$, but with non-lagged separation $f$ and with the geometric angle of attack. Finally, $\Delta C_{Dp}$ is added to the steady $C_D$. This approach will center the unsteady $C_D$ around the steady $C_D$.

The Risø Beddoes-Leishman model has been compared with different wind tunnel data. Results from one case are illustrated in Figures 5.9 and 5.10. The measurements were performed on the 14% Risø-1 airfoil in the *Velux* wind tunnel in Jutland [19]. The reduced frequency $k$ is equal to 0.11 and the pitch amplitude is 2°.

The simulations were performed with the model parameters, $\tau_f$ =6.0 and $\tau_p$ = 1.5, where $\tau_p$ is the time constant for the inviscid pressure response.

The overall agreement between computations and measurements is good, but in general the model under-estimates the hysteresis for increasing angle of attack. However, the slope of the main axis in the loops is represented quite well.

Both the computed and the measured hysteresis loops on $C_D$ are in clockwise direction, and the general characteristics of the loops are comparable. However, the measured hysteresis loops are bigger, and the average values are different, which might be due to the fact that the measurements only contain the pressure drag.

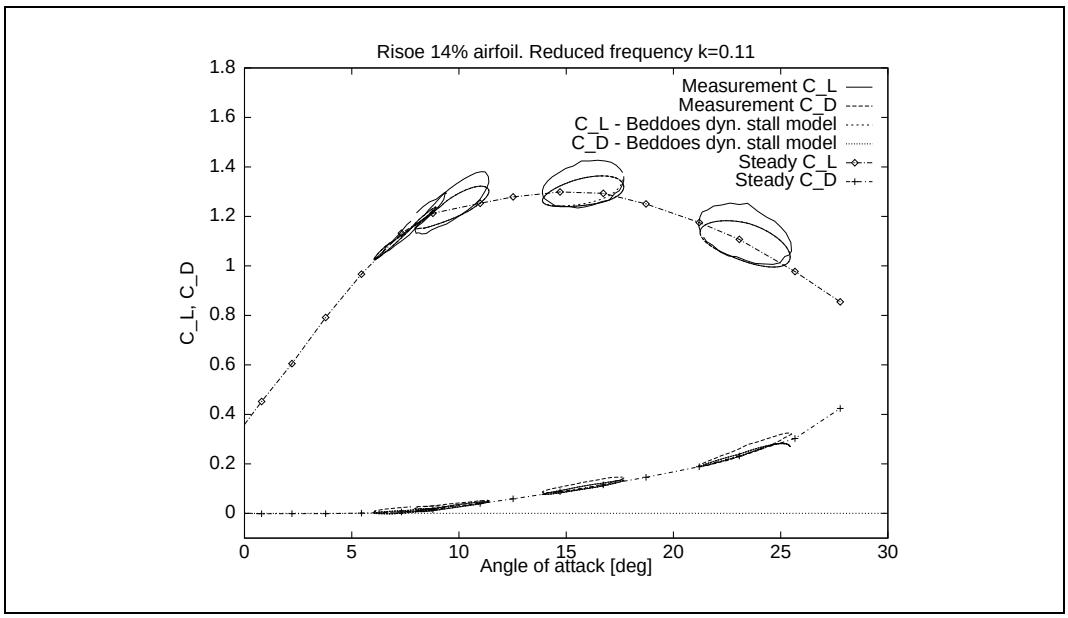


*Figure 5.9. Resulting $C_L$- and $C_D$-loops after adjustment of parameters.*

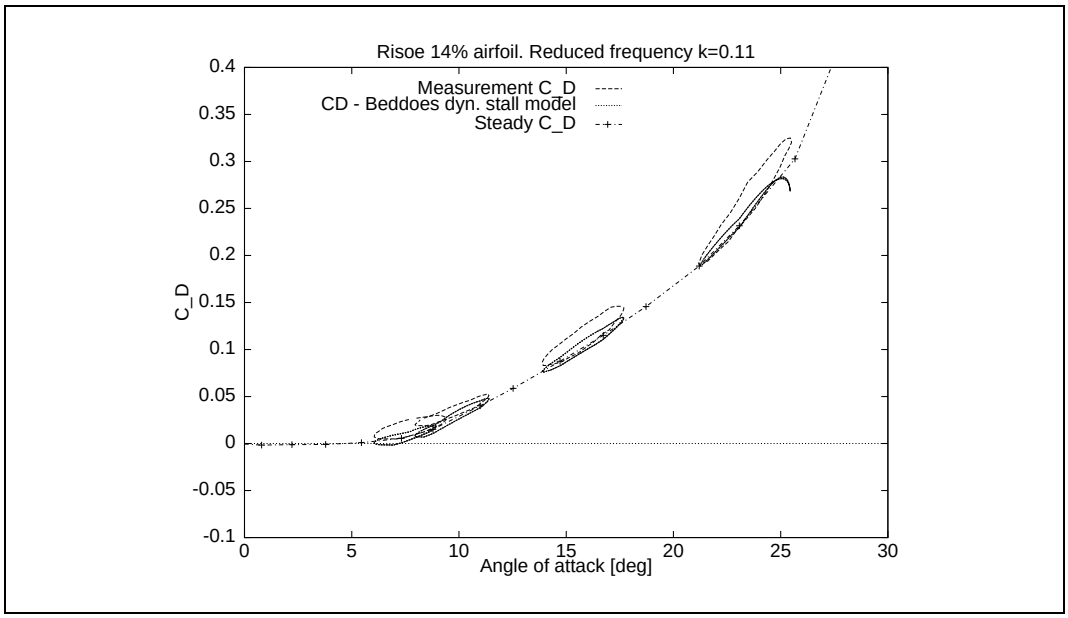


*Figure 5.10. Resulting $C_D$-loops after adjustment of parameters.*

### 5.3.1 Implementation in HawC aeroelastic code

Results from implementation of the Risø version of the Beddoes-Leishman dynamic stall model in the aeroelastic code HawC [6] is shown below. The aerodynamic damping is calculated in the fundamental edgewise and flapwise blade modes for different parameter settings in the dynamic stall model. Further, the influence of offset of vibration direction is shown with and without application of dynamic stall.

The wind turbine data is the same as applied for the calculations in Section 3.2. The data are listed in Table 3.1. The aerodynamic damping is now derived from work per cycle by use of the expressions shown in Appendix A, Section A.2. The mode shape vibration is obtained by forced excitation at the natural frequency for the actual mode.

In Figure 5.11 the aerodynamic damping is shown for the edgewise mode, both the modal damping and the damping per unit length at 20 m/s. The parameters in the dynamic stall model are the same as used in the simulation in Section 5.3, where the results shown in Figures 5.9 and 5.10 were obtained. Generally, the main parameters for the present results are shown in the figures. The results in Figure 5.11 cover four situations. One with no dynamic stall, another with dynamic stall both on $C_L$ and $C_D$, a third with dynamic stall only on $C_L$, and finally a fourth with dynamic stall only on $C_D$. The same four combinations of dynamic stall models have been used for the flapwise mode shape. The flapwise results are shown in Figure 5.13.

From the figures the following characteristics can be observed. Dynamic stall on $C_L$ increases the aerodynamic damping, both for the edgewise and the flapwise mode shapes. Dynamic stall on $C_D$ decreases the damping for the edgewise mode and increases the damping for the flapwise mode. Realizing that the effect of dynamic stall is equivalent to changing the slope of the airfoil data curves versus angle of attack, this is in accordance with the quasi-steady expressions for aerodynamic damping in Equations 2.16-2.19. The slope of the equivalent airfoil data curve is approximately the slope of the principal axis in the hysteresis ellipses. They are shown for the cases with dynamic stall on both $C_L$ and $C_D$ in Figure 5.12 for the edgewise mode and in Figure 5.14 for the flapwise mode. The loops are recorded at radius $r = 15.0$ m and at wind speed 20 m/s. The arrows in the figures show the direction of travelling the hysteresis loops next to the arrows.

The sensitivity of the calculated damping to change of the time constant for trailing edge separation in the dynamic stall model, $\tau_f$, is shown in Figure 5.15. A change of the time constant with $\Delta\tau_f = 3$ relative to the starting value, $\tau_f = 6$, which we expect to be a realistic candidate for relevant airfoils, increases the edgewise damping with less than $\frac{1}{2}\%$ and the flapwise with approximately 10% in the wind speed range with lowest damping.

As we from previous results know that a change of the vibration direction redistributes the damping between the edgewise and the flapwise modes, we have shown results for a moderate uniform offset of the vibration direction of $\Delta\theta_{RB} = -2°$ in Figure 5.16. With this offset the minimum edgewise damping is approximately $-2\%$, and the corresponding flapwise damping is approximately 0%. This seems to be an attractive compromise, which could be aimed at in a design situation.

Altogether, it can be concluded that the dynamic stall model is essential for obtaining realistic results in an aeroelastic calculation. Further, it is recommended to support the choice of parameters in a specific dynamic stall model with sensitivity studies – like the one presented above for $\tau_f$ – in order to clarify the importance of the individual parameters. The major effort should then be put into proper choice of the most important parameters thus minimizing the uncertainty in the model. The choice of parameters is very much a matter of experience, where the knowledge about the actual airfoil plays an important role.

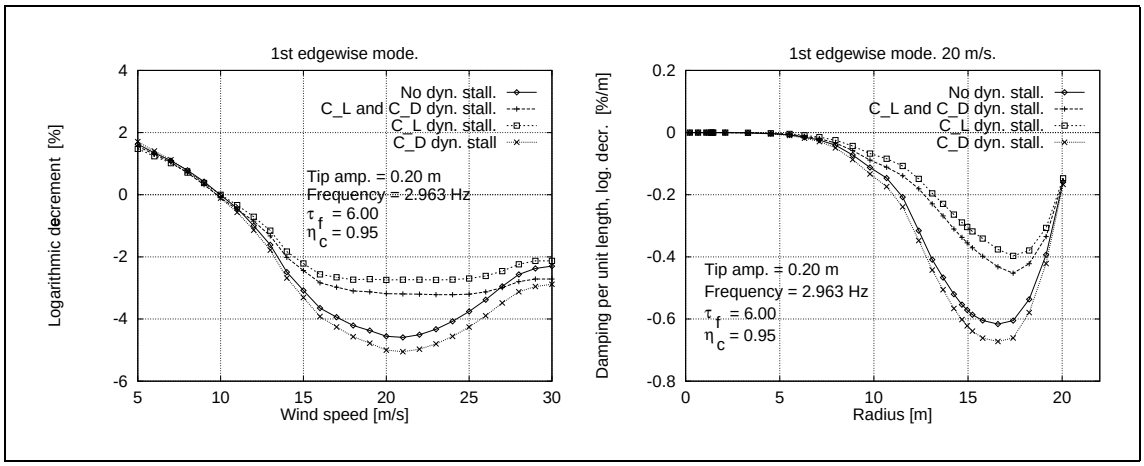


*Figure 5.11. Aerodynamic damping for the 1st edgewise mode shape. With and without dynamic stall on $C_L$ and $C_D$.*

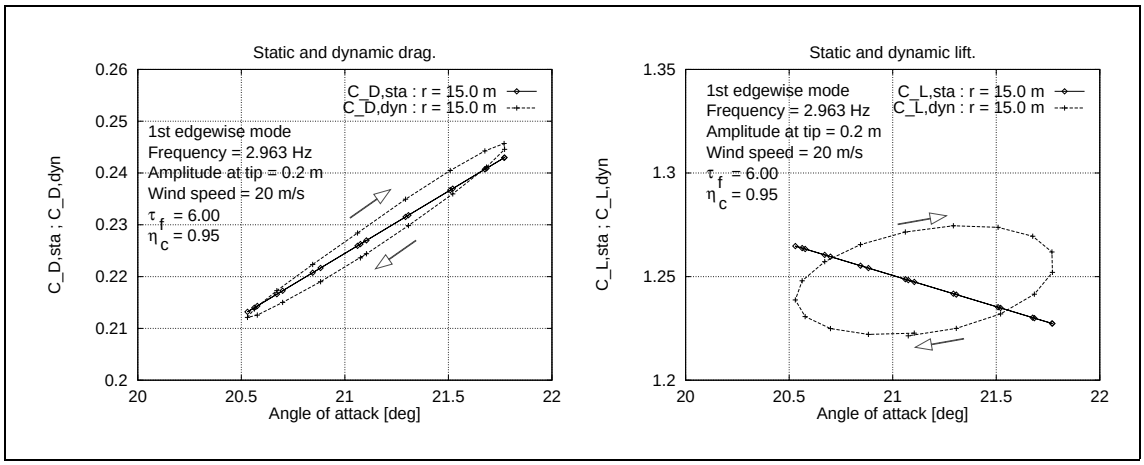


*Figure 5.12. Steady and dynamic airfoil data during harmonic excitation of 1st edgewise blade mode. At radius 15 m and wind speed 20 m/s.*

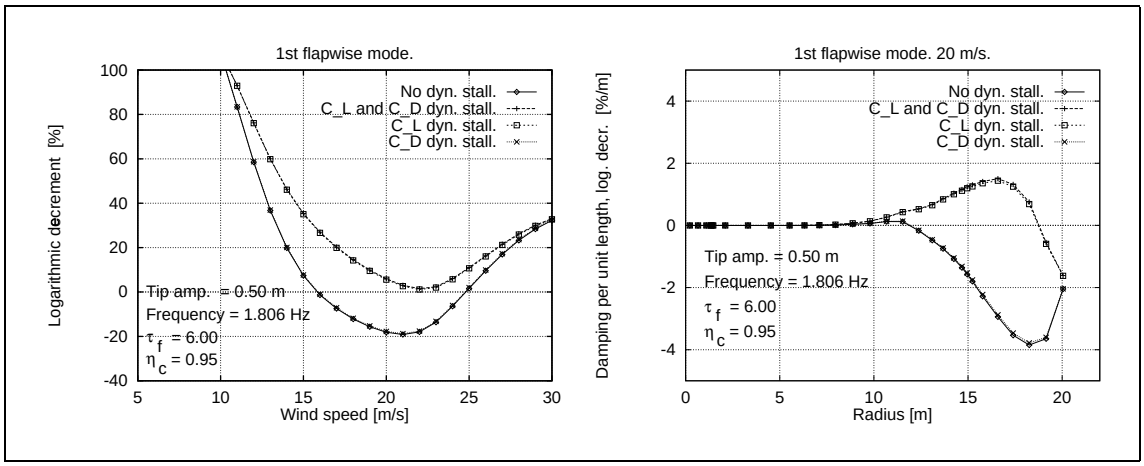


*Figure 5.13. Aerodynamic damping for the 1st flapwise mode shape. With and without dynamic stall on $C_L$ and $C_D$.*

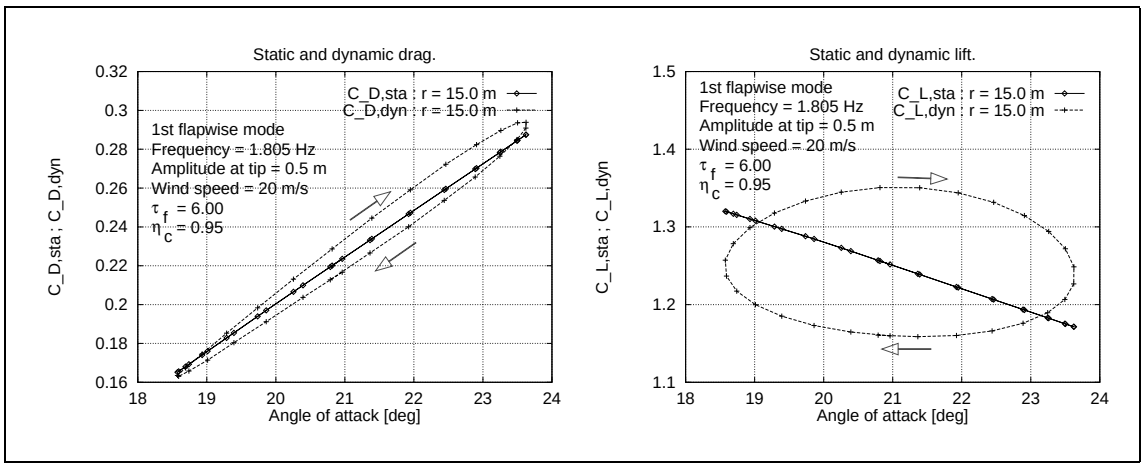


*Figure 5.14. Steady and dynamic airfoil data during harmonic excitation of $1^{st}$ flapwise blade mode. At radius 15 m and 20 m/s.*

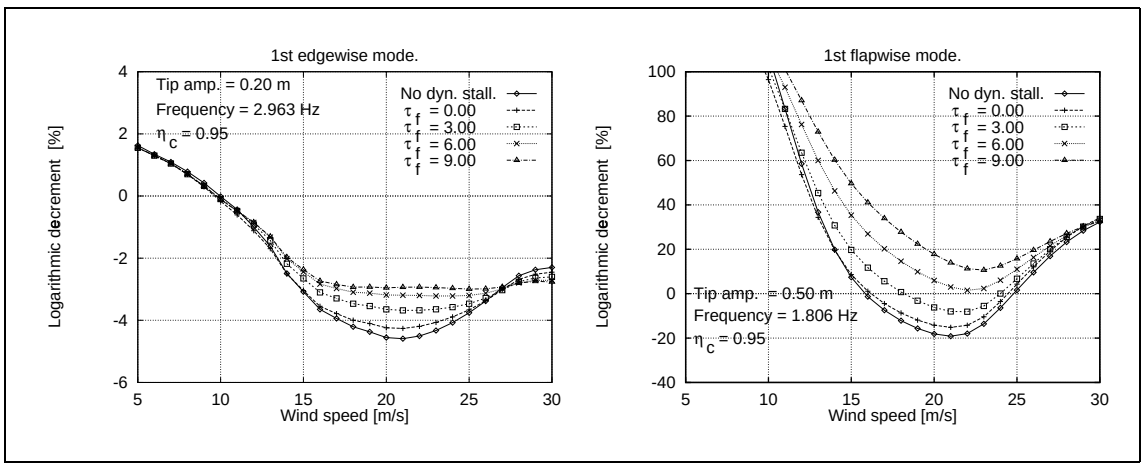


*Figure 5.15. Influence from dynamic stall parameter $\tau_f$ on edgewise and flapwise damping.*

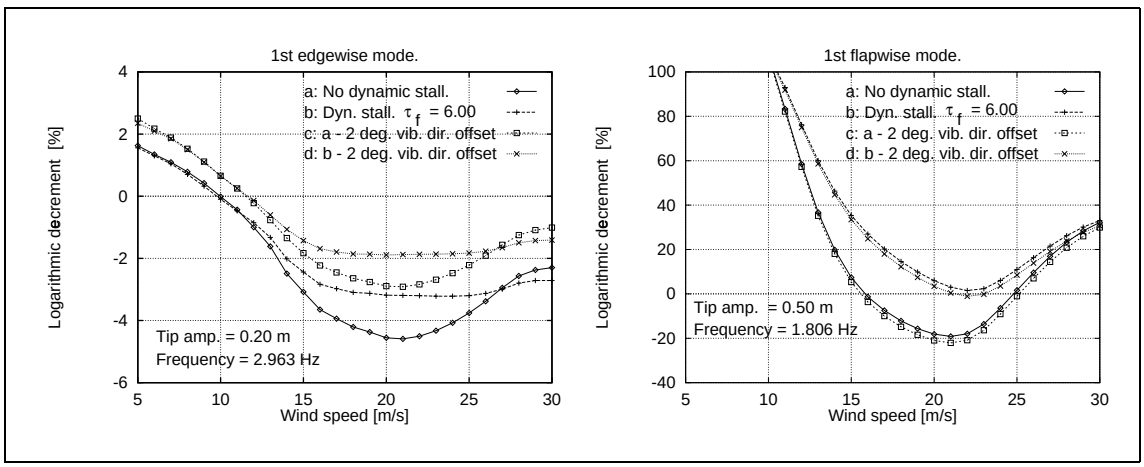


*Figure 5.16. Influence from dynamic stall and uniform vibration direction offset, $\Delta\theta_{RB} = -2°$, on aerodynamic damping.*

# 6 Coupled rotor modes and edgewise vibrations

In the previous sections we have analysed the wind turbine blades and the rotor primarily as isolated structural elements, i.e. elements without structural coupling to the rotor support – the main shaft, the nacelle frame and the tower. As this coupling turns out to play an important role for developing and sustaining stall induced vibrations, we now extend the analysis to the complete wind turbine structure.

We base the investigations on a Bonus 500 kW prototype wind turbine. It is the same turbine, which we use in later full scale aeroelastic calculations and comparisons with measurements presented in Section 7. Further, we use the same turbine in full scale parametric studies presented in Section 8.

Bonus Energy A/S has supplied detailed data, making it possible to generate an aeroelastic model of the turbine. The material supplied by Bonus Energy A/S can be found in the project documents [2], [3] and [4]. The main data for the wind turbine are presented in Section 6.1.

Aeroelastic calculations – aiming at analysing the connection between the edgewise vibrations and the rotor yaw and tilt mode shapes – were performed by project participants DTU, TAB, ECN and Risø. Below, representative calculation results obtained by Risø are presented. It should be noted here that some of the details of coupling between edgewise mode shapes and rotor tilt and yaw modes – primarily with respect to terminology – were still under discussion between project participants, when the work was concluded, but the main results of importance for the design guidelines were confirmed by the calculations carried out by the individual participants. Yet, it should be emphasized that the formulation in the present section is the responsibility of Risø.

The presented simulations are carried out by use of the Risø aeroelastic code HawC described in detail in [5] and in overview in [6]. The HawC model is believed to have a satisfactory representation of the mode shapes involved.

Initially, the natural frequencies and mode shapes are calculated at stand still. The frequencies are compared with the measured frequencies. The natural frequencies – measured and simulated – are listed in Section 6.2, where also three fundamental mode shapes involved in the edgewise vibration phenomena are shown and described.

A simplified model of the rotor, which takes only the in-plane deformation of the blades into account, is presented in Section 6.3. The model shows, how the vibration in the edgewise modes results in an inertia force in the rotor plane, which varies harmonically with the edgewise natural frequency. It turns out that the edgewise mode shapes are dynamically in balance within the rotor with respect to torsional moment about the main shaft.

The in-plane force vector describes an elliptical orbit in the co-rotating rotor coordinates. This force can interact with the rotor yaw and tilt modes, which we during operation denote the *global rotor whirl modes*. In these modes the rotor shaft changes orientation in space, and the rotor center travels along an elliptical orbit in the stationary coordinates. The in-plane inertia force can be considered as resulting from the whirl of an imaginary mass center related to the edgewise blade deformation, and we denote the corresponding deformation in the edgewise blade modes the *local blade whirl*. So, using these terms our concern is the interaction between *local blade whirl* and *global rotor whirl*. Either of the two vibration modes might exist, whether the other mode is present or not.

A thorough description of our definition of the global rotor whirl modes is presented in Appendix B, and the *local blade whirl* is described in detail in Section 6.3.

The interaction is most pronounced, if the edgewise frequency is close to the rotor whirl frequencies. When comparing these frequencies, they have to be referred to a common coordinate system, taking the $\pm\Omega$ shift into consideration, when transforming frequencies between stationary and rotating coordinates. Here, $\Omega$ (equivalent to 1P) is the angular velocity of the rotor. The involved forces or moments and the associated frequencies can be referred either to the rotating frame of reference, which is fixed in the rotor or to the stationary frame of reference, which is fixed in the tower. If we refer to the stationary frame of reference, there are four global rotor whirling frequencies of interest – two corresponding to the $1^{st}$ yaw and tilt modes and two corresponding to the $2^{nd}$ yaw and tilt modes. In the stationary frame of reference the edgewise blade bending frequency is experienced as two, the edgewise frequency $\pm\Omega$. If we, on the other hand, refer the forces or moments and associated frequencies to the rotating frame of reference, the rotor whirling frequencies are experienced as the frequencies in the stationary frame of reference $\pm\Omega$. These two possibilities of comparing frequencies are equivalent.

The application of the presented models is demonstrated through examples at the end of Section 6.3.

A method used for determination of the global whirl frequencies for an operating wind turbine is presented in Section 6.4. The method is based on excitation by an external, harmonic moment in a full aeroelastic model.

Further, a method used for investigation of the influence of changing the rotor whirl frequencies on the development of edgewise vibrations is presented in Section 6.4.

## 6.1 Wind turbine main data

The main data for the wind turbine are listed in Table 6.1. The airfoil data are shown in Figures 6.1 and 6.2, the chord distribution and the aerodynamic pitch in Figure 6.3 and the profile thickness and the blade mass distribution in Figure 6.4.

*Table 6.1. Main data for Bonus 500 kW with LM-19.0 blades.*

| Component | Parameter | Value |
|---|---|---|
| Rotor | Number of blades | 3 |
| | Rotor diameter | 41.0 m |
| | Hub height | 35.0 m |
| | Radius to blade flange | 1.50 m |
| | Radius of hub | 1.50 m |
| | Hub extension | 0.00 m |
| | Rotor overhang | 2.20 m |
| | Tilt | 4° |
| | Blade tip angle, $\theta_{tip}$ | −0.5° |
| | Blade cone angle | 0° |
| | Synchronous speed, 1P, $\Omega$ | 28.9 rpm, 0.482 Hz, 3.026 rad/sec |
| Blade | Make | LM Glasfiber A/S |
| | Type | LM-19.0 |
| | Material | Fibre glass – polyester |
| | Blade length | 19.00 m |
| | Max. chord at $r_{Blade}$ = 4.50 m | 1.650 m |
| | Tip chord at $r_{Blade}$ = 18.75 m | 0.167 m |
| | Twist | 20.0° |
| | Thickness ratio $t/c$ | 53.4% at $r_{Blade}$ = 4.50 m<br>13.0% at $r_{Blade}$ = 18.75 m |
| Drive train | Gear box ratio | 51.94 |
| Generator | Type | Asynchronous, 6 poles |
| | Nominal power | 500 kW |
| | Slip | 0.9% |
| | Rotational speed, high | 1500 rpm |
| Tower | Type | Tapered, tubular – steel |
| | Height | 32.75 m |
| | Diameter at top | 1.5 m |
| | Diameter at root | 3.1 m |

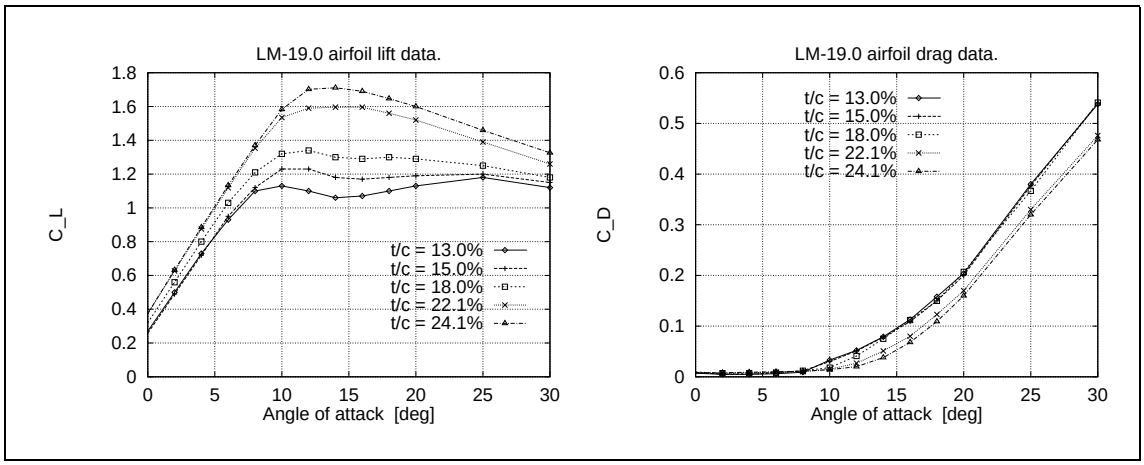


*Figure 6.1. Airfoil data for LM-19.0 blade.*

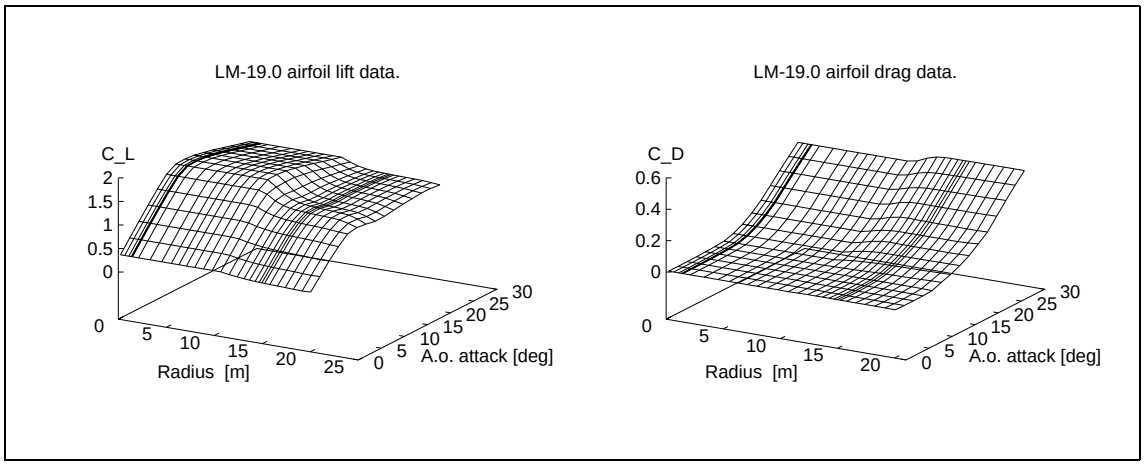


*Figure 6.2. 3-D plot of LM-19.0 airfoil data.*

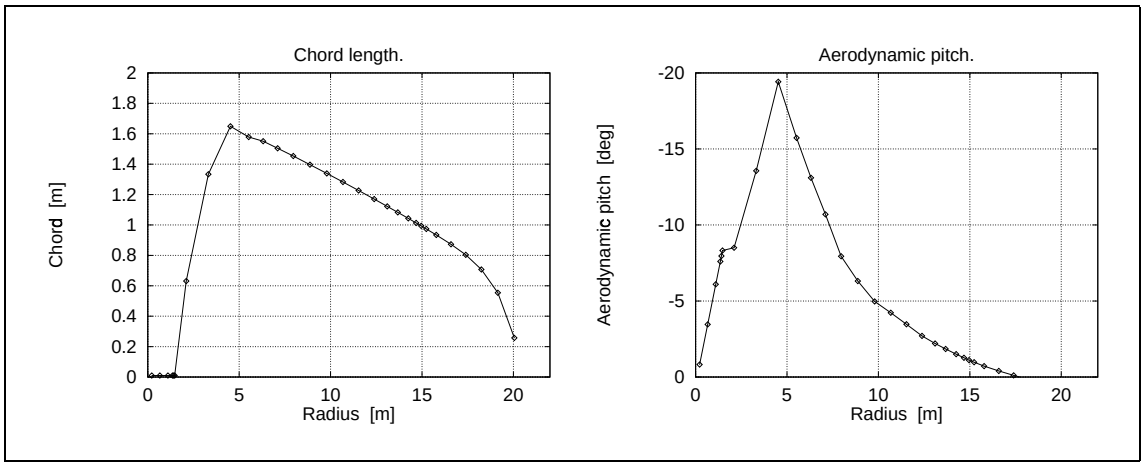


*Figure 6.3. Chord distribution and aerodynamic pitch for the LM-19.0 blade.*

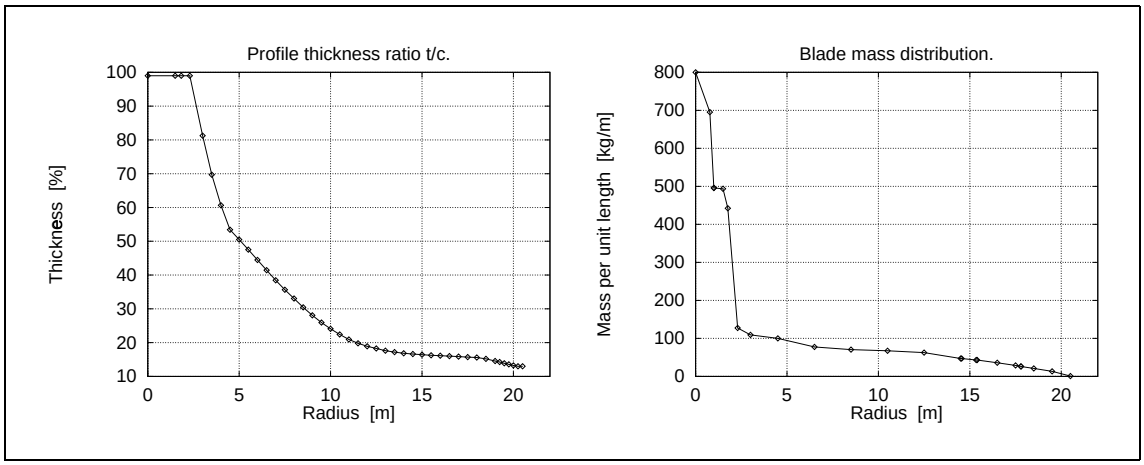


*Figure 6.4. Thickness ratio and mass distribution for the LM-19.0 blade.*

## 6.2 Mode shapes and natural frequencies

The measured and the simulated natural frequencies at stand still are listed in Table 6.2. In the table short descriptions of the actual modes are given as well. Two sets of simulated natural frequencies are involved. They cover two different wind turbine configurations, identified by the labels Rhi1 and Rhi3, respectively. The Rhi1 configuration is the basic turbine, and the Rhi3 configuration is the basic turbine, but with a stiffer main shaft. These configurations are used in aeroelastic calculations both in this section and in Section 7.

Especially two modes are of importance for edgewise vibrations, namely mode number 7 and mode number 8. Mode number 7 is shown in Figure 6.6. In this mode one blade, in the figure denoted blade 1, is practically at rest, and the other two, blade 2 and blade 3, are vibrating in counter-phase with identical amplitude. Mode number 8 is shown in Figure 6.7. Here one blade, blade 1, is vibrating in counter-phase with the other two, blade 2 and blade 3, which have half the amplitude of blade 1. Both mode 7 and 8 can be characterized as isolated rotor modes, in the sense that practically no coupling to the shaft torsional degree of freedom is present, as the inertia forces on the blades are dynamically in equilibrium with respect to moment about the main shaft axis. Still, they are both coupled to the shaft bending modes and through that to the rotor tilt and yaw modes, as the inertia forces on the blades are not dynamically balanced in the rotor plane, and a resulting harmonic inertia force will exist in the plane. This is investigated and described in further detail in Section 6.3. The two edgewise modes have almost the same frequency, close to 2.9 Hz. The frequencies are only different because the rotor yaw and tilt stiffnesses are. If the tilt and the yaw stiffnesses are identical, the natural frequencies are found as a double root in the characteristic equation, and any linear combination of mode 7 and mode 8 will then be a mode shape as well. In this case no preferred directions exist, and any edgewise rotor mode could be described as a superposition of the two basic modes shown in the figures. An appropriate linear combination of the modes shown could for instance transform the mode shapes to two new, where a different blade would be the blade at rest in mode 7. But still, only two mode shapes and natural frequencies exist. The fulfilment of the orthogonality condition for the mode shapes – Equation A.7 in Appendix A – lies behind this statement. When the turbine rotates the two frequencies are changed due to inertia forces, and they are no longer distinct. The analysis in Section 6.3 considers them as coinciding.

The rotor yaw and tilt modes – modes 4,5,9 and 10 – might be important for the stall induced vibration phenomenon as well, because a coupling to the edgewise vibration modes can take place, if any of the tilt and yaw frequencies during operation is close to the edgewise frequencies $\pm 1P$ in a stationary frame of reference. This is rendered probable by the simple model of the in-plane inertia force in Section 6.3 and the simple four degrees of freedom model of the rotor modes during operation in Appendix B and further illustrated by examples in Section 6.4 and Section 8. The $2^{nd}$ rotor yaw mode – mode number 9 – is shown in Figure 6.8. It turns out that primarily this mode is involved the coupling in the presented examples. The vertical blade is practically at rest, and the other two vibrates primarily in a flapwise direction in counter-phase with each other and in counter-phase with the nacelle. The $M_x$ and $M_z$ moment components shown in the figure are used for excitation of the rotating mode as explained later in Section 6.4.

When the turbine rotates, the frequencies of the yaw and tilt modes are changed compared to the ones listed in Table 6.2 due to the influence of the inertia forces, for instance centrifugal and gyroscopic forces. The influence of the gyroscopic forces is described in detail in Appendix B by use of a simple four degree of freedom model with infinitely stiff shaft and blades.

The rotor yaw and tilt modes will combine to what we in the present context choose to

denote *global rotor whirling modes*, where the rotor center describes an elliptical orbit in the stationary coordinates. The elliptical orbit can be decomposed in two circular orbits. One of the circular orbits is travelled by the rotor center in the same direction as the rotor rotates – we denote this component either *forward* or *progressive* whirl – and the other is travelled in the opposite direction – we denote this component either *backward* or *retrograde* whirl. Accordingly, the resulting elliptical orbit might be travelled in *forward* or *backward* direction, depending on the actual size of the circular components. The basics of decomposing an elliptical orbit in its circular components is described in further detail in Section 6.3.

In Appendix B examples of global rotor whirl frequencies obtained by the simple four degree of freedom model for typical turbines with 19 m blades are shown in Figures B.2 and B.3. In this case it turns out that the lower of the $1^{st}$ tilt/yaw whirl frequencies decreases with rotor speed, and that the whirl direction is backward. Accordingly, the higher of the $1^{st}$ tilt/yaw whirl frequencies increases with rotor speed, and the whirl direction is forward. The same characteristics are observed for $2^{nd}$ tilt/yaw whirl frequencies as well, although their dependency on the rotor speed is less pronounced.

The determination of the global rotor whirl frequencies during operation is further addressed in Section 6.4, where they are identified by use of a full aeroelastic code.

*Table 6.2. Measured and simulated natural frequencies at stand still.*

| Frequency number | Measured Frequency [Hz] | Case Rhi1: Simulated Frequency [Hz] | Case Rhi3: Simulated Frequency [Hz] | Description of mode |
|---|---|---|---|---|
| 1 | 0.750 | 0.760 | 0.760 | Tower across wind |
| 2 | 0.790 | 0.809 | 0.809 | Tower along wind |
| 3 | 0.900 | 0.908 | 0.908 | Shaft torsion |
| 4 | 1.390 | 1.380 | 1.462 | $1^{st}$ rotor yaw |
| 5 | 1.560 | 1.550 | 1.711 | $1^{st}$ rotor tilt |
| 6 | 1.850 | 1.854 | 1.854 | $1^{st}$ blade flapwise |
| 7 | 2.910 | 2.921 | 2.922 | $1^{st}$ blade edgewise, Figure 6.6 |
| 8 | 2.930 | 2.972 | 2.973 | $1^{st}$ blade edgewise, Figure 6.7 |
| 9 | 3.540 | 3.550 | 3.756 | $2^{nd}$ rotor yaw, Figure 6.8 |
| 10 | 4.220 | 4.190 | 4.965 | $2^{nd}$ rotor tilt |

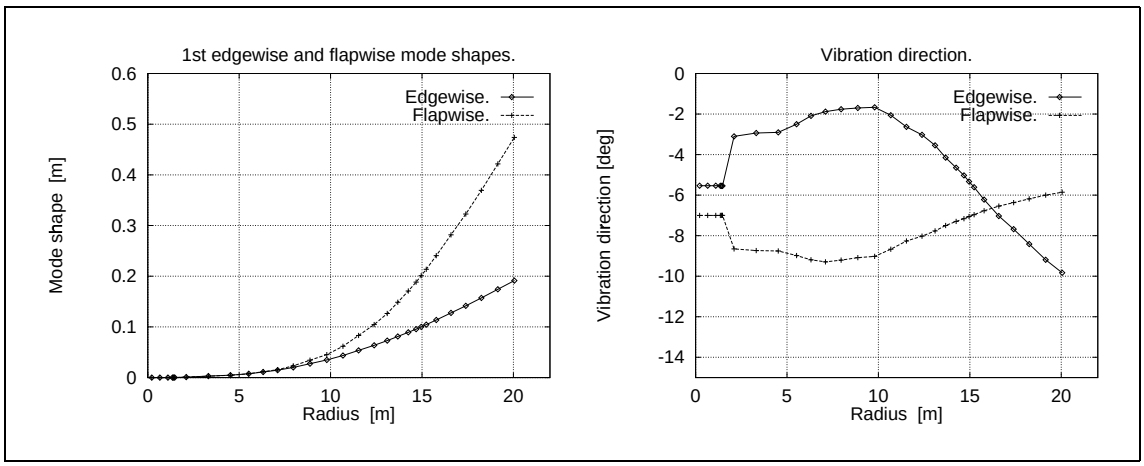


*Figure 6.5. Mode shape amplitudes and vibration direction $\theta_{RB}$ (see Figure 2.9). The flapwise direction is plotted with an offset $\Delta\theta_{RB} = -90°$.*

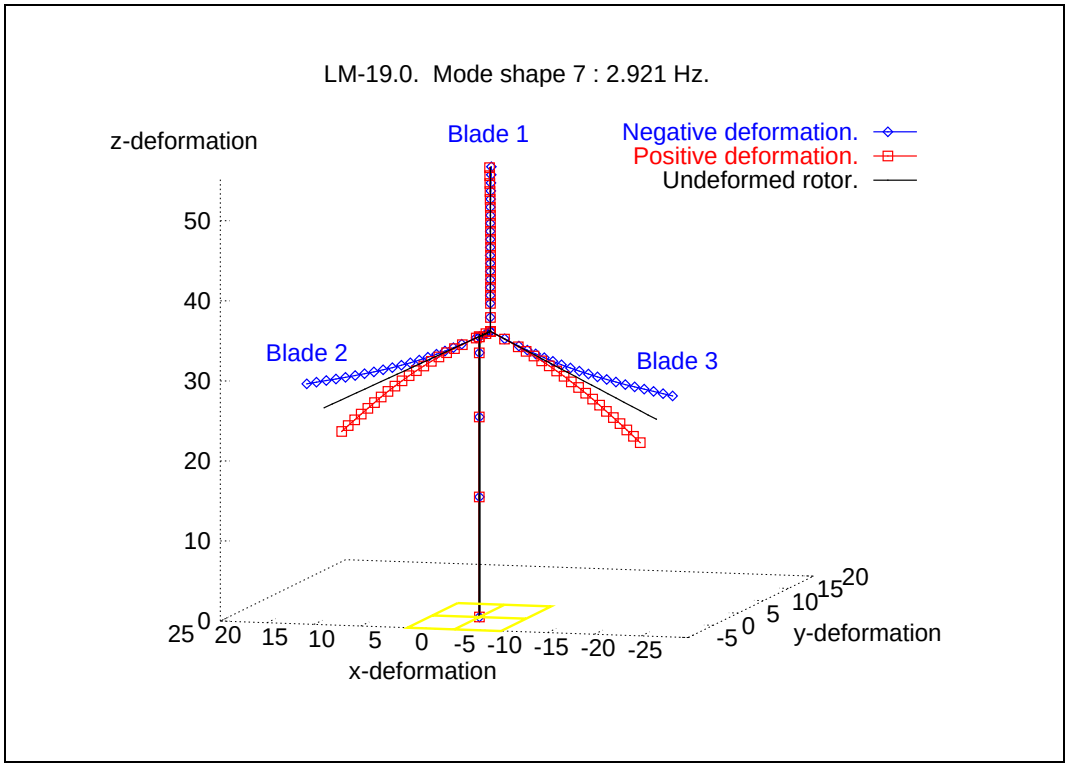


*Figure 6.6. Edgewise mode shape number 7.*

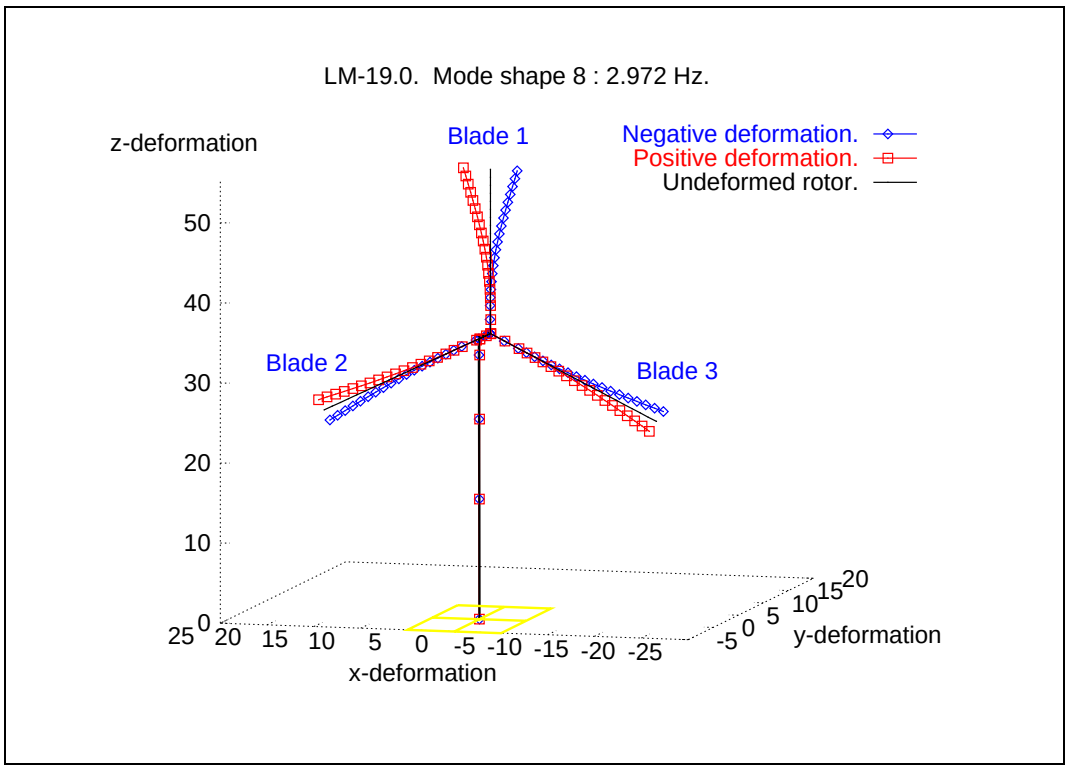


*Figure 6.7. Edgewise mode shape number 8.*

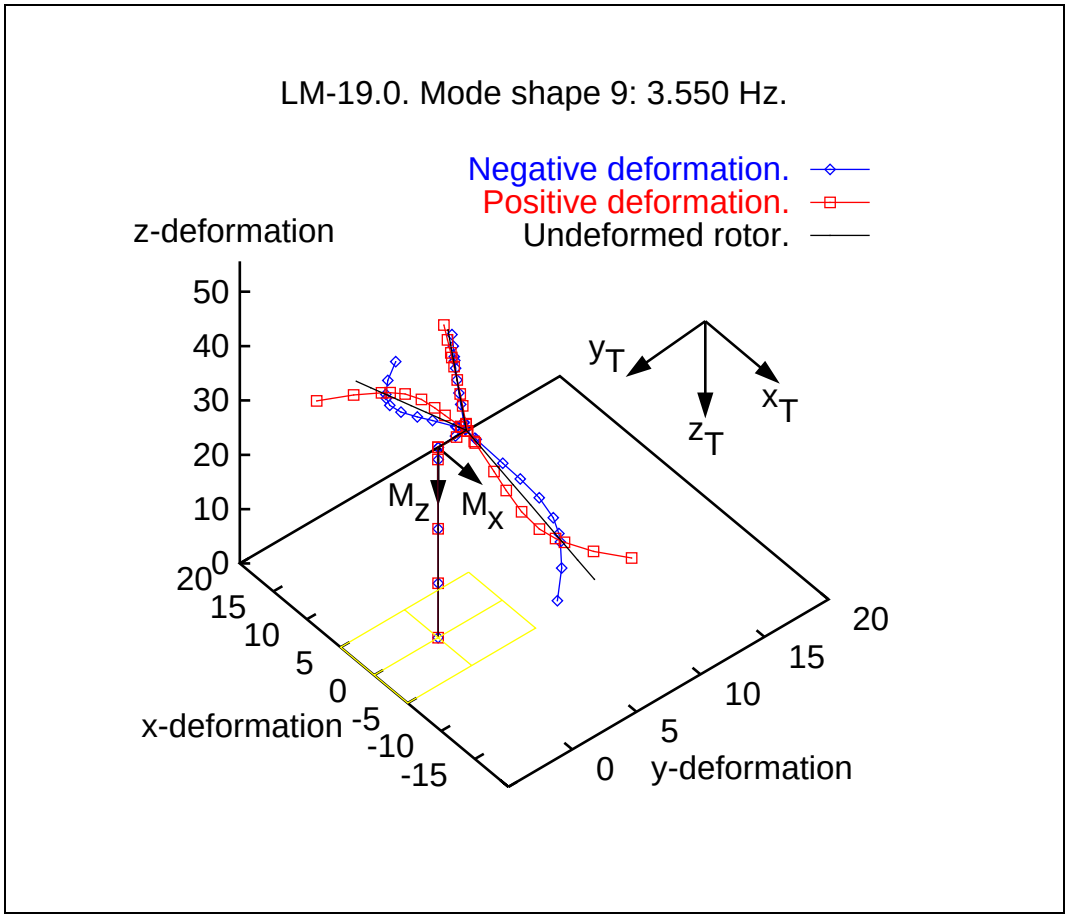


*Figure 6.8. $2^{nd}$ rotor yaw mode shape. The moment components $M_x$ and $M_z$ illustrate the excitation applied, when the rotor whirl frequencies are determined during operation in the calculations in Section 6.4. The sign of the plot axis units is opposite to the orientation of the coordinate axes of the stationary tower coordinates, $(x_T, y_T, z_T)$. See also Figure B.1 in Appendix B for a definition of coordinate systems.*

## 6.3 Interaction between edgewise blade modes and rotor whirl modes

Aeroelastic calculations and measurements show that there is a significant coupling between the *local edgewise blade modes* and the *global rotor whirl modes*. Our definition of the global rotor whirl modes is presented in Appendix B, where a simple four degree of freedom model is used to illustrate examples. For instance, a change of component stiffness that results in a change of the separation between the values of the edgewise frequencies and the global whirl frequencies can change the edgewise vibration response significantly. This is demonstrated through the aeroelastic calculations presented in Section 6.4 and Section 8. From these calculations it is observed that the closer a global rotor whirl frequency – one of the frequencies $\omega_{gw} \pm \Omega$ referenced to the rotating coordinates, see for example Figure B.3 in Appendix B – is to the edgewise blade frequency, the higher the edgewise vibration level will be. In the examples only the $2^{nd}$ whirl frequencies are close enough to the edgewise frequency to be important, but in general the $1^{st}$ whirl frequencies should be considered as well.

The coupling between global rotor whirl modes and edgewise blade modes is complex, primarily due to flexibility of the structural elements, which are involved in the rotating modes. This flexibility has to be represented in a model, if the modelling of inertia forces – including gyroscopic forces – should be adequate. This should be properly taken care of in the respective full aeroelastic codes. However, we would like to get some better understanding of the coupling phenomenon by looking at a simple model of the blade inertia forces, which are believed to be the more important ones for the coupling. This model is presented below. The applied approach assumes that the resulting inertia force from the blades is the forcing on the rotor modes, but it should be remembered that the opposite approach is equally valid, assuming that the acceleration of the hub results in inertia forces on the blades.

### 6.3.1 In-plane blade inertia force resulting from edgewise vibration

The deformations in the fundamental edgewise blade modes, i.e. modes 7 and 8 shown in Figures 6.6 and 6.7, respectively, are described by the orthogonal and normalized mode shape vectors

$$\{\varphi_7(r)\} = \left\{ \begin{array}{c} \varphi_{B1,7}(r) \\ \varphi_{B2,7}(r) \\ \varphi_{B3,7}(r) \end{array} \right\} = \varphi_B(r) \left\{ \begin{array}{c} a_{17} \\ a_{27} \\ a_{37} \end{array} \right\} = \varphi_B(r) \left\{ \begin{array}{c} 0 \\ \frac{1}{\sqrt{2}} \\ -\frac{1}{\sqrt{2}} \end{array} \right\} \tag{6.1}$$

and

$$\{\varphi_8(r)\} = \left\{ \begin{array}{c} \varphi_{B1,8}(r) \\ \varphi_{B2,8}(r) \\ \varphi_{B3,8}(r) \end{array} \right\} = \varphi_B(r) \left\{ \begin{array}{c} a_{18} \\ a_{28} \\ a_{38} \end{array} \right\} = \varphi_B(r) \left\{ \begin{array}{c} \frac{2}{\sqrt{6}} \\ -\frac{1}{\sqrt{6}} \\ -\frac{1}{\sqrt{6}} \end{array} \right\} . \tag{6.2}$$

Here, $\varphi_B(r)$ is the in-plane projection of the *edgewise* curve in Figure 6.5, $r$ is the actual blade radius, index $Bi$ refers to blade number $i$ and $a_{ij}$ is denoted the mode weighting factor for blade number $i$ in mode number $j$. The mode shapes are also illustrated in Figure 6.9.

Vibration in the mode shapes are described by harmonic normal coordinates

$$\{q(t)\} = \left\{ \begin{array}{c} q_7(t) \\ q_8(t) \end{array} \right\} = \left\{ \begin{array}{c} u_{07} \sin(\omega_e t + \gamma_7) \\ u_{08} \sin(\omega_e t + \gamma_8) \end{array} \right\} , \tag{6.3}$$

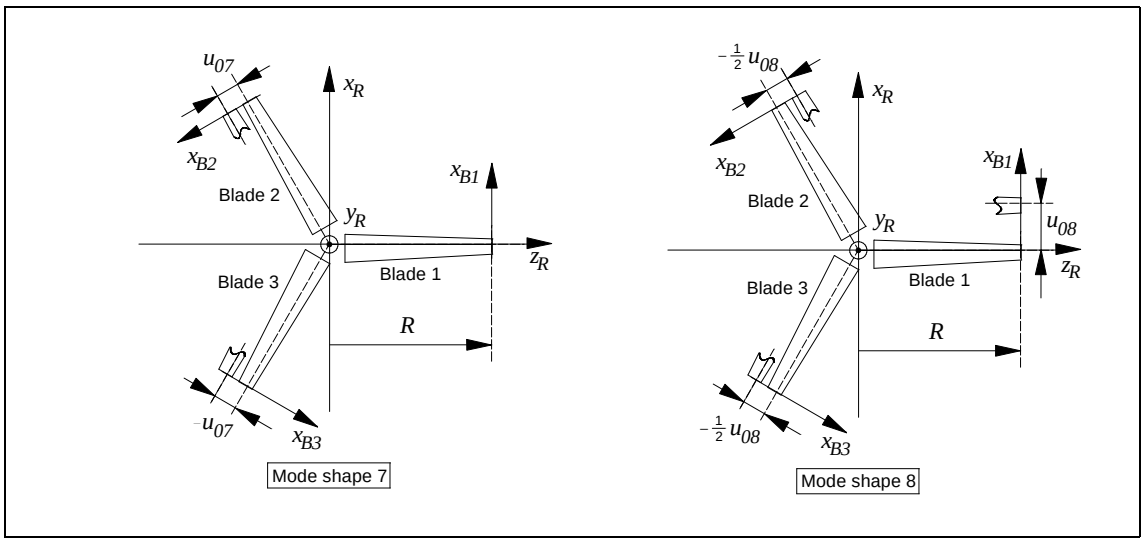


*Figure 6.9. Relative tip deformations in the two basic edgewise mode shapes.*

where $\omega_e$ is the edgewise blade frequency, $t$ is the time and the phases of the modes are denoted $\gamma_7$ and $\gamma_8$, respectively.

These normal coordinates result in the blade deformations

$$\{u(r,t)\} = \left\{ \begin{array}{c} u_{B1x} \\ u_{B2x} \\ u_{B3x} \end{array} \right\} = \left[ \begin{array}{cc} \{\varphi_7(r)\} & \{\varphi_8(r)\} \end{array} \right] \left\{ \begin{array}{c} q_7(t) \\ q_8(t) \end{array} \right\} . \tag{6.4}$$

Using the actual parameter values from Table 6.3 results in the blade tip deflections shown in Figure 6.10, covering one period of the edgewise vibration.

*Table 6.3. Parameter values for presented examples.*

| Parameter | Actual value |
|---|---|
| $u_{07}$ | $\frac{\sqrt{2}}{1}$ m = 1.4142 m |
| $u_{08}$ | $\frac{\sqrt{6}}{2}$ m = 1.2247 m |
| $\gamma_7$ | 0.0° |
| $\gamma_8$ | 45.0° |
| $\omega = \omega_e = \omega_{lw}$ | 3.0 Hz = 18.850 rad/sec |
| $\Omega$ | 0.5 Hz = 3.142 rad/sec |
| $\varphi_B(R)$ | 0.2 |
| $m_B$ | 48.2 kg |

As mentioned in Section 6.2 there is virtually no coupling between the edgewise blade modes and the shaft torsion, as the blades – according to the mode definitions in Equations 6.1 and 6.2 – are obviously dynamically in balance with respect to moment from the inertia force about an axis through the rotor center perpendicular to the rotor plane.

However, the resulting inertia force in the rotor plane is not zero, and a harmonic varying in-plane force is transferred to the main shaft. This force can interact with the global rotor whirl modes by performing work on the hub movement.

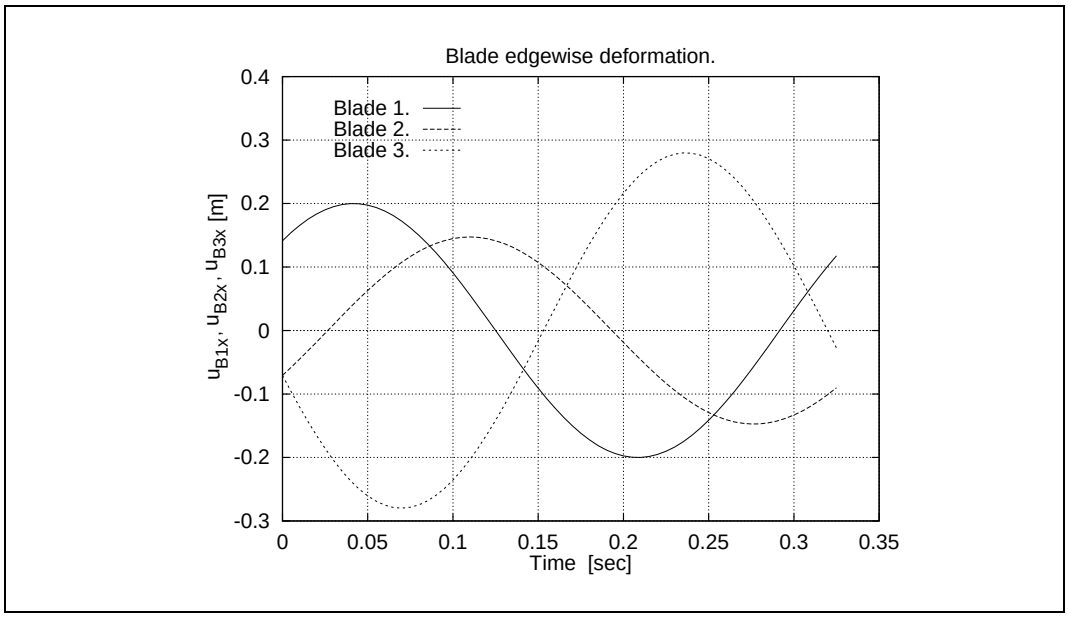


*Figure 6.10. Blade tip deformations in edgewise direction.*

To illustrate this situation, the mass distribution along the blade is considered as well. The in-plane force due to vibration in the rotor plane arising from the associated inertia force is derived with reference to Figure 6.11.

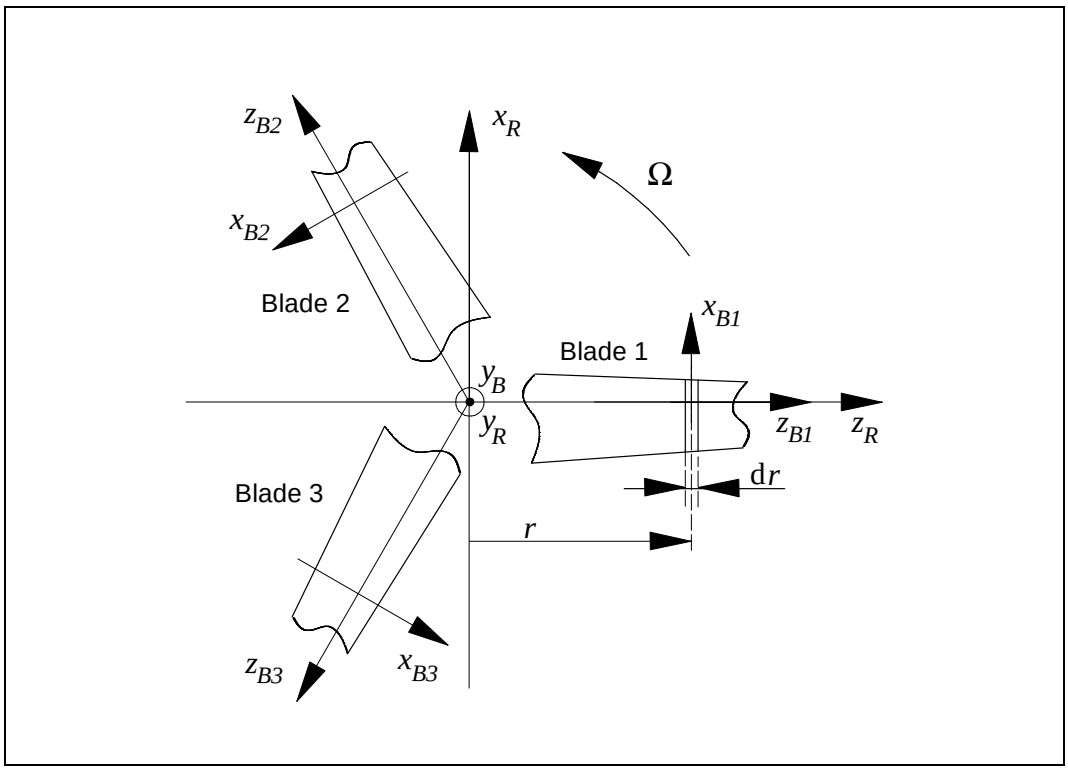


*Figure 6.11. Coordinate systems involved in calculation of the resulting in-plane inertia force due to pure edgewise vibration.*

In the local blade coordinate systems $(x_{Bi}, y_{Bi}, z_{Bi})$ only the force perpendicular to the blade axis is considered, i.e. the force in the $x_{Bi}$-direction. The mass, d$m$, of an infinitesimal

radial blade length, d$r$, is considered

$$\mathrm{d}m = m(r)\mathrm{d}r \ , \tag{6.5}$$

where $m(r)$ is the mass per unit length of the blade, shown in Figure 6.4.

According to d'Alembert's principle, the infinitesimal inertia force yields

$$\mathrm{d}F_{ij}^{xB}(r,t) = \varphi_B(r)a_{ij}\omega_e^2 u_{0j}\sin(\omega_e t + \gamma_j)m(r)\mathrm{d}r \ , \tag{6.6}$$

where the index $i$ refers to the blade number, and $j$ refers to the mode. The $a_{ij}$ terms are the factors from the right side of Equations 6.1 and 6.2.

Assuming small rotations along the blade, the transformations of the local inertia force to the rotor coordinates can be linearized corresponding to assuming that the inertia force is perpendicular to the blade axis also in the deformed state. This means that the inertia force can be integrated along the blade and transformed afterwards.

The integrated inertia force in the $x_{Bi}$-direction yields

$$\begin{aligned} F_{ij}^{xB}(t) &= \left[\int_0^R \varphi_B(r)m(r)\mathrm{d}r\right] a_{ij}\omega_e^2 u_{0j}\sin(\omega_e t + \gamma_j) \\ &= m_B a_{ij}\omega_e^2 u_{0j}\sin(\omega_e t + \gamma_j) \ , \end{aligned} \tag{6.7}$$

which defines the mass

$$m_B = \int_0^R \varphi_B(r)m(r)\mathrm{d}r \ . \tag{6.8}$$

The transformation matrices transforming vectors from local blade coordinates, $(x_{Bi}, y_{Bi}, z_{Bi})$, to the rotor coordinates, $(x_R, y_R, z_R)$, are

$$[T_{B1R}] = \begin{bmatrix} 1 & 0 & 0 \\ 0 & 1 & 0 \\ 0 & 0 & 1 \end{bmatrix} \ , \tag{6.9}$$

$$[T_{B2R}] = \begin{bmatrix} -\frac{1}{2} & 0 & \frac{\sqrt{3}}{2} \\ 0 & 1 & 0 \\ -\frac{\sqrt{3}}{2} & 0 & -\frac{1}{2} \end{bmatrix} \quad \text{and} \tag{6.10}$$

$$[T_{B3R}] = \begin{bmatrix} -\frac{1}{2} & 0 & -\frac{\sqrt{3}}{2} \\ 0 & 1 & 0 \\ \frac{\sqrt{3}}{2} & 0 & -\frac{1}{2} \end{bmatrix} \ . \tag{6.11}$$

Selecting only the terms from these transformation matrices, which influence the $x_B$-components, the transformations from all three blades are collected in one transformation equation considering only the in-plane force components

$$\begin{Bmatrix} F_{xj}^R \\ F_{zj}^R \end{Bmatrix} = \begin{bmatrix} 1 & -\frac{1}{2} & -\frac{1}{2} \\ 0 & -\frac{\sqrt{3}}{2} & \frac{\sqrt{3}}{2} \end{bmatrix} \begin{Bmatrix} a_{1j} \\ a_{2j} \\ a_{3j} \end{Bmatrix} m_B\omega_e^2 u_{0j}\sin(\omega_e t + \gamma_j) \ . \tag{6.12}$$

Inserting the $a_{ij}$-values for the two modes gives the in-plane force components. For mode 7 we get

$$\left\{ \begin{array}{c} F_{x7}^R \\ F_{z7}^R \end{array} \right\} = \left\{ \begin{array}{c} 0 \\ -\frac{\sqrt{3}}{2} \end{array} \right\} m_B \omega_e^2 u_{07} \sin(\omega_e t + \gamma_7) \, , \tag{6.13}$$

and for mode 8

$$\left\{ \begin{array}{c} F_{x8}^R \\ F_{z8}^R \end{array} \right\} = \left\{ \begin{array}{c} \frac{\sqrt{3}}{2} \\ 0 \end{array} \right\} m_B \omega_e^2 u_{08} \sin(\omega_e t + \gamma_8) \, , \tag{6.14}$$

and combined

$$\left\{ \begin{array}{c} F_x^R \\ F_z^R \end{array} \right\} = \frac{\sqrt{3}}{2} m_B \omega_e^2 \left\{ \begin{array}{c} u_{08} \sin(\omega_e t + \gamma_8) \\ -u_{07} \sin(\omega_e t + \gamma_7) \end{array} \right\} \, . \tag{6.15}$$

Basically, this force describes an elliptical orbit in the co-rotating coordinates, which might collapse to a straight line if the phase angles are numerically equal. Using the values from Table 6.3 we get the result presented in Figure 6.12. The force rotates in the same direction as the rotor – as illustrated by the arrows in the plot – with the frequency $\omega_e$, which we also denote the *local blade whirl frequency*, $\omega_{lw}$.

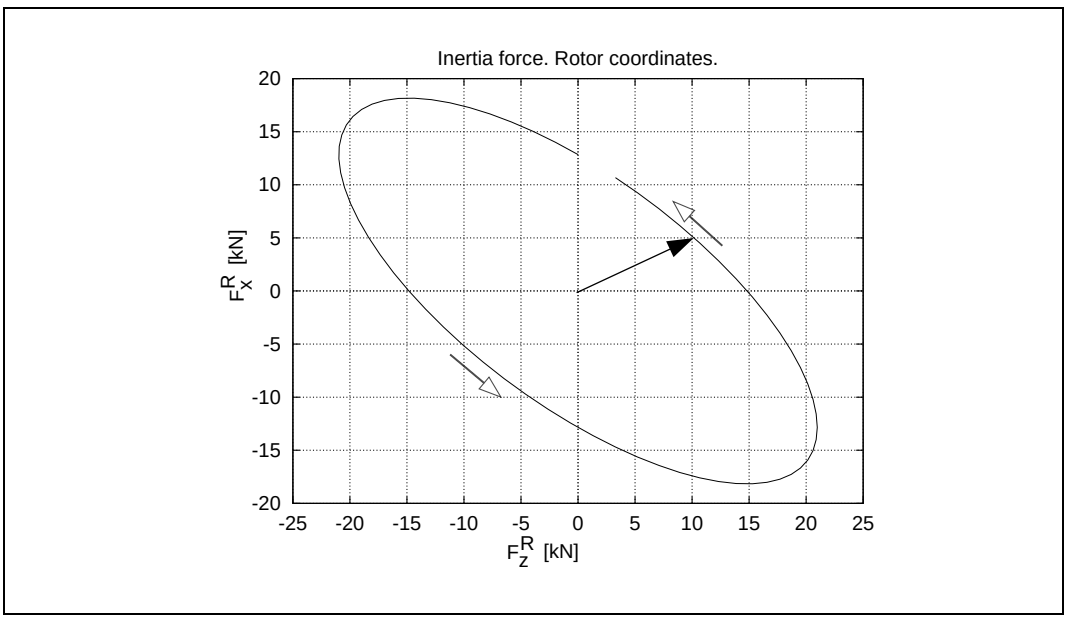


*Figure 6.12. In-plane inertia force in rotating coordinates.*

Transformation to stationary tower coordinates is obtained by the following transformation matrices, covering either 3 or 2 dimensions:

$$[T_{RT}] = \left[ \begin{array}{ccc} \cos(\Omega t) & 0 & \sin(\Omega t) \\ 0 & 1 & 0 \\ -\sin(\Omega t) & 0 & \cos(\Omega t) \end{array} \right] \, , \quad [T_{RT}^{xz}] = \left[ \begin{array}{cc} \cos(\Omega t) & \sin(\Omega t) \\ -\sin(\Omega t) & \cos(\Omega t) \end{array} \right] \, , \tag{6.16}$$

which have been derived according to the definitions in Figure 6.14. Neglecting the $y_T$-component, which is zero, i.e. using the right matrix from Equation 6.16, the transformation results in the force vector in stationary coordinates

$$\begin{Bmatrix} F_x^T \\ F_z^T \end{Bmatrix} = \frac{\sqrt{3}}{2} m_B \omega_e^2 \begin{bmatrix} \cos(\Omega t) & \sin(\Omega t) \\ -\sin(\Omega t) & \cos(\Omega t) \end{bmatrix} \begin{Bmatrix} u_{08} \sin(\omega_e t + \gamma_8) \\ -u_{07} \sin(\omega_e t + \gamma_7) \end{Bmatrix}$$

$$= \frac{\sqrt{3}}{4} m_B \omega_e^2 \begin{Bmatrix} \Big( -u_{07} \left[\cos((\omega_e - \Omega)t + \gamma_7) - \cos((\omega_e + \Omega)t + \gamma_7)\right] \\ \quad + u_{08} \left[\sin((\omega_e - \Omega)t + \gamma_8) - \sin((\omega_e + \Omega)t + \gamma_8)\right] \Big) \\ \Big( -u_{07} \left[\sin((\omega_e - \Omega)t + \gamma_7) - \sin((\omega_e + \Omega)t + \gamma_7)\right] \\ \quad - u_{08} \left[\cos((\omega_e - \Omega)t + \gamma_8) - \cos((\omega_e + \Omega)t + \gamma_8)\right] \Big) \end{Bmatrix} . \quad (6.17)$$

This result shows that the edgewise frequency is experienced as two in the stationary coordinates, namely $\omega_e \pm \Omega$. Using the parameter values from Table 6.3 gives the rotating force in stationary coordinates corresponding to Equation 6.17 as shown in Figure 6.13. The left plot in the figure shows one complete cycle of the edgewise vibration, and the right plot covers one complete rotor revolution. The arrows in the figures show the rotation direction of the force.

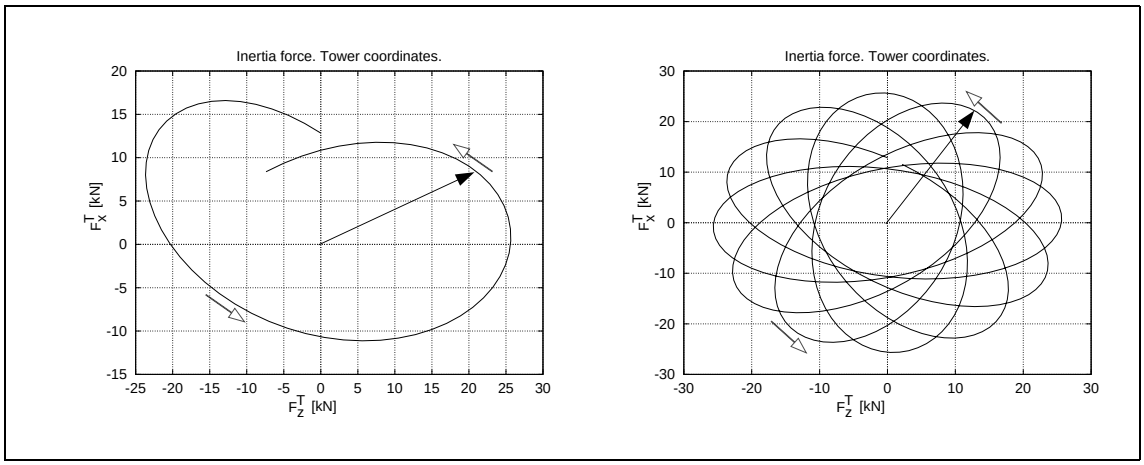


*Figure 6.13. In-plane inertia force in stationary coordinates due to deformation in edgewise mode shapes. The left plot covers one period of the edgewise vibration, and the right plot covers one complete rotor revolution. The arrows show the rotation direction of the force.*

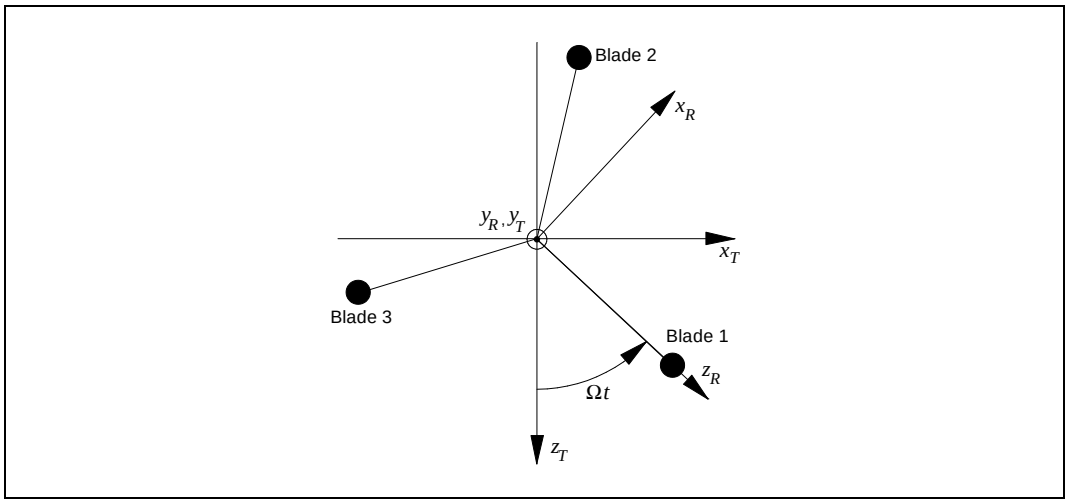


*Figure 6.14. Rotating (R) and stationary (T) coordinate systems.*

### 6.3.2 Decomposing elliptical orbits in circular orbits

The in-plane inertia force shown in Figure 6.12 describes an elliptical orbit in the $(x_R, z_R)$-plane. The force can be composed of two counter-rotating vectors with constant size. The two vectors may have either

- different size, which gives the elliptical orbit,
- same size, which degenerates the ellipse to a straight line, or
- one of the counter-rotating vectors may be zero, which gives a circular orbit.

In the present section we show the decomposition of the force vector in such two vectors, and further we derive the associated components of the blade modes. The purpose is to provide a description that in some aspects supports the understanding of the phenomena, and the decomposition may for instance be useful when analysing measurements.

The parameters and the variables generally used for description of an ellipse are shown in the left plot in Figure 6.15. In the figure the resulting in-plane force is denoted $\{F_i\}$, $a$ is the major semi-axis and $b$ is the minor semi-axis. The angle from the $z_R$-axis to the major semi-axis is $\gamma$, and the angle from the $z_R$-axis to the rotating vector is $\omega_e t + \gamma_a$. The elliptical orbit can also be considered to be composed of two circular orbits – one corresponding to a vector with forward or progressive rotation, $\{F_p\}$, and the other corresponding to a vector with backward or retrograde rotation, $\{F_r\}$, as shown in the right plot of Figure 6.15.

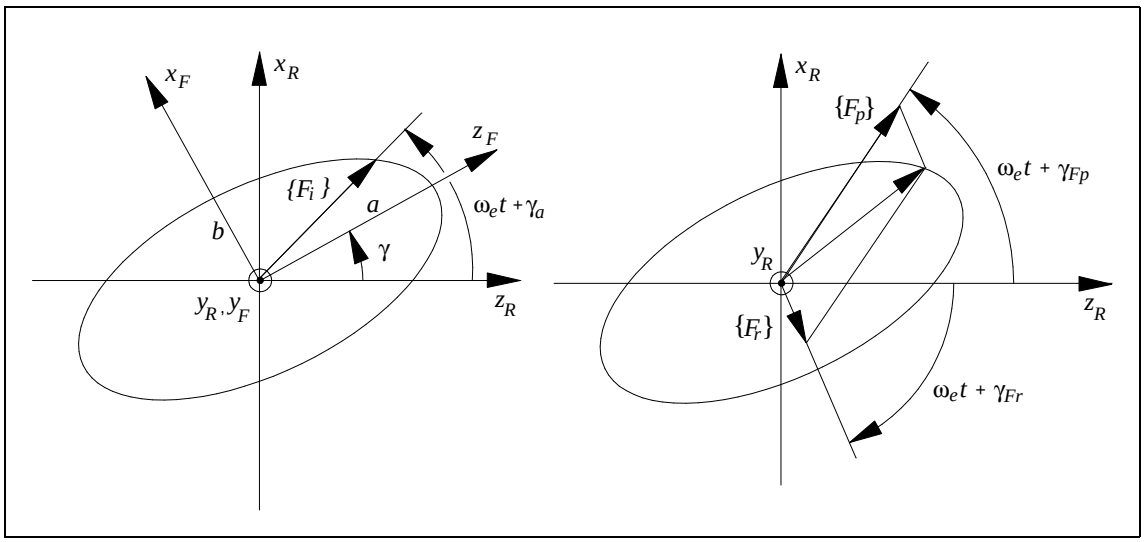


*Figure 6.15. Orbits of in-plane force in rotating coordinates.*

The following relations are valid for these descriptions of the ellipses

$$F_p = |\{F_p\}| \;\; ; \;\; F_r = |\{F_r\}| \;\; ; \text{ (vector size)} \tag{6.18}$$

$$a = F_p + F_r \;\; ; \;\; b = F_p - F_r \;\; ; \tag{6.19}$$

$$\gamma = \frac{1}{2}\left(\gamma_{Fp} - \gamma_{Fr}\right) \;\; ; \tag{6.20}$$

$$\gamma a = \gamma_{Fp} \; . \tag{6.21}$$

The resulting vector rotation is progressive, when $F_p > F_r$ and retrograde, when $F_r > F_p$.

The projection of the two circular orbits on the $(x_R, z_R)$-axis gives the in-plane force vector expressed by the progressive and retrograde components

$$\left\{ \begin{array}{c} F_x^R \\ F_z^R \end{array} \right\} = \left[ \begin{array}{cc} \sin(\omega_e t + \gamma_{Fp}) & -\sin(\omega_e t + \gamma_{Fr}) \\ \cos(\omega_e t + \gamma_{Fp}) & \cos(\omega_e t + \gamma_{Fr}) \end{array} \right] \left\{ \begin{array}{c} F_p \\ F_r \end{array} \right\} . \tag{6.22}$$

By combination of Equations 6.15 and 6.22, the progressive and the retrograde components can be expressed by the amplitudes and the phases of the basic edgewise mode shapes. Equating coefficients to $\sin(\omega_e t)$ and $\cos(\omega_e t)$ terms yields the following four equations with four unknowns, $F_p$, $F_r$, $\gamma_{Fp}$ and $\gamma_{Fr}$:

$$\left. \begin{array}{rcl} F_p \cos(\gamma_{Fp}) + F_r \cos(\gamma_{Fr}) & = & -\frac{\sqrt{3}}{2} m_B \omega_e^2 u_{07} \sin(\gamma_7) \\ F_p \sin(\gamma_{Fp}) + F_r \sin(\gamma_{Fr}) & = & \frac{\sqrt{3}}{2} m_B \omega_e^2 u_{07} \cos(\gamma_7) \\ F_p \sin(\gamma_{Fp}) - F_r \sin(\gamma_{Fr}) & = & \frac{\sqrt{3}}{2} m_B \omega_e^2 u_{08} \sin(\gamma_8) \\ F_p \cos(\gamma_{Fp}) - F_r \cos(\gamma_{Fr}) & = & \frac{\sqrt{3}}{2} m_B \omega_e^2 u_{08} \cos(\gamma_8) \end{array} \right\} , \tag{6.23}$$

giving the solutions

$$F_p = \frac{\sqrt{3}}{4} m_B \omega_e^2 \sqrt{u_{07}^2 + u_{08}^2 + 2u_{07}u_{08} \sin(\gamma_8 - \gamma_7)} , \tag{6.24}$$

$$F_r = \frac{\sqrt{3}}{4} m_B \omega_e^2 \sqrt{u_{07}^2 + u_{08}^2 - 2u_{07}u_{08} \sin(\gamma_8 - \gamma_7)} , \tag{6.25}$$

$$\gamma_{Fp} = \arctan \left[ \frac{u_{07} \cos\gamma_7 + u_{08} \sin\gamma_8}{-u_{07} \sin\gamma_7 + u_{08} \cos\gamma_8} \right] \text{ and} \tag{6.26}$$

$$\gamma_{Fr} = \arctan \left[ \frac{u_{07} \cos\gamma_7 - u_{08} \sin\gamma_8}{-u_{07} \sin\gamma_7 - u_{08} \cos\gamma_8} \right] . \tag{6.27}$$

Transforming the in-plane force from Equation 6.22 to stationary $T$-coordinates yields

$$\begin{aligned} \left\{ \begin{array}{c} F_x^T \\ F_z^T \end{array} \right\} &= [T_{RT}^{xz}] \left\{ \begin{array}{c} F_x^R \\ F_z^R \end{array} \right\} \\ &= \left[ \begin{array}{cc} \sin\left[(\omega_e + \Omega)t + \gamma_{Fp}\right] & -\sin\left[(\omega_e - \Omega)t + \gamma_{Fr}\right] \\ \cos\left[(\omega_e + \Omega)t + \gamma_{Fp}\right] & \cos\left[(\omega_e - \Omega)t + \gamma_{Fr}\right] \end{array} \right] \left\{ \begin{array}{c} F_p \\ F_r \end{array} \right\} . \end{aligned} \tag{6.28}$$

By use of the example data from Table 6.3 the progressive and the retrograde circular components are calculated and shown in Figure 6.16.

Accordingly, the blade deformations corresponding to progressive and retrograde in-plane forces, respectively, can be found by resolving each of them with respect to the basic mode shapes, $\{\varphi_7\}$ and $\{\varphi_8\}$.

Pure progressive in-plane force is obtained with the same amplitude of the two modes, $u_p$, and a phase difference of $\gamma_{8p} - \gamma_{7p} = \frac{\pi}{2}$, which can be observed from Equations 6.24 and 6.25. Correspondingly, pure retrograde in-plane force is obtained by the common mode amplitude $u_r$, and phase difference $\gamma_{8r} - \gamma_{7r} = -\frac{\pi}{2}$.

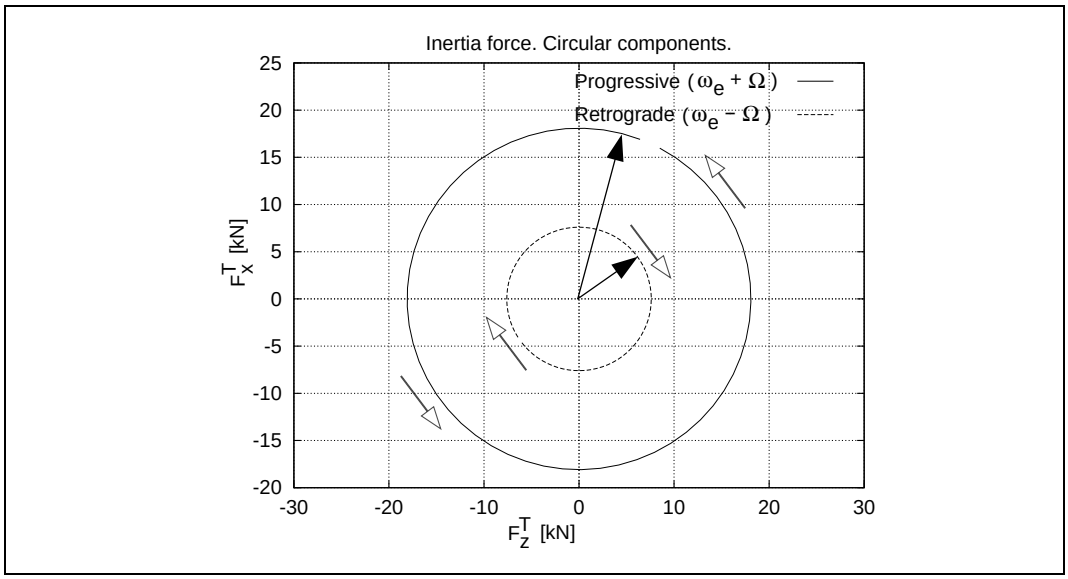


*Figure 6.16. Forward (progressive) and backward (retrograde) whirl components of the in-plane inertia force. The plot axes refer to the T-coordinates. The appearance of the components in R-coordinates is the same, but then the frequency of both components is $\omega_e = \omega_{lw}$, the local blade whirl frequency.*

The constant phase difference implies that only one phase is needed for description of each rotation direction. We choose $\gamma_{7p} = \gamma_{up}$ and $\gamma_{7r} = \gamma_{ur}$ in the derivations below.

The corresponding harmonic normal coordinates are found from Equation 6.3. The progressive coordinates are expressed by

$$\{q_p(t)\} = \left\{ \begin{array}{c} q_{7p}(t) \\ q_{8p}(t) \end{array} \right\} = \left\{ \begin{array}{c} u_p \sin(\omega_e t + \gamma_{up}) \\ u_p \cos(\omega_e t + \gamma_{up}) \end{array} \right\} , \tag{6.29}$$

and the retrograde coordinates by

$$\{q_r(t)\} = \left\{ \begin{array}{c} q_{7r}(t) \\ q_{8r}(t) \end{array} \right\} = \left\{ \begin{array}{c} u_r \sin(\omega t + \gamma_{ur}) \\ u_r \cos(\omega t + \gamma_{ur}) \end{array} \right\} . \tag{6.30}$$

The total blade deformations are obtained by combining these equations, which yields

$$\begin{aligned} \{u(r,t)\} &= \left[ \begin{array}{cc} \varphi_7(r) & \varphi_8(r) \end{array} \right] \Big( \{q_p(t)\} + \{q_r(t)\} \Big) \\ &= \left[ \begin{array}{cc} \varphi_7(r) & \varphi_8(r) \end{array} \right] \left\{ \begin{array}{c} u_p \sin(\omega_e t + \gamma_{up}) + u_r \sin(\omega_e t + \gamma_{ur}) \\ u_p \cos(\omega_e t + \gamma_{up}) - u_r \cos(\omega_e t + \gamma_{ur}) \end{array} \right\} . \end{aligned} \tag{6.31}$$

Equating the coefficients to the $\sin(\omega_e t)$ and the $\cos(\omega_e t)$ terms from Equations 6.3, 6.4 and 6.31 yields the following four equations with four unknowns, $u_p$, $u_r$, $\gamma_{up}$ and $\gamma_{ur}$, equivalent to Equations 6.23:

$$\left. \begin{array}{rcl} u_p \sin(\gamma_{up}) + u_r \sin(\gamma_{ur}) &=& u_{07} \sin(\gamma_7) \\ u_p \cos(\gamma_{up}) + u_r \cos(\gamma_{ur}) &=& u_{07} \cos(\gamma_7) \\ u_p \cos(\gamma_{up}) - u_r \cos(\gamma_{ur}) &=& u_{08} \sin(\gamma_8) \\ u_p \sin(\gamma_{up}) - u_r \sin(\gamma_{ur}) &=& -u_{08} \cos(\gamma_8) \end{array} \right\} , \tag{6.32}$$

giving the solutions

$$u_p = \frac{1}{2}\sqrt{u_{07}^2 + u_{08}^2 + 2u_{07}u_{08}\sin(\gamma_8 - \gamma_7)}\,, \tag{6.33}$$

$$u_r = \frac{1}{2}\sqrt{u_{07}^2 + u_{08}^2 - 2u_{07}u_{08}\sin(\gamma_8 - \gamma_7)}\,, \tag{6.34}$$

$$\gamma_{up} = \arctan\left[\frac{u_{07}\sin\gamma_7 - u_{08}\cos\gamma_8}{u_{07}\cos\gamma_7 + u_{08}\sin\gamma_8}\right] \text{ and} \tag{6.35}$$

$$\gamma_{ur} = \arctan\left[\frac{u_{07}\sin\gamma_7 + u_{08}\cos\gamma_8}{u_{07}\cos\gamma_7 - u_{08}\sin\gamma_8}\right]. \tag{6.36}$$

It is observed that the rotating force components from Equations 6.24 and 6.25 can be expressed by the progressive and the retrograde mode amplitudes

$$F_p = \frac{\sqrt{3}}{2}m_B\omega_e^2 u_p \text{ and} \tag{6.37}$$

$$F_r = \frac{\sqrt{3}}{2}m_B\omega_e^2 u_r\,. \tag{6.38}$$

Considering the deformations corresponding to progressive and retrograde resolutions separately shows that the blades are vibrating with the same amplitudes, but with different phases.

From Equation 6.31 the following is obtained by rewriting the trigonometric functions and inserting the mode shape components from Equations 6.1 and 6.2

$$\{u_p\} = u_p\varphi_B(r)\sqrt{\frac{3}{2}}\begin{Bmatrix} \cos(\omega_e t + \gamma_{up}) \\ \cos(\omega_e t + \gamma_{up} + \frac{4\pi}{3}) \\ \cos(\omega_e t + \gamma_{up} + \frac{2\pi}{3}) \end{Bmatrix} \text{ and} \tag{6.39}$$

$$\{u_r\} = u_r\varphi_B(r)(-\sqrt{\frac{3}{2}})\begin{Bmatrix} \cos(\omega_e t + \gamma_{ur}) \\ \cos(\omega_e t + \gamma_{ur} + \frac{2\pi}{3}) \\ \cos(\omega_e t + \gamma_{ur} + \frac{4\pi}{3}) \end{Bmatrix}. \tag{6.40}$$

We denote these blade deformations *local blade whirl*, and refer them to the rotation direction as *forward* and *backward* (or alternatively *progressive* and *retrograde*), respectively.

By use of the example data from Table 6.3 the progressive and the retrograde deformation components are calculated and shown in Figure 6.17.

### 6.3.3 Decomposing the blade response for an operating turbine

In the previous example we assumed that the normal coordinates were known. If we, on the other hand, know the edgewise blade response for all three blades – either as deformations or as moments – we are able to determine the normal coordinates corresponding to this response approximately, and subsequently to apply the decomposition presented above. The principle is outlined below, and an example for a turbine operating in free wind is presented.

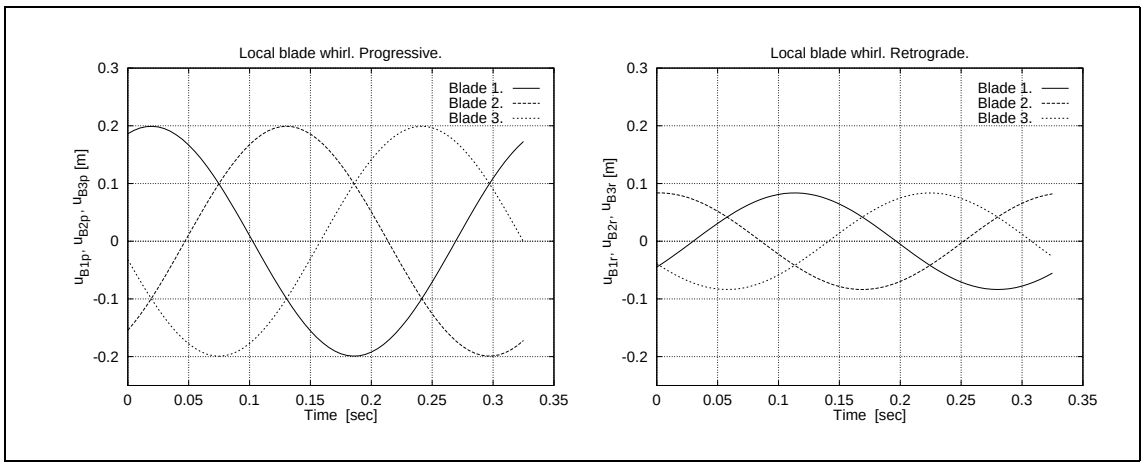


*Figure 6.17. Progressive and retrograde components of edgewise blade deformations.*

The response of an operating turbine is time varying due to the time varying excitation, and the *local blade whirl components* are changing with time, accordingly.

Assuming that the fundamental edgewise mode shapes dominate the response, the blade deformation in the edgewise direction can be determined from the deformation at one radial blade station – say at the tip, i.e. at radius $r = R$, meaning that $\{u(R,t)\}$ is known – or from the moment – say the moment at the blade root, $\{M_{B0}(t)\}$ – assuming that the moment is proportional to the deformation

$$\{M_{B0}\} = \left\{ \begin{array}{c} M_{B10}(t) \\ M_{B20}(t) \\ M_{B30}(t) \end{array} \right\} = K_{uM} \{u_R(R,t)\} = K_{uM} \left\{ \begin{array}{c} u_{B1x}(R,t) \\ u_{B2x}(R,t) \\ u_{B3x}(R,t) \end{array} \right\} , \tag{6.41}$$

where $K_{uM}$ is the proportionality factor equivalent to a stiffness with dimension [Nm/m].

As the edgewise deformations are influenced by the aerodynamic driving force and the 1P gravity force we choose to remove the mean deformation and the harmonic 1P deformation per rotor revolution.

The total response is expressed as the sum

$$\{u_R(R,t)\} = \{u_m(R)\} + \{u_{1P}(R,t)\} + \{u_e(R,t)\} , \tag{6.42}$$

where

$\{u_m(R)\}$ is the mean deformation calculated over one complete revolution,

$\{u_{1P}(R,t)\}$ is the deformation due to the gravity force and the 1P aero-force and

$\{u_e(R,t)\}$ is the deformation due to the vibration in the fundamental edgewise mode shape and the higher order modes.

When the fundamental edgewise mode shapes dominate $\{u_e\}$, this vector can be resolved in its components with good approximation according to the theory presented in the previous Sections 6.3.1 and 6.3.2.

Calculation for one complete rotor revolution gives the mean

$$\{u_m(R)\} = \frac{1}{T_P}\int_0^{T_P} \{u_R(R,t)\}\,\mathrm{d}t \ , \tag{6.43}$$

where $T_P = \frac{2\pi}{\Omega}$ is the period for one revolution.

Correspondingly, the 1P contribution is expressed by the truncated Fourier series

$$\{u_{1P}(R,t)\} = \left[ \left\{ \begin{array}{c} a_1 \\ a_2 \\ a_3 \end{array} \right\} \cos(\Omega t) + \left\{ \begin{array}{c} b_1 \\ b_2 \\ b_3 \end{array} \right\} \sin(\Omega t) \right] \ , \tag{6.44}$$

where the coefficients are calculated from

$$\left\{ \begin{array}{c} a_1 \\ a_2 \\ a_3 \end{array} \right\} = \frac{2}{T_P}\int_0^{T_P} \{u_R(R,t)\}\cos(\Omega t)\mathrm{d}t \tag{6.45}$$

and

$$\left\{ \begin{array}{c} b_1 \\ b_2 \\ b_3 \end{array} \right\} = \frac{2}{T_P}\int_0^{T_P} \{u_R(R,t)\}\sin(\Omega t)\mathrm{d}t \ . \tag{6.46}$$

Having determined the mean and the 1P component, the remainder of the response, which we expect to be dominated by the vibration in the fundamental edgewise mode shapes, can be found from

$$\{u_e(R,t)\} = \{u_R(R,t)\} - \{u_m(R)\} - \{u_{1P}(R,t)\} \ , \tag{6.47}$$

which we expand in the modal components according to Equation 6.4

$$\{u_e(R,t)\} = \left\{ \begin{array}{c} u_{B1x}(R,t) \\ u_{B2x}(R,t) \\ u_{B3x}(R,t) \end{array} \right\} = \left[ \begin{array}{cc} \{\varphi_7(R)\} & \{\varphi_8(R)\} \end{array} \right] \left\{ \begin{array}{c} q_7(t) \\ q_8(t) \end{array} \right\} \ . \tag{6.48}$$

Solving for the normal coordinates we get

$$\left\{ \begin{array}{c} q_7(t) \\ q_8(t) \end{array} \right\} = \left[ \begin{array}{c} \{\varphi_7(R)\}^T \\ \{\varphi_8(R)\}^T \end{array} \right] \{u_e(R,t)\} \ , \tag{6.49}$$

where $T$ denotes transposition, and the modal vectors are the rows of the transposed modal matrix.

Now, the theory from the previous Sections 6.3.1 and 6.3.2 can be used for decomposition and analysis.

**Example with response during normal operation**

The response from the Bonus 500 kW turbine with LM-19.0 blades is considered. We analyse the first 256 seconds of the simulated response at 23.2 m/s from the case study presented in Figures 8.11 and 8.12 in Section 8.2. Here, the responses for two different wind turbine configurations have been calculated. One is the basic configuration (Rhi1), and the other is with the stiffness of the main shaft increased (Rhi3). The natural frequencies at stand still for the two configurations are listed in Table 6.2. The calculated edgewise blade root moments for the two cases are shown in Figure 6.18.

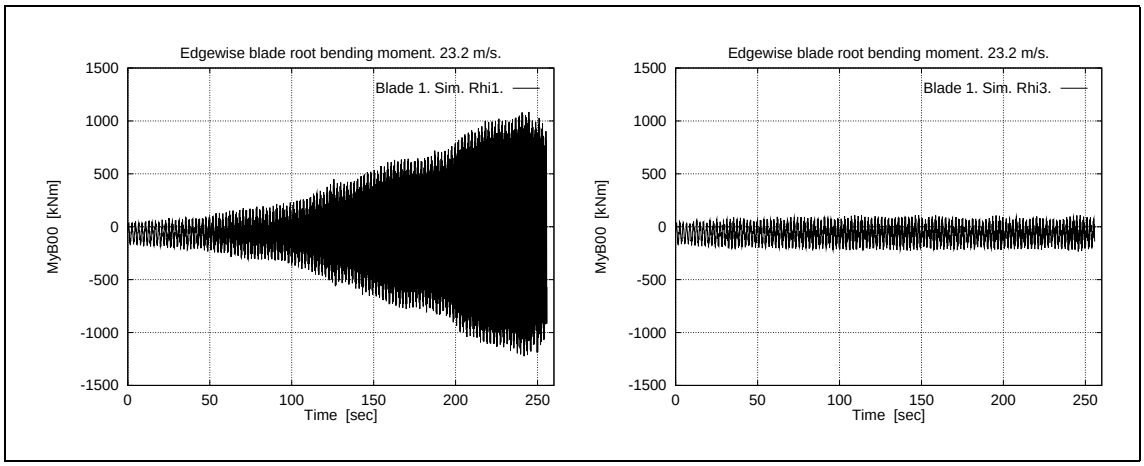


*Figure 6.18. The simulated edgewise blade root moments for two cases.* Left*: Basic configuration.* Right*: Shaft stiffness increased.*

The analysis is based on these moments, and therefore the proportionality factor $K_{uM}$ from Equation 6.41 is involved in the calculations. The actual value of $K_{uM}$ is approximately 1200 kNm/m.

In Figures 6.19-6.22 the analysis results for the basic case are shown. Figure 6.19 shows 1 second of the time trace for all three edgewise blade tip deformations and the power spectral densities. The edgewise vibration at 2.9 Hz dominates the response. The 1P frequency is 0.49 Hz. In Figure 6.20 the time trace for blade 1 is shown for 2.5 rotor revolutions. The 1P component, calculated according to Equation 6.44, is shown in the figure. The discontinuities in the 1P curve are due to the averaging per rotor revolution and basically caused by the time varying 1P aero-load.

The right plot in Figure 6.20 shows the local blade whirl deformation components calculated according to Equations 6.33 and 6.34. They vary with time due to the increasing edgewise vibration. The whirl components are calculated for each complete cycle of the edgewise vibration, assuming that the vibration is harmonic during this period. This calculation is equivalent to the 1P expansion described in Equation 6.44, but now the frequency is $\omega_e$, and the period is $\frac{2\pi}{\omega_e}$. It is observed that the backward (or retrograde) component is dominating. This component has the frequency $\omega_e - \Omega$ in the stationary coordinates. The corresponding in-plane inertia force is shown in the left plot in Figure 6.21 for the time period 190-200 seconds. The arrows indicate that the rotation direction is backwards.

The tower top tilt and yaw bending moments for the same 190-200 seconds time period are shown in the right plot of Figure 6.21, where the curve shows the trace of the rotating moment at the tower top. A 5 seconds period of the time traces of these moments are shown in Figure 6.22 together with the power spectral densities. The dominating rotating moment at the tower top shown in Figure 6.21 has the frequency $\omega_e - \Omega \simeq 2.4$ Hz, but in the power

spectrum the $\omega_e + \Omega \simeq 3.4$ Hz is identified as well. Both these frequencies might be essential for the coupling between *local blade whirl* and *global rotor whirl*. If any of them are close to the global rotor whirl frequencies, significant exchange of energy might take place, which seems to be the case here.

Obviously, the explanation of this energy exchange is not straightforward. The frequency of the $2^{nd}$ backward rotor whirl mode, which we would expect to participate in the coupling with the in-plane inertia force, is approximately 3.4 Hz as shown later in Section 6.4. If we consider the in-plane inertia force to be the excitation, it is surprising to observe that the progressive component, which has the same frequency in the stationary coordinates, is practically zero, and no excitation should take place. However, theory based on calculations of work performed by the in-plane force on the hub indicates that the progressive component exchanges energy via the rotor whirl mode at 3.4 Hz with the retrograde blade component, which increases and excites the rotor whirl, not at a whirl frequency, but in a forced whirl movement at the 2.4 Hz frequency.

The importance of the coinciding frequencies is further demonstrated by the other calculation case, for which the shaft stiffness has been increased. This case is analyzed and the results are shown in Figures 6.23-6.26. The increased stiffness changes the global rotor whirl frequencies, and the edgewise vibration is much less dominating than in the previous case. The backward rotor whirl frequency is now increased to approximately 3.6 Hz as shown later in Section 6.4.

In a design situation it is important to determine the actual values of both the local blade whirl frequencies and the global rotor whirl frequencies, if we want to know, whether coincidence is taking place. The blade frequencies can be determined with good accuracy from the power spectra of the edgewise response as demonstrated for instance in Figure 6.19. The determination of the rotor whirl frequencies is less straightforward, as they are less dominating in the spectra and often difficult to distinguish from other frequencies. In Section 6.4 a method is demonstrated, which can be used to determine these frequencies.

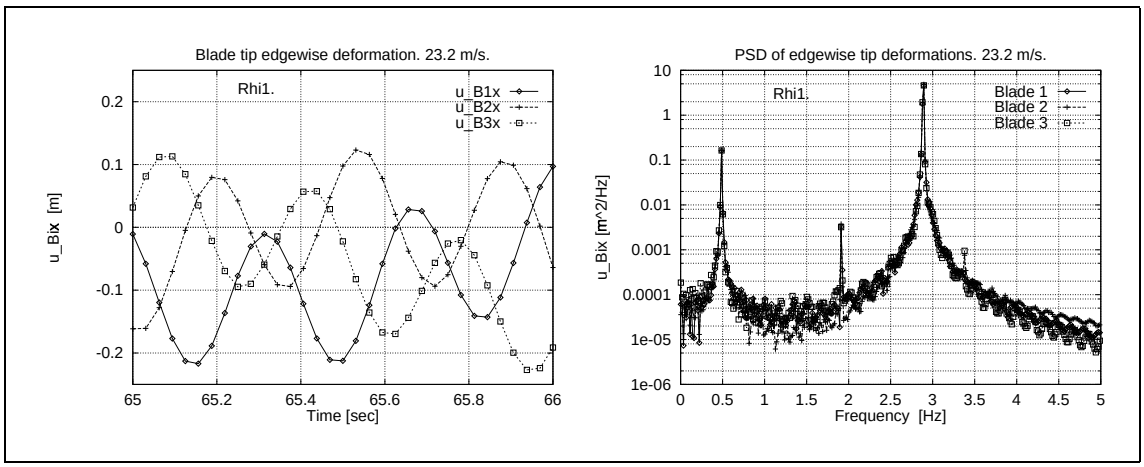


*Figure 6.19. Basic case. Time traces and power spectral densities of edgewise blade tip deformations.*

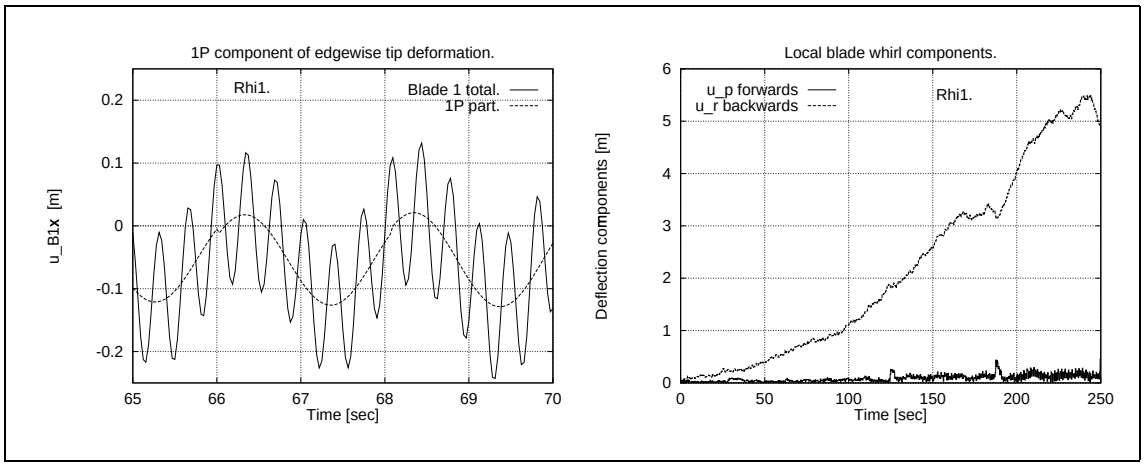


*Figure 6.20. Basic case.* Left: *Total edgewise blade tip deformation and 1P component.* Right: *Progressive ($u_p$) and retrograde ($u_r$) local blade whirl components.*

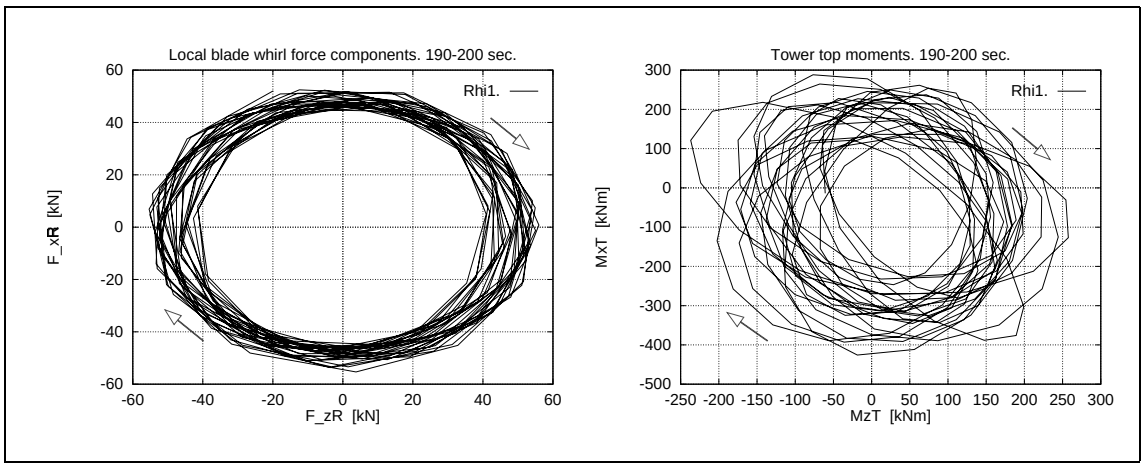


*Figure 6.21. Basic case.* Left: *Local blade whirl inertia force components.* Right: *Tower top tilt and yaw bending moments.*

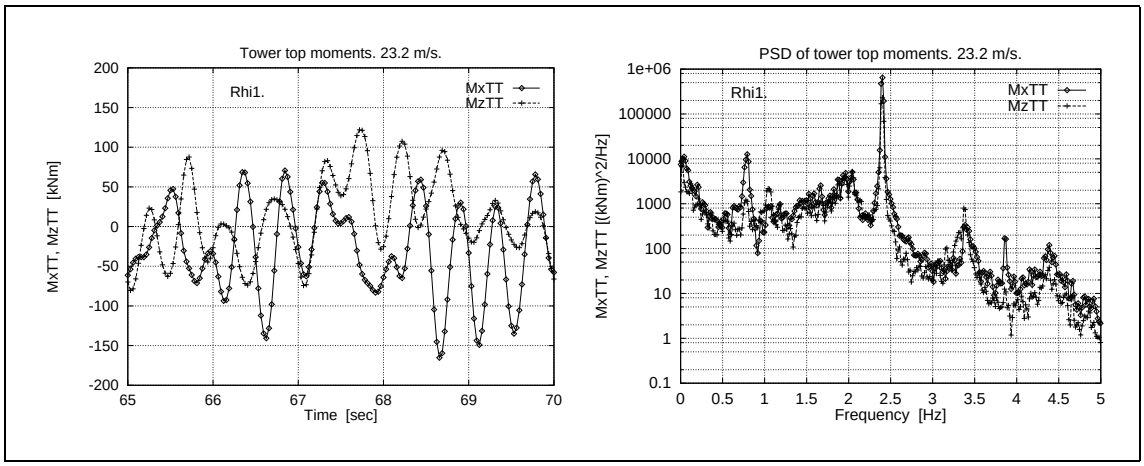


*Figure 6.22. Basic case.* Left: *Time trace of tower top tilt and yaw moments.* Right: *Power spectral densities of tower top moments.*

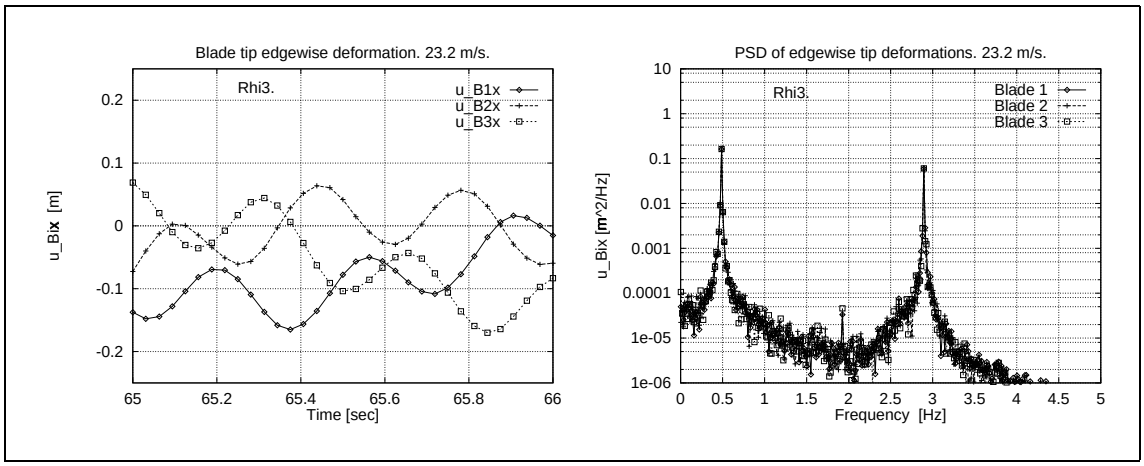


*Figure 6.23. Increased shaft stiffness. Time traces and power spectral densities of edgewise blade tip deformations.*

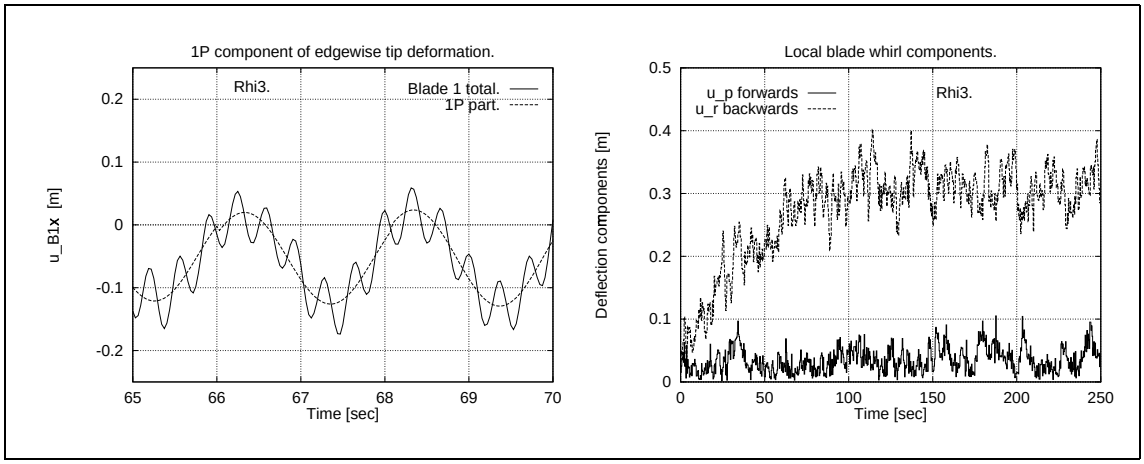


*Figure 6.24. Increased shaft stiffness.* Left: *Total edgewise blade tip deformation and 1P component.* Right: *Progressive ($u_p$) and retrograde ($u_r$) local blade whirl components.*

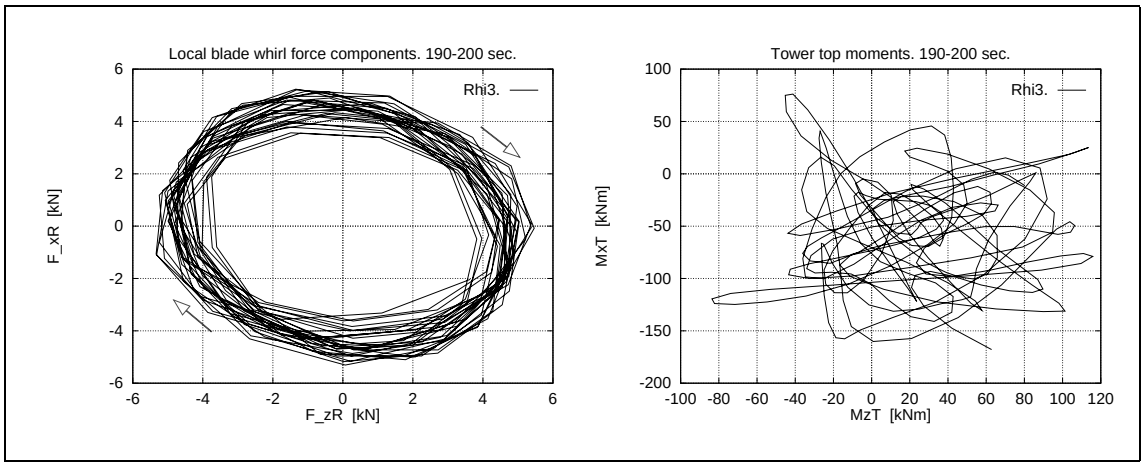


*Figure 6.25. Increased shaft stiffness.* Left: *Local blade whirl inertia force components.* Right: *Tower top tilt and yaw bending moments.*

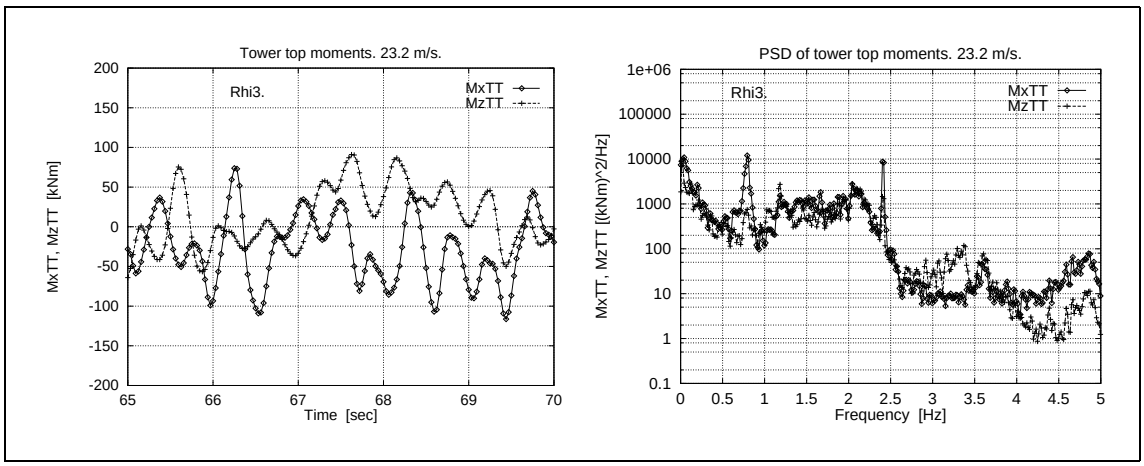


*Figure 6.26. Increased shaft stiffness.* Left: *Time trace of tower top tilt and yaw moments.* Right: *Power spectral densities of tower top moments.*

## 6.4 Example investigation of rotor whirl and blade whirl

The influence of the wind turbine global structural dynamics on the edgewise blade vibration phenomena is illustrated for instance in the previous section in Figure 6.18. In this figure the simulated edgewise blade root moments of two different wind turbine configurations are shown. The turbine is operating in stall at 23.2 m/s. It is seen that one of the configurations are subject to severe edgewise vibrations. The difference between the two cases is different shaft stiffnesses.

As pointed out previously, the actual values of the local blade whirl frequencies and the global rotor whirl frequencies are important for the interaction between the two vibrations – if the frequencies are close to each other, a significant energy exchange might take place, and both vibrations might develop more easily than otherwise. In a design situation it might therefore be of interest to gain some knowledge about their actual values in order to try to avoid the coupling by proper design choices.

Normally, the blade frequency is easy to determine, as it usually can be detected very clearly from the power spectra of normal operation response. Further, it will be rather close to the non-rotating blade frequency, which can be determined from an eigenvalue analysis. The opposite is the case for the rotor whirl frequencies. They are difficult to detect directly from the power spectra of normal operation response. Primarily, because they are less pronounced in the spectra and often in the vicinity of other frequencies. An eigenvalue analysis of the non-rotating turbine is not directly applicable, as the rotating frequencies might deviate significantly from these due to gyroscopic forces as shown in Appendix B.

Below we demonstrate a method for finding the approximate values of the rotor whirl frequencies. The method is based on aeroelastic calculation with excitation during operation by use of a known harmonic moment at the tower top.

Still, the significance of the coupling can not be predicted merely by knowing the involved frequencies. Usually, the designer should aim at separating the frequencies as much as possible and finally verify that the resulting response is acceptable by use of full aeroelastic calculations. One possible systematic approach for determining favourable structural properties with respect to limitation of the influence of the coupling phenomena on the

edgewise vibrations is shown below. The rotor whirl frequencies are changed in steps by changing the tower top stiffness, and the accompanying change of standard deviation of the edgewise response is used as a measure of the influence of the structural change, and the most favourable solutions can be sought through this procedure.

### Determination of global rotor whirl frequencies

The global rotor whirl frequencies can be approximately determined by use of an aeroelastic code. During operation the whirl modes can be excited by use of harmonic forces or moments, and analysis of the response, e.g. by calculation of the power spectral densities, can provide the frequency values. We demonstrate a method, where the whirl modes are excited by a harmonic moment at the tower top. The frequency of the moment, $f_e(t)$, is varied linearly during the calculation period, $T$. The variation of the excitation frequency around a chosen center frequency, $f_c$, follows the expression

$$f_e(t) = f_c \left(1 - p + 2p\frac{t}{T}\right) , \tag{6.50}$$

where $p$ is the percentage the variable frequency lies below the center frequency at time $t = 0$ sec and above at $t = T$ sec.

The excitation is equivalent to the excitation by the harmonic force from the local blade whirl described in Section 6.3, but it is obtained by applying a time varying moment at the tower top as shown in Figure 6.8, where the moment components, $M_x$ and $M_z$, vary harmonically with the amplitude $M_0$ and with the specific frequency, $f_e$, according to

$$\left\{ \begin{array}{c} M_x(t) \\ M_y(t) \\ M_z(t) \end{array} \right\} = \left\{ \begin{array}{c} M_0 \cos\left(2\pi f_c \left[(1-p)\,t + p\frac{t^2}{T}\right]\right) \\ 0 \\ M_0 \sin\left(2\pi f_c \left[(1-p)\,t + p\frac{t^2}{T}\right]\right) \end{array} \right\} , \tag{6.51}$$

which results in a constant size moment rotating in the vertical plane with the time dependent frequency $f_e(t)$. The shown moment rotates in opposite direction of the rotor, in the present context denoted the *backward* direction, and to reflect the changing frequency we denote the excitation *backward sweep*. *Forward* excitation could have been applied as well, and the response would be almost the same.

The results of aeroelastic calculations with this moment is shown in Figure 6.27, where the time traces of the tower top tilt moments for the previously mentioned two turbine configurations, Rhi1 and Rhi3, are presented. $M_0$ is 2.5 kNm, $f_c$ is 3.0 Hz and $p$ is 60%. The gravity and the aerodynamic forces are eliminated in the calculations. The structural damping is increased with a factor 2.0, resulting in a structural damping of approximately 5% logarithmic decrement.

The left plot shows the result for the original configuration. From the plot the approximate values of the rotor whirl frequencies can be detected in the ranges where resonance is observed. At time $t = 0$ sec the resonance corresponds to the $1^{st}$ backward whirl frequency, at time $t = 140$ sec to the $1^{st}$ forward whirl frequency, at $t = 380$ sec to the $2^{nd}$ backward frequency and finally at $t = 520$ sec to the $2^{nd}$ forward frequency. Two peaks are observed in the range where the $2^{nd}$ backward mode is excited. This indicates that different coupling patterns exist, probably due to different participation of the blade flapwise modes.

The frequencies can also be detected from the power spectral densities of the tower top moments as presented in the left plot in Figure 6.28.

The right plots in Figures 6.27 and 6.28 show the corresponding time traces and power spectra for the turbine configuration with stiffened shaft. It is observed that all the whirl frequencies are increased with approximately 0.1-0.2 Hz. Especially the change of the $2^{nd}$ backward whirl frequency from 3.4 Hz to 3.6 Hz seems to be important for the coupling to the blade vibrations. The 3.4 Hz is the blade whirl frequency +1P. The change of the whirl frequency by +0.2 Hz is obviously sufficient to reduce the influence from coupling.

The time traces of the tower top moments for the original configuration is shown in Figure 6.29, showing as $xy$-plots the moments corresponding to $2^{nd}$ backward whirl and $2^{nd}$ forward whirl, respectively. The plots cover 16 sec of the time traces from $t$ =380 sec for the backward mode and from $t$ = 520 sec for the forward mode. The arrows in the plots indicate the rotation direction. By appropriate scaling of the shown moments the corresponding movement of the rotor center would be obtained with good approximation. So the plots can also be viewed as the movement of the rotor center in a vertical plane.

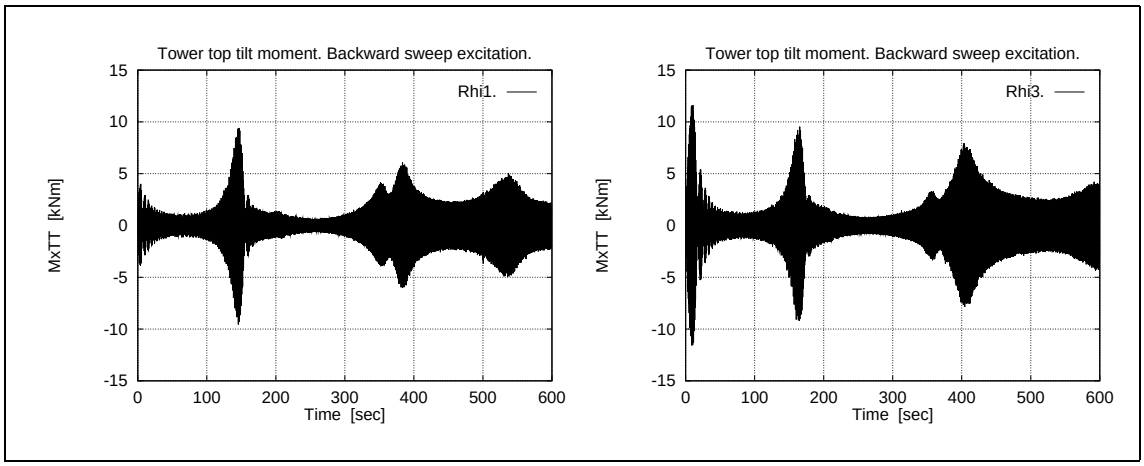


*Figure 6.27. Tower top tilt moment during excitation with a harmonic moment with linearly varying frequency at the tower top.* Left: *The original configuration.* Right: *Shaft stiffened.*

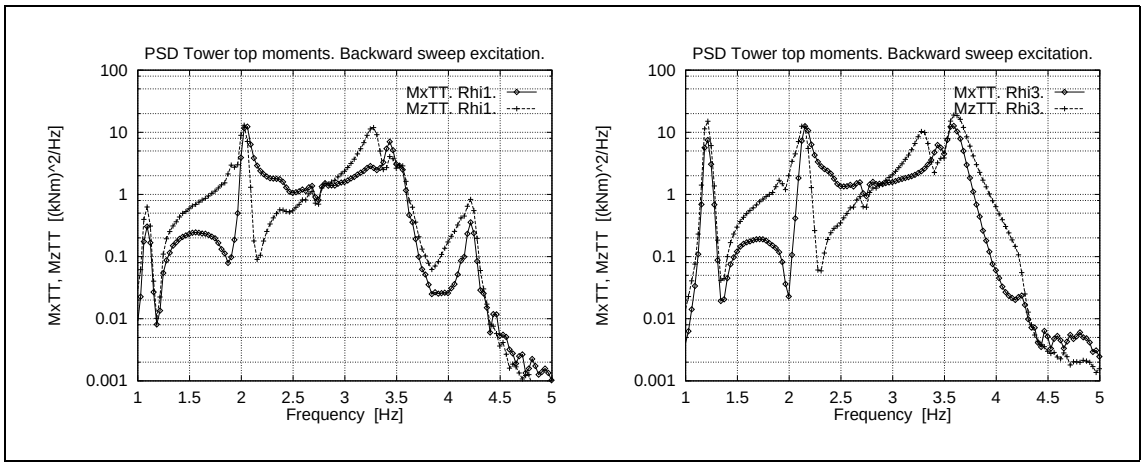


*Figure 6.28. Power spectral densities of tower top moments for the whole 10 minutes excitation period. Backward sweep excitation.* Left: *Original configuration.* Right: *Stiffened shaft.*

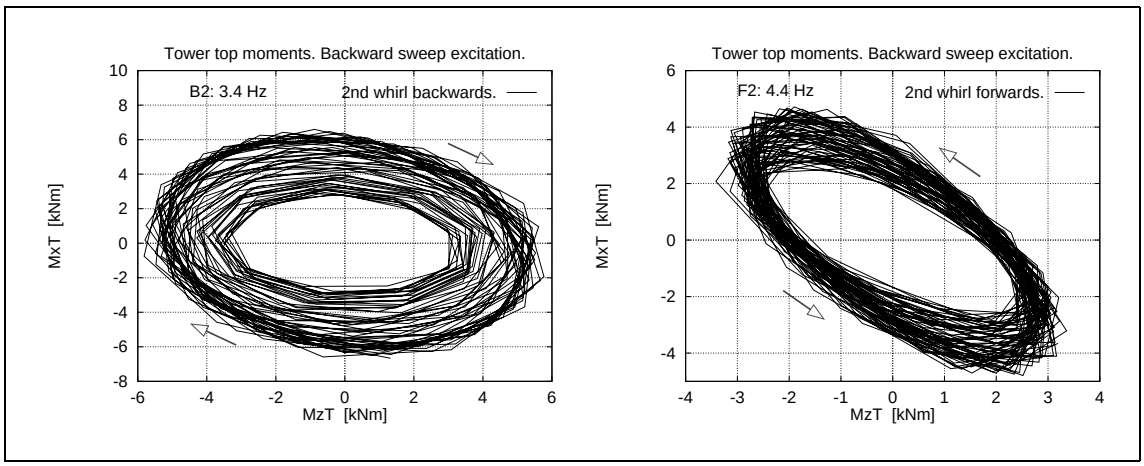


*Figure 6.29. Tower top moments during excitation with harmonic moment with linearly varying frequency at the tower top.* Left: *$2^{nd}$ whirl mode, whirling backwards, 3.4 Hz.* Right: *$2^{nd}$ whirl mode, whirling forwards, 4.4 Hz.*

### Seeking favourable coupling properties

For different structural configurations – in the present context different tower top stiffnesses – the sensitivity to edgewise vibrations are shown in Figure 6.30. The results are obtained with the turbine operating under identical wind conditions for each configuration, and for these simulations no excess structural damping is added. The simulation time is 10 minutes. The difference between the edgewise natural frequency and the nearest $2^{nd}$ whirl frequency in the rotating frame of reference is plotted on the abscissa axis. The whirl frequencies are determined for each configuration by the method described above. On the ordinate, a measure of the magnitude of the vibration level is plotted. This value is the standard deviation of the edgewise blade bending moment at the root, band-pass filtered around the natural frequency. The value is averaged over all three blades.

The results in the figure show that an increase of the $2^{nd}$ rotor whirl frequency of the order of magnitude 0.1 Hz results in a significant reduction of the edgewise vibration, in agreement with the results from the previous sections.

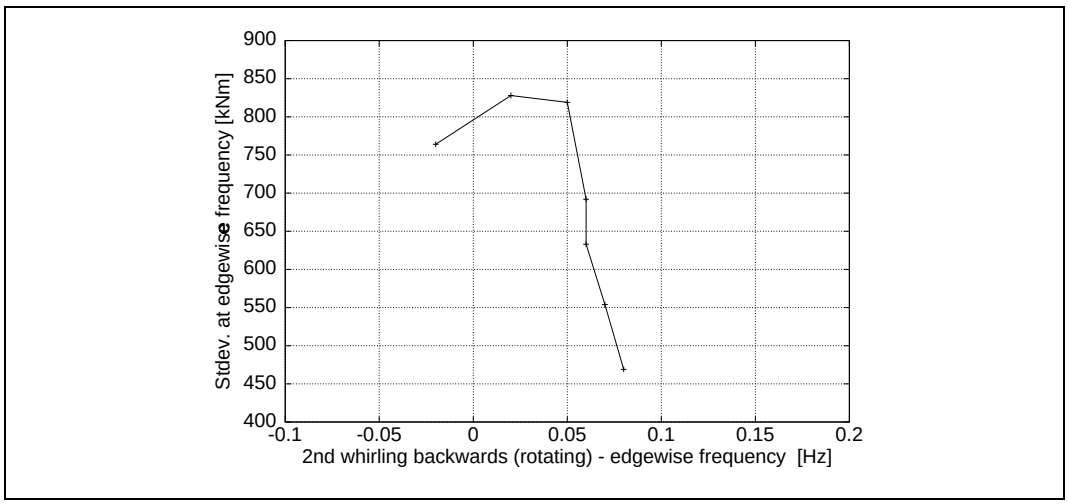


*Figure 6.30. Standard deviation of edgewise moment in band around edgewise natural frequency.*

# 7 Aeroelastic calculations and measurements

As part of the project work investigations have been carried out on a Bonus 500 kW prototype wind turbine located in Dybe, Jutland. Bonus Energy A/S has supplied selected measurements and detailed data for the wind turbine, making it possible to generate an aeroelastic model of the turbine and carry out simulations and comparisons. The material supplied by Bonus Energy A/S can be found in the project documents [2], [3] and [4].

Aeroelastic calculations and comparisons were performed by DTU, TAB, ECN and Risø as planned and agreed upon during project meetings. Generally, good agreement was found in the results among participants. Below, the calculation results obtained by Risø are presented and compared with measurements. The simulations are carried out by use of the Risø aeroelastic code HawC described in detail in [5] and in overview in [6].

The main data for the wind turbine are presented in Section 6.1. The natural frequencies – measured and simulated – are listed in Section 6.2, where also the two fundamental rotor mode shapes involved in edgewise vibrations are shown and described.

Mainly four sets of simulations and comparisons have been performed:

1. Calculation of quasi-steady aerodynamics and aerodynamic damping in edgewise and flapwise mode shapes. Reported in Section 7.1.
2. Parked situation at 24.2 m/s mean wind speed. Reported in Section 7.2.
3. Operation below stall at 9.5 m/s mean wind speed. Reported in Section 7.3.
4. Operation above stall at 23.2 m/s mean wind speed. Reported in Section 7.4.

The comparisons are based on power spectral densities of wind speed, shaft torsional moment, edgewise and flapwise bending moments at the blade root, bending moment on stationary main shaft (denoted the rotor tilt moment) and torsional moment at the tower top (denoted the rotor yaw moment). Further, the power spectral densities of the electrical power are compared for the cases where the turbine operates. The power spectral densities are based on time periods of 10 minutes, and the statistical degrees of freedom in the spectra are 16. The sampling frequency in the simulations is 32 Hz and in the measurements 25 Hz. The cup anemometer is placed at 37 m height on a slender mast 2.5 turbine diameters upwind, and the line connecting the turbine and the mast is in the middle of the 90° measuring sector. The location of the actual strain gauges are listed in Table 7.1.

*Table 7.1. Location of strain gauges*

| Signal | Strain gauge position |
|---|---|
| Blade root edgewise bending moment | 1.3 m from rotor center |
| Blade root flapwise bending moment | 1.3 m from rotor center |
| Bending moment at fixed shaft (rotor tilt) | 0.8 m from rotor center |
| Torsional moment at tower top (rotor yaw) | 32.50 m from tower base |
| Main shaft torsional moment (rotor torque) | 1.6 m from rotor center |

Further, simulations have been carried out in order to investigate the influence of selected main parameters on stall induced vibrations. This full scale parametric study is reported in Section 8.

## 7.1 Calculation of rotor aerodynamics and damping

The calculated and the measured power curves are shown in Figure 7.1. The calculation overestimates the power significantly in a wind speed range around stall onset. The explanation is probably uncertainty both on the applied airfoil data and the measurements. This indicates that some differences should be expected in the load calculations as well. The calculated power and thrust coefficients are shown in Figure 7.2.

The aerodynamic damping has been calculated by use of the models presented in previous sections. The results are shown in Figure 7.3. One blade is exposed to forced vibration in the actual mode, using the mode shapes shown in Figure 6.5. The results referred to as *quasi-steady* is obtained by the model presented in Section 2. This model does not take the induction into account. The *non-linear* results are calculated with a full aerodynamic model based on blade element theory, but without dynamic stall. This model calculates the damping as work per cycle of the aerodynamic forces without linearizations. The *dynamic stall* results are obtained by the same non-linear model, but now with dynamic stall on both $C_L$ and $C_D$. The dynamic stall model is the Risø version of the Beddoes-Leishman model presented in Section 5.3, and the model parameters are $\tau_f = 6.0$, $\tau_p = 1.5$ and $\eta_c = 0.95$. The results show that the edgewise mode has a minimum aerodynamic damping around 22 m/s of approximately $-4\%$ logarithmic decrement. The actual structural damping assumed in the calculations for the basic model is 3% for both the edgewise and the flapwise mode shapes. This means that the resulting damping for the edgewise mode is negative in a wind speed range around 22 m/s. This is in good agreement with the simulation results at 23.2 m/s presented in Section 7.4, where edgewise vibrations are observed. The total damping for the flapwise mode will be positive, assuming the 3% structural damping.

The simulations presented in the following sections are obtained with dynamic stall only on $C_L$, and the model parameters are the same as above, $\tau_f = 6.0$ and $\tau_p = 1.5$.

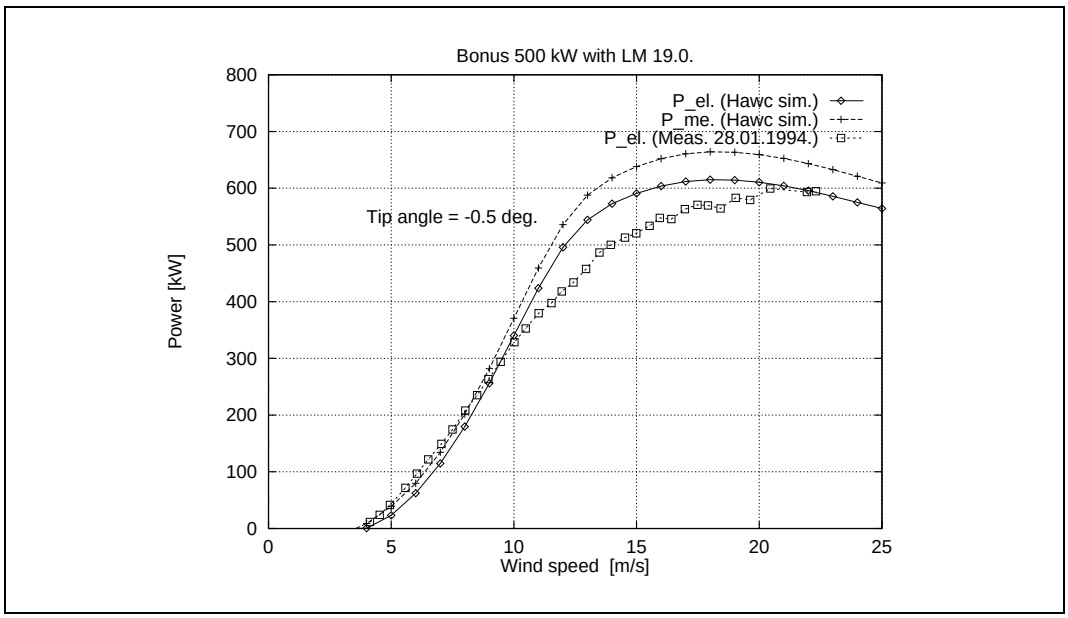


*Figure 7.1. Power curves, measured and simulated with airfoil data from Figure 6.1. The simulated power curves correspond to electrical* (el) *and mechanical* (me) *power, respectively. The measured curve is electrical power.*

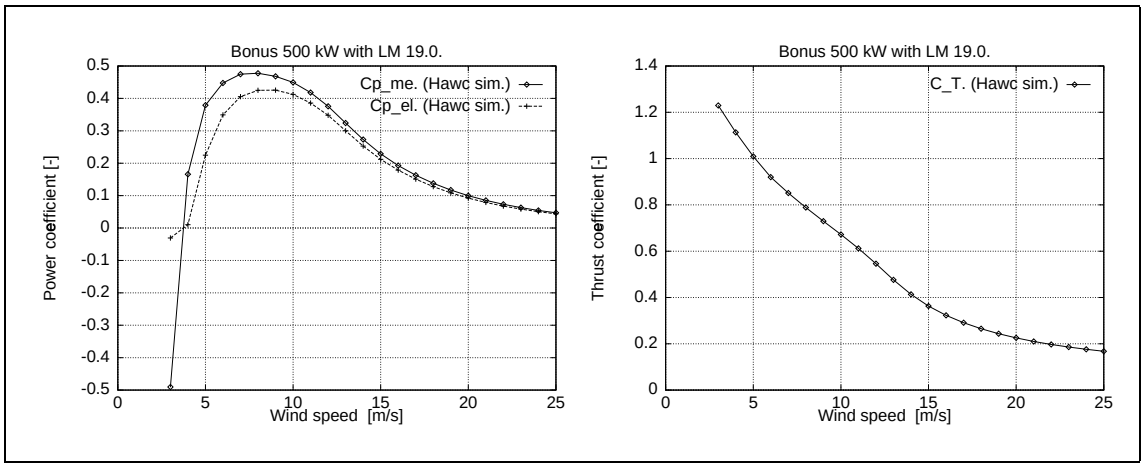


*Figure 7.2. Calculated rotor power and thrust coefficients.*

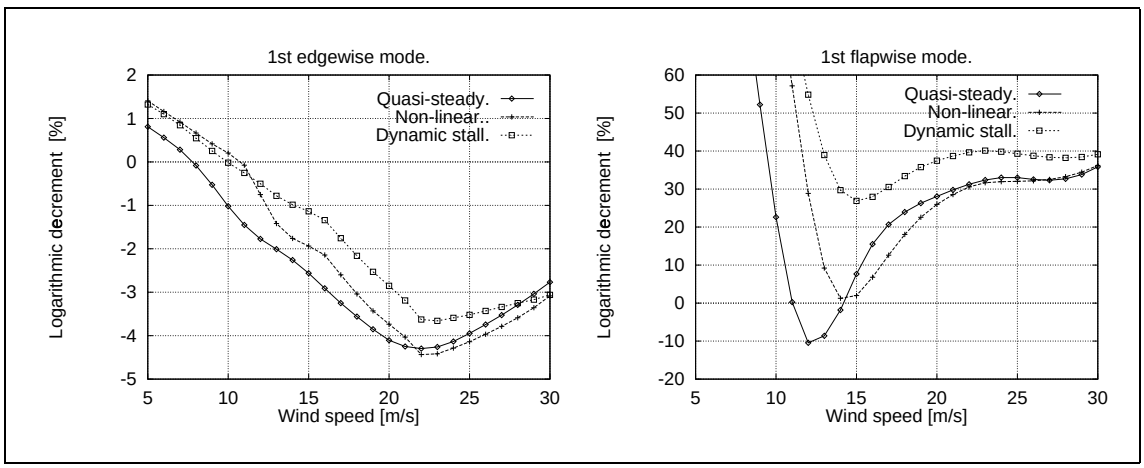


*Figure 7.3. Calculated aerodynamic damping.* Quasi-steady: *Linear model without induction.* Non-linear: *Work per cycle, induction included.* Dynamic stall: *Work per cycle, induction and dynamic stall on both $C_L$ and $C_D$ included.*

## 7.2 Stand still

Initially, measurements and calculations are compared for a case with the wind turbine standing still. The mean wind speed is 24.2 m/s and the turbulence intensity is 10.5%. A power spectrum of the wind is shown in Figure 7.4. During the calculations the rotor position is as shown in Figure 6.6, with one blade vertically upwards. The rotor position during the measurements is not known.

The case serves to compare the most dominating frequencies in the response, here represented as the moments listed in Table 7.1. The measured frequencies are marked in the figures of power spectral density, Figures 7.5-7.9. The frequencies were listed in Table 6.2 and repeated below in Table 7.2. Good agreement between measured and calculated frequencies is obtained.

During operation the frequencies for modes in which rotating parts participate will change somewhat due to inertia forces, e.g. centrifugal and gyroscopic forces.

It should be noted that generally the calculated energy level is lower than the measured at higher frequencies. The exact explanation is not known at present, but the main reason is assumed to be a lack of energy at higher frequencies in the simulated turbulence applied in the simulations. However, this is not important for the present work.

*Table 7.2. Measured and simulated natural frequencies at stand still.*

| Frequency number | Measured Frequency [Hz] | Simulated Frequency [Hz] | Description of mode |
|---|---|---|---|
| 1 | 0.750 | 0.760 | Tower across wind |
| 2 | 0.790 | 0.809 | Tower along wind |
| 3 | 0.900 | 0.908 | Shaft torsion |
| 4 | 1.390 | 1.380 | $1^{st}$ rotor yaw |
| 5 | 1.560 | 1.550 | $1^{st}$ rotor tilt |
| 6 | 1.850 | 1.854 | $1^{st}$ blade flapwise |
| 7 | 2.910 | 2.921 | $1^{st}$ blade edgewise, Figure 6.6 |
| 8 | 2.930 | 2.972 | $1^{st}$ blade edgewise, Figure 6.7 |
| 9 | 3.540 | 3.550 | $2^{nd}$ rotor yaw, Figure 6.8 |
| 10 | 4.220 | 4.190 | $2^{nd}$ rotor tilt |

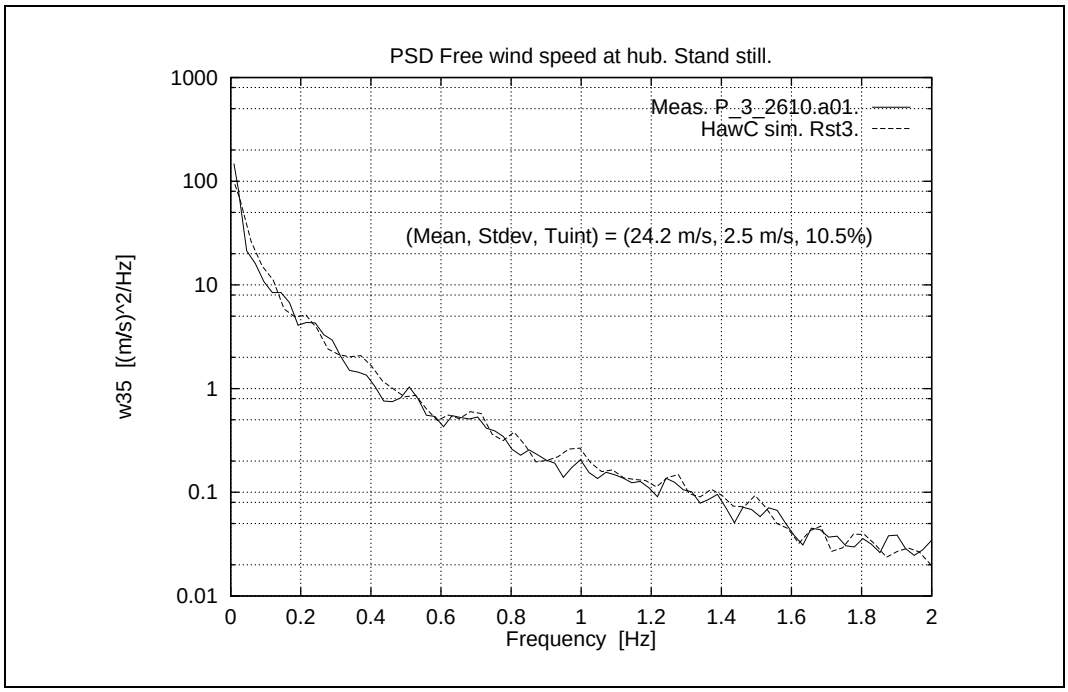


*Figure 7.4. Power spectral density of free wind speed at height 37 m.*

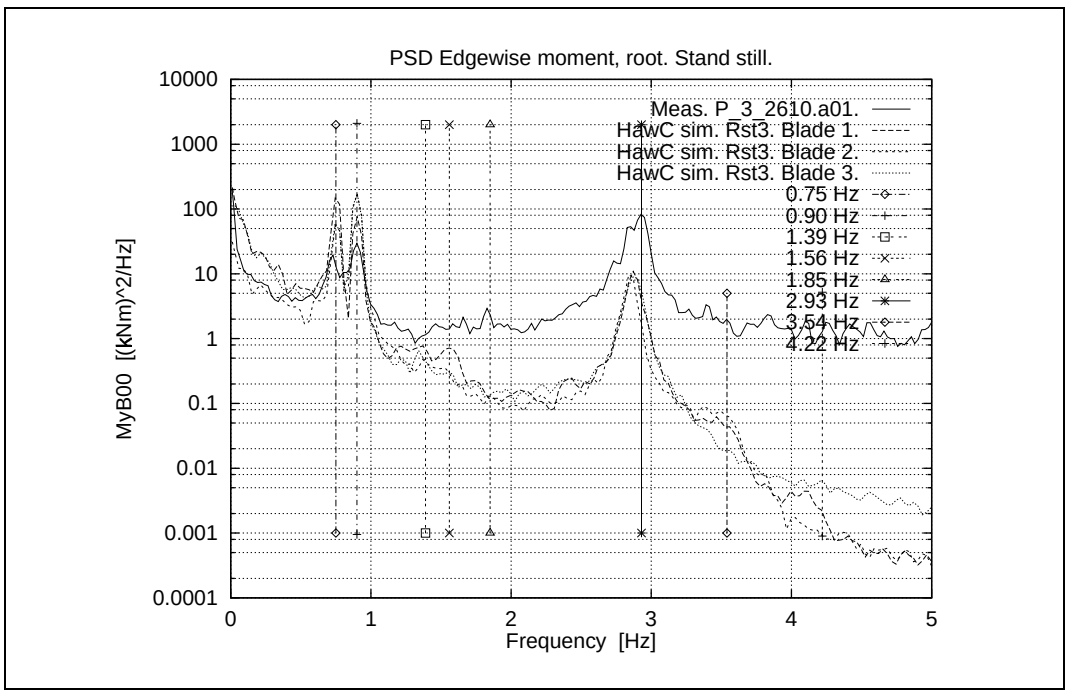


*Figure 7.5. Power spectral density of edgewise blade root bending moment.*

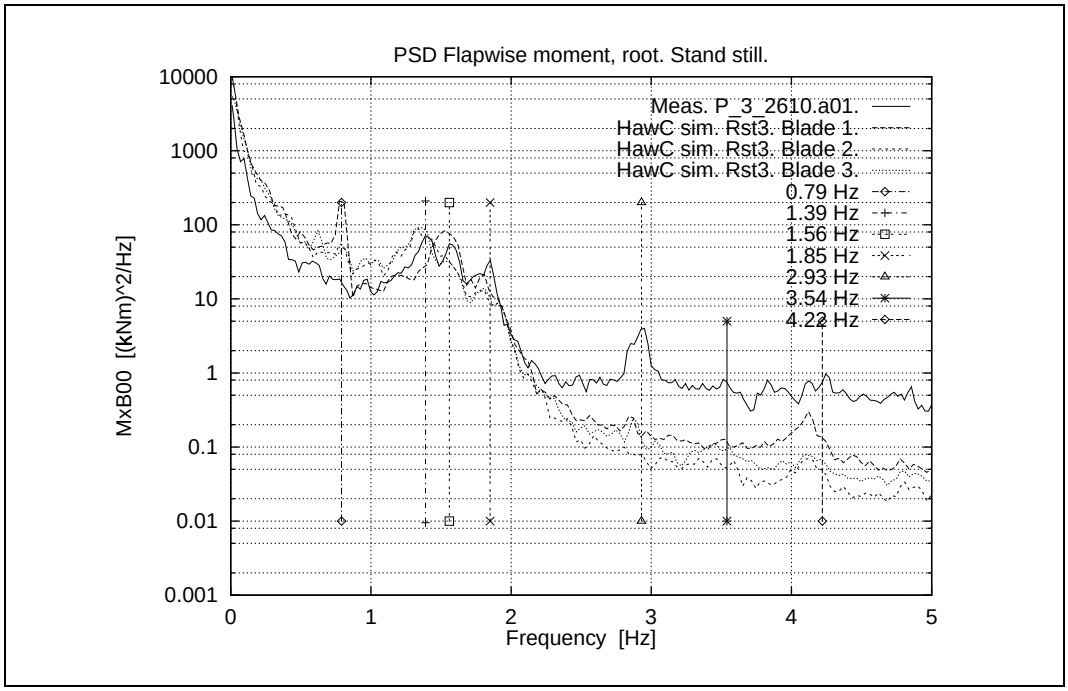


*Figure 7.6. Power spectral density of flapwise blade root bending moment.*

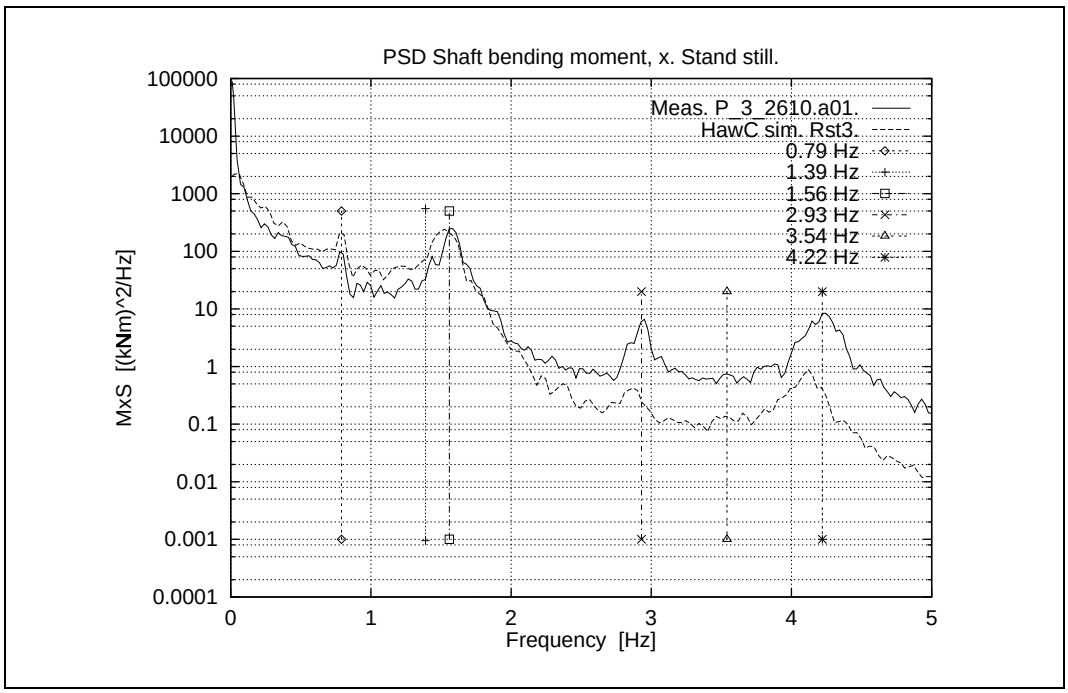


*Figure 7.7. Power spectral density of rotor tilting moment.*

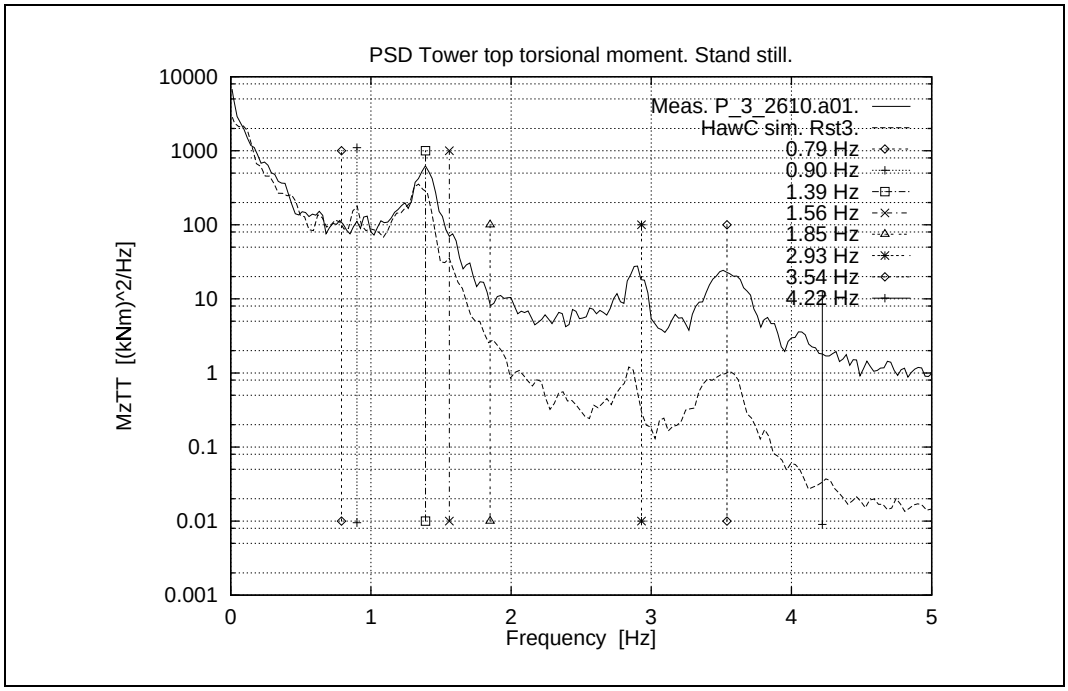


*Figure 7.8. Power spectral density of rotor yawing moment.*

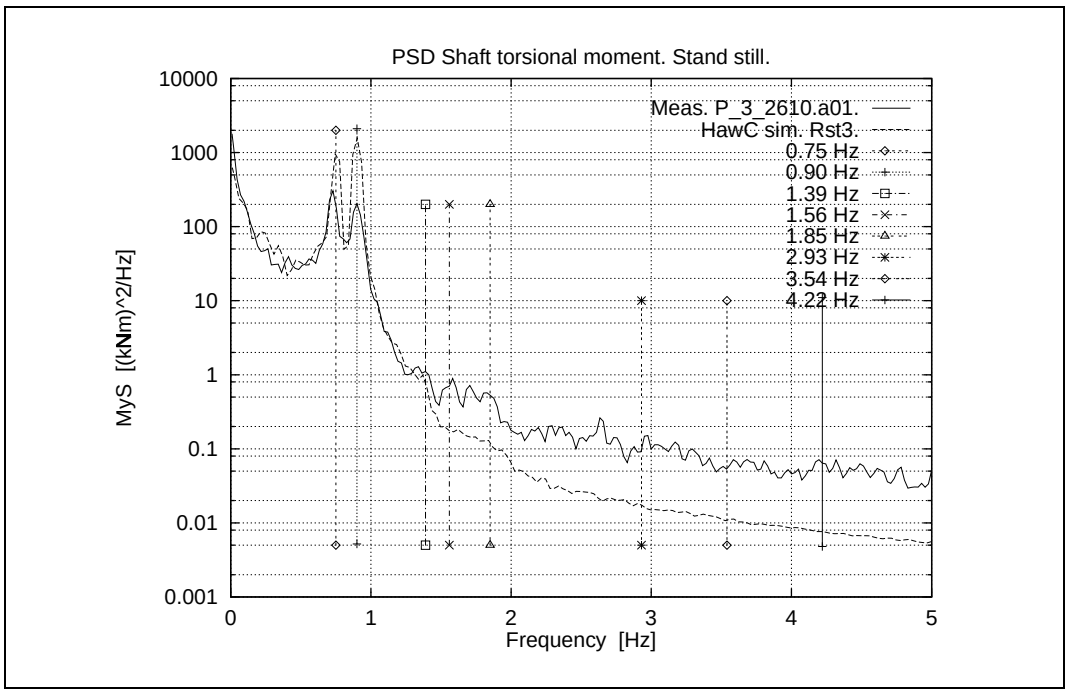


*Figure 7.9. Power spectral density of rotor torque.*

## 7.3 Operation before stall onset, wind speed 9.5 m/s

In order to examine the level of agreement between simulation and measurement in a wind speed range where negligible influence from stall is expected, a comparison of the wind turbine response during operation at mean wind speed 9.5 m/s has been carried out. The turbulence intensity is 10.4%. The power spectra of the measured and the simulated wind speeds are shown in Figure 7.10. Here it is observed that the simulated turbulence lacks energy for frequencies above approximately 0.6 Hz. However, this is not important, because the main excitation from the turbulence originates from turbulence, which is rotationally sampled below this frequency.

In Figures 7.11-7.16 power spectral densities are shown of the signals listed in Table 7.1 and the electrical power. In the figures multiples of the rotational frequency, 1P = 0.486 Hz, are marked with vertical lines. In addition other clearly identified peaks in the spectra are marked the same way.

Generally, good agreement is observed. The response at the edgewise frequency is somewhat overestimated in the simulated edgewise blade root moment shown in Figure 7.11. This might indicate that the structural damping should be increased in the turbine model. It was chosen to 3% logarithmic decrement rather arbitrarily. In the power spectrum of the rotor tilting moment in figure 7.13 a 5P peak is observed in the simulation. This peak is not present in the measurement at this wind speed, but it is found in the measurements as well at higher wind speeds . The spectrum of the rotor yawing moment in Figure 7.14 shows that the simulation underestimates the energy for frequencies just below the dominating 3P frequency. The opposite is the case for both the rotor torque in Figure 7.15 and the electrical power in Figure 7.16. These discrepancies might be due to differences in the spatial structure of the turbulence in the measured and the modelled turbulence, respectively.

Still, it is believed that the simulation model has a satisfactory representation of the physics, which is important for our investigation of the stall induced vibration phenomena.

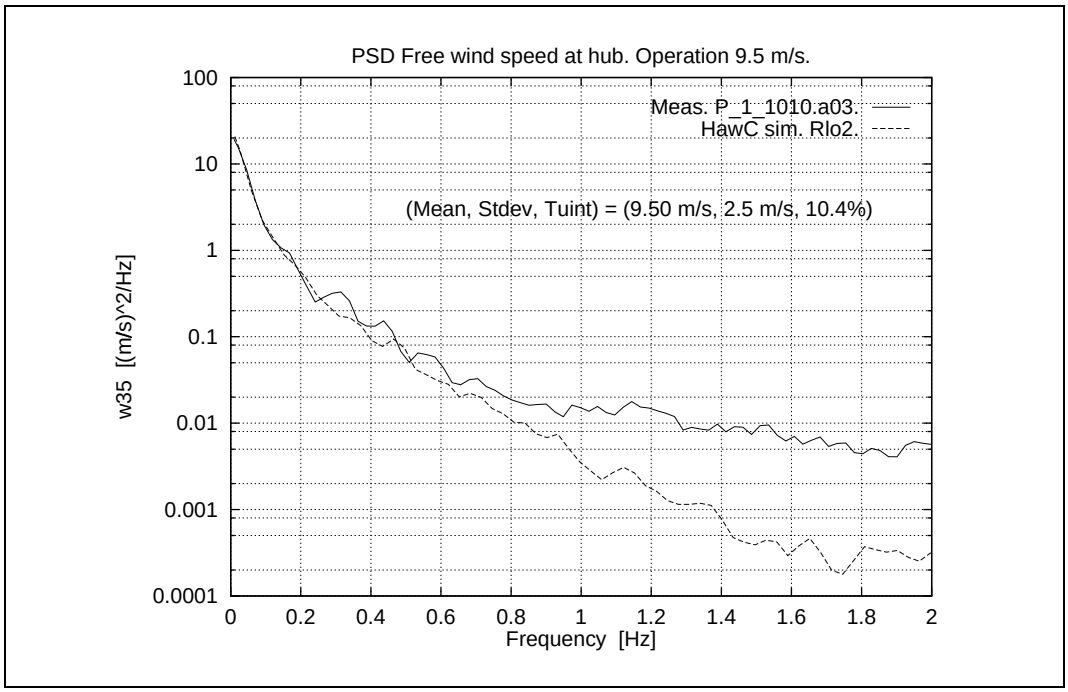


*Figure 7.10. Power spectral density of free wind speed at height 37 m.*

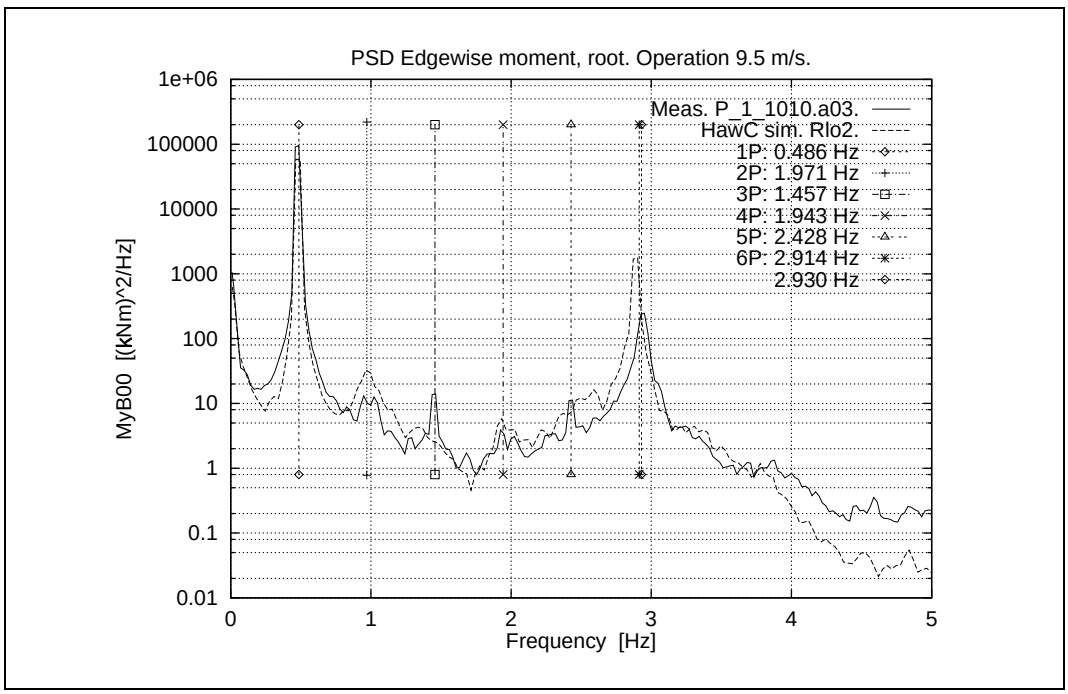


*Figure 7.11. Power spectral density of edgewise blade root bending moment.*

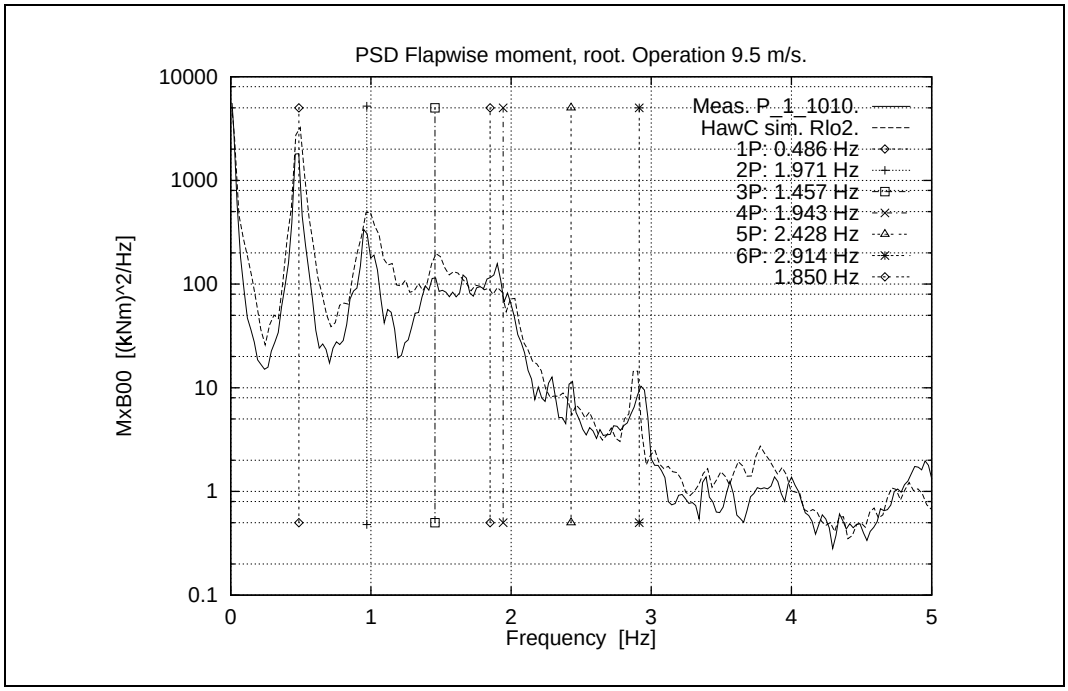


*Figure 7.12. Power spectral density of flapwise blade root bending moment.*

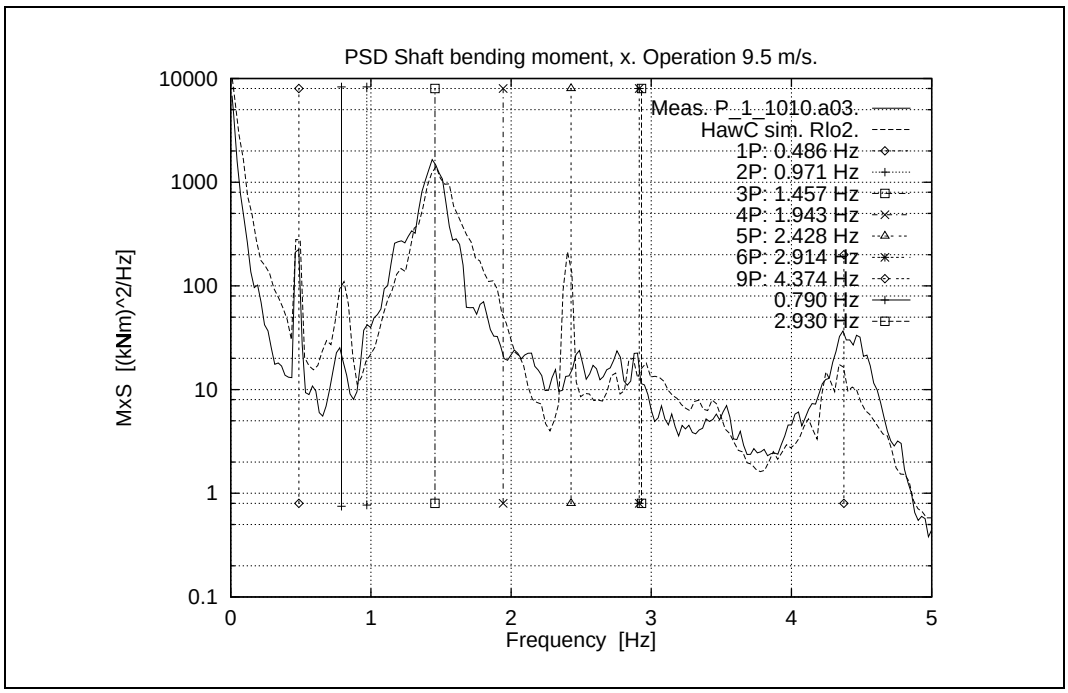


*Figure 7.13. Power spectral density of rotor tilting moment.*

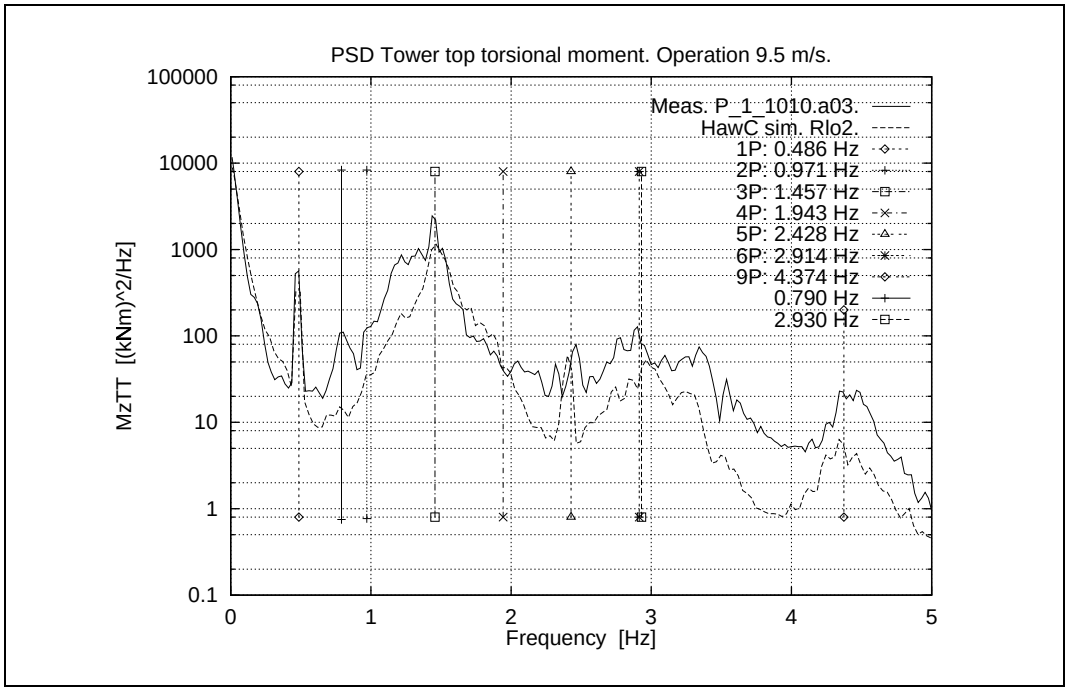


*Figure 7.14. Power spectral density of rotor yawing moment.*

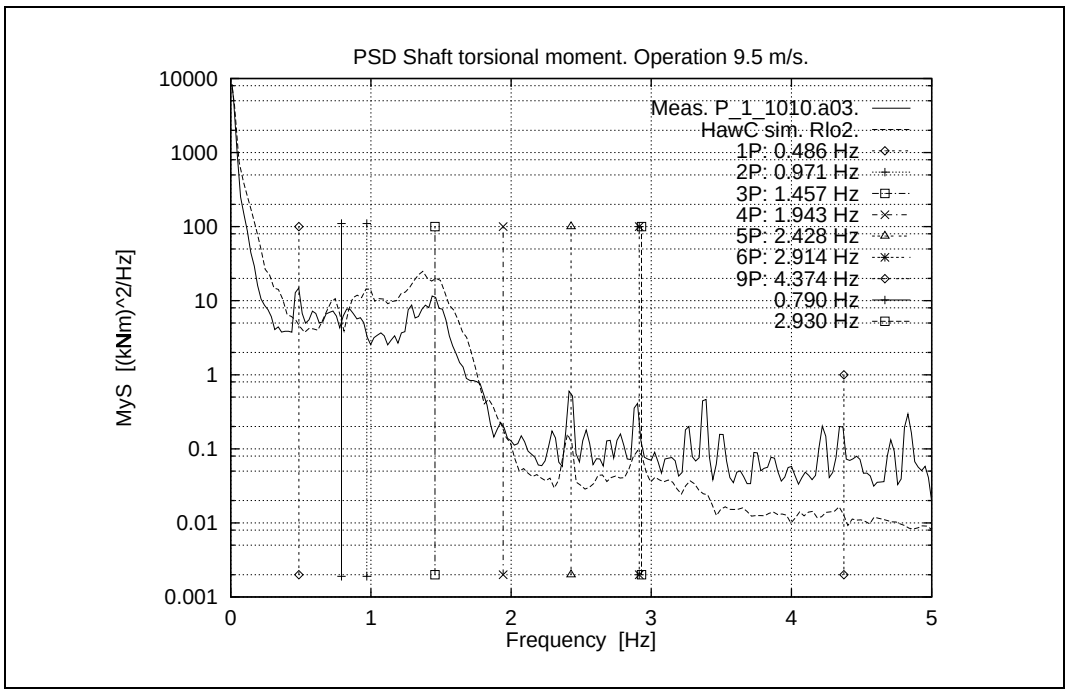


*Figure 7.15. Power spectral density of rotor torque.*

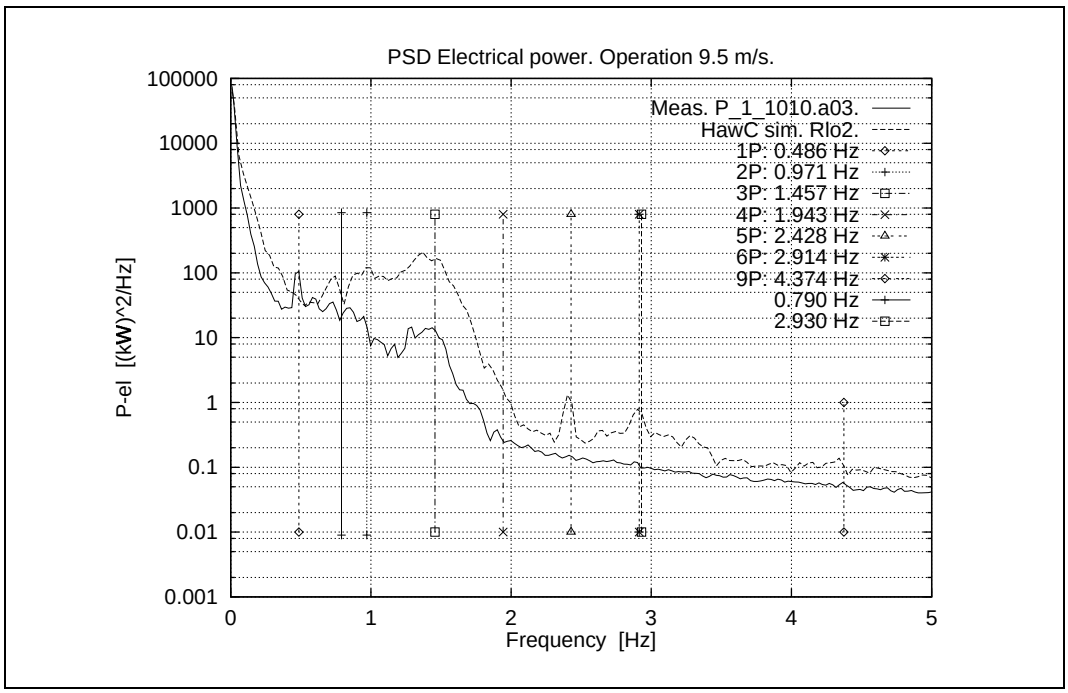


*Figure 7.16. Power spectral density of electrical power.*

## 7.4 Operation after stall onset, wind speed 23.2 m/s

The response during operation after stall onset is examined in this section. A case with mean wind speed 23.2 m/s is chosen. The turbulence intensity is 12.1%. Power spectra of the wind is shown in Figure 7.17. Here the agreement is good. The lack of energy in the simulation at the higher frequencies – as observed in the low wind speed case in Section 7.3, Figure 7.10 – is now shifted to frequencies above 2 Hz, outside the shown frequency range. The reason is that the along wind resolution in the simulated turbulence is more adequate at higher wind speeds.

The power spectra of the chosen response signals are shown in Figures 7.18-7.23. Again, the peaks corresponding to multiples of the rotational frequency, 1P = 0.486 Hz, and clearly identified peaks in the spectra are marked with vertical lines along the frequency axis. The most important observation from the spectra is the dominating influence from the edgewise blade vibration. This is also clearly seen in the time traces of the measured and the simulated edgewise moments in Figures 7.24 and 7.25, respectively. Severe edgewise vibrations are observed in both measurement and simulation.

Generally, good agreement between measurement and simulation is observed with respect to location of the peaks along the frequency axis. The simulation overestimates the response due to edgewise vibration, which is most clearly seen in the spectrum of the edgewise blade root moment in Figure 7.18. Adjustment of the structural damping in the model can result in almost perfect agreement between measurement and simulation. The influence of increasing the structural damping in the model with 1.0% logarithmic decrement is shown in Section 8.1. This results in reduction of energy at the dominating peaks below the measured energy levels.

From the spectra of rotor tilt and yaw moments in Figures 7.20 and 7.21, the characteristic $\pm$1P transformation of the edgewise frequency to the stationary coordinates – as described in Section 6.3 – is observed. This transformation of the edgewise frequency gives approximately 2.4 Hz and 3.4 Hz, respectively. The higher of these frequencies is close to the second backward rotor whirl frequency, which from Section 6.4 is found to be approximately 3.4 Hz. This indicates that the coupling between edgewise vibrations and the rotor whirl mode is significant. The calculation with increased shaft stiffness presented in Section 8.2 confirms this conclusion. The stiffness increase changes the frequencies of the whirl modes and reduces the edgewise blade vibration response by reducing the influence of the coupling.

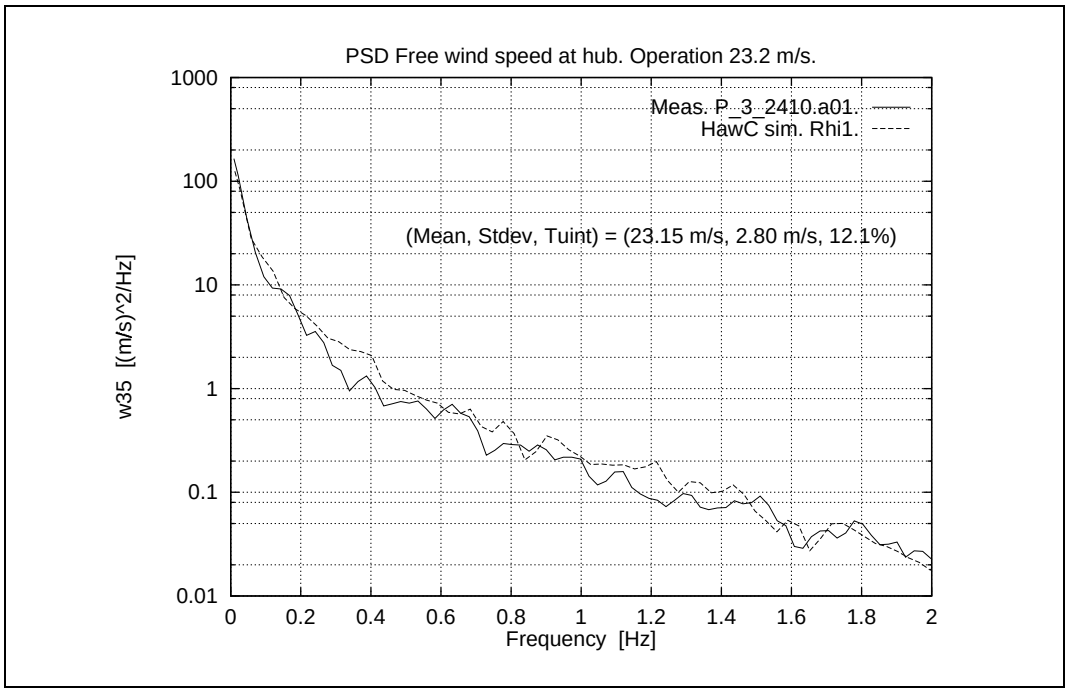


*Figure 7.17. Power spectral density of free wind speed at height 37 m.*

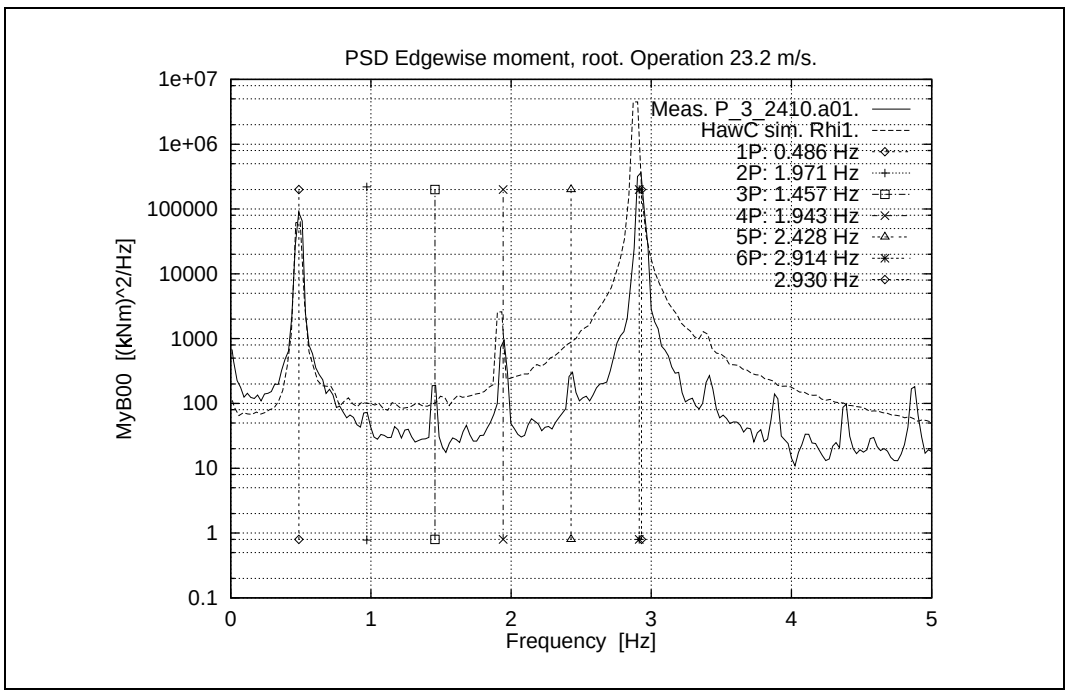


*Figure 7.18. Power spectral density of edgewise blade root bending moment.*

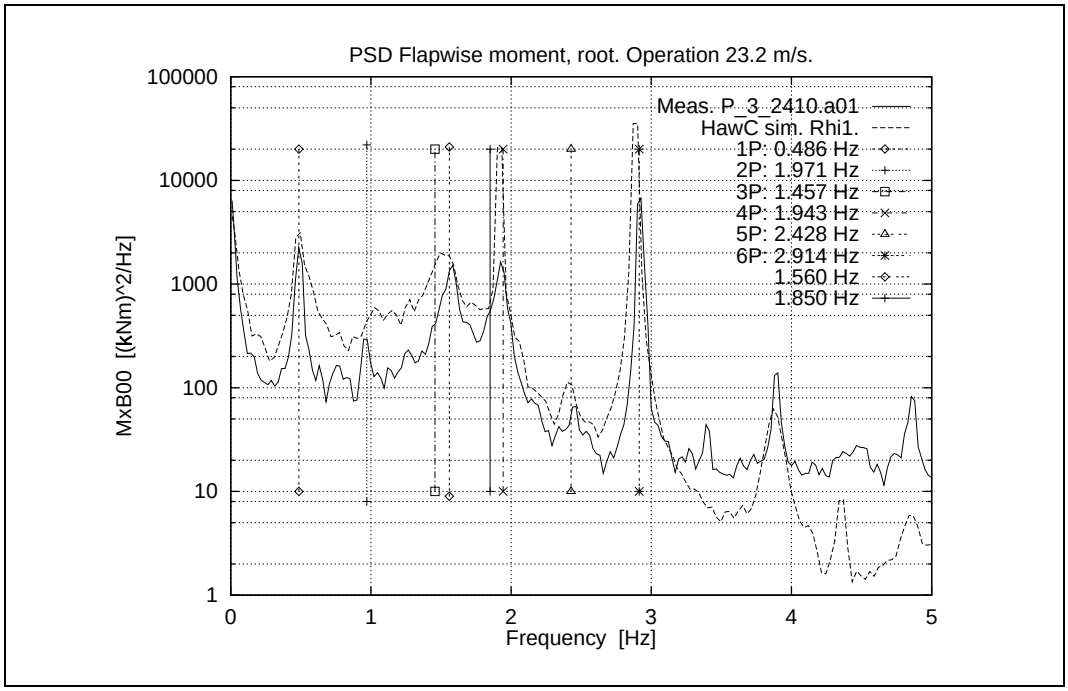


*Figure 7.19. Power spectral density of flapwise blade root bending moment.*

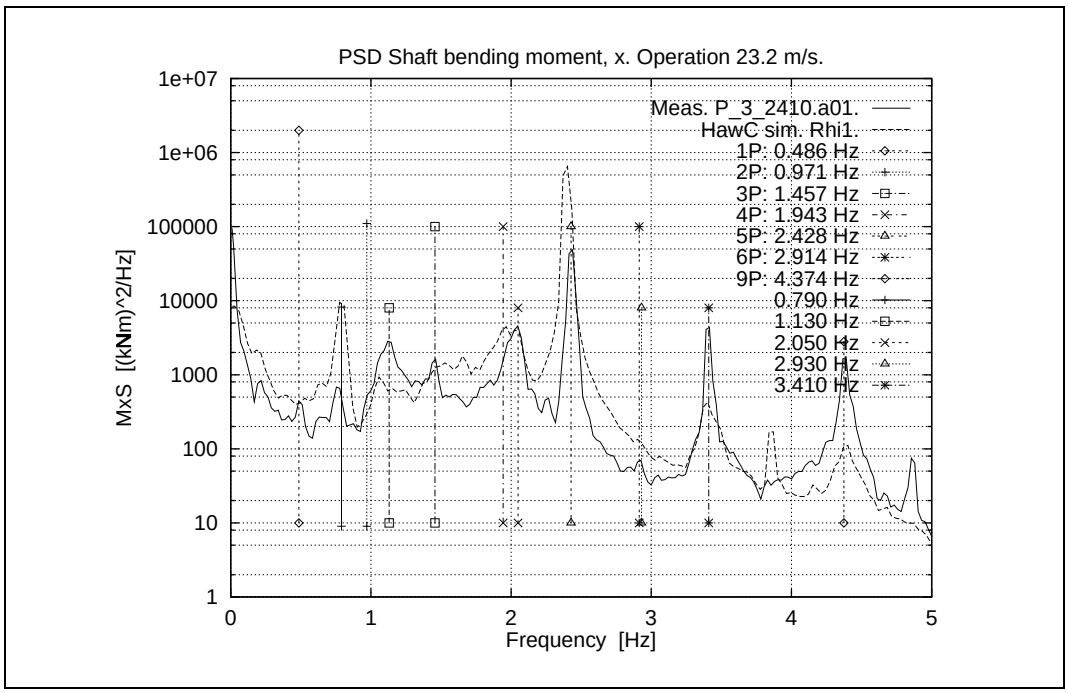


*Figure 7.20. Power spectral density of rotor tilting moment.*

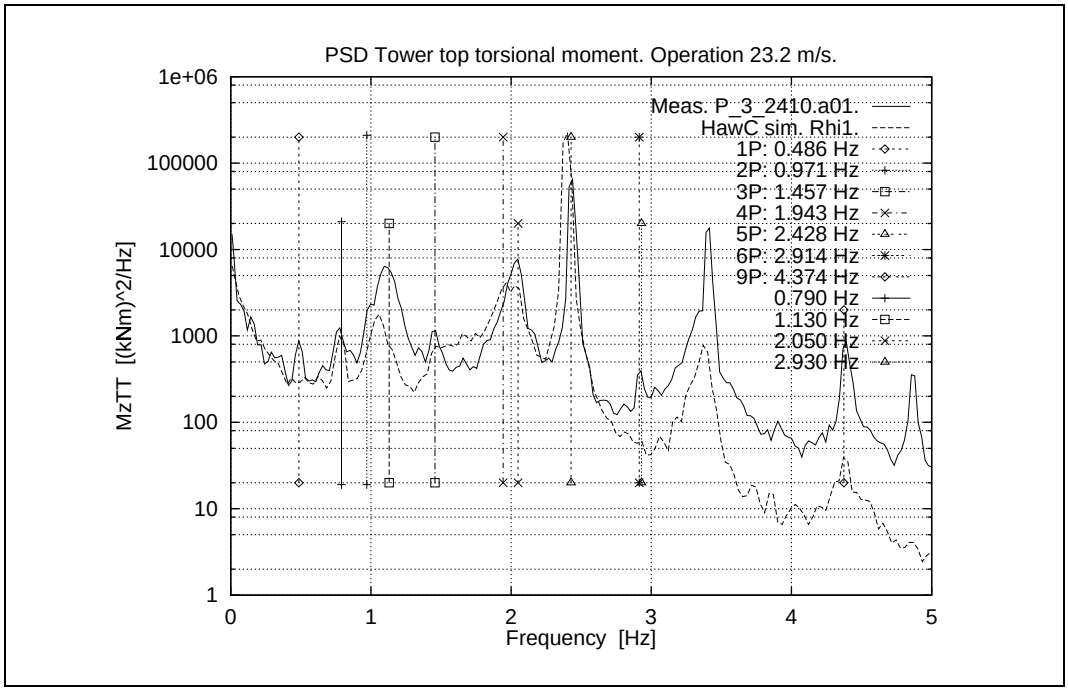


*Figure 7.21. Power spectral density of rotor yawing moment.*

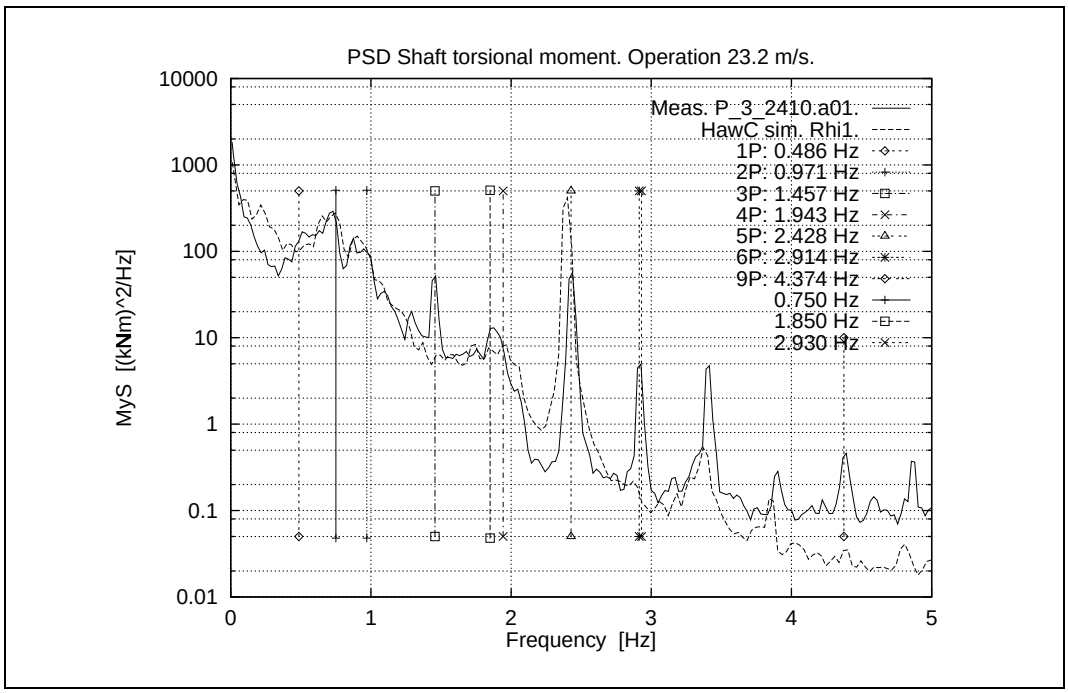


*Figure 7.22. Power spectral density of rotor torque.*

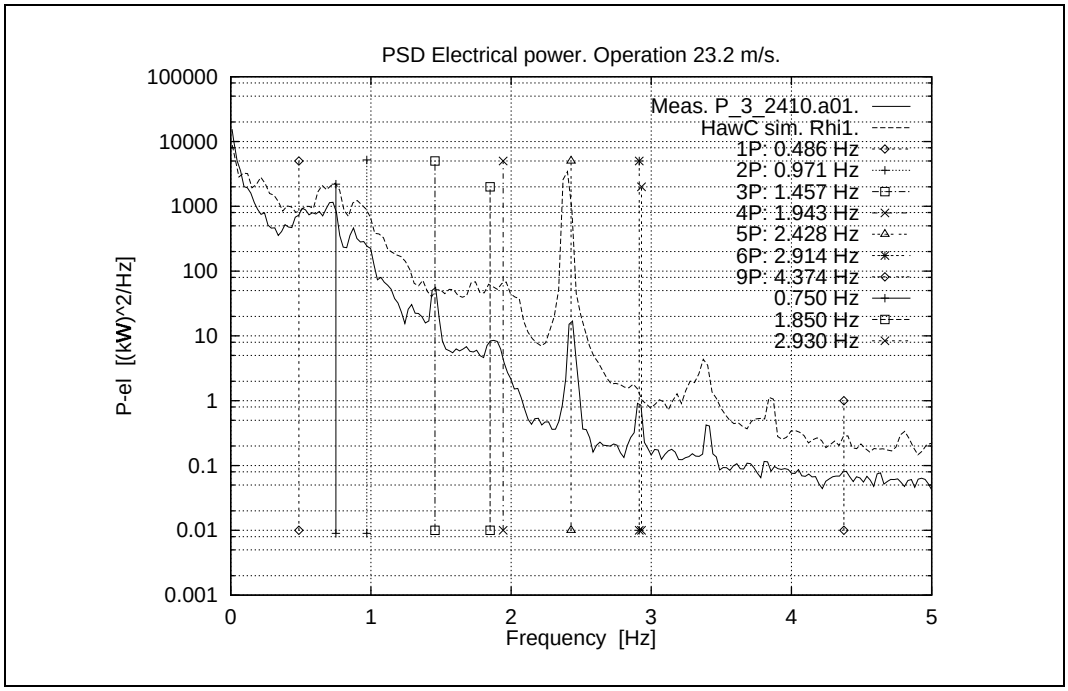


*Figure 7.23. Power spectral density of electrical power.*

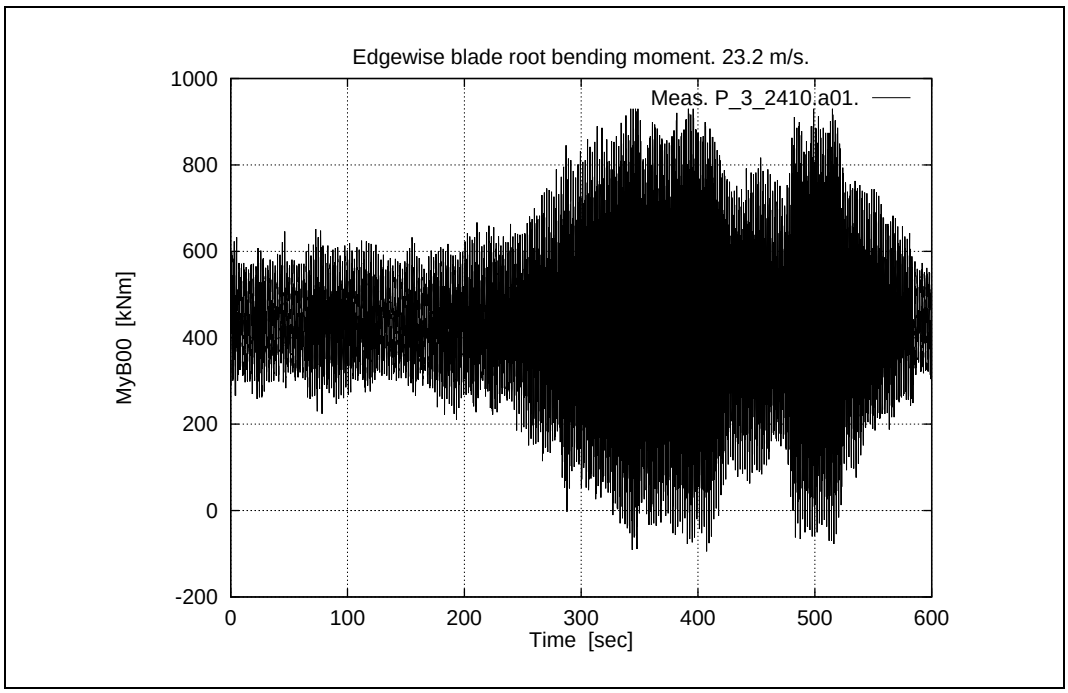


*Figure 7.24. Measured blade root edgewise bending moment.*

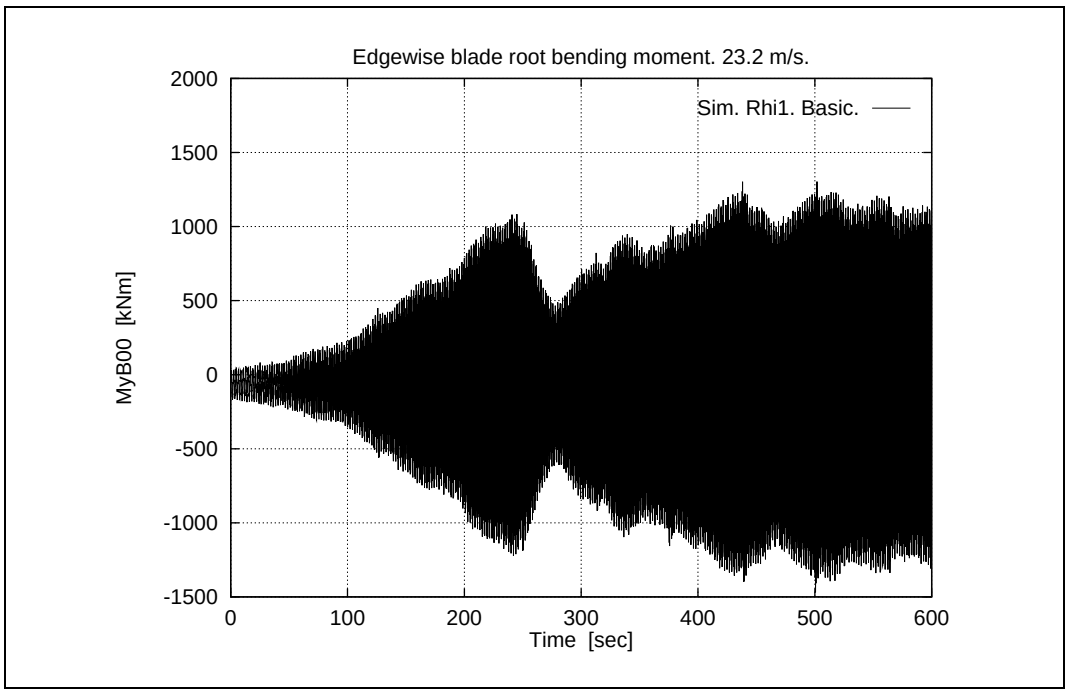


*Figure 7.25. Simulated blade root edgewise bending moment with basic shaft stiffness.*

# 8 Full scale parametric study

In order to illustrate the influence of selected structural parameters, which have proven to be of major importance for stall induced vibrations, simulations on the Bonus 500 kW turbine are carried out, with these parameters changed relative to the basic configuration presented in Sections 6 and 7. The wind speed is the same as for the case presented in Section 7.4, 23.2 m/s mean wind and 12.1% turbulence intensity.

Three cases are considered

1. Addition of 1.0% structural damping. Presented in Section 8.1, Figures 8.1-8.5.
2. Increase of shaft stiffness. Presented in Section 8.2, Figures 8.6-8.12.
3. Uniform structural pitch offset. Presented in Section 8.3, Figures 8.13-8.17.

The calculated power spectra of the moments listed in Table 7.1 are compared with the corresponding spectra of the measurements from the high wind case previously presented in Section 7.4. The three cases are commented next.

### 1. Addition of structural damping

Addition of 1.0% structural damping to totally 4.0% (logarithmic decrement) in the edgewise mode shape reduces the edgewise vibration significantly. The total damping in the edgewise mode is now close to zero, as indicated through the damping calculations presented in Section 7.1, Figure 7.3, and the unstable character of the edgewise vibration response observed in the original model (see Figure 7.25) has been changed to a stable character.

### 2. Increase of shaft stiffness

The increase of shaft stiffness changes the frequencies of the whirling modes, and the coupling between the edgewise vibration and these modes are much less pronounced than before the change. The effect on edgewise vibrations is comparable with the effect of increasing the damping, reported above. Time traces of the original measurement and the present simulation are shown in Figures 8.11 and 8.12, illustrating the now stable edgewise bending response. Tests performed by Bonus on a modified prototype turbine confirms that this tendency is true also for the real turbine. The stand still frequencies for the original turbine (case Rhi1) and the modified turbine (case Rhi3) are listed in Table 6.2.

### 3. Uniform structural pitch offset

A uniform structural pitch offset corresponding to a uniform change of vibration direction along the blade of $\Delta\theta_{RB} = -5.0°$ – refer to Section 2.1.3, Figure 2.9 – results in significant reduction of the edgewise blade vibration, again to a level which can be characterized as stable. This $-5°$ change is probably difficult to obtain with a standard blade, but even a smaller change, say $-2°$, which would be more realistic, will improve the damping conditions significantly.

### Conclusion

The conclusion drawn from the full scale aeroelastic studies is that calculation of absolute stability margin might be subject to significant uncertainty, probably the order of magnitude 1-2% logarithmic decrement, primarily due to uncertainty on structural damping and airfoil data. However, the full aeroelastic calculations are well suited to calculate the relative change of stability margin due to change of a wide range of design parameters.

## 8.1 Addition of structural damping

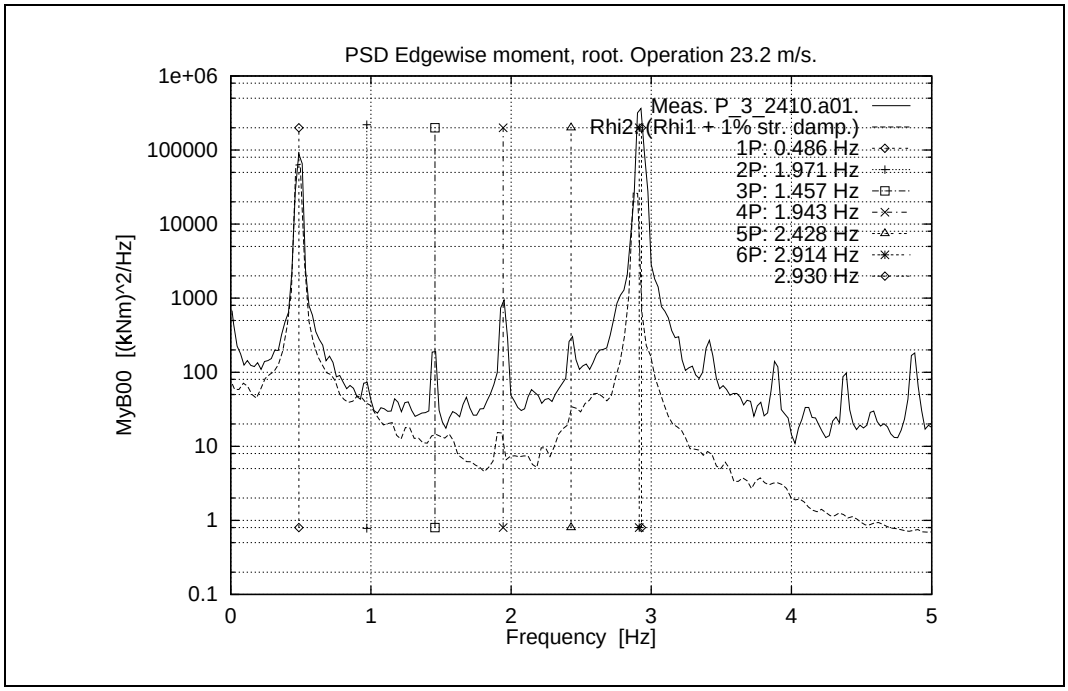


*Figure 8.1. Power spectrum of blade root edgewise moment.*

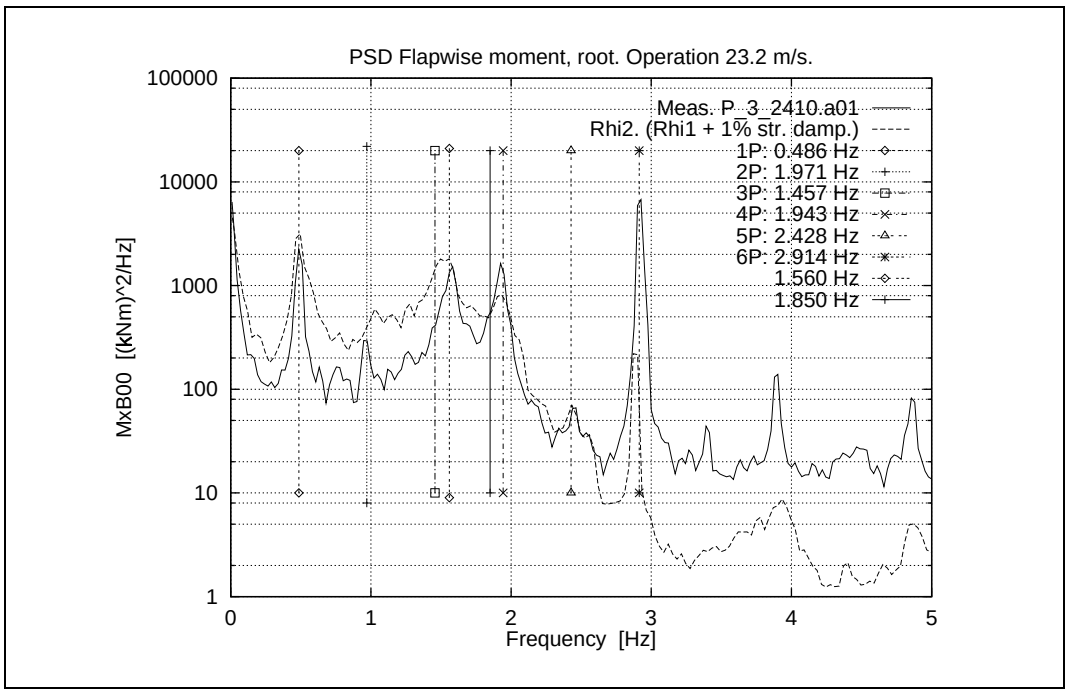


*Figure 8.2. Power spectrum of blade root flapwise moment.*

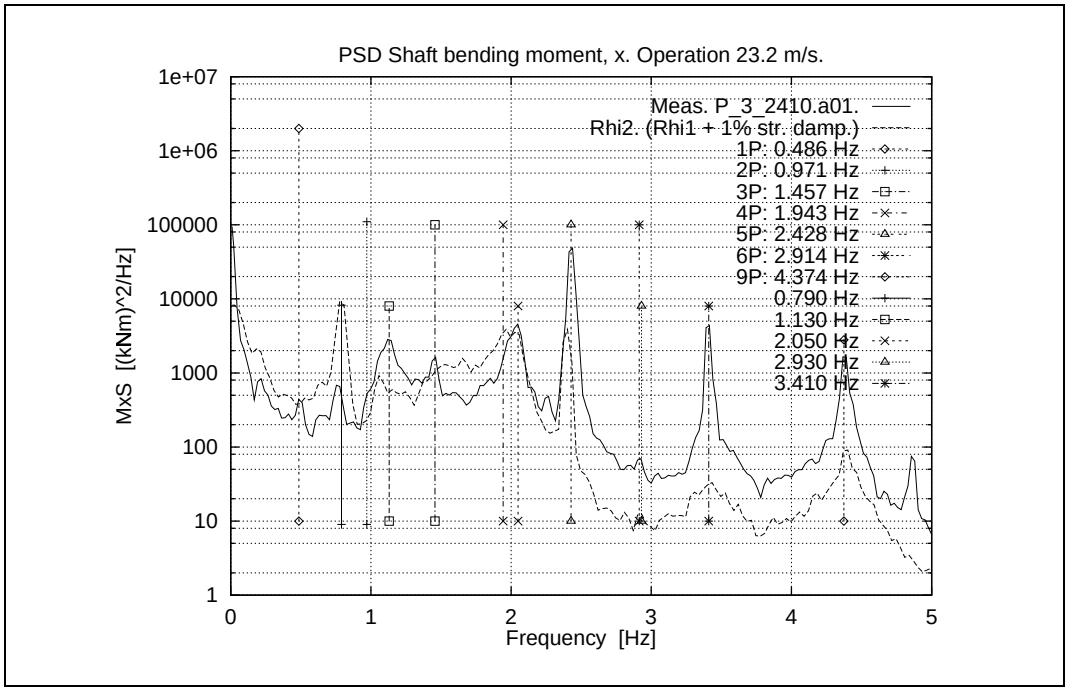


*Figure 8.3. Power spectrum of shaft tilting moment.*

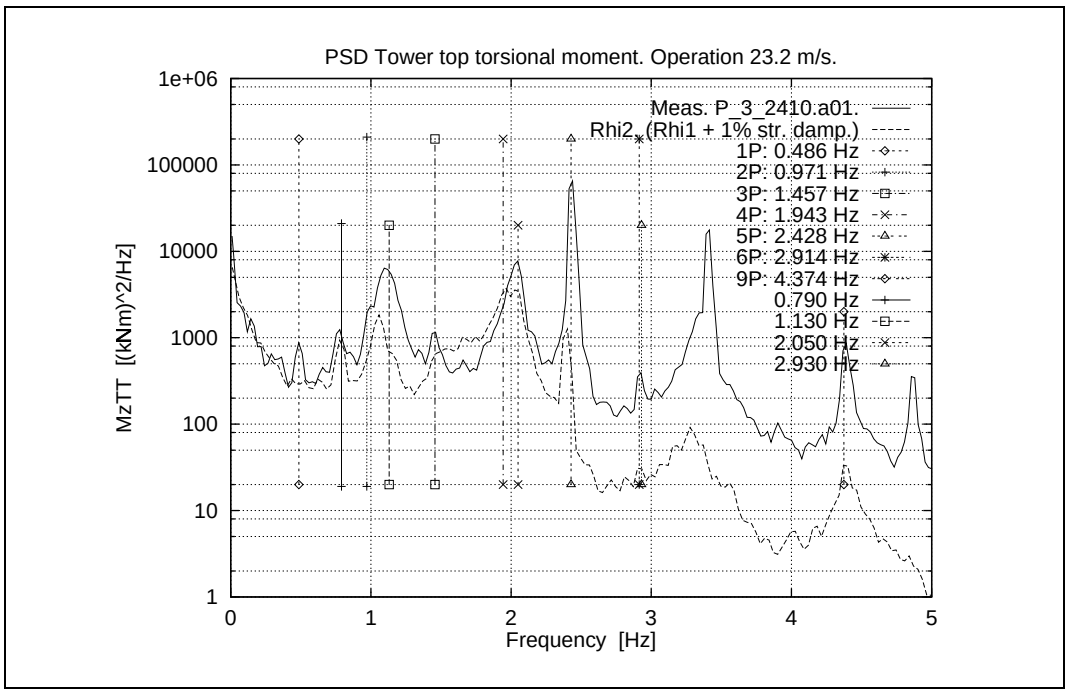


*Figure 8.4. Power spectrum of tower top yawing moment.*

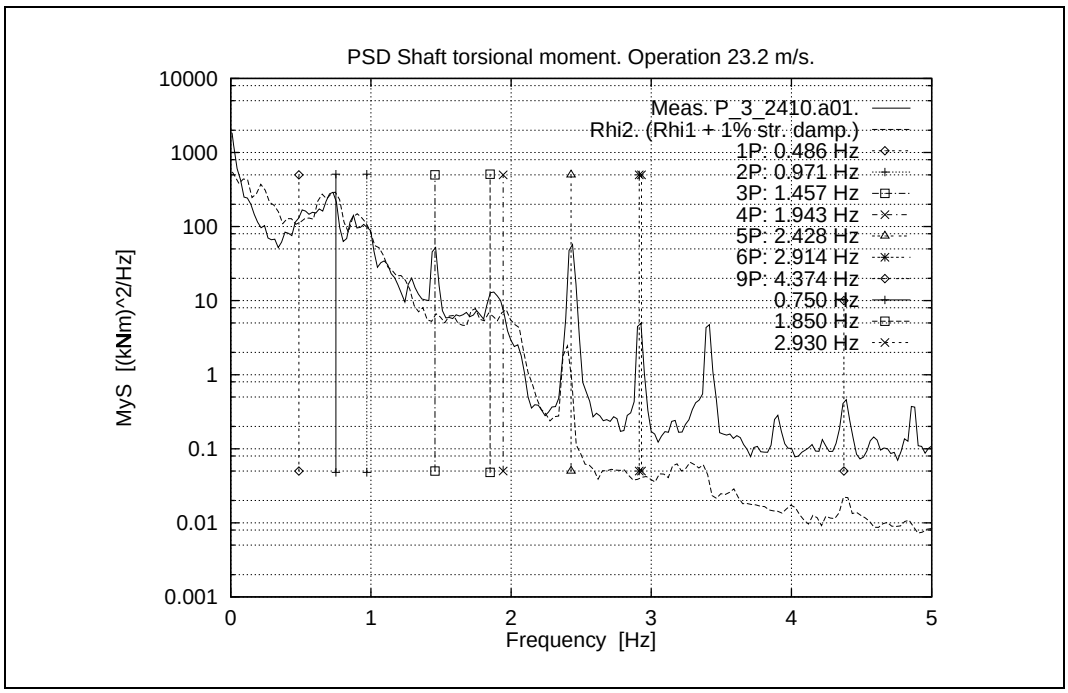


*Figure 8.5. Power spectrum of shaft torque.*

## 8.2 Increase of shaft stiffness

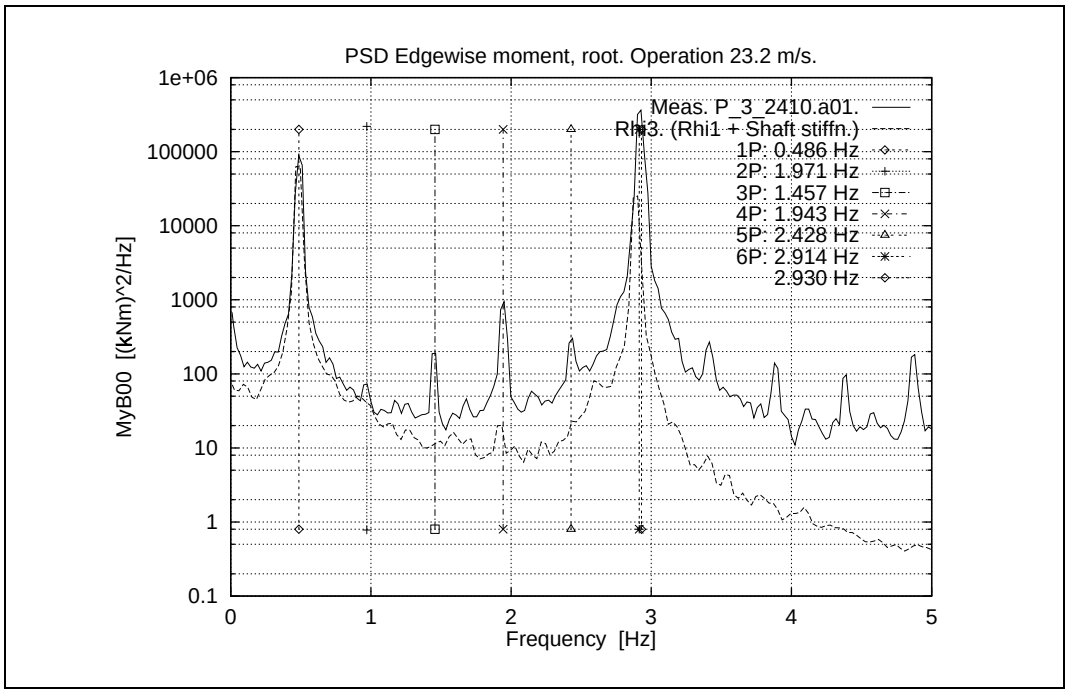


*Figure 8.6. Power spectrum of blade root edgewise moment.*

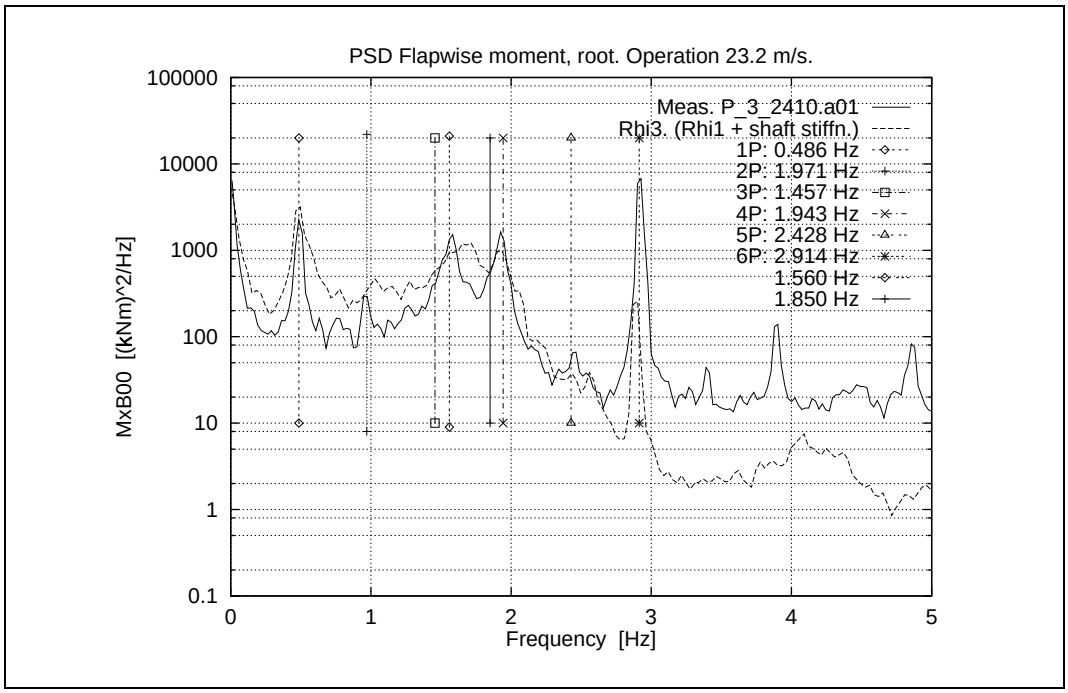


*Figure 8.7. Power spectrum of blade root flapwise moment.*

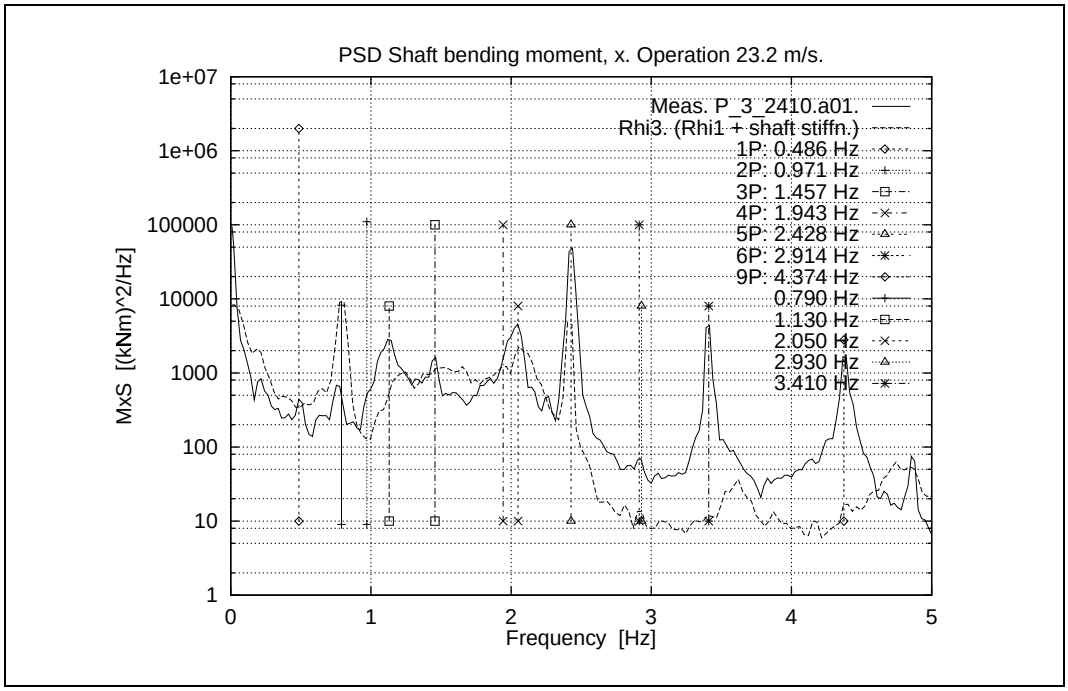


*Figure 8.8. Power spectrum of shaft tilting moment.*

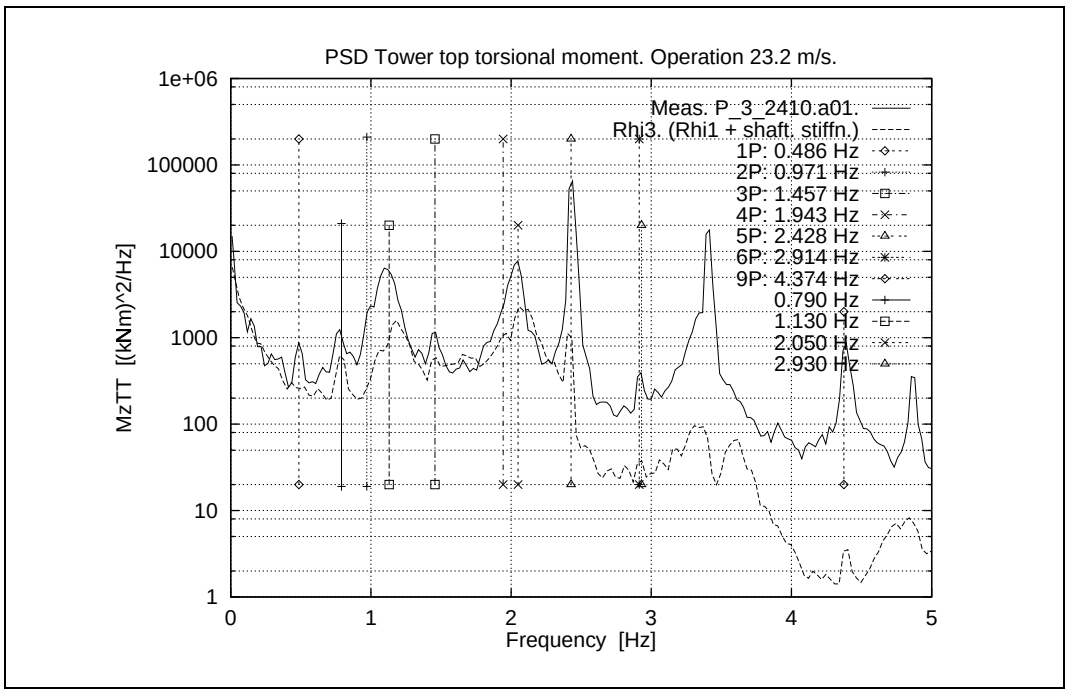


*Figure 8.9. Power spectrum of tower top yawing moment.*

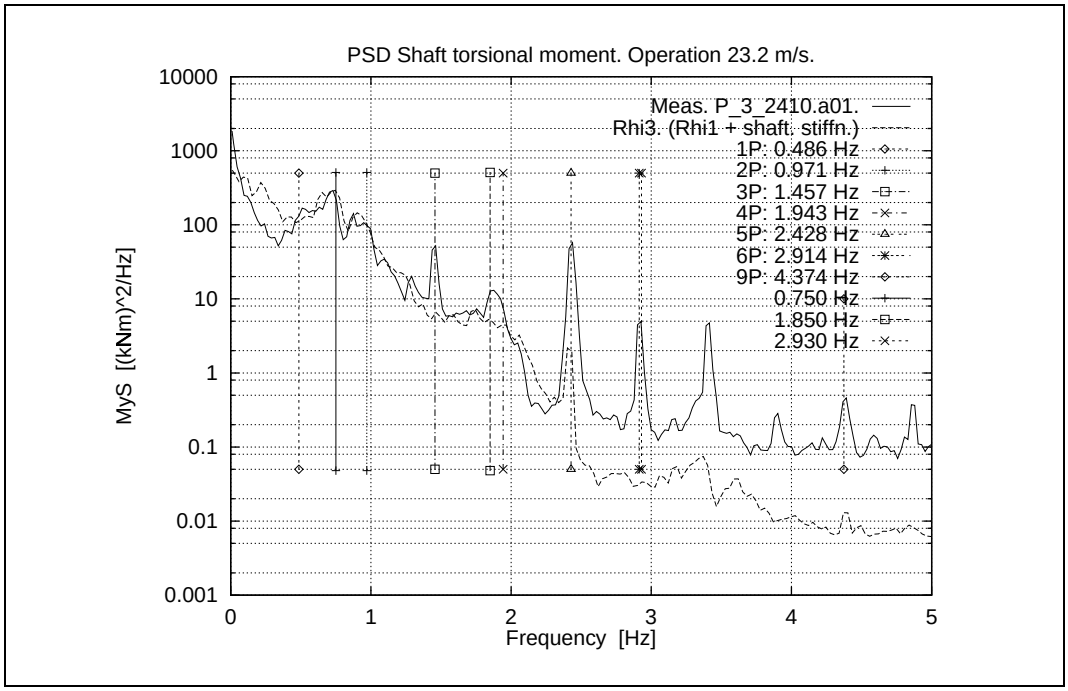


*Figure 8.10. Power spectrum of shaft torque.*

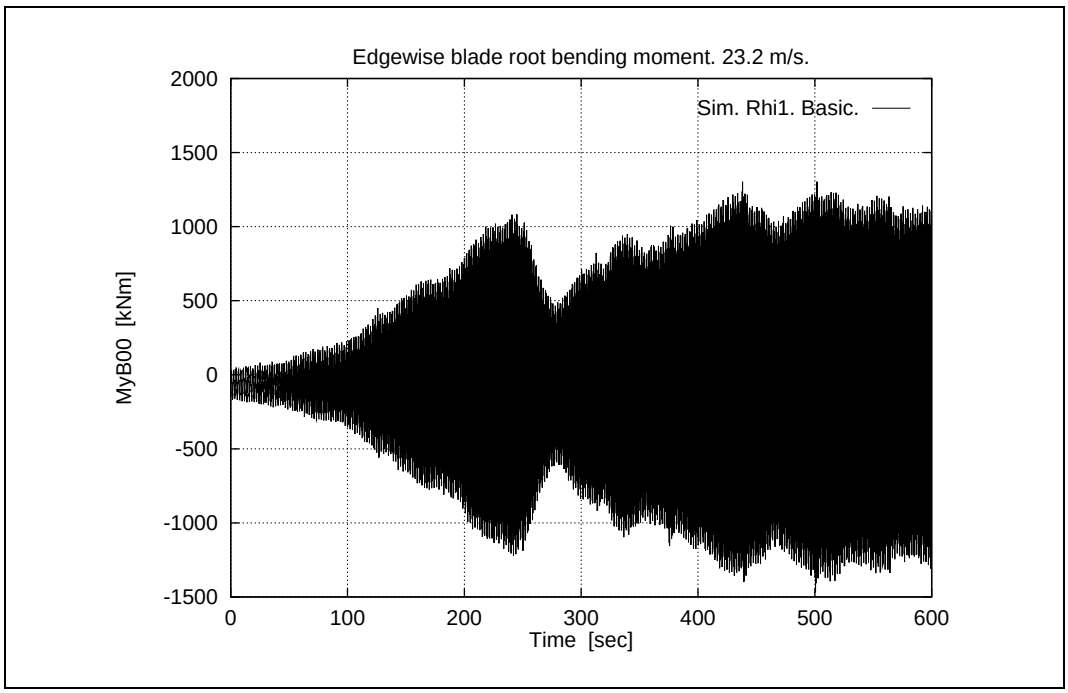


*Figure 8.11. Simulated blade root edgewise bending moment with basic shaft stiffness.*

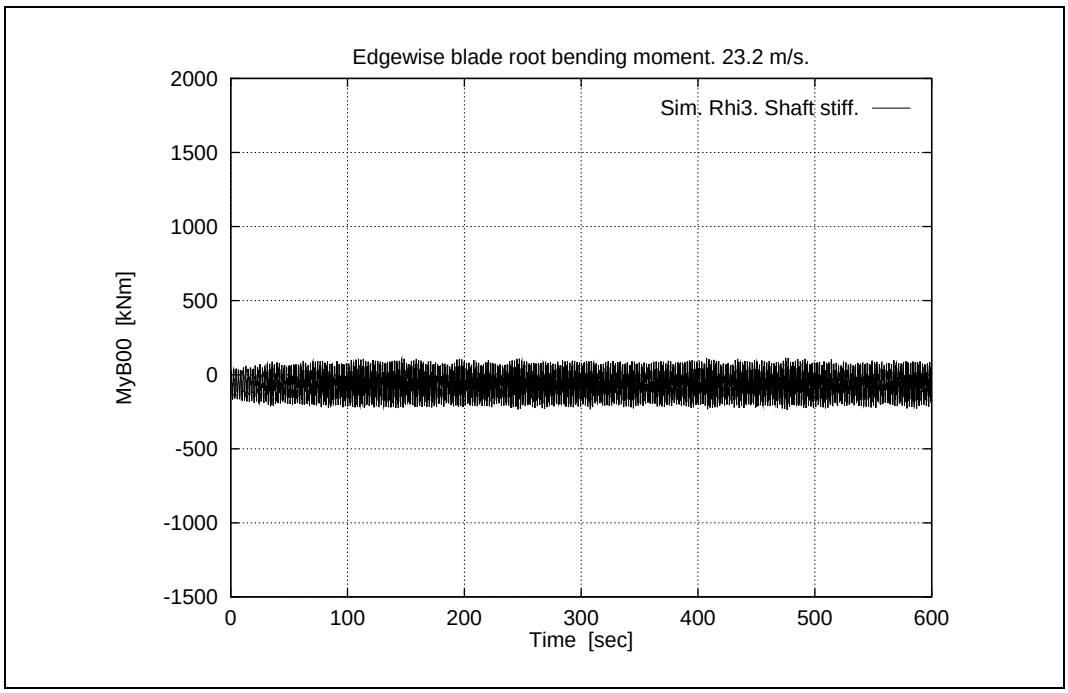


*Figure 8.12. Simulated blade root edgewise bending moment with increased shaft stiffness.*

## 8.3 Uniform structural pitch offset

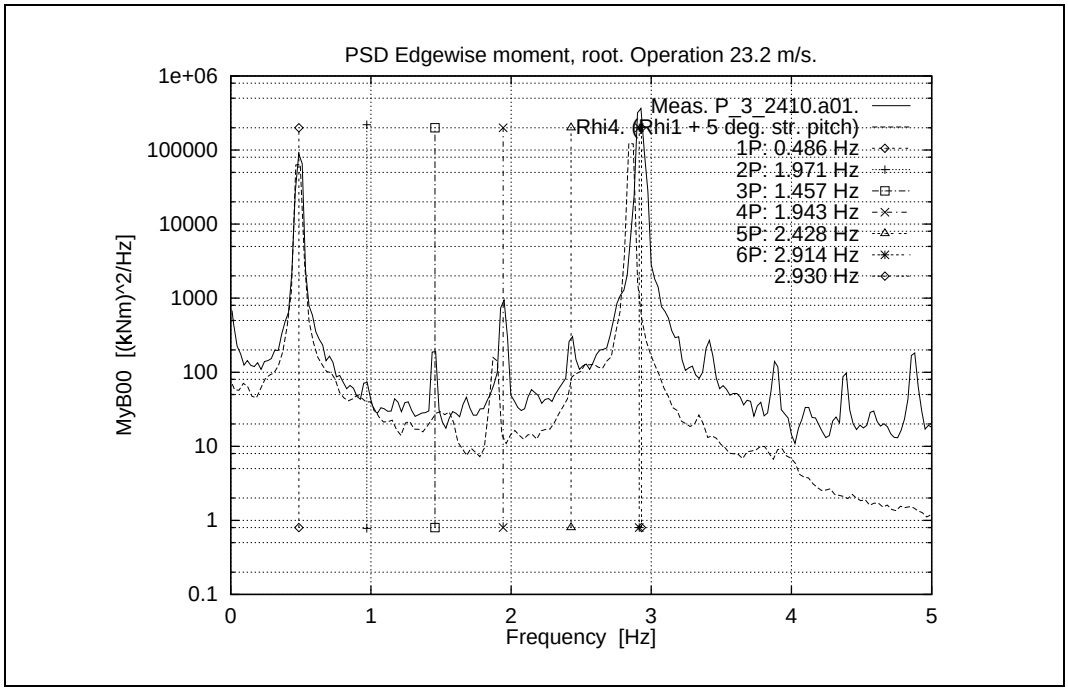


*Figure 8.13. Power spectrum of blade root edgewise moment.*

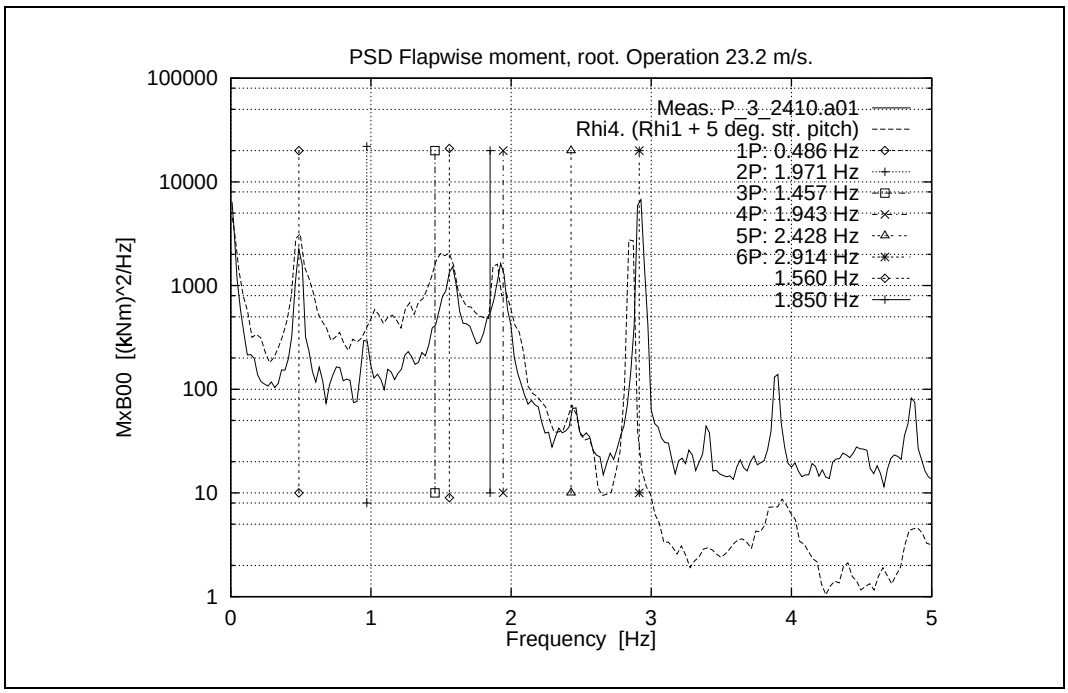


*Figure 8.14. Power spectrum of blade root flapwise moment.*

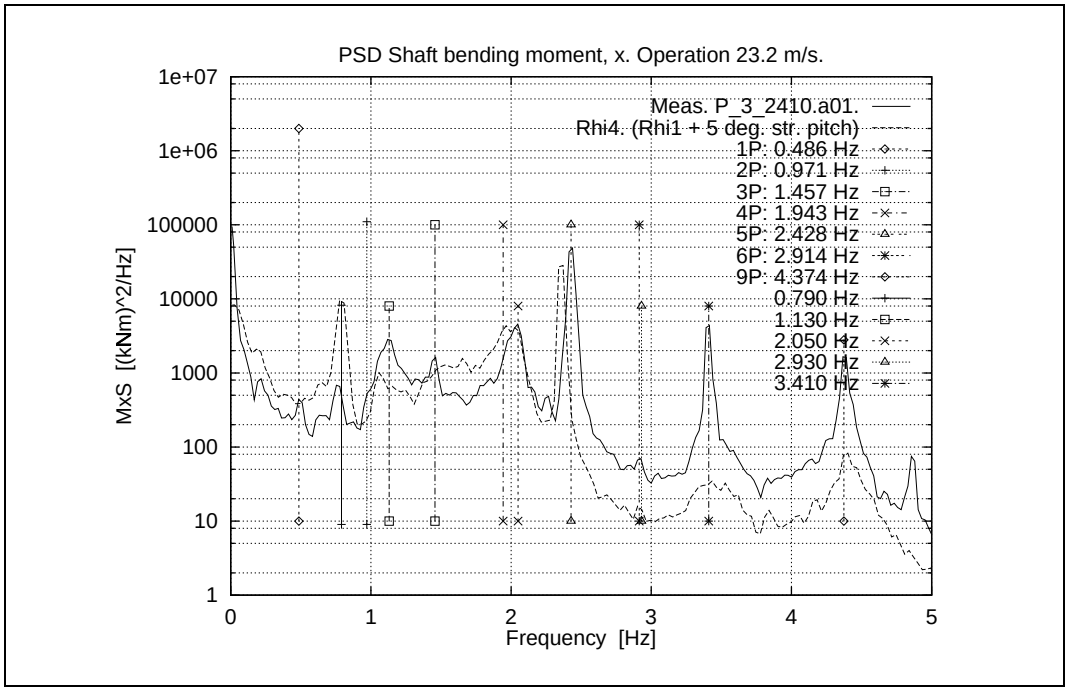


*Figure 8.15. Power spectrum of shaft tilting moment.*

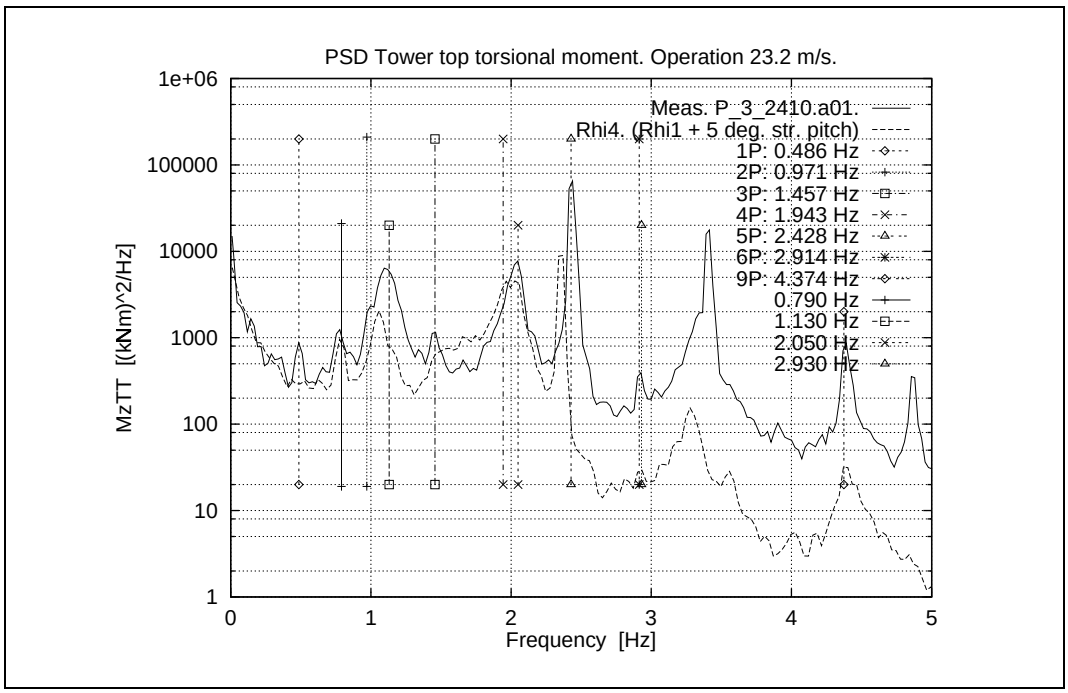


*Figure 8.16. Power spectrum of tower top yawing moment.*

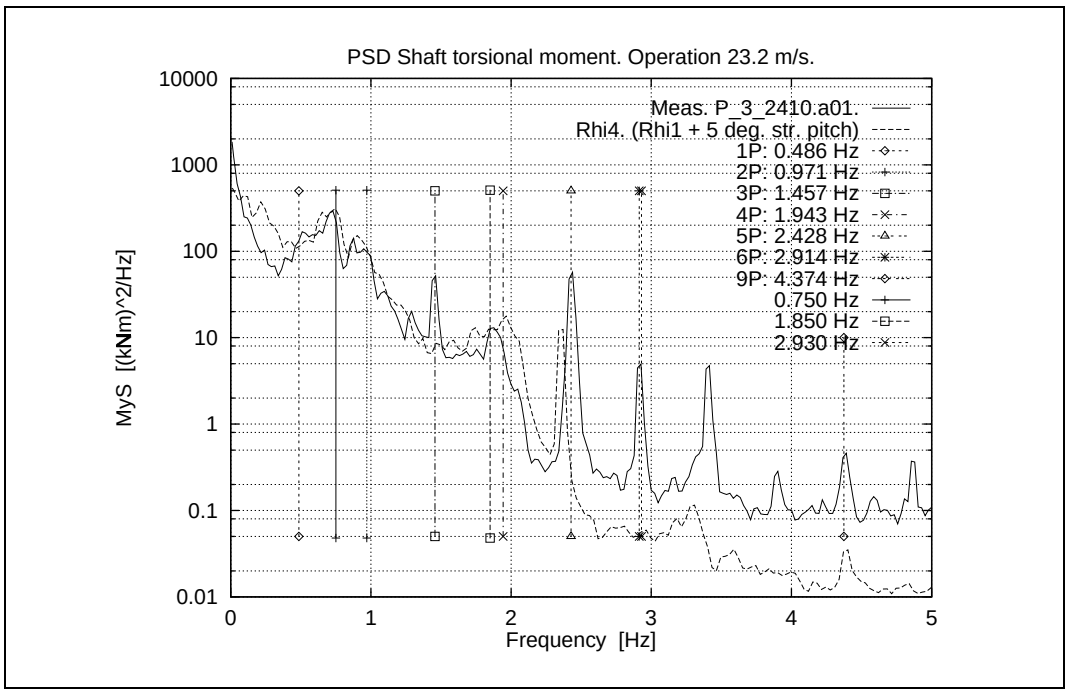


*Figure 8.17. Power spectrum of shaft torque.*

# 9 Design guidelines

The results from the investigations performed during the present work have been used for formulation of a set of design guidelines and recommendations, particularly aiming at supporting the design of wind turbines with an adequate safety margin against stall induced vibrations. The majority of guidelines and recommendations are general, but some are based on investigations on the typical European 3-bladed concept with fixed blades and rather stiff support of both individual blades and rotor, and these guidelines might therefore be specific to this turbine type.

The relevance of specific design guidelines depend on the actual design situation and in particular on the freedom the designer has with respect to choosing design parameters. For example, it could be the design of a new turbine, where a considerable freedom to choose design parameters should be expected. Or it could be a situation, where re-design of an existing turbine is considered, for instance due to detected problems with stall induced vibrations.

Initially, the general background is summarized and the main findings from the work are mentioned. Next, the guidelines covering the *new design* situation are listed and finally a few additional recommendations will be given with respect to *re-design*.

## 9.1 Summary of findings

Basically, the results confirm that the edgewise vibrations are caused by negative aerodynamic damping, i.e. energy supplied to the vibrating blade by the aerodynamic forces. It is shown that the occurrence of stall induced vibrations are controlled primarily by properties related to 4 principal areas, which influence partly the *aerodynamic damping*, partly the *structural damping* and partly the *properties* of the *complete structure* with respect to either damping or amplification of an existing edgewise vibration:

1. The *aerodynamic characteristics* of the blade, represented by the *quasi-steady* and the *dynamic* lift and drag coefficients.
2. The *structural characteristics* of the blade, which influence the mode shape and the natural frequency. Especially the orientation of the principal bending axes are of great importance, because the aerodynamic damping depends heavily on the resulting direction of the vibration.
3. The material and structural properties, which influence the *structural damping* of the blade.
4. The properties of the *supporting structure*, i.e. the main shaft, the nacelle and the tower. The rotor support participates in coupled mode shapes with the blades and influences the resulting blade movement and damping.

These main areas are commented next.

## 1: Aerodynamic characteristics

Within this area the most important design parameters are:

- The airfoil type and the associated characteristics,
- the variation of the airfoil type along the blade and
- the blade planform.

The present design guidelines impart a recommendation to the designer – which might be new compared with previous common design approaches – namely that the requirements on aerodynamic damping characteristics should be taken into account already when initiating the design of a new blade in parallel with requirements on rotor performance. The expressions for aerodynamic damping for a section as well as for the whole blade using quasi-steady aerodynamics are simple (Equations 2.16-2.19 and 2.40), and they can easily be programmed and computed. In fact, they are well suited to be used in a numerical optimization algorithm.

Results from examples in the present work suggest some recommendations with respect to choice of airfoil characteristics and distribution of properties along the blade. To minimize the negative aerodynamic damping low lift airfoils should be preferred on the outboard part of the blade in order to reduce the resulting contributions from negative lift curve slope, $\partial C_L/\partial\alpha$, to both flapwise and edgewise aerodynamic damping. However, in order to obtain a favourable power production and a slender blade, it might be desirable with high lift airfoils on the inboard part of the blade, e.g. obtained by vortex generators. This differentiation of outboard and inboard properties with respect to damping and power production is favourable due to different weighting along the blade of the local properties, when the integrated power and modal damping is determined. The weighting of the local damping is the actual mode shape squared. This means for instance that considerable negative damping, associated with high lift on the inner part of the blade, will contribute only marginally to the integrated damping for the blade. The more precise weighting of the properties can be obtained from the expressions in Section 2. The total power per blade, $P_b(V)$, is obtained from Equation 2.49, which integrates the power per unit length, $P_u(r,V)$, from Equation 2.20. The aerodynamic modal damping based on power and axial force per unit length is calculated from Equation 2.43.

Usually, a high camber is desirable in order to achieve a high lift coefficient at zero angle of attack, which makes it possible to obtain a more favourable vibration direction along the blade, thus reducing the negative damping in edgewise direction. Further, airfoil data with smooth stall characteristics are preferable in order to avoid local peaks in the damping characteristics as function of wind speed.

As can be noted from the expressions for aerodynamic damping the profile chord length scales the aerodynamic damping, meaning that a negative damping becomes more negative by increasing the chord and vice versa. This is contrary to the desires when regarding the influence from stiffness and structural damping, where generally a blade with large chord is wanted. By compromising and choosing a proper distribution along the blade some favourable solution should be looked for.

### 2+3: Structural characteristics of the blade

Within this area the most important design parameters are:

- The local structural pitch, $\theta_{RB}$, controlling the vibration direction and
- the modal mass and stiffness of the blade.

The local vibration direction or the structural pitch is a very important parameter for the damping. Due to structural design limits this parameter cannot be chosen arbitrarily, but it is important to aim at pitch values, which are favourable with respect to damping. Usually the structural pitch, $\theta_{RB}$, should be chosen as negative as possible. But as a change of vibration direction mainly redistributes the damping between edgewise and flapwise mode shapes, a proper damping of both the edgewise and flapwise vibrations must be considered.

With respect to mass and stiffness, the blade structure should be designed for the highest possible edgewise stiffness even at the expense of added weight. Blades with relatively large blade chords at the inner and middle part of the blade will have improved edgewise stability compared to more slender blades as a result of increased structural stiffness and damping in the edgewise direction. Yet, as mentioned above, the larger chord will scale the aerodynamic part of the damping in opposite direction. Some optimal radial distribution must be looked for.

### 4: Properties of the supporting structure

If any of the rotor yaw and/or tilt frequencies gets close to the frequency range of the edgewise natural frequency $\pm$1P, careful analysis of the dynamics of the complete turbine is needed in order to predict the damping properties of the edgewise blade vibrations, as significant coupling might take place.

The investigations in the present work of this coupling are specific to the typical European 3-bladed wind turbine concept. The conclusion from these investigations are that the stiffness of the rotor support in the tilt and yaw direction (resulting from bending stiffness of the shaft, nacelle frame stiffness, tower top torsion and bending stiffness) should be chosen as high as possible.

## 9.2 Proposed design sequence

### New design

Considering a *new design*, where a great deal of freedom to choose design variables can be expected, the formulated *design guidelines* are in brief:

1. Base the airfoil choice on well documented airfoil data.
2. Choose airfoils, blade planform (chord, aerodynamic twist) and blade structural properties (stiffness, mass, mode shapes – i.e. amplitude and direction of deformation, structural damping, modal mass, modal stiffness and modal natural frequency) considering not only the rotor performance, but also the aerodynamic damping characteristics. Especially, the blade twist should be considered, not only in relation to power performance, but also in relation to mode shape vibration direction.
3. Use the quasi-steady approach presented in Section 2 to calculate the basic aerodynamic damping characteristics for a single blade, considering both the fundamental flapwise and edgewise mode shapes. If not satisfactory – repeat from 2.

4. Extend the quasi-steady analysis and include verified models for dynamic stall on both airfoil lift and drag. Still considering a single blade. If not satisfactory repeat from 2.
5. When the single blade analysis results in appropriate aerodynamic damping, continue the analysis by use of the full aeroelastic model, including verified models for stall hysteresis on both airfoil lift and drag. The structural model must have a sufficiently detailed representation of the blade bending modes and the rotor whirling modes.
6. Carry out full aeroelastic calculations for the wind speeds of interest. These wind speeds can to a wide extent be identified through the single blade analysis.
7. Investigate the damping characteristics by looking at the response at the blade natural flapwise and edgewise frequencies, for instance based on the power spectral densities of the blade root bending moments.
8. Repeat from 2 if the results are unsatisfactory.

### Re-design

In the situation where the designer is dealing with *re-design* of an existing wind turbine, the possibilities are much more limited. Still, it will often be possible to achieve considerable improvement of the damping by modifying the existing design. Generally the scheme presented above should be applied. The *aerodynamic* properties can for instance be changed by modifying the airfoil characteristics by use of different aerodynamic devices, e.g. stall strips and vortex generators. In addition, it might be possible to change the *structural* properties in more favourable direction. For instance local mass and stiffness changes could be applied to change the relevant mode shapes and natural frequencies. Finally, the possibility of applying mechanical damping devices, either on the blades or on the supporting structure, should be mentioned. The purpose of such devices will be removal of the energy supplied by the aerodynamic forces – they will not influence the source of the problem.

# 10 Conclusions

The project work has covered a wide range of areas related to the main subject – stall induced vibrations.

- Engineering models for stall hysteresis, both on $C_L$ and $C_D$.
- Implementation of engineering models in aeroelastic codes.
- Theoretical analysis of the physics of the phenomenon stall induced vibrations and identification of the main parameters.
- Considering the vibration in two dimensions, meaning that the blade mode shapes are described as vectors covering both the edgewise and the flapwise components of the mode shapes.
- Examples of modification of the main parameters related to stall induced vibrations for an isolated blade.
- Full scale analysis including rotor dynamics.
- Comparison of aeroelastic calculations with measurements.
- Variation of parameters in the full aeroelastic calculations.
- Formulation of design guidelines based on the project tasks.

Basically, the results confirm that the edgewise vibrations are caused by negative aerodynamic damping, i.e. energy supplied to the vibrating blade by the aerodynamic forces. It is shown that the occurrence of stall induced vibrations are controlled primarily by properties related to 4 principal areas, which influence partly the aerodynamic damping, partly the structural damping and partly the properties of the complete structure with respect to either damping or amplification of an existing edgewise vibration:

1. The aerodynamic characteristics of the blade, represented by the quasi-steady and the dynamic lift and drag coefficients.
2. The structural characteristics of the blade, which influence the mode shape and the natural frequency. Especially the orientation of the principal bending axes are of great importance, because the aerodynamic damping depends heavily on the resulting direction of the vibration.
3. The material and structural properties, which influence the structural damping of the blade.
4. The properties of the *supporting structure*, i.e. the main shaft, the nacelle and the tower. The rotor support participates in coupled mode shapes with the blades and influences the resulting blade movement and damping.

By suitable choice of these properties it is possible to design a stall regulated wind turbine, which has an adequate safety margin against stall induced vibrations.

To obtain realistic calculation results with an aeroelastic code, it is important to represent the above mentioned properties adequately. The aerodynamic model should include dynamic stall on both $C_L$ and $C_D$, and the structural model should have a suitable representation of the mode shapes of importance for stall induced vibrations, i.e. the coupled blade bending modes and the rotor whirling modes.

The work in the project has confirmed that the present generation of aeroelastic codes can be used for choosing a wide range of the design parameters aiming at eliminating the risk for stall induced vibrations.

# 11 Acknowledgments

Many of the calculations carried out at Risø during the project have been performed by Kenneth Thomsen. We thank Kenneth for his substantial contribution to the work, and for the many inspiring discussions about rotor dynamics. Flemming Rasmussen's interest in this field has been very supporting through discussions of areas mostly on the limit of our knowledge. Flemming is thanked for his continuous support to the project.

# 12 References


[1] Madsen, H.Aa., Petersen, J.T, Bruining, A., Brand, A. and Graham. M. *Field Rotor Measurements. Data Sets Prepared for Analysis of Stall Hysteresis.* Risø report. Risø-R-1046(EN). Risø National Laboratory, Roskilde, Denmark. May 1998.

[2] Enevoldsen, P. *Measurements on BONUS 500 kW with LM-19.0 blades.* (In minutes Risø-I-1159, Risø National Laboratory, June 1997). BONUS Energy A/S. Brande, Denmark, June 1997.

[3] Enevoldsen, P. *Information for measurements on BONUS 500 kW with LM-19.0 blades.* (In minutes Risø-I-1284, Risø National Laboratory, May 1998). BONUS Energy A/S. Brande, Denmark, July 4, 1997.

[4] Enevoldsen, P. *Information for BONUS 500 kW with LM-19.0 blades.* (In minutes Risø-I-1284, Risø National Laboratory, May 1998). BONUS Energy A/S. Brande, Denmark, June 25, 1997.

[5] Petersen, J.T. *Kinematically Nonlinear Finite Element Model of a Horizontal Axis Wind Turbine.* Ph.D. thesis. Part 1 and 2. Risø National Laboratory. Roskilde, Denmark, July 1990.

[6] Petersen, J.T. *The Aeroelastic Code HawC – Model and Comparisons.* In proceedings of *State of the Art of Aeroelastic Codes for Wind Turbine Calculations.* $28^{th}$ Meeting of Experts, International Energy Agency, Annex XI. Editor B. Maribo Pedersen, Technical University of Denmark. Lyngby, April 11-12 1996, pp. 129-135.

[7] Rasmussen, F., Peteresen, J.T., Winkelaar, D. and Rawlinson-Smith, R. *Response of Stall Regulated Wind Turbines – Stall Induced Vibrations.* Final report for Joule I Project, Contract no. JOUR-0076, DG XII. Report Risø-R-691(EN). Risø National Laboratory, June 1993.

[8] Björck, A. *Dynamic Stall and Three-dimensional Effects.* Final report for EC DGXII JOULE II Project, Contract no. JOU2-CT93-0345. Report FFA TN 1995-31. The Aeronautical Research Institute of Sweden, January 1996.

[9] Hoffmann, M.J. et al. *Unsteady Aerodynamic Performance of Wind Turbine Airfoil.* Presented at American Wind Energy Association Wind Power 94 Conference, Minneapolis, Minnesota, May 9-13, 1994.

[10] Øye, S. *Dynamic Stall Simulated as a Time Lag of Separation.* In proceedings of $4^{th}$ IEA Symposium on Aerodynamics of Wind Turbines. Edited by K.F. McAnulty, ETSU-N-118. Rome, 1991.

[11] Øye, S. *A Revised Dynamic Stall Model*. AFM Report 95-06. Department of Fluid Mechanics, Technical University of Denmark. November 1995.

[12] Leishman, J.G. and Beddoes, T.S. *A Generalised Model for Unsteady Airfoil Behaviour and Dynamic Stall Using the Indicial Method.* Presented at the $42^{nd}$ Annual Forum of the American Helicopter Society, Washington D.C. June 1986.

[13] Winkelaar, D. *Application of a Version of the ONERA Model – Comparison with Measured Dynamic Stall Data.* ECN-C-95-062, Netherlands Energy Research Foundation ECN, June 1995.

[14] Rasmussen, F. *Dynamic Stall of a Wind Turbine Blade Section.* Proceedings (edited by B. Maribo Petersen) of the $8^{th}$ IEA Joint Action Symposium on Aerodynamics of Wind Turbines, held at DTU, Lyngby, November 21-22, 1994.

[15] Rasmussen, F., Petersen, J.T. and Madsen, H.Aa. *Response Predictions by Application of a New Dynamic Stall Model.* Proceedings of the 1996 European Union Wind Energy Conference, Göteborg, Sweden, May 20-24, 1996. Pp. 838-842.

[17] Petersen, J.T. and Madsen, H.Aa. Prediction of Dynamic Loads and Induced Vibrations in Stall. Minutes of the $2^{nd}$ Plenary Meeting held at Delft University, Delft, The Netherlands, September $26^{th}$-$27^{th}$, 1996. Risø-I-1092(EN), Risø National Laboratory, December 1996.

[18] Ericsson, L.E. *Is Any Free Flight/Wind Tunnel Equivalence Concept Valid for Unsteady Viscous Flow.* Paper 85-0378 at the AIAA $23^{rd}$ Aerospace Sciences Meeting, Reno, January 14-17 1985.

[19] Fuglsang, P., Antoniou, I., Bak, C. and Madsen H.Aa. *Wind Tunnel Test of the Risø-1 Airfoil.* Risø report, Risø-R-999(EN), Risø National Laboratory, February 1998.

[20] Clough, R.W. and Penzien, J. *Dynamics of Structures.* McGraw-Hill, Inc. New York, 1975.

[21] Björck, A. *The FFA Dynamic Stall Model. The Beddoes-Leishman Dynamic Stall Model Modified for Lead-Lag Oscillations.* In proceedings of $10^{th}$ IEA Symposium on Aerodynamics of Wind Turbines. Edinburgh, December 16-17, 1997. Editor B. Maribo Pedersen, DTU, Denmark.

[22] Petersen, J.T., Thomsen, K. and Madsen, H.Aa. *Stall Strips Can Control Edgewise Vibrations.* Risø Fact-Sheet AED-RB-6(EN). Risø National Laboratory, April 1998.

[23] Rasmussen, F., Petersen, J.T. and Madsen, H.Aa. *Dynamic Stall and Aerodynamic Damping.* Paper no. AIAA-98-0024. Contribution to $17^{th}$ ASME Wind Energy Symposium held at the $36^{th}$ Aerospace Sciences Meeting and Exhibit, Reno, NV, USA, January 12-15, 1998.

[24] Petersen, J.T. and Madsen, H.Aa. Prediction of Dynamic Loads and Induced Vibrations in Stall. Minutes of the $5^{th}$ Plenary Meeting held at Imperial College, London, UK, November $27^{th}$-$28^{th}$, 1997. Risø-I-1284(EN), Risø National Laboratory, May 1998.

[25] Madsen, H.Aa. *Aerodynamics of a Horizontal-Axis Wind Turbine in Natural Conditions.* Risø report. Risø-M-2903. Risø National Laboratory, Roskilde, Denmark. September 1991.

# A Fundamental modal equations and damping

For a one-dimensional distributed-parameter structure, the equation of motion per unit length for deformation in the transversal plane is formulated by

$$\left[m^R(r)\right]\left\{\ddot{u}^R(r,t)\right\} + \left[c^R(r)\right]\left\{\dot{u}^R(r,t)\right\} + \left[k^R(r)\right]\left\{u^R(r,t)\right\} = \left\{f^R(r,t)\right\} \tag{A.1}$$

where the $[\dot{}]$-operator expresses differentiation with respect to time and

$\left\{u^R\right\}$ is the deformation vector in the transversal-plane,

$t$ is the time,

$\left[m^R(r)\right]$ is the mass matrix per unit length,

$\left[c^R(r)\right]$ is the damping matrix – structural and aerodynamic damping contributions – per unit length,

$\left[k^R(r)\right]$ is the stiffness matrix per unit length and

$\left\{f^R(r,t)\right\}$ is the external force vector per unit length.

The mode-shapes and the natural frequencies for the undamped structure are obtained by solution of the eigenvalue problem described by the homogeneous Equation A.1 with the damping neglected and by substituting harmonic solutions for the deformation

$$\left\{u^R(r,t)\right\} = \left\{\varphi_n^R(r)\right\}\cos(\omega_n t)\ . \tag{A.2}$$

This results in the eigenvalue problem

$$-\omega_n^2\left[m^R(r)\right]\left\{\varphi_n^R(r)\right\} + \left[k^R(r)\right]\left\{\varphi_n^R(r)\right\} = \{0\}\ . \tag{A.3}$$

The solution of this eigenvalue problem gives the mode-shapes, $\left\{\varphi_n^R\right\}$, and the natural frequencies, $\omega_n$.

The modal mass is defined by

$$M_n = \int_0^R \left\{\varphi_n^R(r)\right\}^T\left[m^R(r)\right]\left\{\varphi_n^R(r)\right\}\mathrm{d}r\ , \tag{A.4}$$

the modal damping coefficient by

$$C_n = \int_0^R \left\{\varphi_n^R(r)\right\}^T\left[c^R(r)\right]\left\{\varphi_n^R(r)\right\}\mathrm{d}r\ , \tag{A.5}$$

and the modal stiffness by

$$K_n = \int_0^R \left\{\varphi_n^R(r)\right\}^T\left[k^R(r)\right]\left\{\varphi_n^R(r)\right\}\mathrm{d}r\ . \tag{A.6}$$

Above the upper index $T$ denotes transposition.

The mode-shapes are orthogonal with respect to the mass matrix in the sense that

$$\int_0^R \left\{\varphi_m^R(r)\right\}^T \left[m^R(r)\right] \left\{\varphi_n^R(r)\right\} \mathrm{d}r = \begin{cases} M_n & \text{for } m = n \\ 0 & \text{for } m \neq n \end{cases} , \tag{A.7}$$

and with respect to the stiffness matrix, expressed by

$$\int_0^R \left\{\varphi_m^R(r)\right\}^T \left[k^R(r)\right] \left\{\varphi_n^R(r)\right\} \mathrm{d}r = \begin{cases} M_n\omega_n^2 & \text{for } m = n \\ 0 & \text{for } m \neq n \end{cases} . \tag{A.8}$$

The resolution of the deformation vector $\left\{u^R(r,t)\right\}$ in mode-shapes and normal coordinates is expressed by

$$\left\{u^R(r,t)\right\} = \left[\varphi^R(r)\right] \left\{q^R(t)\right\} , \tag{A.9}$$

or alternatively by

$$\left\{u^R(r,t)\right\} = \sum_{n=1}^{N} \left\{\varphi_n^R(r)\right\} q_n^R(t) . \tag{A.10}$$

It is here assumed that the mode shapes are included from number 1 to number $N$. In Equation A.9 the mode-shapes are arranged as the $N$ columns in the modal matrix $[\varphi(r)]$ and the normal coordinates $q_n^R$ as the $N$ components of the normal-coordinate vector $\left\{q^R\right\}$. In Equation A.10 the matrix product is written as a sum.

For use in numerical calculations a discrete version of Equation A.5 is often used. The integral is calculated as a sum of contributions from $M$ radial sections of finite length

$$C_n = \sum_{i=1}^{M} \left\{\varphi_{n,i}^R\right\}^T \left[c_i^R\right] \left\{\varphi_{n,i}^R\right\} \Delta r_i , \tag{A.11}$$

where index $i$ refers to the radial element number $i$, and $\Delta r_i$ is the length of the discrete element number $i$.

The modal damping per unit length for the continuous description is the integrand in Equation A.5

$$c_n(r) = \left\{\varphi_n^R(r)\right\}^T \left[c^R(r)\right] \left\{\varphi_n^R(r)\right\} , \tag{A.12}$$

and for the discrete version the terms of the sum

$$c_{n,i} = \left\{\varphi_{n,i}^R\right\}^T \left[c_i^R\right] \left\{\varphi_{n,i}^R\right\} . \tag{A.13}$$

## A.1 Logarithmic decrement

The modal damping expressed as logarithmic decrement is defined through

$$\begin{aligned} \delta_n &= \ln \frac{q_n(t)}{q_n(t+T_n)} \\ &= \frac{2\pi\zeta_n}{\sqrt{1-\zeta_n^2}} , \end{aligned} \tag{A.14}$$

where $T_n$ is the period of the damped vibration, and $\zeta_n$ is the damping ratio

$$\zeta_n = \frac{C_n}{2M_n\omega_n} . \tag{A.15}$$

Substituting the frequency in Hz for the frequency in radians per second, $f_n = 2\pi\omega_n$, gives the logarithmic decrement expressed by the modal damping, the modal mass and the frequency

$$\begin{aligned} \delta_n &= \frac{C_n}{\sqrt{4M_n^2 f_n^2 - C_n^2/(2\pi)^2}} \\ &\simeq \frac{C_n}{2M_n f_n} \quad \text{for } C_n \ll 1 . \end{aligned} \tag{A.16}$$

The logarithmic decrement per unit length for the continuous version is defined through

$$\begin{aligned} \delta_n(r) &= \frac{c_n(r)}{\sqrt{4M_n^2 f_n^2 - c_n^2(r)/(2\pi)^2}} \\ &\simeq \frac{c_n(r)}{2M_n f_n} \quad \text{for } c_n(r) \ll 1 , \end{aligned} \tag{A.17}$$

and for the discrete case by

$$\begin{aligned} \delta_{n,i} &= \frac{c_{n,i}}{\sqrt{4M_n^2 f_n^2 - c_{n,i}^2/(2\pi)^2}} \\ &\simeq \frac{c_{n,i}}{2M_n f_n} \quad \text{for } c_{n,i} \ll 1 . \end{aligned} \tag{A.18}$$

## A.2 Damping derived from work per cycle

Often we base the derivation of aerodynamic damping on nonlinear models for aerodynamic force, and in this case the damping coefficient can not be derived explicitly. Instead we use an expression based on the work performed by the aerodynamic force during one cycle of a harmonic deformation.

From the theory for forced excitation of a one degree of freedom system [20] the work per cycle, $W_a$, at damped resonance can be related to the damping coefficient, $C_a$, by

$$C_a = \frac{W_a}{\pi \omega q_0^2} \,, \tag{A.19}$$

where $q_0$ is the amplitude of the harmonic deformation expressed by

$$u(t) = q_0 \cos(\omega t) \,, \tag{A.20}$$

and $\omega$ is the angular frequency of the cyclic deformation corresponding to resonance, where maximum dynamic amplification is present. If the damping is linear viscous, the force needed to maintain the vibration will be harmonic as well. At this resonance the force and the deformation is 90° out of phase, and the force is expressed by

$$F(t) = F_0 \cos(\omega t + \frac{\pi}{2}) \tag{A.21}$$

leading the deformation.

For this system the work can be calculated as the area of the ellipse obtained by plotting the deformation as function of the force

$$W_a = \pi q_0 F_0 \,. \tag{A.22}$$

In our case the aerodynamic force is not necessarily harmonic, but the expression in Equation A.19 can still be applied if we define an equivalent force amplitude for a harmonic force, such that the work performed by the true force equals the work performed by the equivalent force. The obtained damping coefficient is then an equivalent viscous damping coefficient.

The work performed by the aerodynamic force on a blade in mode shape number $n$ with only transverse, harmonic blade deformation

$$\left\{u_n^R(r,t)\right\} = \left\{\varphi_n^R(r)\right\} q_{n0} \cos(\omega_n t) \,, \tag{A.23}$$

is calculated in two steps. First we calculate the work per cycle and per unit length as the average work of $M$ full cycles by integrating the scalar product of the force and the velocity vector

$$w_{an}(r) = \frac{1}{M} \int_{t=0}^{MT_n} \left\{F_{an}^R(r,t)\right\}^T \left\{\dot{u}_n^R(r,t)\right\} \mathrm{d}t \,, \tag{A.24}$$

where

$\{F_{an}^R\}$ is the aerodynamic force per unit length,

$\{\dot{u}_n^R\}$ is the local transverse velocity, and

$T_n = \frac{2\pi}{\omega_n}$ is the period of the vibration.

The work for the whole blade is obtained by integrating along the blade span

$$W_{an} = \int_{r=0}^{R} w_{an}(r)\mathrm{d}r \ , \tag{A.25}$$

where $R$ is the blade radius.

Numerical integrations are carried out by using the discrete versions of Equations A.24 and A.25 giving the work per unit length at radial station $i$

$$w_{an,i} = \frac{1}{M} \sum_{j=1}^{MN} \left\{F_{an,ij}^R\right\}^T \left\{\dot{u}_{n,ij}^R\right\} \Delta t_j \ , \tag{A.26}$$

with $N$ time steps per cycle of length $\Delta t_j$ and the total work

$$W_{an} = \sum_{i=1}^{S} w_{an,i} \Delta r_i \ . \tag{A.27}$$

We get the equivalent damping coefficient of the aerodynamic force in mode $n$ by using $W_{an}$ from Equation A.27 and corresponding modal amplitude and angular frequency in Equation A.19

$$C_{an} = \frac{W_{an}}{\pi \omega_n q_{n0}^2} \ . \tag{A.28}$$

Finally, by substituting this damping coefficient in Equation A.16 we arrive at the logarithmic decrement – here assuming small damping

$$\delta_n \simeq \frac{W_{an}}{M_n \omega_n^2 q_{n0}^2} = \frac{W_{an}}{4\pi^2 M_n f_n^2 q_{n0}^2} \ . \tag{A.29}$$

Equivalently we get the logarithmic decrement per unit length, e.g. for the discrete version, by using $w_{an,i}$ from Equation A.26 and Equations A.19 and A.18

$$\delta_{n,i} \simeq \frac{w_{an,i}}{M_n \omega_n^2 q_{n0}^2} = \frac{w_{an,i}}{4\pi^2 M_n f_n^2 q_{n0}^2} \ . \tag{A.30}$$

# B Global rotor whirl

The investigation of stall induced edgewise blade vibrations for a three bladed wind turbine reveals that the coupled modes of the turbine might be of great importance for developing and sustaining the vibrations. During the vibration the local rotor modes, which involve the two basic edgewise blade bending modes described in Section 6 for a three bladed turbine as modes 7 and 8, give rise to an in-plane harmonic inertia force with the blade edgewise natural frequency, $\omega_e$. This force might excite the global rotor whirl modes, when the excitation frequency of the edgewise vibration is close to one of the global rotor whirl frequencies. To provide some further insight in this phenomenon the global rotor whirl modes are described in the present section by use of a simple wind turbine model with only four degrees of freedom (DOFs) roughly corresponding to tilt and yaw rotations at the tower top and at the main bearing. In this model the shaft, the hub and the blades are considered infinitely stiff, and the rotor moves as a rigid body. For a real turbine the flexibility of the shaft, the hub and the blades modify these modes significantly, but the simple model represents the basic behaviour of the global rotor whirl modes with good approximation.

The global rotor whirl modes are related to the $1^{st}$ and $2^{nd}$ rotor yaw and tilt modes as identified at stand still for the three bladed example turbine in Section 6.2 and listed in Table 6.2 as modes 4, 5, 9 and 10. The present simplified model aims at describing these modes and how they depend on the rotational speed of the rotor, $\Omega$.

The simple 4-DOF model is illustrated in Figure B.1.

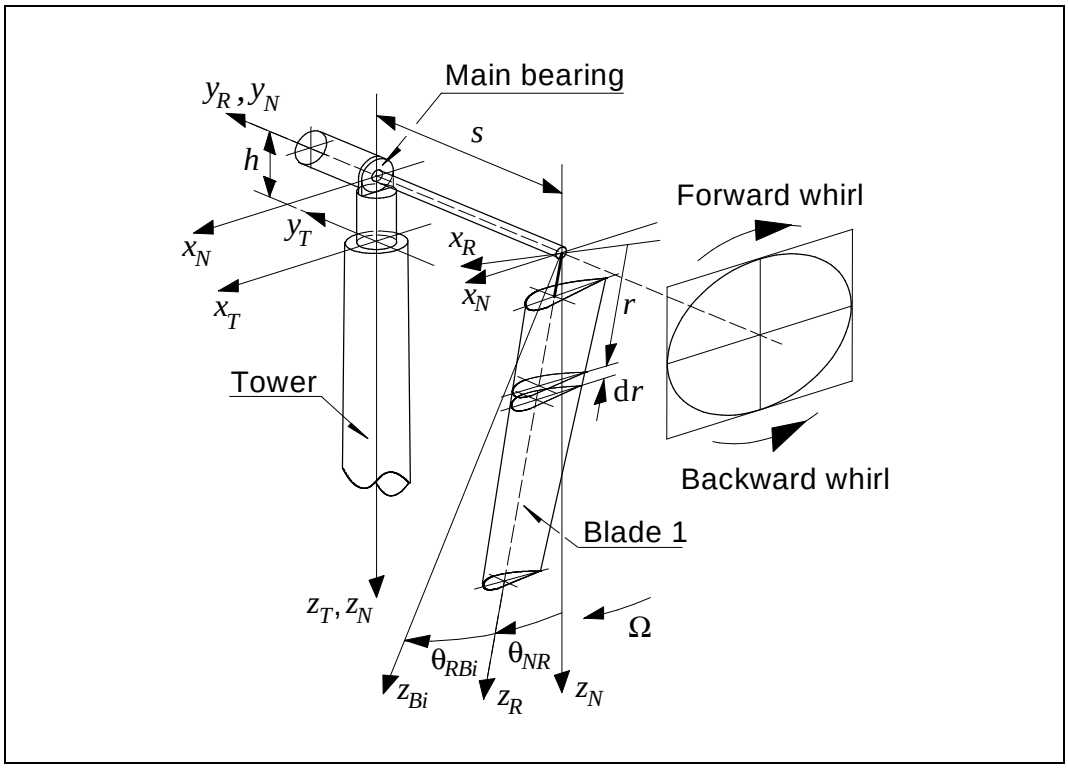


*Figure B.1. Simple 4-DOF model of wind turbine.*

The model considers only the influence of the tower through the rotations in the tilt and the yaw directions at the tower top, i.e. the rotation $\theta_{xT}$ about the $x_T$-axis and the rotation $\theta_{zT}$ about the $z_T$-axis, respectively. A concentrated mass moment of inertia, $I_T$, representing the

tower and the nacelle is assigned to these DOFs. The corresponding rotational stiffnesses belonging to these DOFs are denoted $k_{xT}$ and $k_{zT}$, respectively. The remaining two degrees of freedom represent the elastic rotations in the tilt and yaw directions of the main bearing, $\theta_{xN}$ and $\theta_{zN}$, about the axes $x_N$ and $z_N$, respectively. The corresponding rotational stiffnesses are denoted $k_{xN}$ and $k_{zN}$, respectively. No concentrated mass moment of inertia is assigned to these bearing rotations, as the inertia is assumed small compared to the mass moment of inertia of the rotor. Thus, all the deformations take place in a stationary frame of reference, and the equations of motion can be derived without the periodic azimuthal dependency. This approximation might be rather rude for a real turbine, because the deformations of the shaft, the hub and the blades usually have a significant influence on the considered vibration modes. However, the model is well suited for the purpose of illustrating the basic behaviour of the global rotor whirl modes, which we have in mind.

The sign of the rotations are chosen according to a right-hand screw convention, meaning that the sign is positive, when the equivalent rotation of a right-hand screw moves it in the positive direction of the actual coordinate axis.

In summary, the model degrees of freedom are:

1. $\theta_{xT}$, rotation about the tower top $x_T$-axis, corresponding to rotor tilt rotation.
2. $\theta_{zT}$, rotation about the tower top $z_T$-axis, corresponding to rotor yaw rotation.
3. $\theta_{xN}$, rotation about the bearing $x_N$-axis, corresponding to rotor tilt rotation.
4. $\theta_{zN}$, rotation about the bearing $z_N$-axis, corresponding to rotor yaw rotation.

The deformations are assumed small, so that the rotations can be added as vectors, and the total rotations of the rotor $y_R$-axis, which coincides with the rotor shaft, become:

$$\theta_{xS} = \theta_{xT} + \theta_{xN} \tag{B.1}$$

and

$$\theta_{zS} = \theta_{zT} + \theta_{zN} \ . \tag{B.2}$$

This four DOF system has four natural frequencies, and the corresponding mode shapes are characterized by the phase of the rotations. For instance, the phase of the rotations for the two mode shapes, which involve tiltwise rotation, are

1. $\theta_{xT}$ and $\theta_{xN}$ in *phase* and
2. $\theta_{xT}$ and $\theta_{xN}$ in *counter-phase.*

The mode with the rotations in phase has the lower frequency of the two.

The next step in establishing the model is the derivation of the equations of motion for the turbine with the rotor rotating with constant angular velocity, $\Omega$. The most important part of this task is the derivation of the inertia forces on the rotor, which finally provides us with the mass matrix and the gyroscopic matrix. We go through the details of this derivation. We apply Newton's method for calculation of the inertia force on an infinitesimal mass element at radius $r$ on a blade, e.g. blade number $i$:

$$\mathrm{d}m = m\,(r, \theta_{RBi})\,\mathrm{d}r \ , \tag{B.3}$$

where

$m(r, \theta_{RBi})$ is the mass per unit length at radius $r$ for blade number $i$ and

$\theta_{RBi}$ is the angular position in the rotor plane of blade number $i$, measured from the $z_R$-axis of the $(x_R, y_R, z_R)$-coordinate system, which is fixed in the rotor, with the $z_R$-axis coinciding with the axis of blade 1, $z_{B1}$.

The mass element is shown in Figure B.1.

The acceleration is derived as the second derivative with respect to time of the position vector to the mass element. Assuming that the distance between the origin of the $T$-coordinate system and the origin of the $N$-coordinate system – denoted $h$ in Figure B.1 – is zero, the position in stationary $T$-coordinates yields

$$\begin{aligned} \{r^T\} &= [T_{NT}] \left[ \left\{ \begin{array}{c} 0 \\ -s \\ 0 \end{array} \right\} + [T_{RN}] \left\{ \begin{array}{c} r\sin(\theta_{RBi}) \\ 0 \\ r\cos(\theta_{RBi}) \end{array} \right\} \right] \\ &= [T_{NT}] \left[ \{r_N^N\} + [T_{RN}] \{r_{Bi}^R\} \right] , \end{aligned} \tag{B.4}$$

which implicitly defines the local position vectors $\{r_N^N\}$ and $\{r_{Bi}^R\}$. The upper vector index identifies the actual coordinate system, to which the vector components are referenced, and the lower index is just a part of the vector name. In Equation B.4 $s$ is the horizontal distance from the center-line of the tower to the center of the rotor and

$$[T_{NT}] = \left[ \begin{array}{ccc} 1 & -\theta_{zS} & 0 \\ \theta_{zS} & 1 & -\theta_{xS} \\ 0 & \theta_{xS} & 1 \end{array} \right] \tag{B.5}$$

is a linearized transformation matrix, which transforms a vector from nacelle-coordinates $(N)$ to tower-coordinates $(T)$, and

$$[T_{RN}] = \left[ \begin{array}{ccc} \cos(\theta_{NR}) & 0 & \sin(\theta_{NR}) \\ 0 & 1 & 0 \\ -\sin(\theta_{NR}) & 0 & \cos(\theta_{NR}) \end{array} \right] \tag{B.6}$$

is a transformation matrix, which transforms a vector from rotor-coordinates $(R)$ to nacelle-coordinates $(N)$.

Differentiation of the position vector with respect to time – here expressed with the operator $\left[\frac{\mathrm{d}}{\mathrm{d}t}\right] = [\,\dot{}\,]$ – gives the velocity of the mass element

$$\begin{aligned} \{\dot{r}^T\} = [T_{NT}] \Big[ \{\omega_{NT}^N\} \times \Big( \{r_N^N\} + [T_{RN}] \{r_{Bi}^R\} \Big) \\ + [T_{RN}] \Big( \{\omega_{RN}^R\} \Big) \Big] . \end{aligned} \tag{B.7}$$

After linearization the rotation vectors are derived to

$$\{\omega_{NT}^N\} \simeq \left\{ \begin{array}{c} \dot{\theta}_{xT} + \dot{\theta}_{xN} \\ 0 \\ \dot{\theta}_{zT} + \dot{\theta}_{zN} \end{array} \right\} \tag{B.8}$$

and

$$\{\omega_{RN}^R\} = \left\{ \begin{array}{c} 0 \\ \Omega \\ 0 \end{array} \right\} , \tag{B.9}$$

where $\Omega$ is the constant angular velocity of the rotor.

Finally, derivation of the velocity vector with respect to time yields the acceleration of the mass element. The acceleration is transformed to rotor coordinates (upper index $R$) merely to simplify the expression

$$\begin{aligned} \{\ddot{r}^R\} \;=\; & \Big([T_{NR}]\{\omega_{NT}^N\}\Big) \times \Big[\Big([T_{NR}]\{\omega_{NT}^N\}\Big) \times \Big([T_{NR}]\{r_N^N\} + \{r_{Bi}^R\}\Big) \\ & \qquad + 2\{\omega_{RN}^R\} \times \{r_{Bi}^R\}\Big] \\ & + \{\omega_{RN}^R\} \times \Big(\{\omega_{RN}^R\} \times \{r_{Bi}^R\}\Big) \\ & + \Big([T_{NR}]\{\dot{\omega}_{NT}^N\}\Big) \times \Big([T_{NR}]\{r_N^N\} + \{r_{Bi}^R\}\Big) , \end{aligned} \tag{B.10}$$

where $[T_{NR}]$ is the transposed of $[T_{RN}]$.

The moment from the inertia forces with respect to the rotation degrees of freedom are obtained by integration over the three blades. For example for the rotations in the tower coordinates ($T$) we get

$$\{M^T\} = \sum_{i=1}^{3} \left[ \int_0^R \{r^T\} \times \Big( - [T_{NT}][T_{RN}]\{\ddot{r}^R\}\, m\,(r, \theta_{RBi})\Big) \mathrm{d}r \right] . \tag{B.11}$$

Finally, the linearized equations of motion are obtained by requiring moment equilibrium at each degree of freedom between inertia forces, elastic forces and external forces, resulting in the equation

$$[M]\left\{\ddot{\theta}\right\} + [C]\left\{\dot{\theta}\right\} + [K]\{\theta\} = \{F\} \tag{B.12}$$

with the mass matrix

$$[M] = \begin{bmatrix} I_T + I_R + s^2 M_R & 0 & I_R + s^2 M_R & 0 \\ 0 & I_T + I_R + s^2 M_R & 0 & I_R + s^2 M_R \\ I_R + s^2 M_R & 0 & I_R + s^2 M_R & 0 \\ 0 & I_R + s^2 M_R & 0 & I_R + s^2 M_R \end{bmatrix} , \tag{B.13}$$

the gyroscopic matrix

$$[C] = \begin{bmatrix} 0 & -\Omega J & 0 & -\Omega J \\ \Omega J & 0 & \Omega J & 0 \\ 0 & -\Omega J & 0 & -\Omega J \\ \Omega J & 0 & \Omega J & 0 \end{bmatrix} , \tag{B.14}$$

the stiffness matrix

$$[K] = \begin{bmatrix} k_{xT} & 0 & 0 & 0 \\ 0 & k_{zT} & 0 & 0 \\ 0 & 0 & k_{xN} & 0 \\ 0 & 0 & 0 & k_{zN} \end{bmatrix} , \tag{B.15}$$

the vector with the elastic angular deformations

$$\{\theta\} = \begin{Bmatrix} \theta_{xT} \\ \theta_{zT} \\ \theta_{xN} \\ \theta_{zN} \end{Bmatrix} \tag{B.16}$$

and the vector with moments resulting from external forces

$$\{F\} = \begin{Bmatrix} M_{xT} \\ M_{zT} \\ M_{xN} \\ M_{zN} \end{Bmatrix} , \tag{B.17}$$

where

| | |
|---|---|
| $I_R$ | is the mass moment of inertia of the rotor about an axis in the rotor plane, e.g. $x_R$, |
| $J = 2I_R$ | is the mass moment of inertia of the rotor about an axis perpendicular to the rotor plane, i.e. $y_R$, and |
| $M_R$ | is the total mass of the rotor. |

Now, assuming that the solutions to Equation B.12 are harmonic with angular frequency $\omega$

$$\{\theta\} = \begin{Bmatrix} \theta_{xT0} \\ \theta_{zT0} \\ \theta_{xN0} \\ \theta_{zN0} \end{Bmatrix} \exp^{i\omega t} = \{\theta_0\} \exp^{i\omega t} \tag{B.18}$$

and that the external forces are zero, $\{F\} = \{0\}$, the natural frequencies are determined from the equation

$$\Big( -\omega^2 [M] + i\omega [C] + [K] \Big) \{\theta_0\} \exp^{i\omega t} = \{0\} , \tag{B.19}$$

where $i$ is the imaginary unit.

The characteristic equation (the determinant of the matrix sum in the left parenthesis in Equation B.19) is derived and the roots of this equation are found to give the natural frequencies, $\omega = \omega_n = \omega_{gw}$, which we identify as the *global rotor whirl* frequencies

$$\mathrm{Det}\Big( I_T, I_R, s^2 M_R, J, \Omega, k_{xT}, k_{zT}, k_{xN}, k_{zN}, \omega_n \Big) = 0 . \tag{B.20}$$

The determinant expression is rather complex (a polynomial with $\omega_n$ in the $8^{th}$ power) and the solutions are most conveniently found by numerical methods. If we assume that the

stiffnesses are symmetric, i.e. $k_{xT} = k_{zT} = k_T$ and $k_{xN} = k_{zN} = k_N$, we get the somewhat reduced determinant expression

$$\begin{aligned}
\mathrm{Det}(\omega_n) \quad = \quad & \Big[ I_T(I_B + s^2 M_R)\omega_n^4 - I_T J\Omega\omega_n^3 \\
& - \Big( I_T k_N + \left(I_B + s^2 M_R\right)(k_T + k_N) \Big)\omega_n^2 \\
& + J\Omega\,(k_T + k_N)\,\omega_n + k_T k_N \Big] \times \\
& \Big[ I_T(I_B + s^2 M_R)\omega_n^4 + I_T J\Omega\omega_n^3 \\
& - \Big( I_T k_N + \left(I_B + s^2 M_R\right)(k_T + k_N) \Big)\omega_n^2 \\
& - J\Omega\,(k_T + k_N)\,\omega_n + k_T k_N \Big] \,. \qquad \text{(B.21)}
\end{aligned}$$

## B.1 Examples

Below we show examples of solution of the characteristic equation. We choose values for structural parameters typical for a wind turbine with 19 m blades. Two configurations are chosen with different stiffnesses in the rotational DOFs. The actual values of the structural parameters are listed in Table B.1.

*Table B.1. Structural parameters for the example turbines.*

| Variable | Units | Example 1 | Example 2 |
|---|---|---|---|
| $I_T$ | kgm$^2$ | $2.5\,10^5$ | $2.5\,10^5$ |
| $I_R$ | kgm$^2$ | $1.9\,10^5$ | $1.9\,10^5$ |
| $s^2 M_R$ | kgm$^2$ | $4.3\,10^4$ | $4.3\,10^4$ |
| $k_{xT}$ | Nm/rad | $1.6\,10^8$ | $6.0\,10^7$ |
| $k_{zT}$ | Nm/rad | $0.70 \times k_{xT}$ | $0.75 \times k_{xT}$ |
| $k_{xN}$ | Nm/rad | $1.4\,10^7$ | $4.0\,10^7$ |
| $k_{zN}$ | Nm/rad | $k_{xN}$ | $k_{xN}$ |

In Figure B.2 the natural frequencies for Example 1 are shown as function of rotor speed. The two lowest frequencies correspond to the $1^{st}$ yaw and tilt mode shapes, respectively. It is observed that the natural frequencies depend considerably on the rotational speed, due to the gyroscopic forces. The yaw and tilt rotations are uncoupled at stand still, but when the turbine rotates, the two deformations couple due to the gyroscopic forces. The degree of coupling depends on how much the direction of the rotor shaft – the direction of the $y_R$-axis – is changed due to the elastic deformations. In general, the coupling results in deformations, which makes the rotor center follow an elliptical orbit as indicated in Figure B.1. In the present context we denote this motion of the rotor *global rotor whirl*. The orbit is characterized by the direction in which the rotor center travels the elliptical path. Depending on the actual stiffnesses the direction might be either *forward* or *backward*. *Forward whirl* means that the elliptical orbit is travelled in the same direction as the turbine rotates, i.e. in the same direction as $\Omega$, and vice versa for *backward whirl*. The actual directions for the example are indicated in Figure B.2. The direction of the whirl motion has been found by solving the equations of motion in the time domain by applying a harmonic excitation at the actual natural frequency.

The two highest frequencies for Example 1 correspond to the $2^{nd}$ yaw and tilt mode shapes. In the present case they depend only very little on the rotor speed, which means that the deformations at the tower top and at the main bearing are almost identical, but in counter-phase, so that the direction of the rotor shaft is practically unchanged during the vibration.

The natural frequencies for Example 2 are shown in Figure B.3. The changed stiffnesses make the $1^{st}$ yaw and tilt modes less dependent on the rotor speed, while the $2^{nd}$ yaw and tilt modes are now more influenced by the rotor speed, when compared to Example 1.

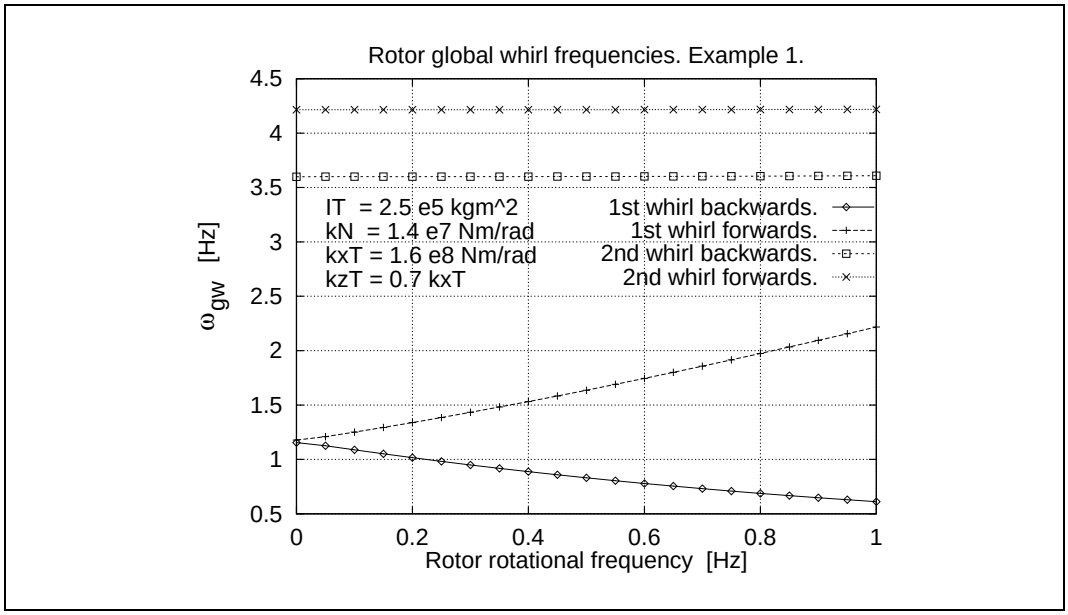


*Figure B.2. Natural frequencies for Example 1 as function of rotor speed.*

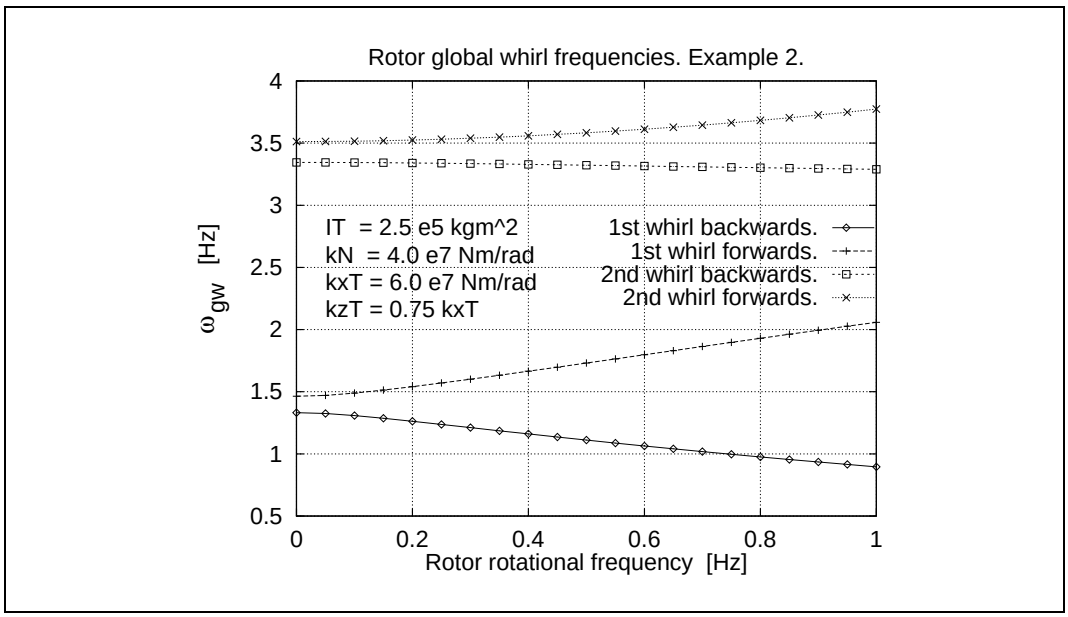


*Figure B.3. Natural frequencies for Example 2 as function of rotor speed.*

**Bibliographic Data Sheet** **Risø-R-1045(EN)**

Title and author(s)

Prediction of Dynamic Loads and Induced Vibrations in Stall.

Jørgen Thirstrup Petersen, Helge Aagaard Madsen, Anders Björck,
Peder Enevoldsen, Stig Øye, Hans Ganander, Danny Winkelaar

| ISBN | ISSN |
|---|---|
| 87–550–2284–3 ; 87–550–2437–8 (Internet) | 0106–2840 |

| Dept. or group | Date |
|---|---|
| Wind Energy and Atmospheric Physics | May 1998 |

| Groups own reg. number(s) | Project/contract No. |
|---|---|
| AED 04493-00 ; AED 04659-00 | JOR3-CT95-0047 ; ENS-1363/96-0001 ; ENS-1363/97-0002 |

| Pages | Tables | Illustrations | References |
|---|---|---|---|
| 160 | 9 | 154 | 25 |

Abstract (Max. 2000 char.)

Results from research in an EC Joule-III project and from national projects are presented. The objectives are improvement of design methods for stall regulated wind turbines with emphasis on stall induced vibrations and dynamic stall. The primary concern is limitation of the edgewise vibrations in the fundamental blade natural mode shape, which have caused trouble on modern wind turbines of approximate size 500 kW nominal power and 40 m rotor diameter. A theoretical study of quasi-steady aerodynamics confirms that the vibrations are driven basically by energy supplied from the aerodynamic forces during stalled operation. This energy exchange is equivalent to negative aerodynamic damping. The theoretical approach identifies the main parameters controlling the phenomenon. These parameters describe the steady and the dynamic airfoil characteristics, the overall aerodynamic layout of the blade, e.g. chord length and twist, the structural properties of the blade, e.g. structural damping and properties controlling the resulting vibration direction. Furthermore, full aeroelastic calculations and comparison with measurements show that the properties of the supporting structure, i.e. the main shaft, the nacelle and the tower, are important, as the global vibration of the rotor on its support may exchange energy with the blade vibration, when the blade natural frequency is close to one of the frequencies of the coupled rotor tilt-yaw mode shapes, usually denoted the global rotor whirl frequencies. It is confirmed that the influence of changing the primary design parameters can be determined by use of qualified aeroelastic calculations. Presented design guidelines therefore build on both the simple quasi-steady models, which can be used for the preliminary choice of the design variables mentioned above, and on full aeroelastic calculations. The aeroelastic calculations refine the design basis and should be used for choosing the final design variables and for final verification of the design. Through this design procedure it is possible to assess the required safety margin against stall induced vibrations.

Descriptors INIS/EDB

AERODYNAMICS; AIRFOILS; HORIZONTAL AXIS TURBINES; MATHEMATICAL MODELS; MECHANICAL VIBRATIONS; STALL; STEADY-STATE CONDITIONS; WIND LOADS

Available on request from:
Information Service Department, Risø National Laboratory
(Afdelingen for Informationsservice, Forskningscenter Risø)
P.O. Box 49, DK–4000 Roskilde, Denmark
Phone (+45) 46 77 46 77, ext. 4004/4005 · Fax (+45) 46 77 40 13 · Telex 43 116